Improving Precision for Hadronic Observables in the Standard Model and Beyond

DISSERTATION
zur Erlangung des akademischen Grades eines Doktors
der Naturwissenschaften

vorgelegt von

Matthew Black, M.Phys.

eingereicht bei der Naturwissenschaftlich-Technischen Fakultät
der Universität Siegen

Siegen
October 2024

Betreuer und erster Gutachter

Prof. Dr. Alexander Lenz

Universität Siegen

Zweiter Gutachter

Prof. Dr. Christopher Monahan

Colorado College

Weitere Mitglieder der Promotionskommission

Prof. Dr. Thomas Mannel

Universität Siegen

und

Prof. Dr. Christoph Wunderlich

Universität Siegen

und

Prof. Dr. Robert Harlander

RWTH Aachen University

Tag der mündlichen Prüfung

8. Oktober 2024

Abstract

Searching for new physics not described by the Standard Model (SM) is of great importance to enhance our understanding the universe. One possibility to discover new physics is to perform precision tests of the SM by comparing experimental measurements with theoretical predictions. Taking advantage of the vast set of experimental results, we first perform global fits to test and constrain a class of extensions to the SM referred to as Two-Higgs-Doublet models (2HDMs). In addition, we discuss a motivation for collider searches for the rare process $B_s \to e^+e^-$ which can be greatly enhanced in a 2HDM without conflicting with other data. Large uncertainties from non-perturbative hadronic observables limit the ability to constrain the parameter space of 2HDMs or other new physics scenarios.

Next we focus at improving predictions for hadronic observables by non-perturbatively calculating matrix elements of four-quark operators for neutral meson mixing and heavy meson lifetimes using lattice quantum chromodynamics (QCD). In particular, we perform a pilot study establishing a non-perturbative renormalisation procedure via the gradient flow and its short-flow-time expansion allowing us to quote final results in the $\overline{\text{MS}}$ scheme. Considering for simplicity a neutral charm-strange (D_s) meson on the lattice, we determine the $\mathcal{O}_1$ operator for neutral meson mixing as well as the $\mathcal{O}_1$ and T_1 operators describing heavy meson lifetimes. Our short-distance contribution to mixing for a neutral D_s meson is $B_s^{\overline{\text{MS}}}(3\,\text{GeV}) = 0.787(5)$ where the quoted error accounts for statistical and perturbative truncation uncertainties only. This value is in good agreement with literature results for short-distance D^0 mixing where only the spectator quark differs. In addition we pioneer the calculation of the four-quark operators $\mathcal{O}_1$ and T_1 for heavy meson lifetimes in lattice QCD. Essential for this determination is that our gradient flow procedure suppresses the mixing with operators of lower mass dimension on the lattice. Although our lattice calculation does not include all diagrams and also the perturbative matching to the $\overline{\text{MS}}$ scheme is still incomplete, we observe that our values $B_1^{\overline{\text{MS}}} = 1.110(2)$ and $\epsilon_1^{\overline{\text{MS}}} = 0.119(1)$ have the same order of magnitude as corresponding determinations based on HQET sum rules.

Zusammenfassung

Die Suche nach neuer Physik, die nicht durch das Standardmodell (SM) beschrieben wird, ist von großer Bedeutung, um unser Verständnis des Universums zu verbessern. Eine Möglichkeit, neue Physik zu entdecken, besteht darin, Präzisionstests des SM durchzuführen, bei denen experimentelle Messungen mit theoretischen Vorhersagen verglichen werden. Unter Ausnutzung der großen Menge an experimentellen Resultaten führen wir zunächst globale Fits durch, um eine Klasse von Erweiterungen des SM zu testen und einzuschränken, die als Two-Higgs-Doublet-Modelle (2HDMs) bezeichnet werden. Darüber hinaus diskutieren wir die Motivation für Kollidersuchen nach dem seltenen Prozess $B_s \to e^+e^-$, der in einem 2HDM deutlich verstärkt sein kann, ohne Konflikte mit anderen Daten zu erzeugen. Große Unsicherheiten durch nicht-perturbative hadronische Observablen schränken die Möglichkeit ein, den Parameterraum von 2HDMs oder anderen Szenarien der neuen Physik einzugrenzen.

Als nächstes konzentrieren wir uns auf die Verbesserung der Vorhersagen für hadronische Observablen, indem wir nicht-perturbative Matrixelemente von Vier-Quark-Operatoren für neutrale Mesonenmischung und Lebensdauern schwerer Mesonen mit Hilfe der Gitter-Quantenchromodynamik (QCD) berechnen. Insbesondere führen wir eine Pilotstudie durch, um ein nicht-perturbatives Renormierungsverfahren mittles Gradient-Flow und dessen Short-Flow-Time-Entwicklung zu etablieren und Endergebnisse im $\overline{\text{MS}}$-Schema anzugeben. Zur Vereinfachung des Problems, betrachten wir ein auf dem Gitter neutrales Charm-Strange-Meson (D_s) und bestimmen den $\mathcal{O}_1$-Operator für neutrale Mesonenmischung, sowie die $\mathcal{O}_1$- und T_1-Operatoren für die Lebensdauer schwerer Mesonen. Unser Nahdistanzbeitrag zur Mischung für ein neutrales D_s-Meson beträgt $B_s^{\overline{\text{MS}}}(3\,\text{GeV}) = 0.787(5)$, wobei der angegebene Fehler nur statistische Unsicherheiten und perturbative Abbruchfehler berücksichtigt. Dieser Wert ist in guter Übereinstimmung mit Literaturwerten für Nahdistanz-D^0-Mischung, bei der sich nur das "Zuschauer-Quark" unterscheidet. Desweiteren haben wir Pionierarbeit bei der Berechnung der Vier-Quark-Operatoren $\mathcal{O}_1$ und T_1 für Lebensdauern schwerer Mesonen in der Gitter-QCD geleistet. Wesentlich für diese Bestimmung ist, dass unsere Gradient-Flow-Methode das Mischen mit Operatoren niedrigerer Massendimensionen auf dem Gitter unterdrückt. Obwohl unsere Gitterrechnung nicht alle Diagramme umfasst und auch die perturbative Konvertierung ins $\overline{\text{MS}}$-Schema noch unvollständig ist, haben unsere Werte für $B_1^{\overline{\text{MS}}} = 1.110(2)$ und $\epsilon_1^{\overline{\text{MS}}} = 0.119(1)$ die gleiche Größenordnung, wie entsprechende Bestimmungen, die auf HQET-Summenregeln basieren.

Acknowledgements

First and foremost, I would like to express my deepest gratitude to Prof. Dr. Alexander Lenz and Dr. Oliver Witzel for their unwavering guidance and support throughout my PhD journey. Both of you have been exceptional mentors, and I am incredibly fortunate to have had the privilege to learn from and work with you both.
To Oliver, your expertise, insight, and meticulous attention to detail have been invaluable in shaping my future as a researcher. I am immensely grateful for the endless patience and constant encouragement you have given me, always driving me towards deeper understanding and higher quality of research.
To Alex, your profound knowledge and boundless energy have been a tremendous source of inspiration. I deeply appreciate the positivity you bring to all and how your excitement for physics has greatly enriched my academic journey.

I would also like to express my sincere appreciation to all my collaborators and the members of the TP1 group in Siegen for creating such amazing working environments. You have all helped shaped my journey and deepen my knowledge further. The camaraderie and enthusiasm I have shared with you all have truly enhanced my experiences in the last three years. I am grateful for the shared knowledge and mutual support which have been instrumental in my progress.

My heartfelt gratitude goes out to my family and friends for their unwavering love and support. Your constant encouragement and support have been a source of strength and motivation throughout my journey. Thank you for always being there to provide a listening ear or a moment of laughter whenever I needed it, this journey would not have been possible without you all.

Vielen Dank euch allen für eure Unterstützung.

Finally, I gratefully acknowledge computing resources provided by the OMNI cluster at the University of Siegen, the HAWK cluster at the High-Performance Computing Center Stuttgart, and LUMI-G at the CSC data center Finland (DeiC National HPC g.a. DEIC-SDU-L5-13 and DEIC-SDU-N5-2024053). I thank the RBC/UKQCD collaboration for generating and making the 2+1 flavour DWF + Iwasaki gauge field ensembles publicly available. This work relied on the `Grid` and `Hadrons` software, and I particularly thank Felix Erben, Ryan Hill, and J. Tobias Tsang for their advice. I received support from the Deutsche Forschungsgemeinschaft (DFG, German Research Foundation) through grant 396021762 - TRR 257 "Particle Physics Phenomenology after the Higgs Discovery". I further thank ECT* for support at the Workshop "The Gradient Flow in QCD and other strongly coupled field theories" during which work in chapter 6 has developed.

"Each man delights in the work that suits him best."

Homer, The Odyssey

Contents

List of Figures

List of Tables

Chapter 1

Introduction – Colour Meets Flavour

The Standard Model of particle physics (SM) [1–3] is the most successful theory developed so far to describe elementary particles and their interactions via the strong, weak, and electromagnetic forces – gravity is not included in the SM. With the discovery of the Higgs boson in 2012 at the Large Hadron Collider (LHC) by the ATLAS [4] and CMS [5] experiments, all expected elementary particles of the SM have been discovered. To date, no observed phenomena at particle colliders have a confirmed deviation from the SM's predicted behaviour, with the exception of the existence of neutrino masses [6, 7]. While the success of the Standard Model is remarkable and to be celebrated, it is clear from further phenomenological and cosmological arguments that there is more to add to our theory than just neutrino masses:

- insufficient CP violation in the SM to account for the observed matter-antimatter asymmetry of the universe [8];
- the existence of dark matter (see e.g. [9]);
- the SM is not an ultraviolet (UV) complete theory and must only be a low-energy limit of a more complete model (see for instance [10–12]) – this includes a unification with gravity in a renormalisable theory.

In addition, there are currently a number of known tensions between the SM and experiment, however none of these are yet interpreted as accepted signatures of new physics; improved precision in experimental measurements and theoretical predictions is the focus for many researchers in order to either confirm the deviations or reaffirm the SM.

Some examples of these tensions are:

- The 'Cabibbo angle anomaly' which observes a $\sim 3\sigma$ deficit from expected unitarity in the first row of the Cabibbo-Kobayashi-Maskawa (CKM) quark mixing matrix [13–17]. This observation also comes with disagreement between measurements using the highly-precise super-allowed beta decays [18]. This tension is in spite of a theoretically very clean calculation since it is a pure vector transition free from uncertainties due to the nuclear structure.

- The so-called 'golden modes' of non-leptonic tree-level B meson decays, e.g. $\bar{B}^0_{(s)} \to D^{(*)+}_{(s)} L^-$ (for a light pseudoscalar meson $L = K, \pi$), where all final-state flavours are distinct [19]. In this scenario, many usual contributions to two-body non-leptonic decays are absent and therefore these are expected to be the most theoretically clean of the non-leptonic decays. However, when comparing to experimental measurements, one finds a theoretical excess of $2 - 5\sigma$ depending on the specific channel, and in fact, a combined analysis can result in a tension as much as 7σ [20–24]. The theoretical predictions stem from the leading power estimates of *QCD factorisation* and the big question remains of how large these power corrections really are. There is also recent work suggesting that these tensions can be resolved by improved treatment of the hadronic effects [25].

- The *flavour anomalies* in semileptonic B meson decays are a group of processes all showing some tension with the Standard Model. Many processes in this group stem from the $b \to s\ell^+\ell^-$ transition, such as those in the differential branching ratios and angular observables of $B \to K^{(*)}\mu^+\mu^-$ and $B_s \to \phi\mu^+\mu-$. The tensions here vary and can reach as much as 5σ; see, e.g. [26–30]. These are loop-level processes in the SM and therefore rather suppressed; it is simple to introduce some model of new physics where these processes would occur at tree-level and therefore have sizeable contributions compared to the SM, such as Z' models [31] or type-III Two-Higgs-Doublet models (see chapter 4).

- *Lepton flavour universality* (LFU) ratios compare processes differing only by lepton flavour. These channels are extremely clean theoretically with much of the 'dirty' hadronic physics cancelling out, and so they are expected to be useful tests of the Standard Model, with these ratios in semileptonic B meson decays receiving a lot of attention. For a long time however, there was as much as $\sim 4\sigma$ tension in the $B \to K^{(*)}\ell^+\ell^-$ channels which have since been resolved back to agreement with the SM with new updates to the experimental measurements [32, 33]. The LFU ratios in $B \to D^{(*)}\ell\nu$, $R_{D^{(*)}}$, remain with a $\sim 3\sigma$ tension to the SM [26]. Unlike the B anomalies discussed above, $B \to D^{(*)}\ell\nu$ is a tree-level decay in the SM and therefore most new physics scenarios do not immediately come with enhanced contributions versus the SM for these processes.

From this list, it should be clear that the area of quark flavour physics is well-suited to looking for tensions with the Standard Model and testing models of new physics to resolve these tensions. Many experiments over the past 20 years have provided a huge array of high-precision data for flavour observables, see e.g. the summary of the Heavy Flavour Averaging Group (HFLAV) which collects all these measurements [26]. To complement these experiments, the theoretical understanding of quark flavour processes has developed over many years and is by now well-advanced, with the perturbative calculations reaching next-to-next-to-next-to-leading order (N^3LO) in QCD for the case of the free quark semileptonic decay [34–36]. The large scale introduced by a heavy charm or bottom quark mass (in contrast to the hadronic confinement scale Λ_{QCD}) provides many interesting simplifications and one can implement the frameworks of the Heavy Quark Effective Theory and the Heavy Quark Expansion to great success. Using these frameworks allows for high-precision comparisons between theory and experiment which are necessary to better resolve the afore-mentioned tensions or find new physics explanations for these.

In many of the heavy flavour processes with exciting prospects towards constraining the SM and finding new physics, typically the non-perturbative hadronic contributions to their predictions also contribute the largest uncertainties and so it is of great importance to better constrain these matrix elements to increase the precision of our analysis. Non-perturbative physics can be studied with various theoretical tools such as QCD sum rules [37–39] and the systematically-improvable lattice QCD [40], which presents the most promising prospects for increasing the theoretical precision over time in line with the steady advancement of the experimental precision.

In this thesis, we will discuss the power of the 'colour' physics of non-perturbative QCD and how it complements the use of flavour physics in studying and constraining the Standard Model and beyond. In chapter 4, we will give details on the study of new physics through indirect searches in the flavour sector (amongst others) and in particular study the Two-Higgs-Doublet Model in multiple scenarios, with emphasis on the hadronic matrix elements contributing to the studied observables and how increased precision for these can in turn increase our sensitivity to new physics. The research of chapter 4 is the result of four publications which were carried out in the first half my PhD:

- O. Atkinson, M. Black, A. Lenz, A. Rusov and J. Wynne, *Cornering the Two Higgs Doublet Model Type II*, JHEP **04** (2022) 172 [arXiv:2107.05650], [41].
- O. Atkinson, M. Black, C. Englert, A. Lenz, A. Rusov and J. Wynne, *The flavourful present and future of 2HDMs at the collider energy frontier*, JHEP **11** (2022) 139 [arXiv:2202.08807], [42].

- O. Atkinson, M. Black, C. Englert, A. Lenz and A. Rusov, *MUonE, muon g-2 and electroweak precision constraints within 2HDMs*, Phys. Rev. D **106** (2022) 115031 [arXiv:2207.02789], [43].

- M. Black, A. D. Plascencia and G. Tetlalmatzi-Xolocotzi, *Enhancing $B_s \to e^+e^-$ to an observable level in the two-Higgs-doublet model*, Phys. Rev. D **107** (2023) 035013 [arXiv:2208.08995], [44].

I was integral to the efforts of writing the code for the many fits and scans need for these papers, which I also subsequently ran on OMNI (a CPU cluster at the University of Siegen). Furthermore, I worked on understanding and interpreting their results and phenomenological impacts.

With the theoretical and phenomenological prospects laid out, we will turn our focus to non-perturbative methods to predict hadronic observables, with a particular focus on lattice QCD. Chapter 6 will outline a pilot study towards the calculation for the first time in full lattice QCD of the dimension-six four-quark $\Delta B = 0$ operators contributing to the lifetime predictions of heavy B mesons. This research is ongoing and will continue beyond the scope of this thesis, however early work was already presented in the proceedings

- M. Black, R. Harlander, F. Lange, A. Rago, A. Shindler and O. Witzel, *Using Gradient Flow to Renormalise Matrix Elements for Meson Mixing and Lifetimes*, PoS **LATTICE2023** (2024) 263 [arXiv:2310.18059], [45],

and we plan to publish the findings of these pilot studies later this year. A significant portion of my PhD program has consisted of personally driving this pilot study to success, starting from early work implementing the fermionic gradient flow in `Hadrons`, a `C++` library utilising `Grid` to perform valence sector measurements in QCD-like theories. Later I performed the large-scale simulations on OMNI, HAWK (a CPU cluster at the High-Performance Computing Center Stuttgart), and LUMI-G (a GPU-accelerated cluster at the CSC data center in Finland), as well as all the steps of the current data analysis.

Chapter 2

The Standard Model of Particle Physics

The Standard Model is a quantum gauge theory, being described by its local gauge symmetry

$$\mathrm{SU}(3)_C \otimes \mathrm{SU}(2)_L \otimes \mathrm{U}(1)_\mathrm{Y}, \tag{2.1}$$

with C representing *colour*, L the *left-handed weak isospin*, and Y the *weak hypercharge*. $\mathrm{SU}(2)_L \otimes \mathrm{U}(1)_\mathrm{Y}$ forms the *electroweak interaction*. The elementary particle content of the SM will be discussed in section 2.1 before considering the electroweak interaction in section 2.2 and how its symmetry is spontaneously broken, giving rise to interesting and important phenomena of the Standard Model, including the $U(1)_Q$ symmetry of the electric charge Q more familiar to us from electromagnetism. Then discussed in section 2.3 is $\mathrm{SU}(3)_C$ as the symmetry of the *strong interaction* and its formulation as quantum chromodynamics (QCD). Throughout this chapter, we follow closely the textbooks [10, 46], to which we refer for a more comprehensive overview of the Standard Model and further references within.
There are three discrete symmetries important to the SM:

- charge conjugation (C): a particle is interchanged with its antiparticle, e.g.

$$e^- \xrightarrow{\mathrm{C}} \bar{e} = e^+; \tag{2.2}$$

- parity (P): a reversal of the spatial coordinates

$$x^\mu = (x_0, \vec{x}) \xrightarrow{\mathrm{P}} (x_0, -\vec{x}); \tag{2.3}$$

➤ time reversal (T): a reversal of the temporal coordinate:

$$x^\mu = (x_0, \vec{x}) \xrightarrow{\mathrm{T}} (-x_0, \vec{x}). \tag{2.4}$$

Both electromagnetism and the strong interaction are found experimentally to obey P symmetry, however the weak interaction was found experimentally to violate parity [47, 48]. The combined CP symmetry was then proposed as the fundamental symmetry, however the weak interaction was also found to violate CP, famously discovered in 1964 in kaon decays [49]. The Lagrangian of the strong interaction in principle allows for a CP-violating term, however there is currently no experimental evidence to support this. All three forces of the Standard Model obey the combined CPT symmetry.

Elementary particles are described by dynamical quantum fields permeating across spacetime, and their interactions stem from the gauge fields of the constituent gauge symmetries of the theory. The resulting Standard Model Lagrangian can be written as

$$\begin{aligned}\mathcal{L} = &-\frac{1}{4}F^{\mu\nu}F_{\mu\nu} + i\bar{\Psi}\not{D}\Psi \\ &+(D_\mu\Phi)^\dagger(D^\mu\Phi) - V(\Phi) - Y_{ij}\bar{\Psi}_i\Phi\Psi_j + h.c.\end{aligned} \tag{2.5}$$

In this chapter, we will first introduce the particle content of the Standard Model in section 2.1, before outlining the theories of electroweak (EW) and strong interactions in sections 2.2 and 2.3 respectively. Finally, quark mixing and the Cabibbo-Kobayashi-Maskawa (CKM) matrix will be discussed in section 2.4.

2.1 Elementary Particles

Here we give a brief summary of the known elementary particles of the universe as described by the SM; by *elementary* we refer to particles which are currently considered to be fundamental and not composed of other particles. The elementary particles can be categorised into those with spin-$\frac{1}{2}$ (fermions) and those with integer spin-$0, 1$ (bosons).

After accounting for electric and colour charges, there are in total thirteen bosons. From the EW interaction, after spontaneous symmetry breaking, comes five: of the weak sector, there are Z^0 and $W^\pm$ (spin-1); of electromagnetism, there is the photon γ (spin-1); and finally as a result of the spontaneous symmetry breaking, there is the Higgs boson h^0 (spin-0). From QCD, there is the gluon g which has eight independent colour combinations. After showing how the bosons of the spontaneously-broken Lagrangian are formed, the properties of these bosons are summarised in table 2.1.

The fermions come in three generations, broadly following a mass hierarchy from first to third[1], and are further split into two categories: quarks, which have colour charge and interact with the strong force, and leptons, which do not. The leptons are separated into the charged leptons (electron e, muon μ, tau τ) and the neutral leptons called neutrinos (ν_e, ν_μ, ν_τ) where each gets its label from the charged lepton of the same generation. After discussing how these arise from the EW theory, the properties of the leptons in the SM are summarised in table 2.2.

The quarks are separated into up-type quarks (up u, charm c, top t) with electric charge $+\frac{2}{3}$ and down-type quarks (down d, strange s, bottom b) with electric charge $-\frac{1}{3}$. Due to a property of QCD called *confinement*, quarks (i.e. particles with colour charge) cannot exist as free particles but are instead observed as constituent particles of (colour-neutral) bound states called hadrons. Excluding more exotic types which are less well-studied, hadrons appear in two forms: mesons, formed of one quark and an anti-quark, and baryons, formed of three quarks. After covering how the quarks interact with the electroweak and strong theories, the properties of quarks are summarised in table 2.3.

2.2 Electroweak Interaction and Spontaneous Symmetry Breaking

The electroweak interaction [1, 2, 50] of the Standard Model is the unification of quantum electrodynamics (QED, i.e. the theory of electromagnetism) and the weak interaction. This forms the $\mathrm{SU}(2)_L \otimes \mathrm{U}(1)_Y$ part of the SM gauge group. In this section we will show how this gauge group is broken into $\mathrm{U}(1)_Q$ through spontaneous symmetry breaking (SSB) of the Higgs potential, which will also yield the massive gauge bosons of the weak force – $W^\pm$, Z^0 – and the photon of the electromagnetic force – γ [51–53].

2.2.1 Electroweak Gauge Fields

We first consider the gauge sector of the EW Lagrangian, which reads[2]

$$\mathcal{L}^{\mathrm{EW}}_{\mathrm{gauge}}(x) = -\frac{1}{4} B_{\mu\nu}(x) B^{\mu\nu}(x) - \frac{1}{4} W^i_{\mu\nu}(x) W^{i\mu\nu}(x), \tag{2.6}$$

where $B_{\mu\nu}$ is the field strength tensor of the $\mathrm{U}(1)_Y$ symmetry and $W^i_{\mu\nu}$ of the $\mathrm{SU}(2)_L$ symmetry, with $i = 1, 2, 3$ the indices for the generators of $\mathrm{SU}(2)_L$. In general, a field

[1] It is not known if massive neutrinos will follow this same hierarchy.
[2] Unless otherwise stated, from now we assume the Einstein summation convention.

strength tensor $F_{\mu\nu}$ is defined

$$F_{\mu\nu}(x) = [D_\mu, D_\nu], \tag{2.7}$$

where the covariant derivative D_μ is dependent on the gauge symmetry. The EW covariant derivative of $\mathrm{SU}(2)_L \otimes \mathrm{U}(1)_Y$ is defined as

$$D_\mu = \partial_\mu + igW^i_\mu(x)\tau^i + i\frac{g'}{2}B_\mu(x)Y, \tag{2.8}$$

where g, g' are the gauge couplings of $\mathrm{SU}(2)_L$, $\mathrm{U}(1)_Y$ respectively, Y is the generator of $\mathrm{U}(1)_Y$, and $\tau^i = \frac{1}{2}\sigma^i$ are the $\mathrm{SU}(2)_L$ generators defined using the Pauli matrices σ^i.
For the Abelian symmetry group U(1), the covariant derivative is defined

$$D_\mu = \partial_\mu + i\frac{g'}{2}B_\mu(x)Y. \tag{2.9}$$

There are therefore no self-interactions of the B-field, i.e.

$$B_{\mu\nu}(x) = \partial_\mu B_\nu(x) - \partial_\nu B_\mu(x). \tag{2.10}$$

For the non-Abelian $\mathrm{SU}(2)_L$, the covariant derivative is defined

$$D_\mu = \partial_\mu + igW^i_\mu(x)\tau^i. \tag{2.11}$$

Now one does find self-interactions between the gauge bosons W^i, i.e.

$$\begin{aligned} W^i_{\mu\nu}(x) &= \partial_\mu W^i_\nu(x) - \partial_\nu W^i_\mu(x) + ig[W^b(x), W^c(x)] \\ &= \partial_\mu W^i_\nu(x) - \partial_\nu W^i_\mu(x) - g\epsilon^{abc}W^b(x)W^c(x). \end{aligned} \tag{2.12}$$

One should note that the mass term for a gauge boson $m^2A^\mu A_\mu$ cannot appear in our Lagrangian since it would violate gauge symmetry, and therefore the gauge bosons B, W^i are so far massless.

2.2.2 Chiral Fermions

For fermion interactions in the EW sector, we can start by considering the Dirac Lagrangian term,

$$\mathcal{L}_{\mathrm{Dirac}}(x) = \sum_\ell \bar{\psi}_\ell(x)(i\not{D} - m_\ell)\psi_\ell(x), \tag{2.13}$$

where ℓ sums over the 6 leptons and $\not{D} = \gamma^\mu D_\mu$. γ^μ are the Dirac gamma matrices as described in appendix A.2 and D_μ is the appropriate covariant derivative for each fermion, e.g. equation (2.8) for leptons. However, simply adding this term to the EW

Lagrangian does not work because the mass term will not be gauge invariant due to the chiral nature of the EW interaction which must be introduced to describe the parity violation seen in nature. This chiral nature leads to the decomposition of fermion fields ψ into left- and right-handed chiral components:

$$\begin{aligned} \psi &= \psi_L + \psi_R, \\ \psi_L &= P_L\psi = \frac{1}{2}(1-\gamma_5)\psi, \\ \psi_R &= P_R\psi = \frac{1}{2}(1+\gamma_5)\psi, \end{aligned} \tag{2.14}$$

where $\gamma_5 = i\gamma_0\gamma_1\gamma_2\gamma_3$. Under the $\mathrm{SU}(2)_L$ symmetry, these components interact differently: left-handed fermions are contained within SU(2) doublets and transform under this interaction, while right-handed fermions are SU(2) singlets and do not. Each generation of lepton or quark forms its own doublet pair and singlet, i.e.

$$L_i = \begin{pmatrix} \nu_{e_i} \\ e_i \end{pmatrix}_L, \; R = e_{iR} \qquad Q_{iaL} = \begin{pmatrix} u_{ia} \\ d_{ia} \end{pmatrix}_L, \; U_{iaR} = u_{iaR}, \; D_{iaR} = d_{iaR}, \tag{2.15}$$

with i the fermion generation and a the colour index of the quarks (to be discussed in section 2.3). This leads to parity violation of the EW sector as required by nature.

The separation of chiralities in equation (2.14) rewrites equation (2.13) (neglecting the sum over ℓ), leading to

$$\mathcal{L}_{\mathrm{Dirac},\chi}(x) = \bar{\psi}_L i\not{D}\psi_L + \bar{\psi}_R i\not{D}\psi_R - m\left(\bar{\psi}_L\psi_R + \bar{\psi}_R\psi_L\right), \tag{2.16}$$

where one can see a mixing of left-handed and right-handed fields in the mass term, such that the Lagrangian is not gauge invariant for $m \neq 0$. Therefore at this stage of constructing the EW Lagrangian, only massless gauge bosons and fermions appear; this is in disagreement with nature where we observe massive fermions and massive gauge bosons, $W^{\pm}, Z^0$.

2.2.3 The Higgs Mechanism

In order to solve the problem of massive gauge bosons, a complex scalar field ϕ transforming as a SU(2) doublet can be introduced:

$$\Phi = \frac{1}{\sqrt{2}}\begin{pmatrix} \phi_1 + i\phi_2 \\ \phi_0 + i\phi_3 \end{pmatrix} = \frac{1}{\sqrt{2}}\begin{pmatrix} \phi^+ \\ \phi^0 \end{pmatrix}, \quad \phi^+, \phi^0 \in \mathbb{C}. \tag{2.17}$$

The Higgs Lagrangian is given by

$$\mathcal{L}_{\text{Higgs}}(x) = (D^{\mu}\Phi)^{\dagger}(D_{\mu}\Phi) - V(\Phi), \tag{2.18}$$

where the covariant derivative is that of equation (2.8) and the scalar potential $V(\Phi)$ is defined

$$V(\Phi) = -\mu^2\Phi^{\dagger}\Phi + \lambda(\Phi^{\dagger}\Phi)^2. \tag{2.19}$$

We can choose the unitary gauge such that

$$\Phi = \frac{1}{\sqrt{2}}\begin{pmatrix}\phi^+\\ \phi^0\end{pmatrix} \rightarrow \Phi = \frac{1}{\sqrt{2}}\begin{pmatrix}0\\ \phi^0\end{pmatrix}. \tag{2.20}$$

If $\mu^2 > 0$, then the scalar field acquires a non-zero vacuum expectation value (VEV),

$$\langle\Phi\rangle = \frac{1}{\sqrt{2}}\begin{pmatrix}0\\ v\end{pmatrix} \tag{2.21}$$

resulting in the *spontaneous symmetry breaking* of the EW sector [51–53]. In nature, we observe the $\mathrm{U}(1)_Q$ symmetry of electromagnetism and so this must be a remaining symmetry after SSB. Therefore the scalar field ϕ^0 is taken to have charge $Q = 0$ such that electromagnetism is left intact. Under this scheme, both the hypercharge Y and the weak isospin T_3 are not conserved. However the combination $Q = T_3 + \frac{1}{2}Y$, defined as the electric charge, is conserved. Thus the EW symmetry $\mathrm{SU}(2)_L \otimes \mathrm{U}(1)_Y$ is spontaneously broken into a U(1) symmetry of electric charge.

In the unitary gauge, the scalar doublet is rewritten as

$$\Phi = \frac{1}{\sqrt{2}}\begin{pmatrix}0\\ v+h\end{pmatrix}, \quad h \in \mathbb{R}, \tag{2.22}$$

where one can compare to equation (2.17) and see that where before we had four degrees of freedom in the Higgs doublet through each of the component fields ϕ_i, now we have one degree of freedom forming the Higgs field h with a mass $m_h = \sqrt{2\mu^2} = \sqrt{2\lambda}v$.

EW boson	mass	spin	T_3	Y	Q
$W^{\pm}$	80.377(12) GeV	1	±1	0	±1
Z^0	91.1876(21) GeV	1	0	0	0
photon, γ	0	1	0	0	0
Higgs, h^0	125.25(0.17) GeV	0	$-\frac{1}{2}$	1	0

TABLE 2.1: Properties of the bosons of the EW sector of the Standard Model after SSB by the Higgs mechanism. T_3 is the weak isospin, Y the weak hypercharge, and Q the electric charge. Masses are taken from [54].

By expanding the Higgs Lagrangian in equation (2.18) in the broken phase, we can redefine the EW fields as linear transformations and collect quadratic terms which yield gauge-invariant mass terms:

$$W_\mu^\pm \equiv \frac{1}{\sqrt{2}}(W_\mu^1 \mp iW_\mu^2), \qquad m_W = \frac{gv}{2}, \tag{2.23}$$

$$Z_\mu \equiv \frac{1}{\sqrt{g^2+g'^2}}(gW_\mu^3 - g'B_\mu), \qquad m_Z = \frac{v}{2}\sqrt{g^2+g'^2}, \tag{2.24}$$

$$A_\mu \equiv \frac{1}{\sqrt{g^2+g'^2}}(g'W_\mu^3 + gB_\mu), \qquad m_A = 0, \tag{2.25}$$

where $W_\mu^\pm$ are the fields associated with the physical $W^\pm$ bosons, Z_μ with the Z^0 boson, and A_μ with the photon. If not coupled to the EW gauge fields, the other three degrees of freedom of the Higgs doublet would form massless Nambu-Goldstone bosons as described by the Nambu-Goldstone theorem [50, 55, 56]. However, with the redefinitions above to yield the gauge fields of the broken EW generators, it is said that these Nambu-Goldstone bosons have been "eaten" by the $W_\mu^\pm, Z_\mu$ fields in order to generate these as massive bosons. The properties of the EW bosons after SSB are summarised in table 2.1.

2.2.4 The Yukawa Interaction

Finally, to solve the problem of fermion masses, we introduce the Yukawa Lagrangian:

$$\mathcal{L}_{\text{Yukawa}} = -Y_{ij}^{(\ell)}\bar{L}_i\Phi R_j + \text{h.c.}, \tag{2.26}$$

which after SSB for the leptons reads

$$\mathcal{L}_{\text{Yukawa},\ell}^{\text{SSB}} = -Y_{ij}^{(\ell)}\begin{pmatrix}\bar{\nu}_{iL} & \bar{e}_{iL}\end{pmatrix}\begin{pmatrix}0\\ \frac{v}{\sqrt{2}}\end{pmatrix}e_{jR} + \text{h.c.} = -Y_{ij}^{(\ell)}\frac{v}{\sqrt{2}}\bar{e}_{iL}e_{jR} + \text{h.c.}, \tag{2.27}$$

where $e_i = (e,\ \mu,\ \tau)$ and $Y^{(\ell)}$ is the 3×3 Yukawa coupling matrix of the leptons. The mass terms of the leptons then read

$$m_i = \frac{Y_i v}{\sqrt{2}}. \tag{2.28}$$

The Yukawa matrix $Y^{(\ell)}$ is chosen to be diagonal such that the weak eigenstates and mass eigenstates of the leptons are equivalent and there is no mixing between generations. We will see in section 2.4 that this is not the case for quarks and what the implications of that are.

In the SM, in order to generate masses from the Yukawa interaction for both components of the SU(2) doublet, the hermitian conjugate term is used where a second Higgs doublet

(not independent of the first, but its charge conjugate) is introduced as

$$\widetilde{\Phi} = i\sigma_2\Phi^* = \begin{pmatrix} \phi^{0*} \\ -\phi^{+*} \end{pmatrix} = \frac{1}{\sqrt{2}} \begin{pmatrix} v+h \\ 0 \end{pmatrix}. \tag{2.29}$$

We will see in chapter 4 how the Standard Model can be extended to include an independent second Higgs doublet instead of using the charge conjugate, and what consequences this brings. This could be used to give mass to the other component of the lepton SU(2) doublet, i.e. the neutrino, however in the Standard Model there are no right-handed neutrinos and therefore this term does not arise. We now know however that experimentally neutrinos do have mass [6, 7], although the mechanism for this is yet to be determined. The properties of the leptons in the SM are summarised in table 2.2. For quarks, the conjugate Higgs field in equation (2.29) generates the mass terms for the up-type quarks, to be discussed in section 2.4.

lepton	mass	T_{3L}	T_{3R}	Y_L	Y_R	Q
electron, e	511 keV	$-\frac{1}{2}$	0	-1	-2	-1
muon, μ	106 MeV	$-\frac{1}{2}$	0	-1	-2	-1
tau, τ	1.78 GeV	$-\frac{1}{2}$	0	-1	-2	-1
electron neutrino, ν_e	-	$+\frac{1}{2}$	-	-1	-	0
muon neutrino, ν_μ	-	$+\frac{1}{2}$	-	-1	-	0
tau neutrino, ν_τ	-	$+\frac{1}{2}$	-	-1	-	0

TABLE 2.2: Properties of the leptons in the Standard Model. T_3 is the weak isospin, Y the weak hypercharge, with $L(R)$ standing for the left(right)-handed projection of each lepton; Q is the electric charge. Despite the experimental proof, neutrino masses are not considered in the Standard Model and therefore are not shown here. Masses are taken from [54].

2.3 Quantum Chromodynamics

We now consider Quantum Chromodynamics, the theory of the interactions between quarks and gluons, also known as the *strong force* [57, 58]. QCD describes the $SU(3)_C$ part of the Standard Model gauge group, and its Lagrangian is given by

$$\mathcal{L}_{\text{QCD}}(x) = -\frac{1}{4}G^a_{\mu\nu}(x)G^{a\mu\nu}(x) + \sum_f \bar{\psi}_{f,\alpha}(x)(i\not{D}_{\alpha\beta} - m_f\delta_{\alpha\beta})\psi_{f,\beta}(x), \tag{2.30}$$

where f runs over the $N_f = 6$ flavours of quark, $a = 1, \ldots, N_c^2 - 1$ runs over the generators of SU(3), and α, β are the colour indices running $1, \ldots, N_c$ for the gauge

group SU(N_c), i.e. $N_c = 3$ for QCD. We can define the covariant derivative of QCD as

$$D_\mu = \partial_\mu + ig_s A^a_\mu(x) T^a, \tag{2.31}$$

where g_s is the strong coupling constant, A^a_μ are the 8 gluon fields, and $T^a = \frac{1}{2}\lambda^a$ are the 8 generators of SU(3). λ^a are the 8 traceless anti-hermitian 3×3 matrices known as Gell-Mann matrices and are the SU(3) equivalent to the Pauli matrices for SU(2); these are shown in appendix A. The field strength tensor is defined

$$\begin{aligned} G^a_{\mu\nu} &= \partial_\mu A^a_\nu - \partial_\nu A^a_\mu + ig_s[A^b_\mu, A^c_\nu] \\ &= \partial_\mu A^a_\nu - \partial_\nu A^a_\mu - g_s f^{abc} A^b_\mu A^c_\nu, \end{aligned} \tag{2.32}$$

where f^{abc} are the *structure constants* of SU(3), or the generators in the adjoint representation. Similarly to SU(2), for the non-Abelian SU(3) self-interaction terms arise between the gluon fields $A^a_\mu(x)$. From expanding the covariant derivative, one will find three-gluon (coupling proportional to g_s) and four-gluon (coupling proportional to g_s^2) self-interaction vertices, as well as interaction vertices between two quarks and a gluon. The quarks will acquire mass terms through the Yukawa interaction discussed above in section 2.2 and will be expanded upon in section 2.4. However, gluons are found to be massless in nature and therefore there is no need to find a mechanism to introduce a mass term for these gauge fields.

2.3.1 Colour Charge

Colour charge is the term given to the property of quarks and gluons defining their place in the SU(3) multiplets and how they interact via the strong force. Where the electric charge has either a positive or negative charge for a fermion and its anti-fermion partner, colour charge has three charges and three 'anti-charges'. Using the analogy of primary colours in the RGB colour picture, the colour charges are referred to as *red*, *blue*, and *green*; the 'anti-charges' are then *anti-red* (cyan), *anti-blue* (yellow), and *anti-green* (magenta). Again in analogy to RGB colours, the combination of the three (anti-)charges is *colourless* or *colour-neutral*; alternatively one charge and its anti-charge (e.g. red + anti-red) is also colour-neutral. Due to confinement (to be discussed in section 2.3.2), only colour-neutral states may exist as free particles.

Quarks exist as components of SU(3) triplets in the fundamental representation and therefore each has a single colour charge (or anti-charge for antiquarks). Quarks then form colour-neutral bound states known as *hadrons*. Three quarks of different colour charge together form a *baryon*, while one quark and an antiquark with opposite colour charges form a *meson*. These two are the most common types of hadrons, however more

exotic states do exist: a tetraquark state composed of two quarks and two antiquarks was first observed in 2013 [59], and a pentaquark state composed of four quarks and one antiquark was observed in 2015 [60].

Gluons are vectors in the adjoint representation of SU(3), forming an octet. Therefore there are eight independent colour states of gluon, which can be represented in many ways as the independent linear combinations of colour-anticolour pairs, such as

$$\begin{aligned}
&\frac{1}{\sqrt{2}}(\text{red}\,\overline{\text{blue}} + \text{blue}\,\overline{\text{red}}), && -i\frac{1}{\sqrt{2}}(\text{red}\,\overline{\text{blue}} - \text{blue}\,\overline{\text{red}}),\\
&\frac{1}{\sqrt{2}}(\text{red}\,\overline{\text{green}} + \text{green}\,\overline{\text{red}}), && -i\frac{1}{\sqrt{2}}(\text{red}\,\overline{\text{green}} - \text{green}\,\overline{\text{red}}),\\
&\frac{1}{\sqrt{2}}(\text{blue}\,\overline{\text{green}} + \text{green}\,\overline{\text{blue}}), && -i\frac{1}{\sqrt{2}}(\text{blue}\,\overline{\text{green}} - \text{green}\,\overline{\text{blue}}),\\
&\frac{1}{\sqrt{2}}(\text{red}\,\overline{\text{red}} - \text{blue}\,\overline{\text{blue}}), && \frac{1}{\sqrt{6}}(\text{red}\,\overline{\text{red}} + \text{blue}\,\overline{\text{blue}} - 2\,\text{green}\,\overline{\text{green}}).
\end{aligned} \tag{2.33}$$

The Standard Model does also predict colour-neutral bound states of gluons, known as *glueballs*. The discovery of one such state was claimed by the TOTEM [61] and DØ [62, 63] experiments, namely a three-gluon vector state.

2.3.2 Colour Confinement and Asymptotic Freedom

In classical gauge theory, the coupling constant g is a constant. In a quantum gauge theory, g depends on the energy scale at which observations are made, e.g. in a scattering experiment at energy scale $E = \sqrt{s}$, $s = (p_1 + p_2)^2$ (for particle momenta p_1, p_2), such that we extract from any measurement $g^2(E)$. More generally, we can write $g^2(\mu)$ where μ is the appropriate energy scale (or *renormalisation scale*) of the process considered. Consider the coupling strength defined

$$\alpha(\mu) \equiv \frac{g^2(\mu)}{4\pi}. \tag{2.34}$$

In QED, we have $\alpha_{\text{EM}} = e^2/4\pi$; in QCD, we have a SU(3) gauge theory with N_f active flavours of quarks[3], leading to (at 1-loop order)

$$\alpha_s^{\text{1-loop}}(\mu) = \frac{g_s^2(\mu)}{4\pi} = \frac{2\pi}{\beta_0 \log \frac{\mu}{\Lambda_{\text{QCD}}}}, \tag{2.35}$$

[3] An "active" quark flavour is one satisfying $m_f \ll \mu$.

where $\Lambda_{\text{QCD}} \approx 300\,\text{MeV}$ is the *confinement scale* of QCD [54]. β_0 is the first coefficient of the β function, defining the *renormalisation group equation* (RGE):

$$\beta(\alpha_s) = \mu^2 \frac{d\alpha_s}{d\mu^2}, \tag{2.36}$$

$$\beta^{\text{1-loop}}(\alpha_s) = -\beta_0 \frac{\alpha_s^2}{2\pi}, \tag{2.37}$$

$$\beta_0 = \frac{11}{3} N_c - \frac{2}{3} N_f. \tag{2.38}$$

The sign of the β function and therefore its first coefficient β_0 determines how the coupling strength will run with energy; for the SM case of $N_f = 6$, β_0 is positive and thus β is negative, which dictates that the coupling strength decreases with increasing energy scales. This effect is known as *asymptotic freedom* – with increasing energies, the interactions of colour-charged particles (quarks and gluons) become asymptotically weak and their predictions are highly perturbative [64, 65].

Conversely, the QCD coupling strength becomes increasingly large for lower energies, such that at energies close to or below Λ_{QCD} it becomes impossible for quarks and gluons to overcome the coupling strength of the strong force. In this limit, they become bound in colour-neutral hadron states. This is the phenomenon of *confinement* – only colour-neutral states can exist as free particles at low energies [40]. As α_s grows for small energies and can no longer be considered a small parameter, the confined phase of QCD cannot be reasonably treated by expanding powers of α_s progressively in perturbation theory and is highly non-perturbative in nature. The non-perturbative nature of the confined phase implies that virtual processes normally suppressed in perturbation theory become highly relevant, such as the emission of gluon fields inside hadrons and their splitting into quark-antiquark pairs which then subsequently annihilate again into a gluon. This process can happen constantly within bound states and as such there is a constant flux of virtual particles in the background of hadrons. This is known as *the sea* and its quark content the *sea quarks*. The effect of the sea is highly important in describing the properties and behaviours of hadrons; neglecting this and only considering the *valence quarks* which contribute to the quantum numbers of the system will lead to inaccurate descriptions.

The running of α_s from confinement at low energy scales to asymptotic freedom at high energy scales is shown in figure 2.1, taken from [54]. When low energy regimes are relevant, such as when considering hadronic bound states, making reasonable predictions in QCD requires some different framework to the quantum field theory standard of perturbation theory in order to capture the hadronic physics embedded at low energies; some non-perturbative methods for hadronic physics will be introduced in chapter 5.

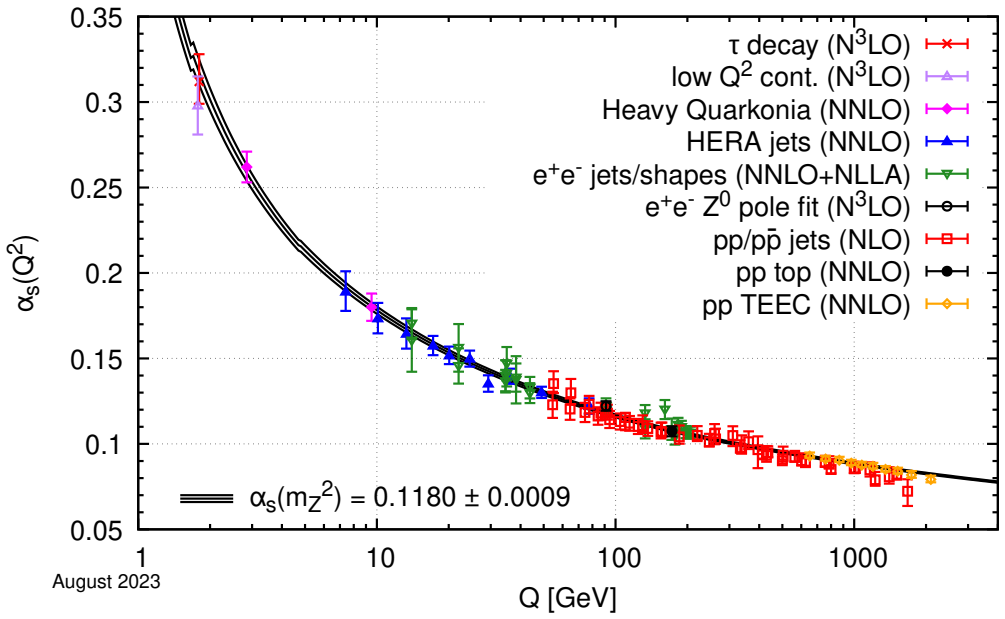

FIGURE 2.1: Experimental observations of the running coupling strength α_s of QCD. This figure is taken from [54].

2.3.3 Chiral Symmetry Breaking in QCD

In the massless limit, fermions exhibit a symmetry where chirality is conserved. The left- and right-handed components of the fermion can be independently transformed and one can form a symmetry group $G_L \times G_R$. This symmetry will however be explicitly broken by the presence of a Dirac mass term in the Lagrangian. In QCD, the *light* quarks u, d, and s are nearly massless (see table 2.3), having masses much smaller than the confinement scale $\Lambda_{\text{QCD}} \approx 300\,\text{MeV}$ [54]. Since the coupling strength at the energy scales where these quarks are present (but not the *heavy* quarks c, b, and t) is large and the light quarks are bound in hadrons with strongly-coupled gluon fields, it is more appropriate to use bound states as degrees of freedom rather than the individual quarks. In this limit, there still exists an approximate chiral symmetry. In the case of a chiral symmetry, the left- and right-handed quarks can be interchanged in hadrons and therefore parity pair mesons, such as (in J^P notation) the pseudoscalar 0^- and scalar 0^+, should have the same mass. However experiment observes much lighter masses for the pseudoscalar 0^- states than scalar 0^+ states [54], implying that this approximate chiral symmetry must be broken.

First, we take the chiral limit $m_{u,d} \to 0$. The Lagrangian describing only the up and down quarks has the global symmetry $\text{U}(2)_L \times \text{U}(2)_R = \text{SU}(2)_L \times \text{SU}(2)_R \times \text{U}(1)_V \times \text{U}(1)_A$.

Firstly the $\mathrm{U}(1)_V$ vector symmetry results in the conservation of *baryon number*,

$$B = \frac{1}{3}\sum_f (n_f - \bar{n}_f), \tag{2.39}$$

where n_f is the number of valence quarks of flavour f and $\bar{n}_f$ the corresponding number of anti-quarks. Next, the $\mathrm{U}(1)_A$ symmetry first appears to exist only in the massless limit, since the divergence of the axial current gives $im\bar{\psi}\gamma_5\psi$, however in quantisation, another term proportional to $\epsilon_{\mu\nu\alpha\beta}G^{\mu\nu}G^{\alpha\beta}$ appears [66, 67]. Therefore $\mathrm{U}(1)_A$ is in fact not a symmetry even in the massless limit; this is known as the *axial anomaly*. Generated by interactions of quarks and gluons, a VEV can arise composed of non-zero quark condensates which spontaneously breaks the $\mathrm{SU}(2)_L \times \mathrm{SU}(2)_R$ chiral symmetry into a $\mathrm{SU}(2)_V$ flavour symmetry referred to as *isospin*, under which the massless u and d quarks form an isospin doublet. This SSB also generates three massless Nambu-Goldstone bosons from the generators of the $\mathrm{SU}(2)_L \times \mathrm{SU}(2)_R$ chiral symmetry. In nature, the u and d quarks are not exactly massless however, which in addition to the SSB causes *explicit* breaking of the symmetry, giving mass to the Nambu-Goldstone bosons, now referred to as pseudo-Nambu-Goldstone bosons. The three bosons resulting from the SSB of $\mathrm{SU}(2)_L \times \mathrm{SU}(2)_R$ chiral symmetry are the pions:

$$\begin{aligned} \pi^0 &= \tfrac{1}{\sqrt{2}}(\bar{u}u - \bar{d}d), & M_{\pi^0} &\approx 135\,\mathrm{MeV}, \\ \pi^+ &= u\bar{d}, & M_{\pi^\pm} &\approx 140\,\mathrm{MeV}, \\ \pi^- &= d\bar{u}, \end{aligned} \tag{2.40}$$

where we take the mass values from [54]. In fact, the chiral symmetry is further explicitly broken by the u and d having different electromagnetic charges, but at the energy scales being considered, the relative coupling strengths of EM and QCD are such that this effect is $\lesssim 1\%$ and can mostly be neglected.

Note that the pion masses are much larger than simply the sum of the valence quark content ($m_u \approx 2\,\mathrm{MeV}$, $m_d \approx 5\,\mathrm{MeV}$). As mentioned previously, the valence content alone is not sufficient to describe QCD bound states; the content of the sea, i.e. the QCD binding energy, and the effects of chiral symmetry breaking are necessary to explain the much larger masses of hadrons compared to the sum of valence quark masses. One can refer to a *dressed mass* of a quark as the effective mass of a valence quark in a hadron, e.g. for pions, $m_{u,d}^{dressed} \sim 70\,\mathrm{MeV}$.

Similarly to the above, the strange quark can also be considered in the chiral limit. Taking $m_{u,d,s} \to 0$, we find the Lagrangian for u, d, and s quarks has the global symmetry $\mathrm{U}(3)_L \times \mathrm{U}(3)_R = \mathrm{SU}(3)_L \times \mathrm{SU}(3)_R \times \mathrm{U}(1)_V \times \mathrm{U}(1)_A$. The $\mathrm{U}(1)_V$ and $\mathrm{U}(1)_A$ symmetries are interpreted exactly as above in the SU(2) case. Now the $\mathrm{SU}(3)_L \times \mathrm{SU}(3)_R$ chiral

symmetry is spontaneously broken into a $\mathrm{SU}(3)_V$ flavour symmetry. In $\mathrm{SU}(3)_V$ representation, there are eight generators to be broken. Including the explicit breaking of the symmetry from quark mass and charge, as well as the pions described in equation (2.40), the $K^{\pm}$, K^0, $\bar{K}^0$, η mesons are generated with quark content and masses (taken from [54]) given by

$$\begin{aligned} K^+ &= u\bar{s}, \quad K^- = s\bar{u}, & M_{K^\pm} &\approx 494\,\mathrm{MeV}, \\ K^0 &= d\bar{s}, \quad \bar{K}^0 = s\bar{d}, & M_{K^0} &\approx 498\,\mathrm{MeV}, \\ \eta &= \frac{1}{\sqrt{6}}(u\bar{u} + d\bar{d} - 2s\bar{s}), & M_\eta &\approx 548\,\mathrm{MeV}. \end{aligned} \tag{2.41}$$

One can write the octet field of $\mathrm{SU}(3)_V$ as

$$\Pi = \begin{pmatrix} \frac{1}{\sqrt{2}}\pi^0 + \frac{1}{\sqrt{6}}\eta & \pi^+ & K^+ \\ \pi^- & -\frac{1}{\sqrt{2}}\pi^0 + \frac{1}{\sqrt{6}}\eta & K^0 \\ \bar{K}^- & \bar{K}^0 & -\sqrt{\frac{2}{3}}\eta \end{pmatrix}. \tag{2.42}$$

We have seen two versions of chiral symmetry breaking for QCD: one based on SU(2) and one on SU(3). Since $m_s \gg m_u, m_d$, the approximation to chiral symmetry in SU(2) should be a more accurate picture than that of SU(3) where the effects of the strange quark mass cannot be as easily neglected as for the up and down quarks. However, the SU(2) picture only results in three pion states, and therefore cannot be applied in scenarios where kaon or η states also enter.

One can further consider mesons with one heavy quark and one light quark (*heavy-light mesons*) as systems where a dynamic light quark is connected to a static heavy quark via the strong interaction. Chiral symmetry breaking can in this case be considered for the single light quark. In this picture, chiral symmetry breaking causes a universal mass gap ΔM between the ground states $0^-, 1^-$ and their excited parity pairs $0^+, 1^+$.

2.3.4 Quark Properties

We have already seen that the concept of quark mass is not so well-defined as for e.g. leptons. In chiral symmetry breaking, the dressed, or effective, mass of a light quark in a hadron can have significant contributions from the QCD sea and chiral symmetry breaking whereas the *implicit mass* of the quark contributes minimally. This effect can be generalised to all quark flavours and all energies, where the running of the QCD coupling strength has an important impact on the quark mass; the dressed mass of a quark will vary from the implicit mass depending on how large the effects of the QCD coupling are. For example, we already saw that light up/down quarks inside a pion are at energies below the confinement scale and have a dressed mass $\sim$ 15 times as large

as their implicit mass, whereas if one considers a heavy b quark inside a heavy-light B meson, the implicit b quark mass $m_b \approx m_B$ constitutes almost all of the mass of the B meson since the energy scale $O(5\,\text{GeV})$ is much larger than the confinement scale. The mass m of a quark therefore *runs* with the energy (or renormalisation) scale μ, i.e. $\overline{m}(\mu)$. At short distances, or high energies, this is defined through the RGE (in the $\overline{\text{MS}}$ renormalisation scheme)

$$\mu^2 \frac{d\overline{m}(\mu)}{d\mu^2} = -\gamma(\overline{\alpha}_s(\mu))\overline{m}(\mu), \tag{2.43}$$

where $\gamma(\overline{\alpha}_s(\mu))$ is the anomalous dimension defining the scaling behaviour of the RGE. This is only valid in the perturbative regime and other, non-perturbative methods, such as lattice QCD, must be used to see the running of quark masses at other energy scales. It is then clear that the quark mass is explicitly associated with its energy scale (and renormalisation scheme) and reference values require the associated energy scale.

Next, we consider the quantum numbers of the quarks. In addition to baryon number (each quark has $B = +\frac{1}{3}$) and the EW quantum numbers T_3, Y, and Q, there are quantum numbers associated with the flavour of quark. Note that the convention for these quantum numbers is that a charged meson carries the same sign on its flavour quantum number as its electric charge. The flavour quantum numbers are as follows:

- Isospin, I_3: originating from nuclear theory where only the first generation of quarks was considered, the up quark is given $I_3 = \frac{1}{2}$ and the down quark $I_3 = -\frac{1}{2}$;
- Strangeness, $\mathcal{S}$: to give a $K^+\,(u\bar{s})$ a strangeness of $\mathcal{S} = 1$, a strange quark has $\mathcal{S} = -1$;
- Charm, $\mathcal{C}$: giving a $D^+\,(\bar{d}c)$ a charm of $\mathcal{C} = 1$ defines a charm quark having $\mathcal{C} = 1$;
- Bottomness, $\mathcal{B}$: giving a $B^+\,(u\bar{b})$ a bottomness of $\mathcal{B} = 1$, a bottom quark has $\mathcal{B} = -1$;
- Topness, $\mathcal{T}$: since the sign on the flavour charge clearly follows the pattern of positive for up-type quarks and negative for down-type quarks, a top quark will have $\mathcal{T} = 1$, however this does not come from the definition of a charged meson since the top quark lifetime ($\tau_t \sim 5 \times 10^{-25} s$) is so short that it decays before it can interact strongly and form a QCD bound state.

The masses and quantum numbers of the quarks in the SM are summarised in table 2.3.

quark	mass	scale	T_{3L}	T_{3R}	Y_L	Y_R	Q	I_3	$\mathcal{S}$	$\mathcal{C}$	$\mathcal{B}$	$\mathcal{T}$
up, u	$2.16^{+0.49}_{-0.26}$ MeV	2 GeV	$+\frac{1}{2}$	0	$\frac{1}{3}$	$\frac{4}{3}$	$+\frac{2}{3}$	$+\frac{1}{2}$	0	0	0	0
down, d	$4.67^{+0.48}_{-0.17}$ MeV	2 GeV	$-\frac{1}{2}$	0	$\frac{1}{3}$	$\frac{2}{3}$	$-\frac{1}{3}$	$-\frac{1}{2}$	0	0	0	0
strange, s	$93.4^{+8.6}_{-3.4}$ MeV	2 GeV	$-\frac{1}{2}$	0	$\frac{1}{3}$	$\frac{2}{3}$	$-\frac{1}{3}$	0	-1	0	0	0
charm, c	1.27 ± 0.02 GeV	m_c	$+\frac{1}{2}$	0	$\frac{1}{3}$	$\frac{4}{3}$	$+\frac{2}{3}$	0	0	$+1$	0	0
bottom, b	$4.18^{+0.03}_{-0.02}$ GeV	m_b	$-\frac{1}{2}$	0	$\frac{1}{3}$	$\frac{2}{3}$	$-\frac{1}{3}$	0	0	0	-1	0
top, t	172.69 ± 0.30 GeV	m_t	$+\frac{1}{2}$	0	$\frac{1}{3}$	$\frac{4}{3}$	$+\frac{2}{3}$	0	0	0	0	$+1$

TABLE 2.3: Properties of quarks in the Standard Model. All quarks also carry baryon number $B = +\frac{1}{3}$. Masses are taken from [54], using the $\overline{\text{MS}}$ renormalisation scheme.

2.3.5 The Strong CP Problem

As discussed above, the $\text{U}(1)_A$ symmetry found in the QCD Lagrangian described in equation (2.30) turns out to not be a symmetry after including another term in the Lagrangian, namely the *theta term* [68]:

$$\mathcal{L}_\theta \propto \theta \epsilon_{\mu\nu\alpha\beta} G_a^{\mu\nu} G^{a\alpha\beta}. \tag{2.44}$$

This theta term would introduce CP violation into QCD, however experiment strongly imposes deviations of θ from 0 to be tiny: $|\theta| \lesssim 10^{-10}$ [54]. The question of why QCD seemingly preserves CP symmetry when it is not required is known as the *strong CP problem*. There are multiple models of new physics beyond the SM which describe a solution to the strong CP problem, such as the Peccei-Quinn theory which introduces new particles called *axions* [69–71].

2.4 Quark Mixing: The Cabibbo-Kobayashi-Maskawa Matrix

In section 2.2.4, we discussed the Yukawa interaction as the way in which a gauge-invariant mass term can be restored to the Lagrangian for the charged leptons. This same interaction exists for the quark sector, however whereas with leptons only one type of right-handed lepton exists (the charged leptons), now both types of quark (up and down type) have right-handed components. The quark-Yukawa Lagrangian (after SSB)

reads

$$\begin{aligned}\mathcal{L}_{\text{Yukawa,q}} &= -Y^{(d)}_{ij}\bar{Q}_{iL}\Phi D_{jR} - Y^{(u)}_{ij}\bar{Q}_{iL}\,\widetilde{\Phi}\,U_{jR} + \text{h.c.} \\ &= -Y^{(d)}_{ij}\begin{pmatrix}\bar{u}_{iL} & \bar{d}_{iL}\end{pmatrix}\begin{pmatrix}0\\ \frac{v}{\sqrt{2}}\end{pmatrix}d_{jR} - Y^{(u)}_{ij}\begin{pmatrix}\bar{u}_{iL} & \bar{d}_{iL}\end{pmatrix}\begin{pmatrix}\frac{v}{\sqrt{2}}\\ 0\end{pmatrix}u_{jR} + \text{h.c.} \\ &= -Y^{(d)}_{ij}\frac{v}{\sqrt{2}}\bar{d}_{iL}d_{jR} - Y^{(u)}_{ij}\frac{v}{\sqrt{2}}\bar{u}_{iL}u_{jR} + \text{h.c.},\end{aligned} \tag{2.45}$$

where Q_{iL}, D_{jR}, U_{jR} are defined in equation (2.15) (suppressing colour index) and the Higgs conjugate field $\widetilde{\Phi}$ is defined in equation (2.29). Previously when discussing the leptons, the Yukawa matrix $Y^{(\ell)}$ was chosen to be a diagonal matrix and no mixing between generations occurs. Now when considering the quarks, the Yukawa matrices $Y^{(u)}$, $Y^{(d)}$ are not necessarily diagonal and the different quark generations may be connected through them. However, these matrices can be diagonalised using unitary matrices such that we consider the mass eigenstates, i.e.

$$\frac{v}{\sqrt{2}}V^{(u)\dagger}Y^{(u)}U^{(u)} = \begin{pmatrix}m_u & & \\ & m_c & \\ & & m_t\end{pmatrix}, \quad \frac{v}{\sqrt{2}}V^{(d)\dagger}Y^{(d)}U^{(d)} = \begin{pmatrix}m_d & & \\ & m_s & \\ & & m_b\end{pmatrix}. \tag{2.46}$$

Introducing these into the Yukawa term, we find the transformations between weak (flavour) eigenstates, denoted as Q', and the mass eigenstates Q, to be

$$U'_{iL} \to V^{(u)}_{ij}U_{iL}, \qquad U'_{iR} \to U^{(u)}_{ij}U_{jR}, \tag{2.47}$$

$$D'_{iL} \to V^{(d)}_{ij}D_{iL}, \qquad D'_{iR} \to U^{(d)}_{ij}D_{jR}. \tag{2.48}$$

When performing such transformations to diagonalise the Yukawa Lagrangian, it is then necessary to implement this throughout the whole Lagrangian. However, it is found that the mass matrices $Y^{(u)}, Y^{(d)}$ cannot be diagonalised simultaneously. This has significant implications for charged interaction terms involving both up-type and down-type quarks, i.e. the flavour-changing charged currents of the weak sector also involving a $W^{\pm}$ boson. The weak current J^{μ}_{W} transforms as

$$J^{\mu}_{W} = \bar{U}'_{iL}\gamma^{\mu}D'_{iL} \to \bar{U}_{jL}V^{(u)\dagger}_{ji}\gamma^{\mu}V^{(d)\dagger}_{ik}D_{kL} = \bar{U}_{jL}\gamma^{\mu}V_{\text{CKM},jk}D_{kL}, \tag{2.49}$$

where we choose to diagonalise the up-type quarks and rotate the down-type quarks between their flavour and mass eigenstates with $V_{ji}^{(u)\dagger} V_{ik}^{(d)} = V_{\mathrm{CKM},jk}$ the Cabibbo-Kobayashi-Maskawa matrix [72, 73]. We can write the rotation between flavour eigenstates d', s', b' and mass eigenstates d, s, b as

$$\begin{pmatrix} d' \\ s' \\ b' \end{pmatrix} = V_{\mathrm{CKM}} \begin{pmatrix} d \\ s \\ b \end{pmatrix} = \begin{pmatrix} V_{ud} & V_{us} & V_{ub} \\ V_{cd} & V_{cs} & V_{cb} \\ V_{td} & V_{ts} & V_{tb} \end{pmatrix} \begin{pmatrix} d \\ s \\ b \end{pmatrix}. \tag{2.50}$$

Now for every weak charged current, an element of the CKM matrix enters as a measure of the interaction strength between the up-type quarks (diagonalised in their mass eigenstates) and the down-type quarks. These CKM matrix elements are in every weak decay process involving quark currents in experiment and can therefore be strongly constrained based on a collection of processes with the same quark content.

To better understand the CKM matrix, forming a parameterisation can give useful insights. One such is the *standard parameterisation* [74] which follows from extending the Cabibbo angle of mixing between the first two generations [72] to all three generations. This requires three Cabibbo-like matrices (each with its own angle) and also the inclusion of a phase by the requirements of a general 3×3 mixing matrix:

$$\begin{aligned} V_{\mathrm{CKM}} &= \begin{pmatrix} 1 & 0 & 0 \\ 0 & \cos\theta_{23} & \sin\theta_{23} \\ 0 & -\sin\theta_{23} & \cos\theta_{23} \end{pmatrix} \begin{pmatrix} \cos\theta_{13} & 0 & \sin\theta_{13} e^{i\delta} \\ 0 & 1 & 0 \\ -\sin\theta_{13} e^{i\delta} & 0 & \cos\theta_{13} \end{pmatrix} \begin{pmatrix} \cos\theta_{12} & \sin\theta_{12} & 0 \\ -\sin\theta_{12} & \cos\theta_{12} & 0 \\ 0 & 0 & 1 \end{pmatrix} \\ &= \begin{pmatrix} c_{12}c_{13} & s_{12}c_{13} & s_{13}e^{-i\delta} \\ -s_{12}c_{23} - c_{12}s_{23}s_{13}e^{i\delta} & c_{12}c_{23} - s_{12}s_{23}s_{13}e^{i\delta} & s_{23}c_{13} \\ s_{12}c_{23} - c_{12}c_{23}s_{13}e^{i\delta} & -c_{12}s_{23} - s_{12}c_{23}s_{12}e^{i\delta} & s_{23}c_{13} \end{pmatrix}, \end{aligned} \tag{2.51}$$

where we introduce the shorthands $c_{ij} = \cos\theta_{ij}$, $s_{ij} = \sin\theta_{ij}$. The complex phase δ introduces CP violation into the weak quark currents and is the only source of CP violation in the Standard Model. In fact one of the main motivations to extend the SM beyond two fermion generations was the observed CP violation in kaon decays, hinting at the quark mixing matrix being at least 3×3 in order to have at least one complex CP phase.

The magnitudes of the CKM matrix elements follow a strong hierarchy, with the diagonal elements being closest to unity and the rest getting smaller as they get further from the diagonal. This fact is not immediately clear from considering the standard parameterisation, however an approximation known as the *Wolfenstein parameterisation* [75], while only accurate to a certain order, strongly features this hierarchy. We introduce

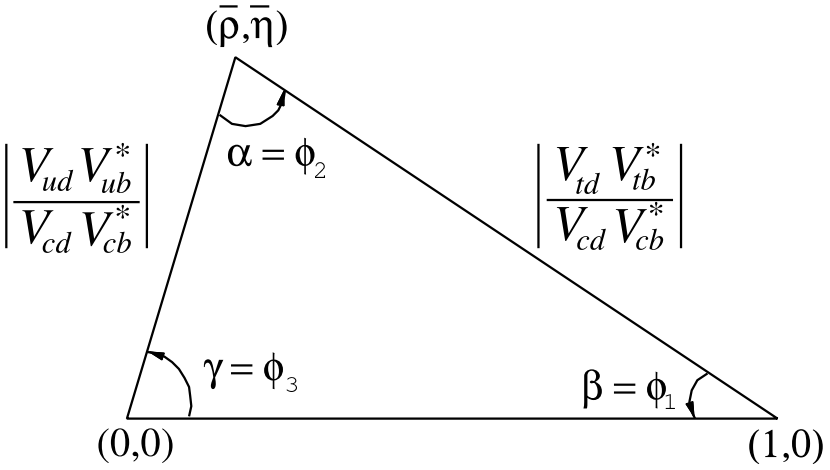

FIGURE 2.2: The unitarity triangle defined by equation (2.57), taken from [54].

the small parameter [76]

$$\lambda = s_{12} \approx 0.22498 \tag{2.52}$$

and can then perform a Taylor expansion of the standard parameterisation. In addition to λ, the parameters A, ρ, η also enter via

$$A\lambda^2 = s_{23}, \qquad A\lambda^3(\rho - i\eta) = s_{13}e^{-i\delta}. \tag{2.53}$$

Traditionally, the Wolfenstein parameterisation is taken to order λ^3 where the CKM matrix then reads

$$V_{\text{CKM}} = \begin{pmatrix} 1 - \frac{\lambda^2}{2} & \lambda & A\lambda^3(\rho - i\eta) \\ -\lambda & 1 - \frac{\lambda^2}{2} & A\lambda^2 \\ A\lambda^3(1 - \rho - i\eta) & -A\lambda^2 & 1 \end{pmatrix} + O(\lambda^4). \tag{2.54}$$

Furthermore in the SM the CKM matrix is constructed to be unitary, i.e.

$$V_{\text{CKM}}^\dagger V_{\text{CKM}} = V_{\text{CKM}} V_{\text{CKM}}^\dagger = \mathbb{1}. \tag{2.55}$$

This leads to the unitarity constraints on the elements of the CKM matrix:

$$\begin{aligned} \sum_k |V_{jk}|^2 &= 1, & \sum_k |V_{kj}|^2 &= 1, \\ \sum_k V_{ik} V_{jk}^* &= 0, & \sum_k V_{ki} V_{kj}^* &= 0. \end{aligned} \tag{2.56}$$

The six vanishing constraints can be drawn as triangles in the complex plane of ρ, η, e.g. from the relation

$$V_{ud}V_{ub}^* + V_{cd}V_{cb}^* + V_{td}V_{tb}^* = 0, \tag{2.57}$$

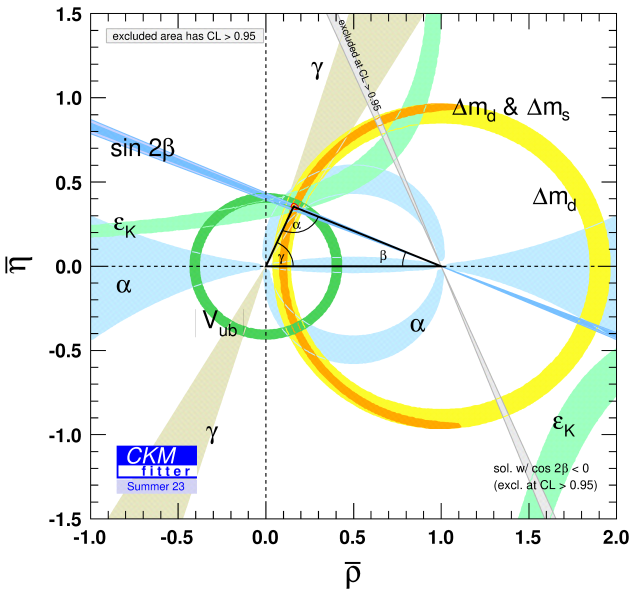

FIGURE 2.3: CKM unitarity constraints in the $(\bar{\rho}, \bar{\eta})$ plane from the CKMfitter collaboration [76] as of May 2024.

a *unitarity triangle* can be defined through dividing by $V_{cd}V_{cb}^*$. This defines a vector path forming a triangle in the complex plane, drawn as shown in figure 2.2 taken from [54]. The sides and angles of the unitarity triangle can be constrained by comparing experimental measurements to theoretical predictions. If unitarity holds, then the triangle will be closed. The unitarity of the CKM matrix further maintains that no tree-level *flavour-changing neutral currents* (FCNCs) exist within the SM. The current status of CKM element constraints and the unitarity triangle is analysed by e.g. the CKMfitter collaboration, where their latest results are shown in figure 2.3 [76]; alternative analysis and results are given by the UTfit collaboration [77–79].

Chapter 3

Theoretical and Phenomenological Foundations

In this chapter, we discuss the theoretical and phenomenological foundations and motivations of the calculations and discussions presented in later chapters. In section 3.1, we discuss the use of effective field theories where one can separate high- and low-energy effects in a general language useful for both high precision calculations within the Standard Model and generalising to models including new physics. Then in section 3.2 an overview of *heavy flavour physics* is given, touching on its important theoretical aspects and phenomenological outlook with specific interest towards B mesons. This will mark the starting point from which the calculations of this thesis begin.

3.1 Effective Field Theories

It is evident in the universe around us that phenomena occur at vastly different scales and through different interactions. Understanding physics at all these different scales would in principle require a complete theory of nature. However, an understanding of the dominant effects at an energy scale E can still be reached by seeing that the large separation of scales in the universe means that physics much larger or smaller than the energy scale E becomes irrelevant at leading approximation. This is largely how physics has progressed in its different disciplines for many years, although not explicitly formulated as such until more recent history. An effective field theory (EFT) is the formal method of acknowledging the separation of scales present in a chosen problem for a more complete physical theory and creating a quantitative framework using appropriate degrees of freedom at the given energy scale to simplify calculations for the chosen problem. Oftentimes using an EFT can also lead to new insights into the sorts of interaction in question.

In the following we will introduce EFTs as they are used in particle physics (with a focus on heavy quark physics) although it is important to note that EFTs are essential tools explicitly used in all area of physics to appropriately focus on whichever problem one considers. In understanding that the complete theory of nature is at a much higher energy scale than physics currently probes, unifying all fundamental interactions (including gravity), one can see that in fact all physical theories used today are simply effective theories of this ultimate theory taken in different limits.

In section 3.1.1, we introduce the common starting point for EFTs as used in modern particle physics, the *weak effective theory* (WET), and in section 3.1.2 it is discussed how the WET can be used to consider the effects of physics beyond the Standard Model. Then, in section 3.1.3, we consider the *heavy quark effective theory* (HQET) which separates a heavy quark from the light degrees of freedom of QCD. Finally in section 3.1.4, we review the *heavy quark expansion* (HQE) as a method to calculate the decay rates of hadrons containing a heavy quark. This section serves as a brief introduction to the very broad and deep subject of EFTs. The content on the WET is inspired by and follows [80–83], and the content on HQET and HQE is derived from [84–90]. These references also serve as broader reviews of effective field theories in particle physics and more in-depth descriptions of the effective theories discussed here.

3.1.1 Weak Effective Theory

Studying the weak sector of the Standard Model often leads to multi-scale problems due to the mediating bosons having much larger masses than all other energy scales in many scenarios. For example, if one studies weak charged currents mediated by $W^{\pm}$ bosons, there exists three scales of interest: the mass scale of the mediator m_W, the mass scale of the decaying fermion m_f, and, in the case of heavy quark decays, the hadronic scale of non-perturbative QCD effects Λ_{QCD}. This results in a problem with the hierarchy $m_W \gg m_f \gg \Lambda_{\text{QCD}}$. To deal with this kind of problem in the full Standard Model formulation is to struggle against the large separation of scales and it is therefore advantageous to introduce an effective theory to reduce this to a much simpler combination of single-scale problems.

Consider the non-leptonic decay $b \to c\bar{u}d$ as an example, shown at tree level in figure 3.1. In the SM, its amplitude is given by

$$\begin{aligned} M &= \frac{g^2}{8} V_{cb}^* V_{ud} \Big(\bar{c}_\alpha(x)(1-\gamma_5)\gamma^\mu b_\alpha(x)\Big) D_{\mu\nu}(x,y) \Big(\bar{d}_\beta(y)(1-\gamma_5)\gamma^\nu u_\beta(y)\Big), \\ D_{\mu\nu}(x,y) &= -\int \frac{d^4q}{(2\pi)^4} \frac{1}{q^2 - m_W^2} \left(g_{\mu\nu} - \frac{q_\mu q_\nu}{m_W^2}\right) e^{-iq\cdot(x-y)}, \end{aligned} \tag{3.1}$$

where g is the SU(2) gauge coupling. Our amplitude is described by the product of two bilinear quark operators at positions x and y with a W boson exchanging between the two. Due to momentum conservation, the momentum q entering the W-boson propagator $D_{\mu\nu}$ saturates at the order of the mass of the decaying quark, i.e. $k \lesssim m_b \ll m_W$. The strong coupling is rather large at the scale m_b, i.e. $\alpha_s(m_b) \sim 0.2$, and

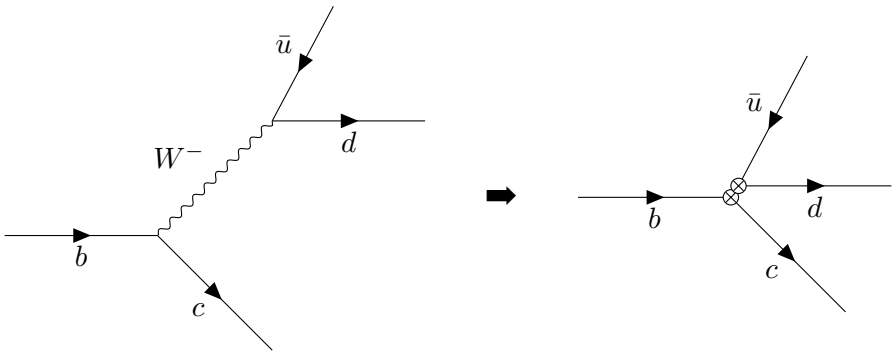

FIGURE 3.1: The non-local tree-level diagram for the non-leptonic $b \to c\bar{u}d$ decay in the full Standard Model theory (left) and the local effective diagram in the weak effective theory (right).

thus QCD corrections in perturbation theory will be significant. Calculating the QCD corrections at 1-loop order (shown in figure 3.2), one finds terms $O(\alpha_s)$ but also terms with *large logarithms* $O(\alpha_s \ln(m_b^2/m_W^2))$. Thus we do not have an expansion in α_s but

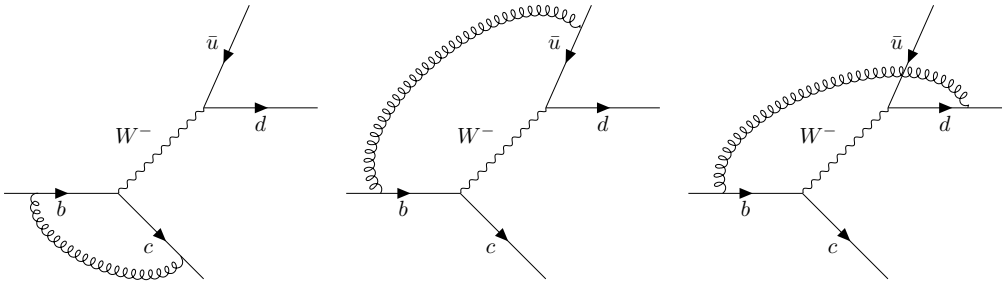

FIGURE 3.2: Diagrams contributing to the $b \to c\bar{u}d$ decay in the full theory at NLO in QCD. Further symmetric diagrams are not shown.

in $\alpha_s \ln(m_b^2/m_W^2) \sim 6\alpha_s$, which is clearly an invalid expansion parameter for $\alpha_s(m_b)$ and thus our perturbative approach in the full theory breaks down.

Expanding the propagator in $1/m_W^2$, we find at leading order

$$D_{\mu\nu}(x,y) \approx \frac{g_{\mu\nu}}{m_W^2}\delta^{(4)}(x-y) + O\left(\frac{q^2}{m_W^4}\right). \tag{3.2}$$

Inserting this into the amplitude, one finds

$$M = \frac{g^2}{8m_W^2} V_{cb}^* V_{ud} \Big(\bar{c}_\alpha(x)(1-\gamma_5)\gamma^\mu b_\alpha(x)\Big)\Big(\bar{d}_\beta(x)(1-\gamma_5)\gamma^\nu u_\beta(x)\Big). \tag{3.3}$$

We have *integrated out* the heavy mediator boson and in place of a non-local product of two operators, we now have a single *local, effective operator*. This reduction is shown in figure 3.1. Reducing the charged weak interaction to a point-like operator between four fermions is actually returning to the Fermi interaction [91, 92] which described β decays before the full theory of the weak interaction was developed. As such, it is common to still express this effective theory with an effective coupling equivalent to the Fermi constant G_F, defined as

$$\frac{G_F}{\sqrt{2}} = \frac{g^2}{8m_W^2}. \tag{3.4}$$

At tree level, the amplitude is given by equation (3.3), however at NLO one also includes the QCD corrections shown in figure 3.2. In fact, one now finds that the gluon exchange at NLO allows for a second colour structure in the four-quark operator, leading to the two local effective four-quark operators defined as

$$\begin{aligned} Q_1 &= \Big(\bar{c}_\alpha(x)(1-\gamma_5)\gamma^\mu b_\beta(x)\Big)\Big(\bar{d}_\beta(x)(1-\gamma_5)\gamma^\nu u_\alpha(x)\Big), \\ Q_2 &= \Big(\bar{c}_\alpha(x)(1-\gamma_5)\gamma^\mu b_\alpha(x)\Big)\Big(\bar{d}_\beta(x)(1-\gamma_5)\gamma^\nu u_\beta(x)\Big). \end{aligned} \tag{3.5}$$

Note that we have simplified things by explicitly choosing the tree-level decay $b \to c\bar{u}d$. In the complete effective Hamiltonian, there are additional four-quark operators from QCD and electroweak penguin diagrams, as well as magnetic penguin diagrams with an on-shell gluon or photon and semileptonic penguin and box diagrams; the corresponding Feynman diagrams are shown in figure 3.3.

Following Wilson's *operator product expansion* (OPE) [93, 94], we can place the perturbative QCD corrections in *Wilson coefficients* (WCs) and write the *effective Hamiltonian* as a sum of local operators multiplied by Wilson coefficients. This reads

$$\mathcal{H}_{\text{eff}}(x) = \frac{G_F}{\sqrt{2}} V_{cb}^* V_{ud} \Big[C_1 Q_1(x) + C_2 Q_2(x)\Big]. \tag{3.6}$$

Clearly at leading order, $C_1 = 0$, $C_2 = 1$. So the perturbative short-distance QCD effects at the scale m_W are contained within the Wilson coefficients C_i and the long-distance QCD effects at the scale Λ_{QCD} are contained in the matrix elements of the operators Q_i. QCD effects at the scale Λ_{QCD} are of course non-perturbative and therefore require methods beyond perturbation theory to be calculated (see chapter 5).

To derive the Wilson coefficients at the scale m_W, we can compare the amplitude in the full theory to that of the effective theory.

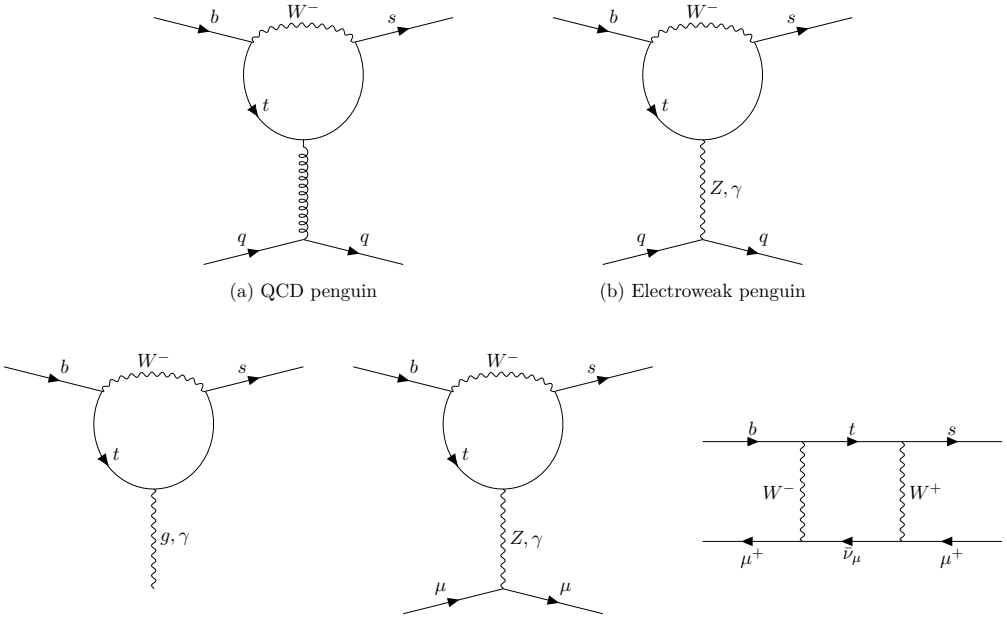

(a) QCD penguin (b) Electroweak penguin

(c) Magnetic penguin (d) Semileptonic penguin (e) Semileptonic box

FIGURE 3.3: Feynman diagrams contributing to the operators of the weak effective Hamiltonian.

The amplitude in the full theory (at 1 loop in QCD) reads

$$\mathcal{A}_{\text{full}} = \frac{G_F}{\sqrt{2}} V_{cb}^* V_{ud} \Bigg[\left(1 + 2C_F \frac{\alpha_s}{4\pi} + \ln\left(\frac{\mu^2}{-p^2}\right)\right) \langle Q_2 \rangle_{\text{tree}} + \frac{3}{N_c} \frac{\alpha_s}{4\pi} \ln\left(\frac{m_W^2}{-p^2}\right) \langle Q_2 \rangle_{\text{tree}} - 3\frac{\alpha_s}{4\pi} \ln\left(\frac{m_W^2}{-p^2}\right) \langle Q_1 \rangle_{\text{tree}} \Bigg], \tag{3.7}$$

where $\langle Q_i \rangle_{\text{tree}}$ indicate the tree-level matrix elements of operators Q_i. For a derivation of this expression, see [81]. Here we work in the *leading logarithm* approximation which equates to keeping terms $O(\alpha_s \ln(\cdot))$ while neglecting terms $O(\alpha_s)$.

In the effective theory, we find the unrenormalised matrix elements of Q_i at NLO in QCD as

$$\langle Q_1 \rangle^{(0)} = \left[1 + 2C_F \frac{\alpha_s}{4\pi} \left(\frac{1}{\epsilon} + \ln\left(\frac{\mu^2}{-p^2}\right)\right)\right] \langle Q_1 \rangle_{\text{tree}} + \frac{3}{N_c} \frac{\alpha_s}{4\pi} \left(\frac{1}{\epsilon} + \ln\left(\frac{\mu^2}{-p^2}\right)\right) \langle Q_1 \rangle_{\text{tree}} - 3\frac{\alpha_s}{4\pi} \left(\frac{1}{\epsilon} + \ln\left(\frac{\mu^2}{-p^2}\right)\right) \langle Q_2 \rangle_{\text{tree}}, \tag{3.8}$$

$$\langle Q_2 \rangle^{(0)} = \left[1 + 2C_F \frac{\alpha_s}{4\pi} \left(\frac{1}{\epsilon} + \ln\left(\frac{\mu^2}{-p^2}\right)\right)\right] \langle Q_2 \rangle_{\text{tree}} + \frac{3}{N_c} \frac{\alpha_s}{4\pi} \left(\frac{1}{\epsilon} + \ln\left(\frac{\mu^2}{-p^2}\right)\right) \langle Q_2 \rangle_{\text{tree}} - 3\frac{\alpha_s}{4\pi} \left(\frac{1}{\epsilon} + \ln\left(\frac{\mu^2}{-p^2}\right)\right) \langle Q_1 \rangle_{\text{tree}}. \tag{3.9}$$

These results are clearly divergent with $1/\epsilon$ poles appearing in each term. The first poles

inside the square brackets are removed with the quark field renormalisation, however the remaining poles require normalisation of the operators. For some 2×2 renormalisation matrix $\hat{Z}$, the renormalisation condition is

$$Q_i^{(0)} = \hat{Z}_{ij} Q_j. \tag{3.10}$$

For the matrix elements of the operators, one must also include the quark field renormalisation Z_q, which translates to

$$\langle Q_i \rangle^{(0)} = Z_q^{-2} \hat{Z}_{ij} \langle Q_j \rangle. \tag{3.11}$$

The renormalisation in the MS scheme [95] to $O(\alpha_s)$ reads

$$Z_q = 1 - \frac{1}{\epsilon} \frac{C_F \alpha_s}{4\pi}, \qquad \hat{Z} = \mathbb{1} + \frac{\alpha_s}{4\pi} \frac{1}{\epsilon} \begin{pmatrix} \frac{3}{N_c} & -3 \\ -3 & \frac{3}{N_c} \end{pmatrix}. \tag{3.12}$$

The renormalised operators are then given by

$$\begin{aligned} \langle Q_1 \rangle = &\left[1 + 2C_F \frac{\alpha_s}{4\pi} \ln\left(\frac{\mu^2}{-p^2} \right) \right] \langle Q_1 \rangle_{\text{tree}} + \frac{3}{N_c} \frac{\alpha_s}{4\pi} \ln\left(\frac{\mu^2}{-p^2} \right) \langle Q_1 \rangle_{\text{tree}} \\ &- 3 \frac{\alpha_s}{4\pi} \ln\left(\frac{\mu^2}{-p^2} \right) \langle Q_2 \rangle_{\text{tree}}, \end{aligned} \tag{3.13}$$

$$\begin{aligned} \langle Q_2 \rangle = &\left[1 + 2C_F \frac{\alpha_s}{4\pi} \ln\left(\frac{\mu^2}{-p^2} \right) \right] \langle Q_2 \rangle_{\text{tree}} + \frac{3}{N_c} \frac{\alpha_s}{4\pi} \ln\left(\frac{\mu^2}{-p^2} \right) \langle Q_2 \rangle_{\text{tree}} \\ &- 3 \frac{\alpha_s}{4\pi} \ln\left(\frac{\mu^2}{-p^2} \right) \langle Q_1 \rangle_{\text{tree}}. \end{aligned} \tag{3.14}$$

Finally, matching the amplitude of the full theory in equation (3.7) with the effective amplitude using these renormalised operators, i.e.

$$\mathcal{A}_{\text{full}} = \mathcal{A}_{\text{eff}} = \frac{G_F}{\sqrt{2}} V_{cb}^* V_{ud} \left[C_1 \langle Q_1 \rangle + C_2 \langle Q_2 \rangle \right], \tag{3.15}$$

we obtain the expressions for the WCs (as long as the same renormalisation prescription has been used for the full and effective theories), reading

$$C_1(\mu) = 0 - 3 \frac{\alpha_s(\mu)}{4\pi} \ln\left(\frac{m_W^2}{\mu^2} \right), \tag{3.16}$$

$$C_2(\mu) = 1 + \frac{3}{N_c} \frac{\alpha_s(\mu)}{4\pi} \ln\left(\frac{m_W^2}{\mu^2} \right). \tag{3.17}$$

Here we can see the expected behaviour that neglecting QCD, i.e. $\alpha_s \to 0$, returns us to the tree-level description with $C_1 = 0$, $C_2 = 1$. Equivalently, setting $\mu = m_W$, i.e. the matching scale between the full and effective theories, also returns this result.

We are seeing one of the powers of the OPE description: in the full theory, large logarithms arise from the ratio of the different scales, while in the effective theory, the short- and long-distance effects can be factorised into the WCs and operators respectively. Explicitly, at $O(\alpha_s)$, we find

$$\overbrace{\left(1+\frac{3}{N_c}\frac{\alpha_s}{4\pi}\ln\left(\frac{m_W^2}{-p^2}\right)\right)}^{\mathcal{A}_{\text{full}}} = \overbrace{\left(1+\frac{3}{N_c}\frac{\alpha_s}{4\pi}\ln\left(\frac{m_W^2}{\mu^2}\right)\right)}^{C_i(\mu)}\overbrace{\left(1+\frac{3}{N_c}\frac{\alpha_s}{4\pi}\ln\left(\frac{\mu^2}{-p^2}\right)\right)}^{\langle Q_i\rangle}. \tag{3.18}$$

So one sees a splitting of the logarithm as

$$\ln\left(\frac{m_W^2}{-p^2}\right) = \ln\left(\frac{m_W^2}{\mu^2}\right)\ln\left(\frac{\mu^2}{-p^2}\right), \tag{3.19}$$

which originates from a splitting in the integration over loop momentum, i.e.

$$\int_{-p^2}^{m_W^2}\frac{dk^2}{k^2} = \int_{\mu^2}^{m_W^2}\frac{dk^2}{k^2} + \int_{-p^2}^{\mu^2}\frac{dk^2}{k^2}. \tag{3.20}$$

So the high-energy perturbative physics $[\mu^2, m_W^2]$ is contained in the Wilson coefficients, and the low-energy non-perturbative physics $[-p^2, \mu^2]$, bounded by the off-shell momentum p, is described by the matrix elements of the local operators. The renormalisation scale $\mu \sim O(\text{GeV})$ acts as a separation scale between short- and long-distance effects.

However, one finds that the calculation of the WCs will become quickly unreliable as the renormalisation scale μ is decreased from m_W, since

$$\alpha_s \ln\left(\frac{m_W^2}{\mu^2}\right) \sim O(1), \quad \text{for } \mu^2 \ll m_W^2, \tag{3.21}$$

which means that a series expansion in these logarithms does not converge at these scales. To combat this, recall the renormalisation group equations discussed in section 2.3.2. For the running coupling $\alpha_s(\mu)$, using $\alpha_s(m_Z)$ as an input value from experiment [54], this can be written as

$$\alpha_s(\mu) = \frac{\alpha_s(m_Z)}{1-\beta_0\frac{\alpha_s(m_Z)}{2\pi}\ln\left(\frac{m_Z}{\mu}\right)}, \tag{3.22}$$

with $\beta_0 = \frac{11}{3}N_c - \frac{2}{3}N_f$. Expanding this, we find

$$\alpha_s(\mu) = \alpha_s(m_Z)\left[1-\sum_{n=1}^{\infty}\left(\beta_0\frac{\alpha_s(m_Z)}{2\pi}\ln\left(\frac{m_Z}{\mu}\right)\right)^n\right]. \tag{3.23}$$

From this result, it is clear that the renormalisation group automatically sums the large logs to all orders in perturbation theory. Now we turn to apply the same principles to the effective Hamiltonian. We first introduce the renormalisation condition for the

Wilson coefficients as

$$C_i = \hat{Z}_{ij}^T C_j^{(0)}, \tag{3.24}$$

where the use of the same renormalisation matrix as for the local operators is enforced by requiring that the effective Hamiltonian is scale independent. It follows that

$$\begin{aligned} \frac{dC_i(\mu)}{d\ln\mu} &= \frac{d\hat{Z}_{ij}^T(\mu)}{d\ln\mu} C_j^{(0)} \\ &= \hat{Z}_{ij}^{T,-1} \frac{d}{d\ln\mu} \hat{Z}_{ij}^T(\mu) C_j^{(0)} \\ &\equiv \hat{\gamma}_{ij}^T C_j(\mu), \end{aligned} \tag{3.25}$$

with the anomalous dimension matrix defined

$$\hat{\gamma} = \hat{Z}^{-1} \frac{d}{d\ln\mu} \hat{Z}(\mu). \tag{3.26}$$

Explicitly, (at leading order) this yields

$$\hat{\gamma}^{(0)}(\alpha_s) = \frac{\alpha_s}{4\pi} \begin{pmatrix} -\frac{6}{N_c} & 6 \\ 6 & -\frac{6}{N_c} \end{pmatrix}. \tag{3.27}$$

It is common to present equation (3.25) in terms of an evolution matrix $\hat{U}(\mu, \mu_0)$ which contains the information from the RGE to 'run' the Wilson coefficients from scale μ_0 to μ, i.e.

$$C_i(\mu) = \hat{U}_{ij}(\mu, \mu_0) C_j(\mu_0), \tag{3.28}$$

where the evolution matrix is defined as

$$\hat{U}(\mu, \mu_0) = \left[\frac{\alpha_s(\mu)}{\alpha_s(\mu_0)} \right]^{-\frac{\hat{\gamma}^{(0)}}{2\beta_0}}. \tag{3.29}$$

To utilise the full strength of the RGE, we set $\mu_0 = m_W$, which results in $C_1(\mu_0) = 0$, $C_2(\mu_0) = 1$, i.e. their tree-level expressions, and all the large logarithms $\ln\left(m_W^2/\mu^2\right)$ are then summed up within the RGE.

Finally, it is important to note that the renormalisation scale μ will affect the number of *effective* quark flavours present in the calculation. The number of effective flavours f is defined as

$$f = \begin{cases} 6, & \mu \gtrsim m_t, \\ 5, & m_b \lesssim \mu \lesssim m_t, \\ 4, & m_c \lesssim \mu \lesssim m_b, \\ 3, & \mu \lesssim m_c. \end{cases} \tag{3.30}$$

As μ decreases below different quark mass thresholds, these quarks can no longer be dynamically produced and thus can similarly be integrated out of the effective theory as the $W^{\pm}$ boson. It turns out there is some freedom at which point a heavy quark is integrated out, e.g. a five-flavour theory can typically be extended to $\mu = m_b/2$[1]. This effect is important in the matching procedure as threshold effects between e.g. five-flavour theory running from the m_W scale to m_b and the four-flavour theory for a process with renormalisation scale $\mu \sim m_c$ must be taken into account.

3.1.2 Weak Effective Vertices from New Physics

We have seen the basic implementation of the weak effective theory as a method of separating short- and long-distance effects in the calculation of a Standard Model process such that we avoid large expansion parameters in our perturbation theory. In fact, the power of the OPE can go further than simply aiding in Standard Model calculations – it can also be used to study new physics effects beyond the SM. Typically (although not always), extensions to the Standard Model consider theories defined at or above the electroweak scale, introducing new mediator particles with masses on the order of this new scale. By analogy to the heavy $W^{\pm}$ boson, these mediators can be integrated out of the new physics amplitudes and a low-energy effective theory can be prescribed. This low-energy effective theory can easily be matched to one used in SM calculations, such as SMEFT (see e.g. [96]) or WET. Extending the effective Hamiltonian to allow for all possible Dirac structures, not just those present in the SM, one has local operators for any heavy mediators from new physics. With the additional Feynman diagrams introduced by the new physics theory, the Wilson coefficients of these new operators can be calculated in perturbation theory, while the matrix elements of the long-distance QCD physics are still calculated non-perturbatively as before[2]. Since the Wilson coefficients simply come from summing all contributing diagrams, if the new physics model contributes to operators also affected by the SM, then the resulting Wilson coefficient is the sum of the two, i.e.

$$C_i(\mu) = C_i(\mu)^{SM} + C_i(\mu)^{NP}. \tag{3.31}$$

One can see that this is actually true for all Dirac structures, with $C_i^{SM} = 0$ for those not present in the Standard Model. The inclusion of new physics effects in our effective theory is then clearly defined and rather straightforward to implement using equation (3.31); we will make use of this when we consider a specific new physics scenario in chapter 4.

[1] It is also the convention to estimate the error from higher-order corrections by using the range $\frac{m_b}{2} < \mu < 2m_b$ which is always done within the same effective theory.

[2] One can also propose some low-energy new physics models which would interfere with the low-energy matrix elements, but typically this is much more constrained and will not be discussed further here.

3.1.3 Heavy Quark Effective Theory

We have already discussed how the phenomena of confinement in QCD leads to a large coupling α_s at scale $O(\Lambda_{\text{QCD}})$ such that the description of hadronic states is in general highly non-perturbative. However, hadronic states containing a heavy quark Q with $m_Q \gg \Lambda_{\text{QCD}}$ can have significant simplifications in their description since the larger scale of the heavy quark results in some physics approaching the perturbative regime with a smaller coupling $\alpha_s(m_Q)$. The most significant examples of this are heavy quarkonia systems, i.e. $Q\bar{Q}$ meson states, which can be modelled very similarly to a hydrogen atom. The description of *heavy-light* hadrons, i.e. a hadronic state with one heavy quark Q, is not as simple as heavy quarkonia, however still simplifications can be found compared to the completely non-perturbative picture of lighter hadrons. These systems can be described as a heavy quark surrounded by a "brown muck" of strongly-interacting gluons and light quarks. Here the heavy quark interacts through the exchange of soft gluons and is mostly on-shell, with fluctuations of the order Λ_{QCD}. Thus in the $\frac{\Lambda_{\text{QCD}}}{m_Q} \to 0$ limit, these fluctuations vanish and the four-velocity v^μ of the heavy quark becomes a conserved quantity. One will find that in this limit, the heavy quark behaves as a static colour source interacting with the "brown muck", which is unable to resolve other quantum numbers such as flavour and spin at leading order. In quark-mass power-suppressed terms, these relativistic effects will come into play and can be accounted for perturbatively as part of an OPE. This is know as the *heavy quark effective theory* (HQET). In this section, we provide a brief introduction to HQET [97–100].

For a hadron containing a heavy quark Q, the foundation of HQET is the assumption that the heavy quark moves with the same velocity as the hadron, v^μ, and is almost on-shell itself. Georgi [97] wrote the momentum of the heavy quark p_Q^μ as

$$p_Q^\mu = m_Q v^\mu + k^\mu, \tag{3.32}$$

for the heavy quark mass m_Q. v^μ is the hadron/heavy quark four-velocity which satisfies $v^2 = 1$ and $k^\mu \sim O(\Lambda_{\text{QCD}})$ is the *residual momentum* describing how off-shell the heavy quark is due to QCD interactions with the light degrees of freedom, i.e. the "brown muck" of gluons and light quarks surrounding the heavy quark. To describe a heavy quark in the limit $m_Q \to \infty$ with fixed v^μ, k^μ, one can consider the simplification of the heavy quark propagator:

$$i\frac{\not{p}_Q + m_Q}{p_Q^2 - m_Q^2 + i\epsilon} = \frac{i}{v\cdot k + i\epsilon}\left(\frac{1+\not{v}}{2}\right) + O\left(\frac{k}{m_Q}\right) \implies \frac{i}{v\cdot k + i\epsilon}P_+, \tag{3.33}$$

where P_+ is the projection operator for the positive energy modes of the Dirac field. Also including the conjugate, these operators satisfy

$$P_\pm = \frac{1 \pm \not{v}}{2}, \qquad P_\pm^2 = P_\pm, \qquad P_\pm P_\mp = 0. \tag{3.34}$$

Considering the heavy quark's rest frame, $v^\mu = (1, \vec{0})$,

$$P_\pm = \frac{1 \pm \gamma_0}{2} \implies P_+ = \begin{pmatrix} \mathbb{1}_2 & 0 \\ 0 & 0 \end{pmatrix}, \quad P_- = \begin{pmatrix} 0 & 0 \\ 0 & \mathbb{1}_2 \end{pmatrix}. \tag{3.35}$$

So the projectors $P_\pm$ project to the upper (lower) two components of the quark spinor. Using the relation

$$P_+ \gamma^\mu P_+ = P_+ v^\mu P_+, \tag{3.36}$$

the heavy quark-gluon coupling can also be simplified as

$$igT_a\gamma^\mu \implies igT_a v^\mu + O\left(\frac{1}{m_Q}\right). \tag{3.37}$$

The Feynman rules for the heavy quark propagator and heavy quark-gluon coupling are given in figure 3.4. The heavy quark field itself can be parameterised as

$$Q(x) = e^{-im_Q v\cdot x} h_v(x) + O\left(\frac{k}{m_Q}\right) \tag{3.38}$$

for the *effective heavy quark field* $h_v(x)$ which satisfies

$$h_v(x) = e^{im_Q v\cdot x}\frac{1+\not{v}}{2} Q(x) \implies P_+ h_v(x) = h_v(x). \tag{3.39}$$

The exponential factor in equation (3.38) removes the large 'kinetic' piece $(m_Q v)$ from

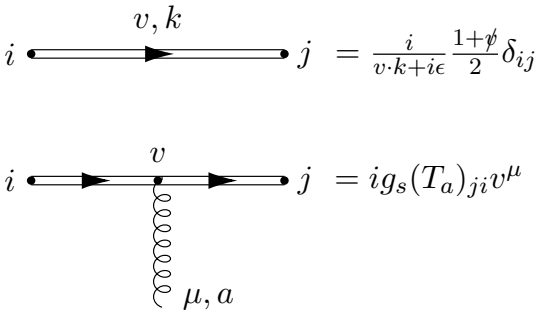

FIGURE 3.4: Feynman rules in the heavy quark effective theory.

the heavy quark momentum, such that $h_v(x)$ only returns the residual momentum k in momentum space. We can now express the effective Lagrangian for HQET as

$$\mathcal{L}_{\text{HQET}}(x) = \bar{h}_v(x) i(v\cdot D)\, h_v(x) = \bar{h}_v(x)\left(iv^\mu\partial_\mu + g_s T_a v^\mu A_\mu^a\right) h_v(x). \tag{3.40}$$

This Lagrangian is only an approximation to the QCD Lagrangian for a heavy quark since, in the rest frame, h_v is a two-component field containing only upper components of the spinor. h_v will annihilate a heavy quark with velocity v^μ but will not create an antiquark, and similarly $\bar{h}_v$ will create a heavy quark with velocity v^μ but will not annihilate an antiquark, i.e. the number of heavy quarks in the effective theory is conserved – heavy pair production is not present. Furthermore, the Lagrangian is independent of the mass of the heavy quark, such that the description is unchanged if the heavy quark Q is replaced by another heavy quark Q', assuming the same velocity v^μ and $m'_Q \gg \Lambda_{\mathrm{QCD}}$; the theory is invariant in flavour space. Finally, one sees that there are no Dirac matrices in the effective Lagrangian, so the spin of the heavy quark is unaffected by interactions with gluons. Combining this with the flavour invariance, one sees there is a heavy quark SU($2N_h$) spin-flavour symmetry in the strong HQET limit, which will clearly be broken by mass correction terms.

The heavy quark field Q actually contains another component, H_v, defined by

$$H_v(x) = e^{im_Q v\cdot x}\frac{1-\not{v}}{2}Q(x), \qquad\qquad P_- H_v(x) = H_v(x). \tag{3.41}$$

So in the rest frame $H_v(x)$ is a two-component field for the lower components of the spinor, and corresponds to the "small" components of Q; it creates a heavy antiquark with velocity v^μ. Now taking H_v into account, the heavy quark field is defined

$$Q(x) = e^{-im_Q v\cdot x}\left[h_v(x) + H_v(x)\right]. \tag{3.42}$$

Then, re-expressing the QCD Lagrangian for heavy quarks with these fields, we find

$$\begin{aligned}
\mathcal{L}_{\mathrm{QCD}} &= \bar{Q}(x)\left(i\not{D} - m_Q\right)Q(x) \\
&= \left[\bar{h}_v(x) + H_v(x)\right]\left(m_Q\not{v} + i\not{D} - m_Q\right)\left[h_v(x) + H_v(x)\right] \\
&= \bar{h}_v(x) i(v\cdot D)\, h_v(x) - H_v(x)\left(iv\cdot D + 2m_Q\right)H_v(x) \\
&\quad + \bar{h}_v(x) i\not{D}_\perp H_v(x) + \bar{H}_v(x) i\not{D}_\perp h_v(x),
\end{aligned} \tag{3.43}$$

where we have introduced the covariant derivative orthogonal to the velocity as

$$D^\mu_\perp = D^\mu - v^\mu(v\cdot D). \tag{3.44}$$

We have now arrived at the Lagrangian for a heavy quark which is still finite, i.e. $m_Q \not\to \infty$. The large component field h_v describes the massless degrees of freedom, while the small component field H_v describes massive fluctuations with mass $2m_Q$. The two fields mix in the terms written on the last line of equation (3.43), which describe pair creation and annihilation of heavy quarks and antiquarks. This also results in virtual

corrections to the heavy quark propagator. Drawing this vertex in figure 3.5, one sees that this corresponds to a heavy quark propagating forwards in time then turning into a heavy antiquark propagating backwards in time before turning back into a heavy quark. The intermediate quantum state formed by this virtual correction has an energy at least

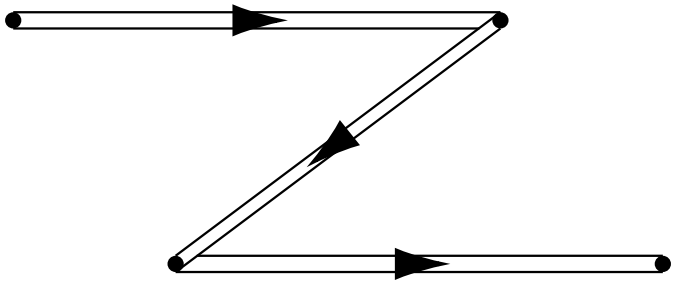

FIGURE 3.5: Virtual fluctuation in the HQET heavy quark propagator via the creation and annihilation of a heavy antiquark, with time flowing from left to right.

$2m_Q$ larger than the initial heavy quark and can only propagate over a distance $\sim 1/m_Q$. At energy scales $O(\Lambda_{\text{QCD}})$, this process looks like a local interaction, reading

$$\bar{h}_v(x) i\not{D}_\perp \frac{1}{2m_Q} i\not{D}_\perp h_v(x), \tag{3.45}$$

where the heavy antiquark propagator is replaced by $i/2m_Q$. More systematically, we can look to integrate out the heavy degrees of freedom described by H_v and derive a non-local effective Lagrangian only for the large component field h_v. To eliminate H_v, one can derive the equations of motion (EoMs) for h_v and H_v, finding

$$-i(v \cdot D) h_v(x) = i\not{D}_\perp H_v(x), \tag{3.46}$$

$$(iv \cdot D + 2m_Q)\, H_v(x) = i\not{D}_\perp h_v(x). \tag{3.47}$$

If the second EoM is inverted, one obtains

$$H_v(x) = \frac{1}{iv \cdot D + 2m_Q - i\epsilon} i\not{D}_\perp h_v(x), \tag{3.48}$$

which confirms the description that H_v is the small component field since it is $O(1/m_Q)$. Inserting this into equation (3.46), we can find the effective Lagrangian

$$\mathcal{L}_{\text{eff}} = \bar{h}_v(x) i(v \cdot D) h_v(x) + \bar{h}_v(x) i\not{D}_\perp \frac{1}{iv \cdot D + 2m_Q - i\epsilon} i\not{D}_\perp h_v. \tag{3.49}$$

This is the generalisation of $\mathcal{L}_{\text{HQET}}$ (see equation (3.40)) for large, but not infinite, heavy quark mass. We now have a description of the QCD interactions of a heavy quark at energy scale $O(\Lambda_{\text{QCD}})$, where the heavy degrees of freedom described by H_v are no longer relevant and we can express the theory only in h_v.

Since the Fourier transform of h_v only returns the small residual momentum $k \ll m_Q$, we can express equation (3.49) as an expansion in iD/m_Q to produce an OPE. Using the identity

$$P_+ i\not{D}_\perp i\not{D}_\perp P_+ = P_+ \left[(iD_\perp)^2 + \frac{g_s}{2}\sigma_{\alpha\beta}G^{\alpha\beta}\right] P_+ \;\because\; [iD^\alpha, iD^\beta] = ig_s G^{\alpha\beta}, \tag{3.50}$$

we can now write the effective Lagrangian as

$$\mathcal{L}_{\text{eff}} = \bar{h}_v(x) i(v\cdot D) h_v(x) + \frac{1}{2m_Q}\bar{h}_v(x)(iD_\perp)^2 h_v(x) + \frac{g_s}{4m_Q}\bar{h}_v(x)\sigma_{\alpha\beta}G^{\alpha\beta}h_v(x) + O\left(\frac{1}{m_Q^2}\right). \tag{3.51}$$

This coincides with the HQET Lagrangian written in equation (3.40) at leading order, with two new operators introduced at $O(1/m_Q)$. In the rest frame, one can easily identify these new operators as:

$$\mathcal{O}_{\text{kin}} = \bar{h}_v(x)(iD_\perp)^2 h_v(x) \to -\bar{h}_v(x)(i\vec{D})^2 h_v(x), \tag{3.52}$$

$$\mathcal{O}_{\text{mag}} = \frac{g_s}{2}\bar{h}_v(x)\sigma_{\alpha\beta}G^{\alpha\beta}h_v(x) \to -2g_s\bar{h}_v(x)\,\vec{S}\cdot\vec{B}_c h_v(x), \tag{3.53}$$

where $\vec{S} = \frac{1}{2}\gamma_5\gamma^0\vec{\gamma}$ is the spin operator and $B_c^i = -\frac{1}{2}\epsilon^{ijk}G^{jk}$ are the colour-magnetic gluon field components, and we have neglected the prefactor $\frac{1}{2m_Q}$ for simpler use later on. The first operator, $\mathcal{O}_{\text{kin}}$, is the covariant extension of the kinetic energy due to the heavy quark's residual off-shell momentum inside the hadron. The second operator, $\mathcal{O}_{\text{mag}}$, is the non-Abelian equivalent to the Pauli term – the chromomagnetic interaction of the heavy quark spin with the gluon field.

Using the expression for H_v found in equation (3.48), we can find a similar expansion in $1/m_Q$ for the heavy quark field $Q(x)$:

$$\begin{aligned} Q(x) &= e^{-im_Q v\cdot x}\left[1 + \frac{1}{iv\cdot D + 2m_Q - i\epsilon} i\not{D}_\perp\right] h_v(x) \\ &= e^{-im_Q v\cdot x}\left[1 + \frac{1}{2m_Q} i\not{D}_\perp + \frac{(-iv\cdot D)}{4m_Q^2} i\not{D}_\perp + \dots\right] h_v(x). \end{aligned} \tag{3.54}$$

This allows us to construct in HQET any operator containing a heavy quark field. Consider, for example, the heavy-light vector current $\mathcal{V}^\mu = \bar{q}(x)\gamma^\mu Q(x)$ for a light quark q with mass $m_q \ll m_Q$. At order $\frac{1}{m_Q}$, this reads

$$\mathcal{V}^\mu(x) = e^{-im_Q v\cdot x}\bar{q}(x)\gamma^\mu\left(1 + \frac{1}{2m_Q} i\not{D}_\perp + \dots\right) h_v(x). \tag{3.55}$$

A matrix element of the vector current, e.g. between a heavy meson $M(v)$ and the vacuum then has the following form:

$$\langle 0|\mathcal{V}^\mu|M(v)\rangle = \langle 0|\bar{q}\gamma^\mu h_v|M(v)\rangle + \frac{1}{2m_Q}\langle 0|\bar{q}\gamma^\mu i\not{D}_\perp h_v|M(v)\rangle + \cdots . \tag{3.56}$$

We would like the matrix elements on the right-hand-side of this relation to be independent of m_Q such that they can be described universally [100, 101], and the higher-order terms give power corrections to the leading term. However, by deriving the EoMs from the Lagrangian in equation (3.51), one finds that h_v itself has an expansion in $\frac{1}{m_Q}$, so the eigenstates of the Lagrangian depend themselves on the heavy quark mass. By choosing to work with the eigenstates of equation (3.40) and treating the higher-dimension operators such as $\mathcal{O}_{\text{kin,mag}}$ as perturbations of this Lagrangian, we can rewrite the effective Lagrangian in equation (3.51) as

$$\mathcal{L}_{\text{eff}} = \mathcal{L}_{\text{HQET}} + \mathcal{L}_{\text{power}}, \tag{3.57}$$

$$\mathcal{L}_{\text{power}} = \frac{1}{2m_Q}\mathcal{L}_1 + \frac{1}{4m_Q^2}\mathcal{L}_2 + \ldots . \tag{3.58}$$

From this, the EoM for h_v is given by

$$i(v\cdot D)h_v(x) = 0, \tag{3.59}$$

such that the eigenstates of our effective theory are now independent of the heavy quark mass. These states are however different from the states found in the full theory. For example, consider again the matrix element of the vector current between a heavy meson and the vacuum:

$$\begin{aligned}\langle 0|V^\mu|M(v)\rangle_{\text{QCD}} = {} & \langle 0|\bar{q}\gamma^\mu h_v|M(v)\rangle_{\text{HQET}} \\ & + \frac{1}{2m_Q}\langle 0|\bar{q}\gamma^\mu i\not{D}_\perp h_v|M(v)\rangle_{\text{HQET}} \\ & + \frac{1}{2m_Q}\langle 0|i\int d^4y\, T\left\{\bar{q}\gamma^\mu h_v(0), \mathcal{L}_1(y)\right\}|M(v)\rangle_{\text{HQET}} \\ & + O\left(\frac{1}{m_Q^2}\right).\end{aligned} \tag{3.60}$$

Expressed this way, the HQET matrix elements are now independent of m_Q, however the QCD matrix element still has mass dependence which is seen in the third line with the appearance of $\mathcal{L}_1$. This time-ordered product can be thought of as a correction to the heavy meson wavefunction. The HQET and QCD matrix elements are therefore evaluated between different eigenstates $|M(v)\rangle_{\text{HQET}}$ and $|M(v)\rangle_{\text{QCD}}$.

Finally, one can use the EoMs again to extract the operators of the power-correction Lagrangian $\mathcal{L}_{\text{power}}$. To order $\frac{1}{m_Q^2}$, one finds

$$\mathcal{L}_1 = \bar{h}_v(x)(iD)^2 h_v(x) + \frac{g_s}{2}\bar{h}_v \sigma_{\alpha\beta} G^{\alpha\beta} h_v(x) = \mathcal{O}_{\text{kin}} + \mathcal{O}_{\text{mag}}, \tag{3.61}$$

$$\mathcal{L}_2 = g\bar{h}_v(x)\sigma_{\alpha\beta} v_\gamma i D^\alpha G^{\beta\gamma} h_v(x) + g\bar{h}_v(x) v_\alpha D_\beta G^{\alpha\beta} h_v(x). \tag{3.62}$$

3.1.4 The Heavy Quark Expansion

The lifetime τ, given by the inverse of the decay width $\tau = \Gamma^{-1}$, is one of the most fundamental properties of an elementary or composite particle. Of particular interest are the lifetimes of hadrons containing heavy quarks, which decay via the weak interaction. We already described in section 3.1.3 how, for instance, heavy-light mesons can be thought of as a static heavy quark Q surrounded by the "brown muck" of non-perturbative light quarks and gluons. In the infinite mass limit, this description is at its simplest, where the heavy quark decouples from the non-perturbative cloud of QCD interactions and the hadron can be described fully by the dynamics of the heavy quark [102]. In this limit, it is clear that all mesons/baryons with any flavour of heavy quark should behave the same, however in reality we find this is not the case. For the heavier bottom quark, hadrons mostly follow this prescription with only small deviations (see e.g. [26]), while for the lighter charm quark, hadrons exhibit larger variation (see e.g. [103]). So the infinite mass limit requires correction terms in order to properly describe hadrons with heavy quarks of physical, finite mass. The *heavy quark expansion* (HQE) is the theoretical framework developed to describe the inclusive decays of heavy hadrons by systematically correcting the infinite mass limit in an OPE through the hierarchy $\Lambda_{\text{QCD}} \ll m_Q$. Below we lay out the construction of the HQE and the theoretical status of its constituents. For a more comprehensive review, we refer to e.g. [89, 104].

First, we recall that in scattering theory, a process is described by the unitary scattering matrix S which connects two asymptotically-free states $|i\rangle, |f\rangle$ for some theory describing the interactions of these states. The scattering matrix can be written as

$$S_{fi} \equiv \langle f|S|i\rangle = \delta_{fi} + iT_{fi}, \tag{3.63}$$

where T_{fi} is the transition amplitude describing the non-trivial dynamics of the system. This in turn can be expressed in terms of $\mathcal{M}_{fi}$ the invariant scattering amplitude as

$$T_{fi} = (2\pi)^2 \delta^{(4)}(p_f - p_i)\mathcal{M}_{fi}, \tag{3.64}$$

where p_i^μ, p_f^μ are the momenta of the initial and final states respectively.

The decay rate of a single-body initial state (from here referring to a meson H_Q with heavy valence quark Q) is described as the sum of the transition from the initial state to all possible final states X, given by

$$\Gamma(H_Q \to X) = \frac{1}{2m_{H_Q}} \sum_X \int_{\mathrm{PS}} (2\pi)^4 \delta^{(4)}(p_{H_Q} - p_X) |\langle X|\mathcal{H}_{\mathrm{eff}}|H_Q\rangle|^2, \tag{3.65}$$

where $\mathcal{H}_{\mathrm{eff}}$ is the effective weak Hamiltonian, and for an N-body final state, the phase space integral is given by

$$\int_{\mathrm{PS}} = \int \prod_{n=1}^{N} \frac{d^3 p_n}{(2\pi)^3 2E_n}. \tag{3.66}$$

To simplify calculations, equation (3.65) can be equivalently expressed using the optical theorem, which we will briefly outline. Following unitarity of the scattering matrix,

$$S^\dagger S = S S^\dagger = \mathbb{1}, \tag{3.67}$$

one can insert a complete tower of states which we both sum over and integrate over their momenta, written as

$$\sum_n \int_{\mathrm{PS}} \langle f|S^\dagger|n\rangle\langle n|S|i\rangle = \delta_{fi}. \tag{3.68}$$

For forward scattering ($|i\rangle = |f\rangle$), from the definition of the scattering matrix (equation (3.63)), we find that

$$\sum_n \int_{\mathrm{PS}} [\delta_{ni} - iT^*_{ni}]\,[\delta_{ni} + iT_{ni}] = \delta_{ii}, \tag{3.69}$$

$$\implies 2\,\mathrm{Im}\,T_{ii} = \sum_n \int_{\mathrm{PS}} |T_{ni}|^2. \tag{3.70}$$

The optical theorem connects the imaginary part of the forward scattering amplitude to the total cross-section for the production of all final states. One can then insert this into equation (3.64) and find

$$2\,\mathrm{Im}\,M_{ii} = \sum_n \int_{\mathrm{PS}} (2\pi)^4 \delta^{(4)} \left(\sum_{n=1}^{N} p_n - p_i \right) |M_{ni}|^2. \tag{3.71}$$

A schematic of the optical theorem is shown in figure 3.6. One can use this relation to simplify the expression for the decay rate of a meson H_Q, such that we calculate the imaginary part of the forward scattering amplitude of $H_Q \to H_Q$.

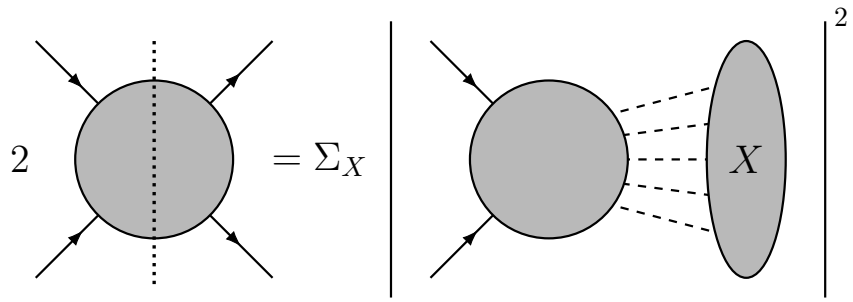

FIGURE 3.6: A schematic of the optical theorem. The imaginary part of a forward scattering amplitude is related to the sum over the squared amplitudes for the production of all final states X.

First, we can express the scattering matrix via the effective Hamiltonian describing the decay of a heavy quark Q into all possible configurations of lighter particles, reading

$$S = \mathrm{T}\left\{\exp\left[-i\int d^4\,\mathcal{H}_{\mathrm{eff}}(x)\right]\right\}, \tag{3.72}$$

for the time-ordering operator T. Then one finds that for the transition operator

$$\mathcal{T} = i\int d^4x\,\mathrm{T}\Big\{\mathcal{H}_{\mathrm{eff}}(x), \mathcal{H}_{\mathrm{eff}}(0)\Big\} \tag{3.73}$$

the total decay rate is

$$\Gamma(H_Q \to X) = \frac{1}{2m_{H_Q}}\mathrm{Im}\langle H_Q|\mathcal{T}|H_Q\rangle. \tag{3.74}$$

So what we see is that the total decay rate of a meson H_Q decaying into all possible final states X is related to the amplitude of the forward scattering of the meson H_Q via the process $H_Q \to X \to H_Q$, i.e. the creation and annihilation of all intermediate states X. One may notice that in this description we have neglected to mention the light valence quark of the H_Q meson system; technically this decay is complicated by the presence of this light quark with the non-perturbative QCD interactions of this and the other light degrees of freedom, however Shifman and Voloshin [105] noted that in the limit of an infinitely massive heavy quark, the decay of a heavy-light meson is equivalent to the decay of the heavy quark. Of course, this is only strictly true in the limit $m_Q \to \infty$, and therefore for large but finite masses of the quark Q, corrections to this limit must be included to more appropriately describe the dynamics of a heavy meson H_Q.

The HQE is the framework through which corrections to the infinite mass limit are systematically included for hadrons with a massive but finite heavy quark constituent. Here we assume that the heavy quark Q inside a heavy hadron interacts with the light

degrees of freedom via momentum exchanges $O(\Lambda_{\text{QCD}}) \ll m_Q$. It follows that a significant portion of the heavy quark's momentum is proportional to its mass, which can then be separated by rewriting the heavy quark field as

$$Q(x) = e^{-im_Q v\cdot x} Q_v(x), \tag{3.75}$$

where v^μ is the velocity of the heavy hadron[3]. From here, a second OPE is performed for the parameter $\frac{\Lambda_{\text{QCD}}}{m_Q} \ll 1$, resulting in the total decay rate being written as

$$\Gamma(H_Q) = \Gamma_3\langle\mathcal{O}_3\rangle + \Gamma_5\frac{\langle\mathcal{O}_5\rangle}{m_Q^2} + \Gamma_6\frac{\langle\mathcal{O}_6\rangle}{m_Q^3} + \ldots + 16\pi^2\left[\tilde{\Gamma}_6\,\frac{\langle\tilde{\mathcal{O}}_6\rangle}{m_Q^3} + \tilde{\Gamma}_7\,\frac{\langle\tilde{\mathcal{O}}_7\rangle}{m_Q^4} + \ldots\right], \tag{3.76}$$

where $\overset{(\sim)}{\Gamma}_d$ are the perturbative Wilson coefficients and $\langle\overset{(\sim)}{\mathcal{O}}_d\rangle$ are the non-perturbatively calculated operator matrix elements at mass dimension d. The operators appearing inside $16\pi^2[\ldots]$ which start at dimension 6 are denoted with a $\sim$ to distinguish these as four-quark operators as opposed to the two-quark operators without tildes outside the square brackets; these operators may be suppressed by additional powers of m_Q compared to the leading two-quark terms, however they are comparatively enhanced by the $16\pi^2$ phase space factor. While the Γ_i are already two-loop calculations at leading order in QCD, the $\tilde{\Gamma}_i$ also have one-loop contributions. Below we now cover the theoretical status of the components of the HQE from dimensions three to six.

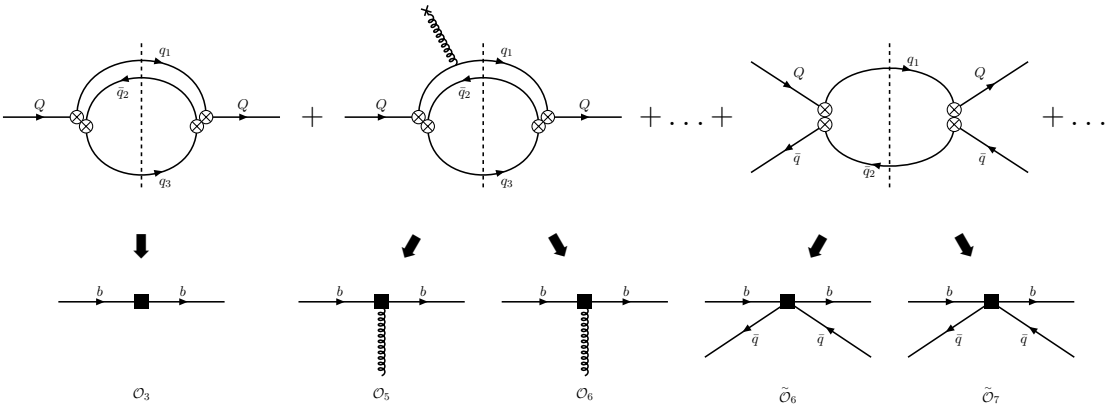

FIGURE 3.7: Diagrams describing the leading operators of the HQE as written in equation (3.76). The imaginary part of the double insertion of the effective weak Hamiltonian is shown in the top line where $\otimes$ represents the $\Delta B = 1$ operators Q_i; this is matched to the local $\Delta B = 0$ operators of the HQE in the bottom line which are denoted with $\blacksquare$ for the two-quark operators $\mathcal{O}_i$ and four-quark operators $\tilde{\mathcal{O}}_i$.

[3]Note that while this redefinition rings similar to what is done in HQET, here the quark field is simply a rescaling of the four-component QCD spinor whereas two-component non-relativistic projections are used in HQET.

Dimension Three

The leading term in the HQE is at mass dimension 3,

$$\mathcal{O}_3 = (\bar{Q}_v Q_v). \tag{3.77}$$

It describes the decay of a free b quark and to only consider this term is to take the infinite heavy quark mass limit.

Γ_3 has been calculated fully at NLO-QCD in [106] for semileptonic decays and in [106–115] for non-leptonic decays. NNLO-QCD corrections have been calculated for semileptonic channels [116–126], while for non-leptonic decays, these were only known for massless final-state quarks without the use of the effective Hamiltonian [127] until recent work which includes the effects of massive quarks [128]. N^{3}LO-QCD corrections for semileptonic channels are also now calculated in [34–36].

By following a HQET expansion, the matrix element of $\mathcal{O}_3$ is given by [129, 130]

$$\frac{\langle H_Q|\bar{Q}_v Q_v|H_Q\rangle}{2m_{H_Q}} = 1 - \frac{\mu_\pi^2(H_Q) - \mu_G^2(H_Q)}{2m_Q^2} + O\left(\frac{1}{m_Q^5}\right), \tag{3.78}$$

where the non-perturbative parameters μ_π^2, μ_G^2 parameterise the matrix elements of the dimension-five kinetic and chromomagnetic operators defined in equations (3.82) and (3.83).

Dimension Four

There are no independent dimension-four operators since these are related to $(\bar{Q}_v Q_v)$ through the EoMs. The absence of these terms in the HQE is known as the CGG/BUV theorem [131].

Dimension Five

At dimension five, two-quark operators appear which correct for the effect of soft gluon emissions and the $\frac{1}{m_Q}$ expansion of lower-dimension operators. The kinetic and chromomagnetic operators respectively appear as

$$\mathcal{O}_\pi = \bar{Q}_v (iD_\mu)(iD^\mu) Q_v, \tag{3.79}$$

$$\mathcal{O}_G = \bar{Q}_v (iD_\mu)(iD_\nu)(-i\sigma^{\mu\nu}) Q_v, \tag{3.80}$$

where the full dimension-five contribution appearing in equation (3.76) can be expressed as

$$\Gamma_5 \frac{\langle \mathcal{O}_5 \rangle}{m_b^2} = \Gamma_0 \left[c_\pi \frac{\langle \mathcal{O}_\pi \rangle}{m_b^2} + c_G \frac{\langle \mathcal{O}_G \rangle}{m_b^2} \right]. \tag{3.81}$$

Γ_5 has been calculated at LO-QCD for both semileptonic and non-leptonic decays [129, 132–134]. NLO-QCD corrections have also been calculated for semileptonic decays [135–137] and non-leptonic decays [138].

The matrix elements of the dimension-five operators are defined

$$\langle H_Q|\bar{Q}_v(iD_\mu)(iD^\mu)Q_v|H_Q\rangle = -2m_{H_Q}\mu_\pi^2(H_Q), \tag{3.82}$$
$$\langle H_Q|\bar{Q}_v(iD_\mu)(iD_\nu)(-i\sigma^{\mu\nu})Q_v|H_Q\rangle = \quad 2m_{H_Q}\mu_G^2(H_Q), \tag{3.83}$$

where μ_π^2, μ_G^2 have been calculated by QCD sum rules [139, 140] and lattice QCD [141, 142] or are alternatively extracted from fits to experimental data of inclusive semileptonic $B \to X_c\ell\bar{\nu}_\ell$ decays [143–148]. One can also use spectroscopy relations to estimate these quantities for B mesons with different light quarks [149].

Dimension Six – Two-Quark Operators

Two two-quark operators arise at dimension six, generated with three covariant derivatives, respectively called the spin-orbit and Darwin operators,

$$\mathcal{O}_{LS} = \bar{Q}_v(iD_\mu)(iv\cdot D)(iD_\nu)(-i\sigma^{\mu\nu})Q_v, \tag{3.84}$$
$$\mathcal{O}_{\rho_D} = \bar{Q}_v(iD_\mu)(iv\cdot D)(iD_\nu)Q_v. \tag{3.85}$$

Γ_6 has been computed for semileptonic decays at LO-QCD in [150–152] and NLO-QCD in [153–155], while for non-leptonic decays, the LO-QCD calculation has been performed for b quarks in [156–158] and for c quarks in [103]. It is worth noting that the coefficient of the Darwin operator is an order of magnitude larger than the corresponding dimension-five operators, such that, although it is suppressed by an additional power of m_Q, it has significant impact on the final results for heavy hadron lifetimes.

The matrix elements of the dimension-six two-quark operators are defined

$$\langle H_Q|\bar{Q}_v(iD_\mu)(iv\cdot D)(iD_\nu)(-i\sigma^{\mu\nu})Q_v|H_Q\rangle = -2m_{H_Q}\rho_{LS}^3(H_Q), \tag{3.86}$$
$$\langle H_Q|\bar{Q}_v(iD_\mu)(iv\cdot D)(iD_\nu)Q_v|H_Q\rangle = \quad 2m_{H_Q}\rho_D^3(H_Q), \tag{3.87}$$

where the non-perturbative parameters ρ_{LS}, ρ_D can similarly be extracted from experimental data as with μ_π^2, μ_G^2 [143–148]. Relations from the equations of motion [159, 160] can also be used, and there even exists a sum rule calculation [149].

Dimension Six – Four-Quark Operators

Four-quark operators also now enter at dimension-six which depend not only on the heavy quark Q but the light 'spectator' quark q. The four dimension-six four-quark

operators are

$$\begin{aligned}
\widetilde{\mathcal{O}}_1 &= \big(\bar{Q}_v\gamma_\mu(1-\gamma_5)q\big)\otimes\big(\bar{q}\gamma^\mu(1-\gamma_5)Q_v\big),\\
\widetilde{\mathcal{O}}_2 &= \big(\bar{Q}_v\quad(1-\gamma_5)q\big)\otimes\big(\bar{q}\quad(1+\gamma_5)Q_v\big),\\
\widetilde{T}_1 &= \big(\bar{Q}_v\gamma_\mu(1-\gamma_5)T^a q\big)\otimes\big(\bar{q}\gamma^\mu(1-\gamma_5)T^a Q_v\big),\\
\widetilde{T}_2 &= \big(\bar{Q}_v\quad(1-\gamma_5)T^a q\big)\otimes\big(\bar{q}\quad(1+\gamma_5)T^a Q_v\big).
\end{aligned} \tag{3.88}$$

$\widetilde{\Gamma}_6$ is known at LO [161–164] and NLO in QCD [165–167]. These operators are referred to as $\Delta B = 0$ operators since they change the Bottom quantum number by 0.

The matrix elements of the dimension-six four-quark operators are defined

$$\langle H_Q|\,\widetilde{\mathcal{O}}_1\,|H_Q\rangle = f_{H_Q}^2 m_{H_Q}^2 B_1, \tag{3.89}$$

$$\langle H_Q|\,\widetilde{\mathcal{O}}_2\,|H_Q\rangle = \frac{m_{H_Q}^2}{(m_Q+m_q)^2} f_{H_Q}^2 m_{H_Q}^2 B_2, \tag{3.90}$$

$$\langle H_Q|\,\widetilde{T}_1\,|H_Q\rangle = f_{H_Q}^2 m_{H_Q}^2 \epsilon_1, \tag{3.91}$$

$$\langle H_Q|\,\widetilde{T}_2\,|H_Q\rangle = \frac{m_{H_Q}^2}{(m_Q+m_q)^2} f_{H_Q}^2 m_{H_Q}^2 \epsilon_2, \tag{3.92}$$

where f_{H_Q} is the decay constant of the meson H_Q,

$$\langle 0|\bar{Q}\gamma_\mu\gamma_5 q|H_Q(p)\rangle = i f_{H_Q} p_\mu. \tag{3.93}$$

The *bag parameters* $B_{1,2}, \epsilon_{1,2}$ describe the deviation of these matrix elements from the *vacuum insertion approximation* (VIA). For a four-quark operator $\bar{Q}\Gamma_1 q\bar{q}\Gamma_2 Q$ with generic Dirac-colour structures $\Gamma_{1,2}$, the VIA assumes that the matrix elements are saturated by the intermediary vacuum state between two quark bilinear currents, i.e.

$$\langle H_Q|\bar{Q}\Gamma_1 q\bar{q}\Gamma_2 Q|H_Q\rangle \overset{\text{VIA}}{=} \langle H_Q|\bar{Q}\Gamma_1 q|0\rangle\langle 0|\bar{q}\Gamma_2 Q|H_Q\rangle. \tag{3.94}$$

In the VIA, $B_{1,2} = 1$ and $\epsilon_{1,2} = 0$. It is expected that the deviation from the VIA of the full matrix elements is not large, however confirming this is an important motivation for calculating these quantities. These matrix elements have been calculated in HQET sum rules for the B_d [168] and B_s [169] mesons and in QCD sum rules for the Λ_b baryon [170]. Apart from early quenched studies [171, 172] and one preliminary unquenched study [173], these matrix elements have received little attention from lattice QCD and to date there is no complete lattice calculation of their values. The calculation of these matrix elements in lattice QCD will be the focus of chapter 6.

Further higher-dimensional two-quark and four-quark operators can be generated by adding more derivatives.

Quark-Hadron Duality

The HQE is built upon the assumption of *quark-hadron duality* (QHD) – this is the statement that the description of a hadronic system by using quarks as the degrees of freedom is equivalent to that using hadronic bound states as the degrees of freedom. This duality manifests here in the expectation that the inclusive rate of a hadron with a heavy quark calculated using the HQE is equivalent to the total sum of all exclusive decay channels. Violations of quark-hadron duality must be considered as a systematic uncertainty to the HQE, since treating the decay rate as a series expansion in $\Lambda_{\mathrm{QCD}}/m_Q$ can result in some terms being neglected. There is a large collection of literature studying quark-hadron duality and its possible violations. However these rely on strong model assumptions, see e.g. [174–177]. While the discussion in theory of quark-hadron duality is still ongoing, there is no evidence of its violation from experiment. One channel that is well-suited to testing quark-hadron duality is the decay $b \to c\bar{c}s$ since the expansion parameter of the HQE for this case is actually modified slightly such that duality violations would be more pronounced. The decay rate difference $\Delta\Gamma_s$ in neutral B_s mesons (see section 3.2.3) is governed by $b \to c\bar{c}s$ and thus a suitable candidate to test for duality violations. However the current status of experimental measurements show good agreement with the prediction from the HQE and thus exclude large violations of quark-hadron duality [26, 54].

3.2 Heavy Flavour Physics

Processes involving heavy quark flavours embody all of the physics of the Standard Model: all three generations of both quarks and leptons can be involved and therefore also the CKM matrix elements can be probed; both QED and weak interactions are present; QCD interactions also play an important role in both the perturbative and non-perturbative regimes. Therefore studying these serves as a way to study the whole SM in a subset of similar processes where the entire range of our theory can be assessed and experiments can be designed in favour of these such that we have high-precision measurements. In addition, the theoretical framework of effective field theories already discussed in this chapter, in particular HQET and the HQE, provides a powerful method to simplify theoretical predictions and separate out the different contributions. So we arrive at reliable, high precision results, with a clear understanding of how the different regimes of the Standard Model work both separately from and together with one another to create the dynamics of the universe. Heavy flavour physics therefore provides an exciting and important laboratory for the ever-ongoing quest to better understand the Standard Model and also search for new physics. In this thesis, we take particular interest in the physics of b quarks and the processes involving B mesons. Below, we will

cover some of the history of B physics phenomenology and its importance in the current landscape of particle physics.

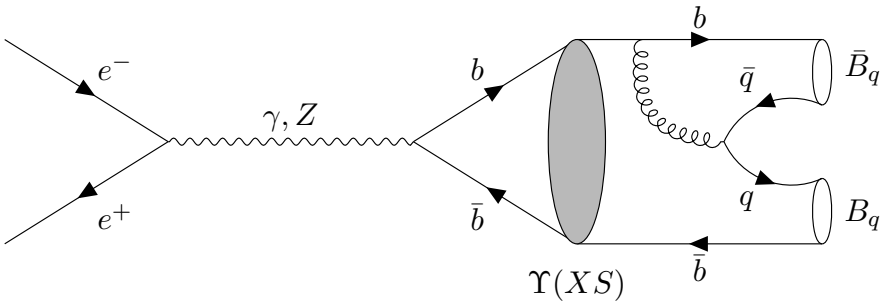

FIGURE 3.8: $B - \bar{B}$ production mechanism in e^+–e^- colliders via the bottomonium resonance $\Upsilon(XS)$ for some integer X; $\Upsilon(4S)$ is used to produce predominantly $B^{\pm,0}$ mesons and $\Upsilon(5S)$ to produce B_s mesons.

3.2.1 Heavy Flavour in Particle Colliders

To study the exciting plethora of processes involving heavy b quarks to high precision and accuracy, particle colliders must be able to create a large number of B mesons (or more generally, b-hadrons) and subsequently measure their properties and dynamics. Below we summarise the various particle collider experiments with successful B physics programs.

The b quark was first discovered in 1977 by Fermilab's E288 experiment [178, 179] via the bottomonium ($\bar{b}b$) resonance Υ, which from its $4S$ state and above, can decay into B-$\bar{B}$ meson pairs as shown in figure 3.8. B mesons were first identified using this process at the e^+-e^- colliders CESR (Cornell) and PEP (SLAC) [180–183]. From here, it became clear that there were exciting prospects in experiment to study B mesons and similarly the tools were being developed in theory to provide clear predictions of these processes; the harmony of experiment and theory for heavy flavour physics is clearly present.

B Factories

To specifically study B meson phenomenology, the collider experiments known as the B *factories* were commissioned through the 1990s: operating from 1999 were the BaBar experiment using the PEP-II collider at SLAC in the USA [184] and the Belle experiment at KEK in Japan [185]. The BaBar experiment collected data until 2008, and Belle until 2010. Three 'next generation' B factories were proposed through the 2010s, however only one of these was actually built: the Belle II experiment as a successor to Belle [186]. Belle II began data collection in 2018 and continues to date.

These experiments are e^+–e^- colliders which produce B mesons via the mechanism

$$e^+ + e^- \to \Upsilon(b\bar{b}) \to B_q + \bar{B}_q. \tag{3.95}$$

The Feynman diagram of this process is shown in figure 3.8. The bottomonium state Υ has to be produced at a specific resonance such that the production of two B mesons is kinematically allowed. The $\Upsilon(4S)$ resonance produces predominantly $B^{\pm,0}$ mesons, while the $\Upsilon(5S)$ resonance also allows the production of B_s mesons. The BaBar experiment used the $\Upsilon(4S)$ resonance and as such only produced $B^{\pm,0}$ mesons, however Belle and Belle II both also collected data at the $\Upsilon(5S)$ resonance.

Hadron Colliders

Hadron colliders such as the p–$\bar{p}$ collider TeVatron at FNAL (see e.g. [187]) or the p–p collider LHC at CERN (see e.g. [188]) are not primarily focused on heavy flavour physics, however they still have very large bottom and charm production cross sections. Consequently, the LHC produces many more $\bar{b}b$ pairs than was done at either BaBar or Belle. While not typically referred to as a B factory since the LHC itself is not designed in the same way as the e^+–e^- colliders discussed above, LHCb is a detector experiment dedicated to studying b physics produced at the LHC and has a very successful program. Furthermore, B_s mesons are fully accessible to LHCb in addition to $B^{\pm,0}$ mesons and also in fact the heavier B_c meson and Λ_b baryon. It is worth noting that while LHCb is the dedicated b physics experiment at the LHC, the other experiments ATLAS and CMS have also contributed to B physics measurements, notably the rare leptonic decay $B_s \to \mu^+\mu^-$ [189–194] (to be discussed further in chapter 4).

3.2.2 B Meson Lifetimes

We already discussed the construction of the HQE in section 3.1.4 as the theoretical framework for systematically addressing corrections to the free heavy quark decay for the prediction of a heavy meson decay rate. We shall now discuss below the phenomenological history of B meson lifetimes and their current experimental status.

In experiment, the great success of the B factories and other particle colliders capable of studying B mesons, such as the LHC, have resulted in the lifetimes of B mesons now being determined to a high precision; see e.g. [26, 54]. In table 3.1, we show the latest averages of the lifetimes of B mesons. In addition to the individual lifetimes, it can be seen that their ratios are extremely close to 1 such that spectator quark effects must be small. The exception to this is $\tau(B_c)/\tau(B_d)$, which is expected since the spectator quark of the B_c meson is a charm quark, clearly much heavier than the other spectator quarks such that the B_c meson is no longer the simple picture of the single heavy b quark

surrounded by the non-perturbative "brown muck" we used for heavy-light mesons. It

	B_d	B^+	B_s	B_c
τ [ps]	1.517 ± 0.004	1.638 ± 0.004	1.520 ± 0.005	0.510 ± 0.009
$\tau(B_q)/\tau(B_d)$	1	1.076 ± 0.004	1.003 ± 0.003	0.336 ± 0.006

TABLE 3.1: The lifetimes and lifetime ratios of B mesons [26, 54].

is impressive to note that the relative precision of these lifetime ratios has increased over the last 20 years from $\sim 4\%$ to $\sim 0.5\%$ (see e.g. [195]). However, it is also of note that recent measurements of $\Gamma(B_s)$ find a $2-4\sigma$ tension between ATLAS [196], LHCb [197, 198] and CMS [199].

At leading order in the HQE, the decay of a B meson is equal to that of a free b quark,

$$\Gamma(B) = \Gamma_b + O\left(\frac{\Lambda_{\text{QCD}}^2}{m_b^2}\right), \qquad \Gamma_b \propto \frac{G_F^2 m_b^5}{192\pi^3}|V_{cb}|^2. \tag{3.96}$$

With the large mass of the b quark, it is expected that the higher-order correction terms are negligible and the relation $\Gamma(B) \approx \Gamma_b$ should be mostly accurate. This implies that the lifetimes of B mesons are shorter than those of e.g. D mesons containing the next heaviest quark, the charm. However, it then came as a surprise that the lifetime of the B meson was measured to be $\sim 1.8\,\text{ps}$, first by the MAC experiment [200] at PEP and then later confirmed by the MarkII [201] and DELCO [202] experiments also at PEP and the TASSO experiment [203] at PETRA, DESY. Therefore experiment implies that higher-order corrections to the free b quark decay, expressed via the HQE in equation (3.76), are indeed necessary to describe the decay of a B meson.

Throughout section 3.1.4, we detailed the many calculations contributing to both the perturbative and non-perturbative factors of the HQE from dimension three to six. It is through all this effort of the community that B meson lifetimes are now known to a high precision with many details of the HQE addressed and understood. However, the precision of experiment is still greater than that of theory and to better compare the two, an increased theoretical precision is strongly desired. Particularly for the lifetime ratios, it is found that the four-quark dimension six matrix elements (recall equations (3.88)-(3.92)) compose a significant proportion of the overall theoretical uncertainty, and as such improved calculations of these can greatly improve the overall precision. Calculations of these quantities from lattice QCD are strongly desired and once these become standard practice, their uncertainties can be systematically improved as the lattice simulations progress.

3.2.3 Neutral B Meson Mixing

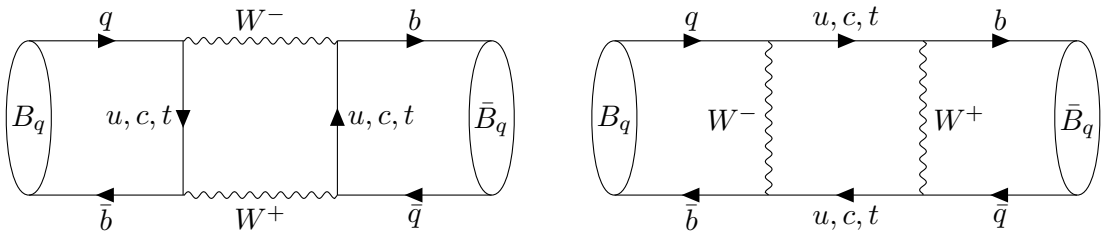

FIGURE 3.9: Standard Model box diagrams resulting in neutral B meson mixing.

Loop-level box diagrams as shown in figure 3.9 introduce the possibility for a neutral B_q^0 meson (with quark content $\bar{b}q$, $q = d, s$) to transition back and forth with its antiparticle $\bar{B}_q^0$ (with quark content $b\bar{q}$). The time evolution of this oscillatory system can be described by

$$i\frac{d}{dt}\begin{pmatrix}|B_q^0(t)\rangle\\|\bar{B}_q^0(t)\rangle\end{pmatrix} = \left(\hat{M}^q - \frac{i}{2}\hat{\Gamma}^q\right)\begin{pmatrix}|B_q^0(t)\rangle\\|\bar{B}_q^0(t)\rangle\end{pmatrix}, \tag{3.97}$$

where $\hat{M}^q, \hat{\Gamma}^q$ are 2×2 matrices describing the contributions to the time evolution from the masses and decay rates of the system respectively. If there were no mixing between the meson and antimeson, non-diagonal entries of these matrices would vanish. However, since there does exist a mixing between the flavour eigenstates, the off-diagonal elements M_{12}^q in $\hat{M}^q$ and Γ_{12}^q in $\hat{\Gamma}^q$ are introduced. Box diagrams with virtual internal lines (all permutations of figure 3.9) contribute to M_{12}^q and diagrams with on-shell internal lines (right of figure 3.9 for u, c only) contribute to Γ_{12}^q.

One can diagonalise the matrices $\hat{M}^q$ and $\hat{\Gamma}^q$ in order to describe the physical eigenstates of the system with definite mass and decay rate. This results in

$$\begin{aligned}|B_{q,L}\rangle &= p|B_q^0\rangle + q|\bar{B}_q^0\rangle,\\ |B_{q,H}\rangle &= p|B_q^0\rangle - q|\bar{B}_q^0\rangle,\end{aligned} \tag{3.98}$$

where the physical eigenstates are named heavy (H) and light (L) and the complex coefficients in this linear transformation fulfil $|p|^2 + |q|^2 = 1$. It is clear $B_{q,L}$ and $B_{q,H}$ will now have a clear difference in their masses and decay rates:

$$\Delta m_q = 2|M_{12}^q|, \tag{3.99}$$

$$|\Delta\Gamma_q| = 2|\Gamma_{12}^q|. \tag{3.100}$$

In this thesis, we will only be interested in Δm_q; for a review on Δm_q and further details on $\Delta\Gamma_q$ and other mixing phenomenology, see e.g. [104]. A brief history of neutral meson mixing follows:

- Neutral meson mixing was first considered in theory by Gell-Mann and Pais [204] in the context of kaons and a significant lifetime difference between the two neutral kaons was measured in 1956 [205].
- Mixing of B_d mesons was then discovered in 1986 by the UA1 experiment at CERN[4] [206] and in 1987 by the ARGUS experiment at DESY [207]. The large mass difference Δm_d measured was already a strong hint towards the surprisingly heavy mass of the top quark [208], still to be measured.
- The B_s system was also established to exhibit mixing effects in 2006 by the CDF collaboration at TeVatron [209] with a large mass difference observed.
- There were many experiments (e.g. BaBar, Belle, CLEO, CDF, E791, E831 FOCUS, LHCb) finding evidence towards D^0 mixing, with the first confirmation above the 5σ discovery threshold announced in 2012 from LHCb [210].

Unlike other neutral meson systems, the masses of B mesons are such that hadronic resonances as intermediate states are not a concern and long-distance interactions can be neglected for B_q^0 mixing. Furthermore, after summing over all contributing diagrams,

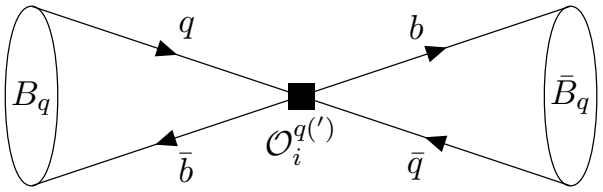

FIGURE 3.10: Local four-quark operator describing neutral B meson mixing in the $\Delta B = 2$ effective Hamiltonian.

one finds a clear simplification via the GIM mechanism [211] such that the dominant contributions by far are those of the diagrams with top quarks. Since all virtual lines in the box diagrams are of very heavy particles, $m_W, m_t \gg m_b$, these can both be integrated out and the calculation of M_{12}^q can be performed via an operator product expansion. This OPE contracts the 'box' to a point and one is left with local four-quark operators in the $\Delta B = 2$ effective Hamiltonian, as shown in figure 3.10, where $\Delta B = 2$ indicates the operators change the Bottom quantum number of the system by 2. In this limit, we express M_{12}^q as

$$M_{12}^q = \frac{\langle B_q | \mathcal{H}_{\text{eff}}^{\Delta B=2} | \bar{B}_q \rangle}{2 m_{B_q}}, \tag{3.101}$$

where the $\Delta B = 2$ effective Hamiltonian can generically be written as

$$\mathcal{H}_{\text{eff}}^{\Delta B=2} = \sum_{i=1}^{5} C_i \mathcal{O}_i^q + \sum_{i=1}^{3} C' \mathcal{O}_i^{q'}, \tag{3.102}$$

[4] UA1 initially interpreted the result as B_s mixing.

for the effective local four-quark operators $\mathcal{O}_i^{q(\prime)}$. The full basis of dimension-six $\Delta B = 2$ operators, covering the Standard Model and all new physics scenarios, is given by

$$\begin{aligned}
\mathcal{O}_1^q &= (\bar{q}^\alpha \gamma^\mu (1-\gamma_5) b^\alpha)(\bar{q}^\beta \gamma_\mu (1-\gamma_5) b^\beta), & \mathcal{O}_1^{q'} &= (\bar{q}^\alpha \gamma^\mu (1+\gamma_5) b^\alpha)(\bar{q}^\beta \gamma_\mu (1+\gamma_5) b^\beta), \\
\mathcal{O}_2^q &= (\bar{q}^\alpha (1-\gamma_5) b^\alpha)(\bar{q}^\beta (1-\gamma_5) b^\beta), & \mathcal{O}_2^{q'} &= (\bar{q}^\alpha (1+\gamma_5) b^\alpha)(\bar{q}^\beta (1+\gamma_5) b^\beta), \\
\mathcal{O}_3^q &= (\bar{q}^\alpha (1-\gamma_5) b^\beta)(\bar{q}^\beta (1-\gamma_5) b^\alpha), & \mathcal{O}_3^{q'} &= (\bar{q}^\alpha (1+\gamma_5) b^\beta)(\bar{q}^\beta (1+\gamma_5) b^\alpha), \\
\mathcal{O}_4^q &= (\bar{q}^\alpha (1-\gamma_5) b^\alpha)(\bar{q}^\beta (1+\gamma_5) b^\beta), \\
\mathcal{O}_5^q &= (\bar{q}^\alpha (1-\gamma_5) b^\beta)(\bar{q}^\beta (1+\gamma_5) b^\alpha).
\end{aligned} \tag{3.103}$$

The operators $\mathcal{O}_i^{q'}$ are the parity transforms of $\mathcal{O}_i^q$ $(i = 1, 2, 3)$, and as such the matrix elements in QCD satisfy $\langle O_i^q \rangle = \langle O_i^{q'} \rangle$. The matrix elements of these four-quark operators are typically parameterised in terms of the decay constant f_{B_q} and Bag parameters $B_{B_q}^i$ which describe the deviation of the matrix element from the VIA (recall the discussion in section 3.1.4), reading

$$\langle O_1^q \rangle(\mu) = \xi_1 f_{B_q}^2 m_{B_q}^2 B_{B_q}^1(\mu), \tag{3.104}$$

$$\langle O_i^q \rangle(\mu) = \xi_i \left(\frac{m_{B_q}}{m_b(\mu) + m_q(\mu)} \right)^2 f_{B_q}^2 m_{B_q}^2 B_{B_q}^i(\mu), \; i = 2, 3, \tag{3.105}$$

$$\langle O_i^q \rangle(\mu) = \xi_i \left[\left(\frac{m_{B_q}}{m_b(\mu) + m_q(\mu)} \right)^2 + b_i \right] f_{B_q}^2 m_{B_q}^2 B_{B_q}^i(\mu), \; i = 4, 5, \tag{3.106}$$

where $\xi_i = \{8/3, -5/3, 1/3, 2, 2/3\}$, $b_4 = 1/6$, and $b_5 = 3/2$. In the Standard Model, only $\mathcal{O}_1$ contributes to M_{12}^q, which can be expressed as

$$M_{12}^q = \frac{G_F^2}{12\pi^2} |V_{ts}^* V_{tb}|^2 m_W^2 S_0 \left(\frac{m_t^2}{m_W^2} \right) \hat{\eta}_B \, f_{B_q}^2 m_{B_q} B_{B_q}^1, \tag{3.107}$$

where the Inami-Lim function [212] is

$$S_0(x) = \frac{4x - 11x^2 + x^3}{4(1-x)^2} - \frac{3x \ln x}{2(1-x)^2}, \tag{3.108}$$

and $\hat{\eta}_B$ is the correction factor from the perturbative 2-loop QCD corrections [213]. From the theory side, it is clear now that the limiting factor in precise predictions for Δm_q is the non-perturbative input of the QCD matrix elements [195]. The QCD matrix element of the Standard Model four-quark operator $\mathcal{O}_1^q$ can be determined from non-perturbative methods such as lattice QCD [214–219] and HQET sum rules [168, 220, 221]. It is expected as time progresses that these calculations are superseded by higher precision results, and importantly also that calculations by different groups and methods can converge more closely than is currently seen; see e.g. [195]. One finds that the best results of theory have uncertainties far larger than those of experiment. The precision

of theory predictions for Δm_s and Δm_d are 3.4% and 3.9% respectively.

The experimental averages quoted by HFLAV [26],

$$\begin{aligned} \Delta m_d &= 0.5069 \pm 0.0019\,\text{ps}^{-1}, \\ \Delta m_s &= 17.765 \pm 0.006\,\text{ps}^{-1}, \end{aligned} \tag{3.109}$$

have reached impressive precisions of 0.38% and 0.03% respectively. This is dominated by the latest result from $B_s^0 \to D_s^- \pi^+$ decays in Run 2 of the LHCb experiment [222], as shown in figure 3.11. This remarkable level of precision from experiment as well as

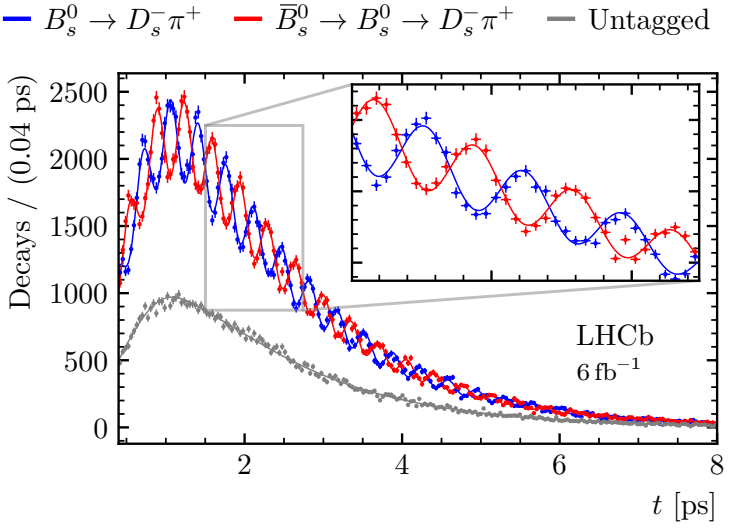

FIGURE 3.11: Decay distributions of $B_s^0 \to D_s^- \pi^+$ decays tagged as the unmixed decay (blue), the mixed decay (red), or untagged (grey) from Run 2 of the LHCb experiment, showcasing the clear observation of neutral B_s^0 meson mixing [222].

the inherent loop-level nature of the theory calculation makes neutral B_q^0 meson mixing an important test subject for either the validity of the Standard Model or searches for new physics. However, it is clear that for either of these goals, the precision of theory predictions must greatly improve to be comparable with experiment.

Chapter 4

Indirect Searches for New Physics

We know that the Standard Model is incomplete and there must be further physics beyond the Standard Model (BSM) to be discovered describing these missing pieces such as neutrino masses. A significant cosmological problem to solve is also that of baryogenesis – the observed matter-antimatter asymmetry in the universe. In order for sufficient baryogenesis during the evolution of the universe, Sakharov [223] found three criteria necessary:

1. Baryon number violation – this is theorised e.g. in sphalerons, although not yet confirmed experimentally [224];
2. C and CP violation – these are present in the SM, but not to a sufficient level;
3. A first-order electroweak phase transition (FOEWPT) in the early universe – while this could have been possible in the SM for $m_h \lesssim 70\,\text{GeV}$ [225], the measured value of $m_h = 125.25 \pm 0.17\,\text{GeV}$ [54] rules this out.

Based on our knowledge of what is missing in the SM, we can write down theories to extend the Standard Model and resolve these problems. Many different theories can be proposed but this does not mean they are observed in nature; any candidate theory must be tested against experiment and verified for it to be the BSM theory of nature.

To search for new physics, there are two approaches. First, one can consider *direct searches*, where experiments such as particle colliders attempt to produce and directly observe the new particles described by a BSM theory; this is the same strategy by which SM particles such as the Higgs boson were discovered. Experiments such as those at the LHC continue to search for new particles in this way. Alternatively, new physics may be discovered through *indirect searches* where a large group of high-precision observables have their theory predictions modified by BSM physics (most commonly introduced

as loop effects) and compared to experiment; the BSM theory of nature should be observed in the experimental measurements and therefore calculating the prediction of the BSM theory should form better agreement with experiment than the Standard Model predictions.

The ever-present caveat with this method is that the chosen observables for such an analysis should be both measured and calculated in the SM to as high precision and accuracy as possible. This ensures we have solid understanding and control over the theoretical calculation and experimental measurement such that the ambiguity that any tension between these comes from new physics is minimised.

Ultimately, the new theory must be confirmed experimentally and its particles observed directly, but understanding the restrictions on a theory by all possible processes affected provides clearer understanding on which types of particles experiment should focus its searches and what values the properties of these particles are likely to have, e.g. for mass, charge, etc. Furthermore, these two methods can be combined in *global fits* where the experimental bounds on the properties of new particles from direct searches are combined with the analytical power of indirect searches to provide the strongest bounds on the parameter space of the BSM theory.

Effective field theories (discussed in section 3.1) provide a powerful language for the search for new physics. Using EFTs, many observables can be connected to a set of operators which can then have BSM physics contributing to their Wilson coefficients. For the method of indirect searches, using effective operators becomes a powerful way to learn what free space is still allowed by a collection of observables, and more importantly, what sort of particles and interactions are suitable to accommodate this free space. These effective operators can be analysed as they are to simply present the kind of new physics to be accommodated, or can be married into specific BSM theories to show how well a new model fits our current data.

When considering extensions to the Standard Model, this ultimately points to some *grand unified theory* (GUT) which is the UV-complete theory of the universe containing all of physics, from which the SM is derived as a low-energy limit. However, when building up towards the energy scale of this GUT from a low-energy limit like the SM, it can be simpler to first consider smaller extensions of the SM to resolve specific problems and work towards the final UV theory step by step. Typically as these theories are extended to higher and higher energies, the masses of new particles introduced by the model are constrained to be larger also, such that experimentally it is more favourable to extend the Standard Model progressively where the next sought-after particle can be one within or near to the current energies probed by particle colliders.

In this chapter, we focus on one of the simplest extensions of the Standard Model: the Two-Higgs-Doublet Model (2HDM) [226] (for reviews see e.g. [227, 228]). In section 4.1, the motivations for and the construction of the model itself will be discussed and then in section 4.2, results are presented for constraining the parameter space of the 2HDM based on phenomenology, particularly dominated by flavour physics observables. The strength of indirect searches for constraining new physics models will be demonstrated. Insight into the current status of flavour physics phenomenology in the Standard Model is presented, addressing questions like where to find powerful processes for constraining new physics and where will we find ourselves limited by the precision of the SM predictions themselves. The work presented throughout this chapter is based on the publications [41–44].

4.1 The Two-Higgs-Doublet Model

Being among the simplest BSM physics scenarios, Two-Higgs-Doublet Models are some of the most well-studied extensions of the SM. After spontaneous symmetry breaking, the 2HDM introduces four new scalar particles alongside the SM zoo: two charged $H^{\pm}$, a CP-odd pseudoscalar A, and a CP-even scalar H^0 – a (typically) heavier counterpart to the SM Higgs h^0. This extension can be motivated as a way to solve one of the problems with the Standard Model, namely baryogenesis [229]. 2HDMs can provide additional CP violation, fulfilling the Sakharov criterion insufficiently answered by the SM, and in addition a FOEWPT in the early universe is also possible in 2HDMs. While not answering all open questions in particle physics itself, 2HDMs commonly appear embedded in more intricate BSM theories, such as the minimal supersymmetric SM (MSSM) or Pati-Salam-like models of quark-lepton unification.

In order to generate mass for both up-type and down-type quarks in the SM, a conjugate of the Higgs doublet is used (recall section 2.2.4). However, there is no particular reason why this must be so, and in fact a Higgs Lagrangian can alternatively be introduced which uses two independent doublets Φ_i with $i = 1, 2$,

$$\mathcal{L}^{\text{2HDM}}_{\text{H+Y}} = \sum_i |D_\mu \Phi_i|^2 - V(\Phi_1, \Phi_2) + \mathcal{L}^{\text{2HDM}}_{\text{Yukawa}}, \quad \Phi_i = \begin{pmatrix} \phi_i^+ \\ (v_i + \phi_i^0 + iG_i^0)/\sqrt{2} \end{pmatrix}. \tag{4.1}$$

After spontaneous symmetry breaking, each doublet will acquire its own VEV v_i, with the current experimentally-observed VEV the quadrature addition of the two [226–228]:

$$\Phi_1 = \frac{1}{\sqrt{2}} \begin{pmatrix} 0 \\ v_1 \end{pmatrix}, \qquad \Phi_2 = \frac{1}{\sqrt{2}} \begin{pmatrix} 0 \\ v_2 \end{pmatrix}, \qquad v^2_{\text{SM}} = v_1^2 + v_2^2. \tag{4.2}$$

In this model, the masses of the $W^{\pm}, Z^0$ bosons are still generated by each 'eating' one of the scalar fields. However now instead of the four degrees of freedom in the SM, the 2HDM has eight degrees of freedom such that after SSB there are five residual scalar fields, and thus five Higgs particles instead of only one: two charged Higgs $H^{\pm}$ and three neutral – two scalar H^0 and h^0 and one pseudoscalar A^0. Typically, and in this work, h^0 is taken to be the lighter of the two CP-even scalars and also identified as the experimentally-observed 'SM' Higgs. The physical Higgs fields are given by the rotations

$$\begin{pmatrix} H^0 \\ h^0 \end{pmatrix} = \begin{pmatrix} \cos\alpha & \sin\alpha \\ -\sin\alpha & \cos\alpha \end{pmatrix} \begin{pmatrix} \phi_1^0 \\ \phi_2^0 \end{pmatrix}, \tag{4.3}$$

$$\begin{pmatrix} G^0 \\ A^0 \end{pmatrix} = \begin{pmatrix} \cos\beta & \sin\beta \\ -\sin\beta & \cos\beta \end{pmatrix} \begin{pmatrix} G_1^0 \\ G_2^0 \end{pmatrix}, \tag{4.4}$$

$$\begin{pmatrix} G^{\pm} \\ H^{\pm} \end{pmatrix} = \begin{pmatrix} \cos\beta & \sin\beta \\ -\sin\beta & \cos\beta \end{pmatrix} \begin{pmatrix} \phi_1^{\pm} \\ \phi_2^{\pm} \end{pmatrix}, \tag{4.5}$$

where $G^0, G^{\pm}$ are the would-be Goldstone bosons.
The general potential for a 2HDM is given by

$$\begin{aligned} V(\Phi_1,\Phi_2) = {} & m_{11}^2\Phi_1^\dagger\Phi_1 + m_{22}^2\Phi_2^\dagger\Phi_2 - m_{12}^2\left[\Phi_1^\dagger\Phi_2 + \text{h.c.}\right] \\ & + \frac{\lambda_1}{2}(\Phi_1^\dagger\Phi_1)^2 + \frac{\lambda_2}{2}(\Phi_2^\dagger\Phi_2)^2 + \lambda_3(\Phi_1^\dagger\Phi_1)(\Phi_2^\dagger\Phi_2) + \lambda_4(\Phi_1^\dagger\Phi_2)(\Phi_2^\dagger\Phi_1) \\ & + \left[\frac{\lambda_5}{2}(\Phi_1^\dagger\Phi_2)^2 + \lambda_6(\Phi_1^\dagger\Phi_1)(\Phi_1^\dagger\Phi_2) + \lambda_7(\Phi_2^\dagger\Phi_2)(\Phi_1^\dagger\Phi_2) + \text{h.c.}\right], \end{aligned} \tag{4.6}$$

where $m_{11}^2, m_{22}^2, \lambda_{1,2,3,4}$ are real and in general $m_{12}^2, \lambda_{5,6,7}$ may be complex [228]. Furthermore, one can define two angles describing the mixing into physical states of the model,

$$\tan 2\alpha = \frac{-2\text{Re}(m_{12}^2) + 3[\text{Re}(\lambda_6)v_1^2 + \text{Re}(\lambda_7)v_2^2] + 2\lambda_{345}v_1v_2}{m_{11}^2 - m_{22}^2 + \frac{3}{2}(\lambda_1v_1^2 - \lambda_2v_2^2) + \frac{1}{2}\lambda_{345}(v_2^2 - v_1^2) + 3[\text{Re}(\lambda_6) - \text{Re}(\lambda_7)]v_1v_2}, \tag{4.7}$$

$$\tan\beta = \frac{v_2}{v_1}, \tag{4.8}$$

where $\lambda_{345} = \lambda_3 + \lambda_4 + \text{Re}(\lambda_5)$ [228]. Use of the λ parameters is known as the 'lambda basis' and is more useful e.g. for considering what theoretical constraints can be placed on the model (as will be discussed in section 4.1.1). However for phenomenology it is more convenient to work in the mass basis where the parameters are the masses of the new Higgses, the mixing angles α, β (commonly represented by $\cos(\beta-\alpha)$ and $\tan\beta$), and m_{12}^2. Expressions for the masses from the lambda basis parameters are dependent on the type of 2HDM, and are shown e.g. in [41, 230]. The 2HDM with the general potential in equation (4.6) is commonly referred to as the type III 2HDM. This model actually

allows tree-level FCNCs, which typically leads to much more sizeable contributions to FCNC processes than can be accommodated in the data, although in some cases this can still be favourable. In order to avoid tree-level FCNCs, it is common to impose a discrete $\mathbb{Z}_2$ symmetry,

$$\mathbb{Z}_2: \quad \Phi_1 \to \Phi_1, \quad \Phi_2 \to -\Phi_2, \tag{4.9}$$

which enforces $\lambda_6 = \lambda_7 = 0$ and $m_{12}^2 = 0$. However keeping $m_{12}^2 \neq 0$ is still allowed resulting in the symmetry being softly broken, i.e. that the $\mathbb{Z}_2$ symmetry is still kept at small distances such that the soft breaking is only relevant for Higgs masses much below the EW scale. When applied to the Yukawa sector, this $\mathbb{Z}_2$ symmetry leads to four possible types of 2HDM *without* tree-level FCNCs, where the right-handed fermions interact with the extended Higgs sector under these different types as shown in table 4.1, while the left-handed doublets transform trivially.

Model	I	II	X	Y
u_R^i	Φ_2	Φ_2	Φ_2	Φ_2
d_R^i	Φ_2	Φ_1	Φ_2	Φ_1
e_R^i	Φ_2	Φ_1	Φ_1	Φ_2

TABLE 4.1: Types of 2HDM forbidding tree-level FCNCs through a $\mathbb{Z}_2$ symmetry requiring that fermions couple to specific doublets.

The Yukawa sector of the 2HDM Lagrangian is written as

$$\begin{aligned}\mathcal{L}_{\text{Yukawa}}^{\text{2HDM}} = &- \sum_{f=u,d,\ell} \frac{m_f}{v} \left(\xi_h^f \bar{f} f h + \xi_H^f \bar{f} f H + i\eta_f \xi_A^f \bar{f} \gamma_5 f A\right) \\ &- \left[\frac{\sqrt{2}V_{ud}}{v} \bar{u}(m_d \xi_A^d P_R - m_u \xi_A^u P_L) d H^+ + \frac{\sqrt{2}}{v} m_\ell \xi_A^\ell (\bar{\nu} P_R \ell) H^+ + \text{h.c.}\right],\end{aligned} \tag{4.10}$$

where $\eta_f = 1$ for $f = d, \ell$ and -1 for $f = u$ [228, 231]. With the fermions coupling to the Higgs doublets as described in table 4.1, the coupling strengths ξ of the Yukawa Lagrangian are given for the different types as shown in table 4.2. Of particular interest in collider studies of Higgs physics are the Higgs *signal strengths*, which compare the strength of the (SM-like) Higgs h^0 couplings found experimentally to theory. To this end, one can write the h^0 couplings of the Lagrangian as

$$\mathcal{L} \subset \kappa_V \frac{m_Z^2}{v} h Z_\mu Z^\mu + \kappa_V \frac{2m_W^2}{v} h W_\mu^+ W^{\mu-} - \sum_{f=u,d,\ell} \kappa_f \frac{m_f}{v} h \bar{f} f, \tag{4.11}$$

where, for example in the type II 2HDM,

$$\kappa_V = \sin(\beta - \alpha), \tag{4.12}$$

$$\kappa_u = \sin(\beta - \alpha) + \cot\beta\cos(\beta - \alpha), \tag{4.13}$$

$$\kappa_{d,\ell} = \sin(\beta - \alpha) - \tan\beta\cos(\beta - \alpha). \tag{4.14}$$

Clearly in the SM, $\kappa_i = 1$ which is consistent with LHC data. To recover this in the 2HDM and match the phenomenology of h^0 exactly with the SM Higgs, one can set $\cos(\beta - \alpha) = 0$, known as the *alignment limit*. However, measurements of the signal

Model	I	II	X	Y
ξ_h^u	$\cos\alpha/\sin\beta$	$\cos\alpha/\sin\beta$	$\cos\alpha/\sin\beta$	$\cos\alpha/\sin\beta$
ξ_h^d	$\cos\alpha/\sin\beta$	$-\sin\alpha/\cos\beta$	$\cos\alpha/\sin\beta$	$-\sin\alpha/\cos\beta$
ξ_h^ℓ	$\cos\alpha/\sin\beta$	$-\sin\alpha/\cos\beta$	$-\sin\alpha/\cos\beta$	$\cos\alpha/\sin\beta$
ξ_H^u	$\sin\alpha/\sin\beta$	$\sin\alpha/\sin\beta$	$\sin\alpha/\sin\beta$	$\sin\alpha/\sin\beta$
ξ_H^d	$\sin\alpha/\sin\beta$	$\cos\alpha/\cos\beta$	$\sin\alpha/\sin\beta$	$\cos\alpha/\cos\beta$
ξ_H^ℓ	$\sin\alpha/\sin\beta$	$\cos\alpha/\cos\beta$	$\cos\alpha/\cos\beta$	$\sin\alpha/\sin\beta$
ξ_A^u	$\cot\beta$	$\cot\beta$	$\cot\beta$	$\cot\beta$
ξ_A^d	$\cot\beta$	$-\tan\beta$	$\cot\beta$	$-\tan\beta$
ξ_A^ℓ	$\cot\beta$	$-\tan\beta$	$-\tan\beta$	$\cot\beta$

TABLE 4.2: Coupling strengths ξ in each flavour-conserving 2HDM between the Higgs particles and fermions.

strengths at the LHC can only determine their magnitude and not the phase of the coupling. Therefore a scenario can be proposed in which

$$\kappa_{W,Z} = 1, \qquad \kappa_u = 1, \qquad \kappa_{d,\ell} = -1, \tag{4.15}$$

where again the phenomenology of the observed h^0 is indistinguishable from the SM, but there is actually a phase difference present. This is known as the *wrong sign limit* [232].

4.1.1 Theoretical Constraints

Before moving on to indirect searches for 2HDMs from phenomenology, constraints can be placed on the model from purely theoretical arguments, namely perturbativity, vacuum stability, and unitarity. Here we consider the theoretical constraints in the flavour-conserving case of the 2HDM, however the results for the more general case are not so different.

Firstly, let us consider perturbativity – the requirement that the parameters of our theory are valued such that the use of a perturbative expansion is valid. We can express

perturbativity of the scalar sector of the 2HDM as [233, 234]

$$|\lambda_i| \leq 4\pi, \tag{4.16}$$

where we have $i = 1 \to 5$ and assume all λ_i to be real. Since this is an argument based on the convergence of perturbation theory, there is clearly some ambiguity in choosing the value of the upper bound for these parameters. We will see that different choices for the upper bound do not change the picture of the theoretical constraints significantly, but it is still informative to compare different values and see this effect.
By considering the Yukawa Lagrangian of the 2HDM, one can also derive two more perturbativity constraints, dependent on the type of 2HDM being considered, e.g.

$$\frac{\sqrt{2}V_{tb}m_t\xi_A^u}{2v} \leq \sqrt{4\pi} \overset{\text{Type II}}{\Longrightarrow} \tan\beta > 0.14, \tag{4.17}$$

$$\frac{\sqrt{2}V_{tb}m_b\xi_A^d}{2v} \leq \sqrt{4\pi} \overset{\text{Type II}}{\Longrightarrow} \tan\beta < 300, \tag{4.18}$$

where again the upper bound of the Yukawa coupling has some freedom to be chosen differently.

Next we can consider the conditions required for a stable vacuum, i.e. that our universe lies in a minimum of the EW potential and either this is the global minimum or the time for quantum tunnelling effects from our local minimum to a deeper one is longer than the age of the universe. In the 2HDM, the conditions for this are written as [235]:

$$\lambda_{1,2} > 0, \tag{4.19}$$

$$\lambda_3 > -\sqrt{\lambda_1\lambda_2}, \tag{4.20}$$

$$\lambda_3 + \lambda_4 - |\lambda_5| > -\sqrt{\lambda_1\lambda_2}. \tag{4.21}$$

Demanding that the vacuum is the global minimum of the potential, one also requires [236]

$$m_{12}^2\left(m_{11}^2 - m_{22}^2\left(\frac{\lambda_1}{\lambda_2}\right)^{\frac{1}{2}}\right)\left(\tan\beta - \left(\frac{\lambda_1}{\lambda_2}\right)^{\frac{1}{4}}\right) > 0. \tag{4.22}$$

Finally, we consider unitarity – the constraint that the scattering matrix S is unitary in our theory (recall equation (3.67)). We account for conditions from both tree-level unitarity (see e.g. [234, 237, 238]) and NLO unitarity are considered, alongside the requirement that NLO corrections to partial wave amplitudes are suppressed relative to LO (see e.g. [239, 240]).

These three types of theoretical constraints can be combined in Monte Carlo scans of the allowed parameter space in the lambda basis and converted to give allowed ranges

for the parameters of the mass basis, specifically $m_{H^+}, m_{H^0}, m_{A^0}, \tan\beta$, and $\cos(\beta-\alpha)$. Two-dimensional projections of these constraints are shown in figure 4.1, where in green the perturbativity bound is taken to be 4π and in amber it is 4 – inspired by [239, 240]; the latter leads to more constrained regions, particularly for lower mass values. The

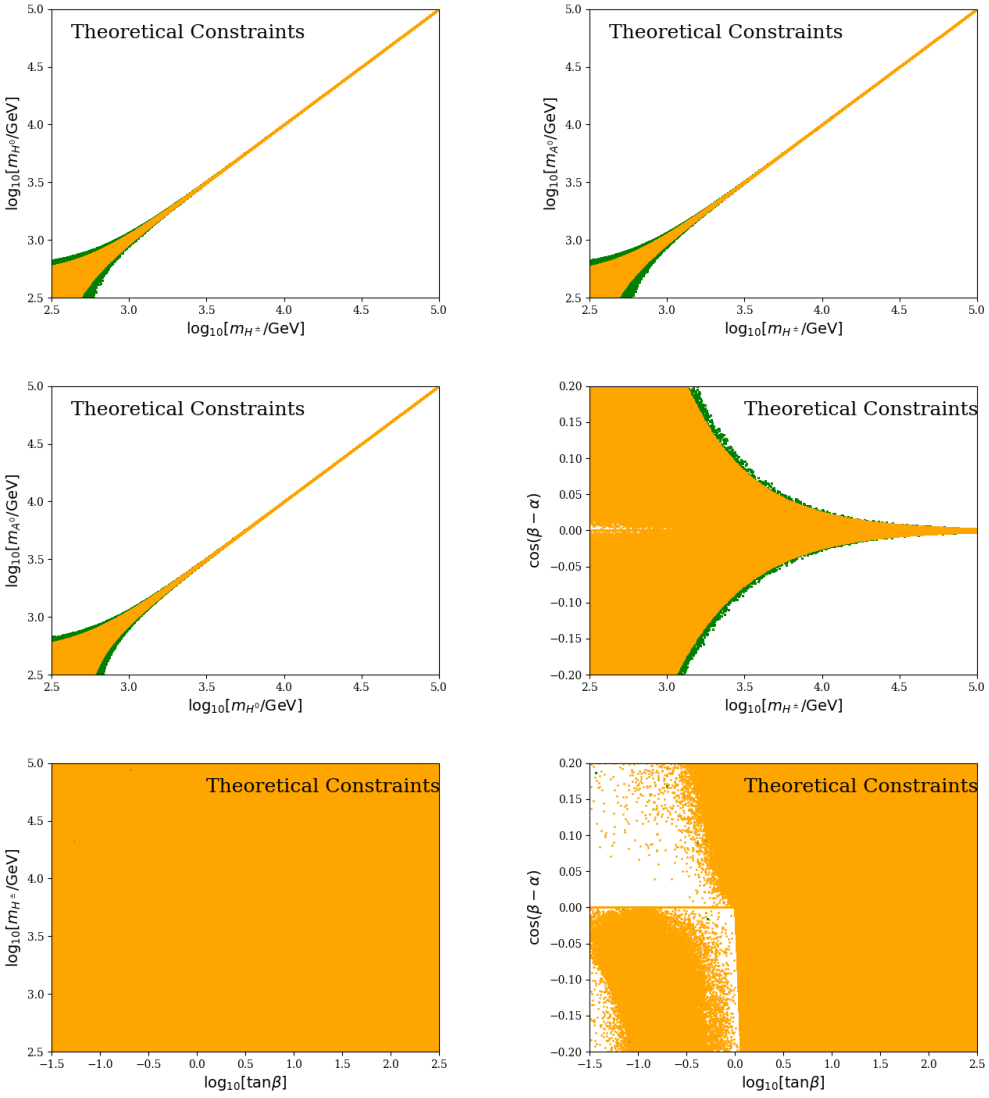

FIGURE 4.1: Bounds on the heavy Higgs masses m_{H^0}, m_{A^0} and m_{H^+}, $\tan\beta$ and $\cos(\beta-\alpha)$ stemming from theoretical constraints (perturbativity, vacuum stability and unitarity conditions). For the plots 10^8 points were generated and only values of $|\beta-\alpha-\frac{\pi}{2}|<0.5$ were considered. The starting values $|\lambda_i|<4\pi$ are given in green, while $|\lambda_i|<4$ is shown in amber.

implications of these theoretical constraints are clear: the mass differences of the new Higgs particles may not be too large and this is more constrained as masses increase past the TeV scale, where also the alignment limit, i.e. $\cos(\beta-\alpha)=0$, is more favoured. Numerical values for the mass separations in bins of 500 GeV are given in table 1 of [41].

4.2 Constraining New Physics from Phenomenology

Extending the SM into the Two-Higgs-Doublet Model introduces new Feynman diagrams for many processes, modifying the theory predictions for these (recall section 3.1.2 and how Wilson coefficients of our effective operators are modified by new physics). Now indirect searches for the 2HDM can be performed where a collection of the new theory predictions can be compared to experimental measurements in order to constrain the parameters of the model. In the 'SM' Higgs sector, the primary effect is the modification of the 'SM-like' Higgs h^0 coupling, which leads to constraints in the $(\tan\beta,\, \cos(\beta-\alpha))$ plane. Meanwhile in the flavour sector, a whole zoo of decay processes are topical since any diagrams mediated by the charged weak current are duplicated replacing $W^\pm$ with $H^\pm$; see e.g. figure 4.3. FCNC penguin diagrams can also be modified by replacing $W^\pm$ with $H^\pm$ and/or Z^0, γ with h^0, H^0, A^0; see e.g. figure 4.9. This primarily leads to constraints in the $(\tan\beta,\, m_{H^+})$ plane from flavour-changing charged processes, with additional FCNC constraints on $\cos(\beta-\alpha)$, m_{A^0}, m_{H^0}. Furthermore, in the type III 2HDM without an imposed $\mathbb{Z}_2$ symmetry, FCNCs are induced at tree-level and mediated by H^0 and A^0; see e.g. figure 4.14.

In this section, we give an overview of the constraints found for the parameters of the 2HDM via indirect searches using different groups of observables. We will find that different observables lead to constraints on the parameters of our model – $\tan\beta, m_{H^+}, m_{H^0}$, $m_{A^0}, \cos(\beta-\alpha)$. Each group of observables will provide different implications into the current state of our theoretical predictions and where theory must improve to better utilise these processes in the search for new physics. In section 4.2.1 we consider 2HDMs with an imposed $\mathbb{Z}_2$ symmetry and present select results from the publications [41–43], then in section 4.2.2 we consider the more general type III 2HDM as embedded in a Pati-Salam-like UV theory, presenting results from [44].

4.2.1 Models with $\mathbb{Z}_2$ symmetry

Higgs Signal Strengths

Before moving on to flavour observables which make up the main body of processes used in these analyses, we first consider the Higgs signal strengths. For a particular cross section σ_i and particular branching fraction $\mathcal{B}_f$, the signal strength μ_i^f is defined

$$\mu_i^f = \frac{(\sigma_i \cdot \mathcal{B}_f)_{\text{Exp.}}}{(\sigma_i \cdot \mathcal{B}_f)_{\text{SM}}}. \tag{4.23}$$

It is clear that a deviation from $\mu_i^f = 1$ is a sign of BSM physics. Currently using data from the ATLAS and CMS collaborations [241–248], there are 31 channels for which the signal strength can be evaluated, including combinations of the main h^0 production modes at the LHC (gluon-gluon fusion, vector boson fusion, weak-boson associated production, top-antitop pair production) and the decay channels $\gamma\gamma, ZZ^*, WW^*, Z\gamma, \tau^+\tau^-$, $b\bar{b}, c\bar{c}$. As mentioned above, in the 2HDM the couplings to h^0 are modified by the factors κ_i (see equation 4.11) compared to the SM, where the κ_i are e.g. for fermions the ξ_h^i given in table 4.2 expressed in terms of $\cos(\beta-\alpha)$ and $\tan\beta$. Of the four flavour-conserving 2HDMs described above, three types (II,X,Y) have couplings which make it possible to consider a wrong sign limit. The possibility of allowing the wrong sign limit may be favourable with the state of experiment where almost all signal strength data agrees with the SM within 2σ, strongly constraining the magnitudes of the couplings, but importantly not the phases.

The results of the global fits in the $(\tan\beta, \cos(\beta-\alpha))$ plane, which in this plane are dominated by the Higgs signal strengths (also receiving marginal contributions from FCNC $b \to q\ell\ell$ processes), are shown in figure 4.2. One finds the largest freedom in the type I 2HDM, where for $\tan\beta \gtrsim 1$, $|\cos(\beta-\alpha)| \lesssim 0.15$ at 2σ. This constraint is much more free than for the other three types, where $|\cos(\beta-\alpha)| \lesssim 0.05$ at 2σ when considering deviation from the alignment limit. This will be a common pattern throughout this section where the type I 2HDM is less constrained than the other types. One can see from the definition of the models in tables 4.1 and 4.2 that this is due to the nature of the couplings where type I has all fermions coupling to only one doublet rather than coupling different fermions to different doublets like the other types. The most obvious impact of this is seen when considering the couplings ξ_A^f, most important for charged current processes. Here type I is only sensitive to $\cot\beta$ and therefore cannot as easily constrain both the upper and lower limits of $\tan\beta$ like the other types can with sensitivity to both $\cot\beta$ and $\tan\beta$.
In types X and Y, another, strongly constrained solution, is the second contour shape curving away from the centre of the figures. This is the wrong sign limit, which is found to be allowed within 2σ for type X and within 4σ for type Y. In all four types, one finds the constraint $\tan\beta \gtrsim 1$, with the additional bound in type II of $\tan\beta \lesssim 30$. So there is most freedom to deviate from the alignment limit in type I, however in all types the alignment limit is strongly favoured, promoting the idea that h^0 is indeed the 'SM-like' Higgs particle. In types X and Y, the possibility of realising the wrong sign limit is also present, however this is in more tension with data than the alignment limit.

Tree-level Leptonic and Semileptonic Decays

Next we begin to consider flavour observables, starting with flavour-changing charged currents. Integrating out the heavy charged Higgs $H^\pm$, one finds 2HDM contributions

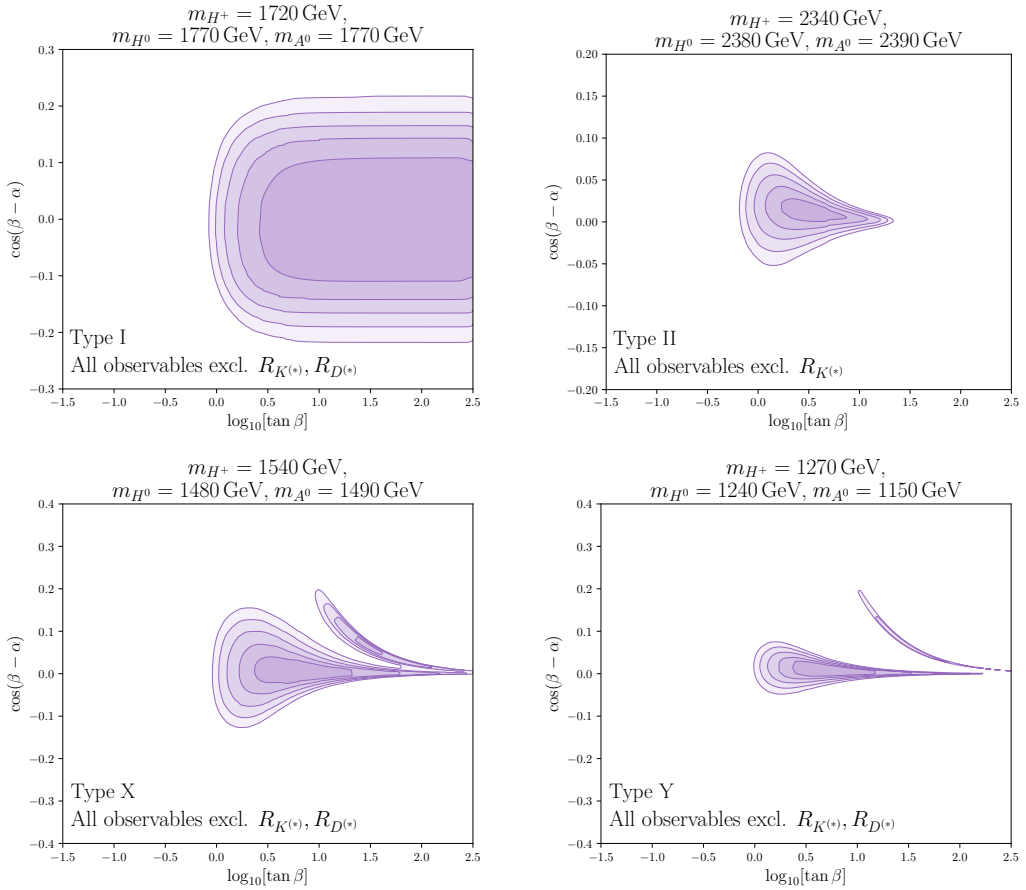

FIGURE 4.2: Contour plots of allowed parameter space in the $(\tan\beta, \cos(\beta-\alpha))$ plane for each flavour-conserving type of 2HDM. The additional parameters are fixed to their best fit point of the global fits performed in [41–43]. The contours indicate allowed parameter space at $1, 2, 3, 4, 5\sigma$ confidence level going from darker to lighter.

to two operators in the weak effective Lagrangian:

$$\mathcal{O}_{S-P} = (\bar{u}P_L d)(\bar{\ell}P_L\nu_\ell), \qquad \mathcal{O}_{S+P} = (\bar{u}P_R d)(\bar{\ell}P_L\nu_\ell), \tag{4.24}$$

$$C_{S-P} = -\frac{m_u m_\ell \xi_A^u \xi_A^\ell}{m_{H^+}^2}, \qquad C_{S+P} = \frac{m_d m_\ell \xi_A^d \xi_A^\ell}{m_{H^+}^2}, \tag{4.25}$$

for a generic up-type quark u and a generic down-type quark d. These operators then contribute to charged current processes such as $\bar{u}d \to \ell^+\nu_\ell$ or $d \to u\ell^-\nu_\ell$ as shown in figure 4.3.

Tree-level leptonic decays are some of the theoretically cleanest processes to calculate and are typically now determined to a high precision. From QCD, all hadronic physics affecting these decays is contained within a single parameter, the decay constant f_M for some meson M. By now, these are well-determined by lattice QCD and typically have uncertainties $\sim 1\%$ [249]. Regarding tree-level semileptonic decays, these are not quite as theoretically clean as leptonic, however their calculations are mostly well-controlled

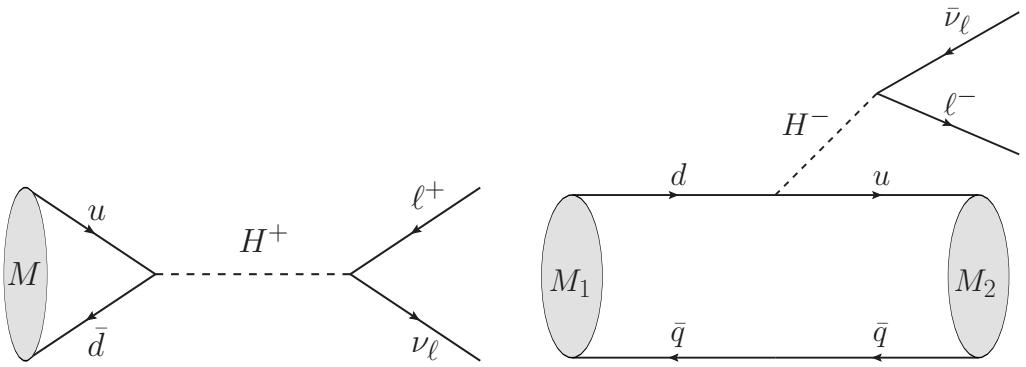

FIGURE 4.3: Diagrams in the 2HDM contributing to leptonic (left) and semileptonic (right) decays [41].

nowadays. The largest source of uncertainty typically stems from the hadronic physics, parameterised in a form factor $f_{M_1 \to M_2}(q^2)$ as a function of the dilepton momentum transfer q^2. Many studies using both lattice QCD and QCD sum rules have been used to understand the form factors for many semileptonic processes across the full q^2 range and precision is once again increasing. Otherwise the most significant uncertainties in both tree-level leptonic and semileptonic decays stem from the CKM matrix element associated with the quark content of the meson and the radiative electromagnetic corrections to the decay. The full list of flavour-changing charged current leptonic and semileptonic modes included in the analyses is given in table 6 of [41]; the SM predictions are based on [250–259] and the experimental measurements are listed from [26, 54, 260, 261].

Also included are the tree-level LFU ratios $R_{D^{(*)}} \equiv \mathcal{B}(B \to D^{(*)}\tau\bar{\nu}_\tau)/\mathcal{B}(B \to D^{(*)}\ell\bar{\nu}_\ell)$ for $\ell = e, \mu$. The experimental measurements of $R_{D^{(*)}}$ have been in tension with the SM predictions now for some time, currently with a $\sim 3.2\sigma$ excess [26], hinting at possible BSM physics creating LFU violation. LFU violation in the 2HDM is possible since the charged Higgs boson couples proportional to the lepton mass m_ℓ and is thus different for the different modes in the ratio. However, the semileptonic $b \to c\ell\bar{\nu}_\ell$ transition receives a negative 2HDM contribution compared to the SM in most parameter regions, therefore decreasing $R_{D^{(*)}}$ and moving them even further away from experiment. Within the physical domain of the model, the 2HDM can only worsen the tension of $R_{D^{(*)}}$ with experiment. It was therefore chosen in the later studies [42, 43] to consider a global fit having removed $R_{D^{(*)}}$ as it was clear that even in a realised 2HDM, these LFU ratios would still point to further new physics. Examples of the constraints on $R_{D^{(*)}}$ for the type II 2HDM are shown in figure 4.4.

Neutral Meson Mixing

Neutral meson mixing is commonly an important process in new physics studies. The high precision of measurements and the nature of the loop-level box diagrams mediating these in the SM and flavour-conserving BSM theories means that the parameters of a

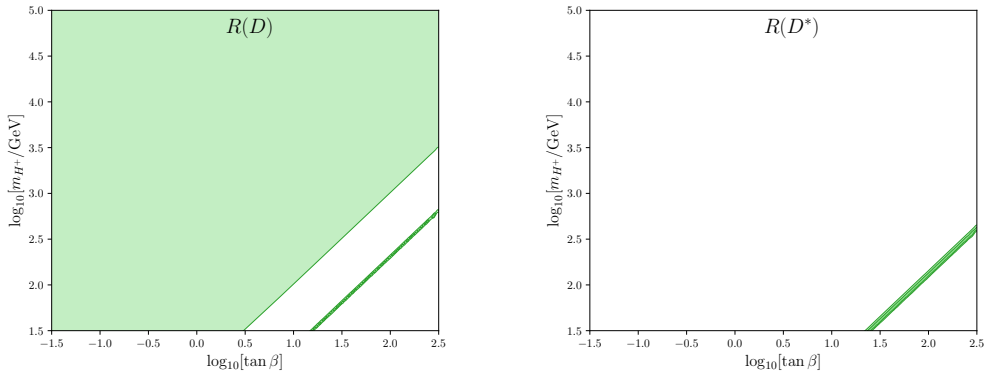

FIGURE 4.4: Contour plots of the allowed parameter space of the type II 2HDM in the $(\tan\beta, m_{H^+})$ plane from the LFU ratios R_D (left) and R_{D^*} (right). The lighter contour indicates allowed parameter space within 2σ confidence, while the darker within 1σ.

new physics model can be strongly constrained by considering the new contributions to e.g. the mass difference of neutral B_q mixing, Δm_q for $q = d, s$. The operators of the $\Delta B = 2$ effective Hamiltonian gaining contributions from the 2HDM are

$$\begin{aligned} \mathcal{O}_1^{(\prime)} &= (\bar{q}^\alpha \gamma^\mu P_{L(R)} b^\alpha)(\bar{q}^\beta \gamma_\mu P_{L(R)} b^\beta), \quad \mathcal{O}_4 = (\bar{q}^\alpha P_L b^\alpha)(\bar{q}^\beta P_R b^\beta), \\ \mathcal{O}_2^{(\prime)} &= (\bar{q}^\alpha P_{L(R)} b^\alpha)(\bar{q}^\beta P_{L(R)} b^\beta), \qquad \mathcal{O}_5 = (\bar{q}^\alpha P_L b^\beta)(\bar{q}^\beta P_R b^\alpha). \end{aligned} \tag{4.26}$$

The 2HDM contributions to the Wilson coefficients of these operators are taken from [231]. Typically the main limitation when considering Δm_q is the non-perturbative matrix elements of the four-quark operators shown above. While a lot of work has been put in using both sum rules and lattice QCD simulations to study these matrix elements, they still remain the primary source of uncertainty in the calculation and further precision would be welcome for both SM and BSM analyses (see e.g. [195, 262] for recent overviews). In this work, we use the averages presented in [262], based on the HQET sum rules evaluations [168, 220, 221] and lattice simulations [217–219]. The perturbative SM corrections are known and implemented to NLO-QCD accuracy [213], and the experimental measurements are listed from [26]. In particular, neutral meson mixing is sensitive to the inclusion of new heavy mediator particles such as the charged Higgs, see figure 4.5. In the flavour-conserving 2HDMs, neutral meson mixing requires that

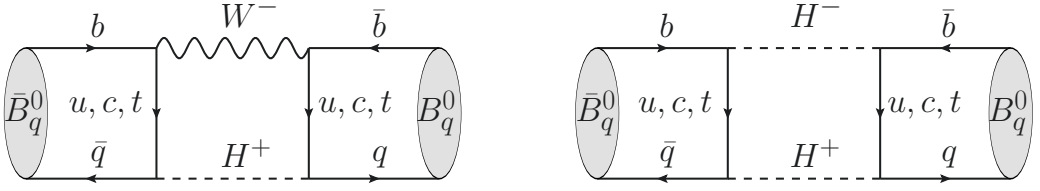

FIGURE 4.5: Examples of box diagrams in the 2HDM contributing to B_d and B_d meson mixing [41].

the charged Higgs mass is not too small and also imposes upper and lower bounds on the value of $\tan\beta$. However, the larger theory uncertainties here mean that the bounds from neutral meson mixing on the flavour-conserving 2HDMs (where the contributions are by default already suppressed to loop level) are not as constraining as those from other observables. The constraints found for types I/X and II/Y are shown in figure 4.6. One can see that types I/X and II/Y result in identical constraints from Δm_q; this is explained by considering the ξ_A couplings in table 4.2, where types I/X and II/Y differ only in the lepton coupling which does not enter into this process. A further reduction of the theory uncertainties in the future could however make neutral meson mixing crucial in constraining new physics such as flavour-conserving 2HDMs.

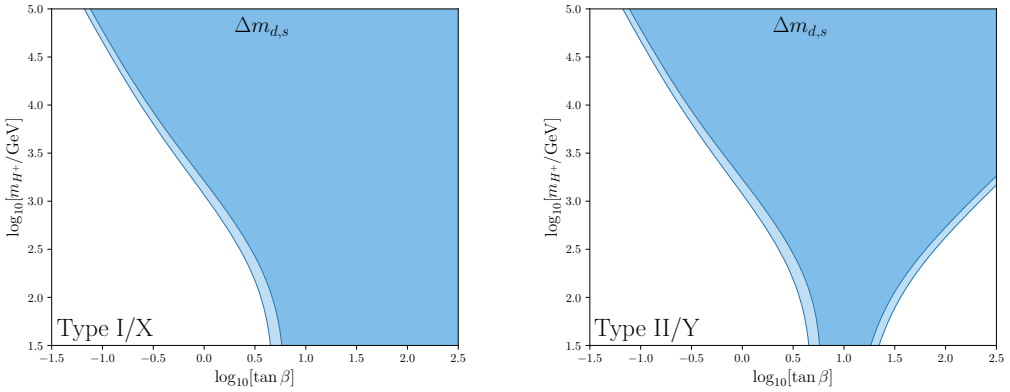

FIGURE 4.6: Contour plots of allowed 2HDM parameter space in the $(\tan\beta, m_{H^+})$ plane from the mass differences Δm_q in neutral B meson mixing for the types I/X (left) and II/Y (right). The lighter contour indicates the allowed parameter space at 2σ confidence level while the darker corresponds to 1σ.

Flavour-Changing Neutral Currents: $b \to s\gamma$ and $b \to q\ell^+\ell^-$

Next we turn to FCNC processes which are induced beyond tree level. Specifically, we consider $b \to q\ell^+\ell^-$ and $b \to s\gamma$ decays which gain contributions via the operators

$$\begin{aligned}
\mathcal{O}_7^{(\prime)} &= \frac{e\, m_b}{16\pi^2}(\bar{q}\sigma^{\mu\nu}P_{R(L)}b)F_{\mu\nu}, & \mathcal{O}_8^{(\prime)} &= \frac{g_s\, m_b}{16\pi^2}(\bar{q}\sigma^{\mu\nu}P_{R(L)}T^a b)G^a_{\mu\nu},\\
\mathcal{O}_9^{(\prime)} &= \frac{e^2}{16\pi^2}(\bar{q}\gamma_\mu P_{L(R)}b)(\bar{\ell}\gamma^\mu\ell), & \mathcal{O}_{10}^{(\prime)} &= \frac{e^2}{16\pi^2}(\bar{q}\gamma_\mu P_{L(R)}b)(\bar{\ell}\gamma^\mu\gamma_5\ell),\\
\mathcal{O}_S^{(\prime)} &= \frac{e^2}{16\pi^2}(\bar{q}P_{L(R)}b)(\bar{\ell}\ell), & \mathcal{O}_P^{(\prime)} &= \frac{e^2}{16\pi^2}(\bar{q}P_{L(R)}b)(\bar{\ell}\gamma_5\ell).
\end{aligned} \tag{4.27}$$

The 2HDM contributions to the Wilson coefficients of these operators are taken from [231]. The radiative decay $\bar{B} \to X_s\gamma$ has historically always been an important observable in the 2HDM, see e.g. [263]. The SM prediction is based on [263–265], and the experimental average from [26] is based on [266–268]. Affected by the operators $\mathcal{O}_7$ and $\mathcal{O}_8$, the 2HDM contributions lead to a clear lower bound on the mass of the charged Higgs in

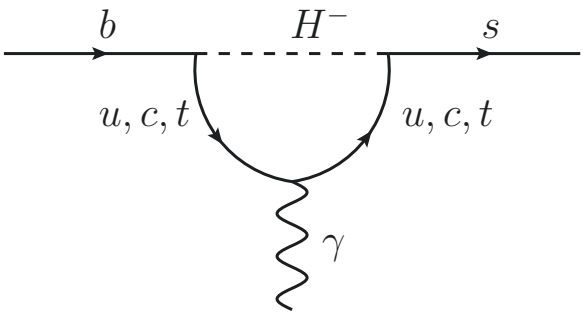

FIGURE 4.7: One-loop 2HDM contribution to the $b \to s\gamma$ radiative decay [41].

types II/Y:

$$m_{H^+} \gtrsim 790\,\text{GeV at } 2\sigma. \tag{4.28}$$

The strong lower bound found for types II/Y, and the lack of this bound in types I/X is shown in figure 4.8. Similarly to the case of Δm_q, the lepton couplings do not enter the

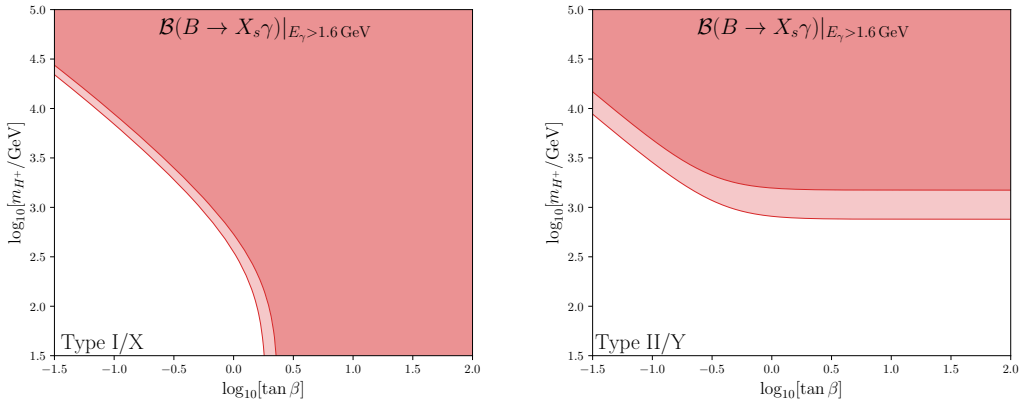

FIGURE 4.8: Contour plots of allowed 2HDM parameter space in the $(\tan\beta, m_{H^+})$ plane from the radiative decay $B \to X_s\gamma$ for the types I/X (left) and II/Y (right). The lighter contour indicates the allowed parameter space at 2σ confidence level while the darker corresponds to 1σ.

2HDM contributions to $B \to X_s\gamma$ and so types I/X and II/Y have identical constraints.

Next we consider the FCNC-mediated leptonic decays $B_{d,s} \to \mu^+\mu^-$. These are particularly sensitive to new scalar contributions from BSM theories, and are therefore well-suited to testing the 2HDM. Further motivation to use these processes is the significant progress made in the last few years to improve the experimental measurements for these challenging and rare decays, having some of the smallest branching ratios ever extracted by experiment:

$$\begin{aligned} \mathcal{B}^{\text{SM}}(B_s \to \mu^+\mu^-) &= (3.55 \pm 0.10) \times 10^{-9}, \quad \mathcal{B}^{\text{SM}}(B_d \to \mu^+\mu^-) = (0.98 \pm 0.04) \times 10^{-10}, \\ \mathcal{B}^{\text{Exp.}}(B_s \to \mu^+\mu^-) &= (2.93 \pm 0.35) \times 10^{-9}, \quad \mathcal{B}^{\text{Exp}}(B_d \to \mu^+\mu^-) = (0.56 \pm 0.70) \times 10^{-10}. \end{aligned} \tag{4.29}$$

We use the experimental combinations [269] and recent ATLAS, CMS, and LHCb results [189–194]. The SM prediction is based on a perturbative element [270–272] and a non-perturbative determination of the decay constants, see e.g. [273–275]. When con-

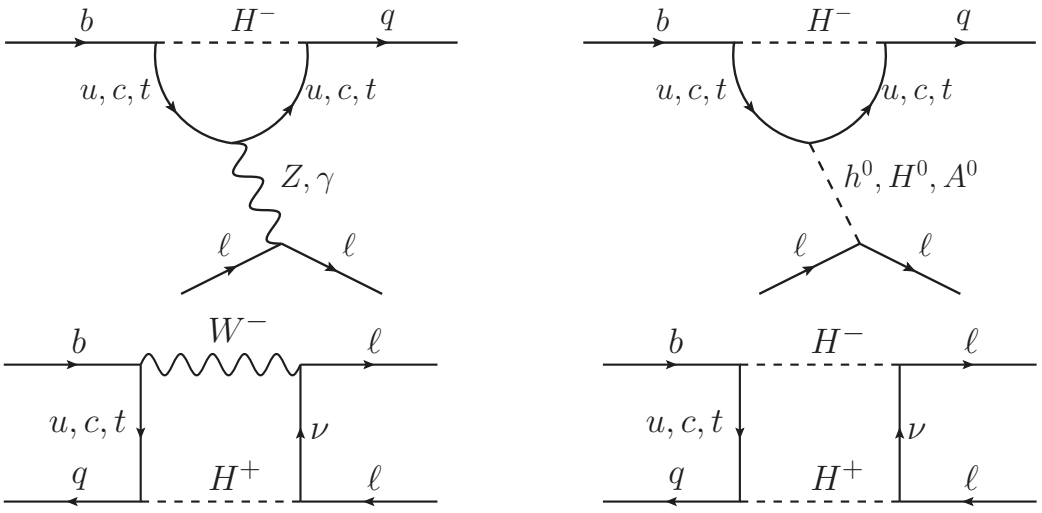

FIGURE 4.9: Examples of penguin and box diagrams in the 2HDM contributing to $b \to q\ell^+\ell^-$ transitions [41].

sidering these decays, the operators $\mathcal{O}_{10}^{(\prime)}, \mathcal{O}_S^{(\prime)}, \mathcal{O}_P^{(\prime)}$ gain contributions from the 2HDM, however instead of only $\tan\beta$ and m_{H^+} which have affected the flavour decays considered so far, the Wilson coefficients of these operators also now introduce dependence on the rest of the 2HDM parameters: $\cos(\beta-\alpha)$, m_{H^0}, m_{A^0}. To consider a 2D fit to $B_{d,s} \to \mu^+\mu^-$ in the $(\tan\beta, m_{H^+})$ plane, we therefore choose to fix the additional 2HDM parameters as $\cos(\beta-\alpha) = 0$ since the alignment limit is favoured in global fits (see e.g. figure 4.2) and $m_{H^0} = m_{A^0} = m_{H^+}$ which is justified by the theoretical constraints (see e.g. figure 4.1). Similarly to $B \to X_s\gamma$, types II and Y share similar constraints from $B_{d,s} \to \mu^+\mu^-$ as do types I and X; this is explained in this case by the fact that the lepton pair couples to the neutral scalars of the 2HDM, which in the alignment limit is the same for all types. Although not as strong as from $B \to X_s\gamma$, types II and Y again find a clear lower bound for m_{H^+} from $B_{d,s} \to \mu^+\mu^-$ as well as a clear correlation between m_{H^+} and the allowed range for $\tan\beta$. The lower bound in types II and Y from $B_{d,s} \to \mu^+\mu^-$ is

$$m_{H^+} \gtrsim 300\,\text{GeV} \text{ at } 2\sigma. \tag{4.30}$$

Within the physical domain of 2HDM parameters, no clearly defined constraints are found for types I and X.

We also include semileptonic $b \to s\ell^+\ell^-$ processes, such as binned branching ratios, angular distributions, asymmetries, etc. For a full list of observables included, see table 7 of [41]; the experimental measurements are listed from [269, 276–290]. Note that

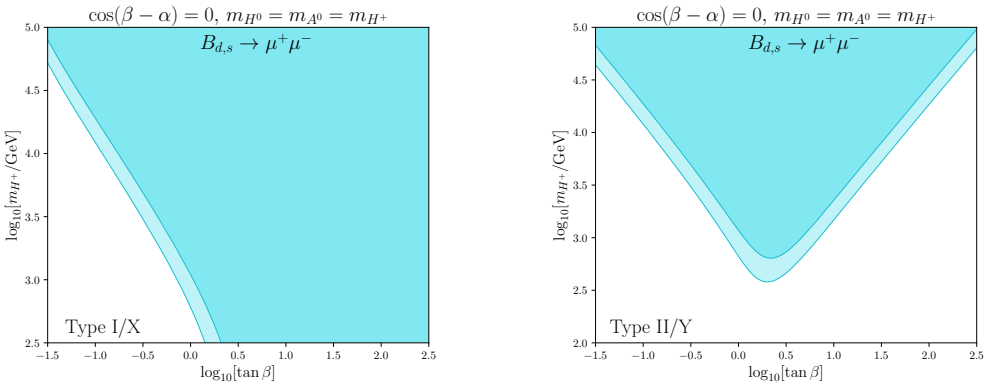

FIGURE 4.10: Contour plots of allowed 2HDM parameter space in the $(\tan\beta, m_{H^+})$ plane from $B_{d,s}\to\mu^+\mu^-$ for the types I/X (left) and II/Y (right). The lighter contour indicates the allowed parameter space at 2σ confidence level while the darker corresponds to 1σ.

some of these observables exhibit tension with the Standard Model; in fact, these are collectively known as the *flavour anomalies* and are commonly the topic of detailed analyses, see e.g. [253, 269, 291–305]. Like the tree-level semileptonic decays, these can suffer from large uncertainties in their hadronic form factors, which, in particular for vector final states, are typically less well-determined than the tree-level equivalents. These are also more challenging in q^2 ranges resonant with $c\bar{c}$ states where long-distance hadronic effects coming from 'charm loops' coupling to the lepton pair appear [291].

For all FCNC $b\to q\ell\ell$ processes, we can combine these in their own global fit, yielding the results presented in table 4.3. All operators listed in equation (4.27) enter these processes with 2HDM contributions, and thus all five 2HDM parameters again enter. When considering the standard $(\tan\beta, m_{H^+})$ plane therefore, the additional 2HDM parameters m_{H^0}, m_{A^0}, $\cos(\beta-\alpha)$ are set to the $b\to q\ell\ell$ best fit point, as seen in figure 4.11. The exact lower bound on m_{H^+} is not as strict as in the single plot for each type, since varying the additional parameters introduces more freedom. What is of note here however is that one can see an upper bound on the charged Higgs mass appear. This is introduced by the observables deviating from the SM predictions such that the decoupling $m_{H^+}\to\infty$ limit (which would recover the SM predictions) is no longer favoured, as has been the case for most processes considered so far.

At the time of analysis, there still existed a significant tension in the SM for the LFU ratios $R_{K^{(*)}}\equiv\mathcal{B}(B\to K^{(*)}\mu^+\mu^-)/\mathcal{B}(B\to K^{(*)}e^+e^-)$ [306], which are calculated in bins of squared dilepton invariant mass q^2. These ratios are theoretically very clean, since almost all hadronic physics cancels out in the ratios and also the electromagnetic corrections are found to be tiny [307]. These ratios therefore serve well in BSM analyses since the theoretical calculation does not suffer from complications that can interfere with

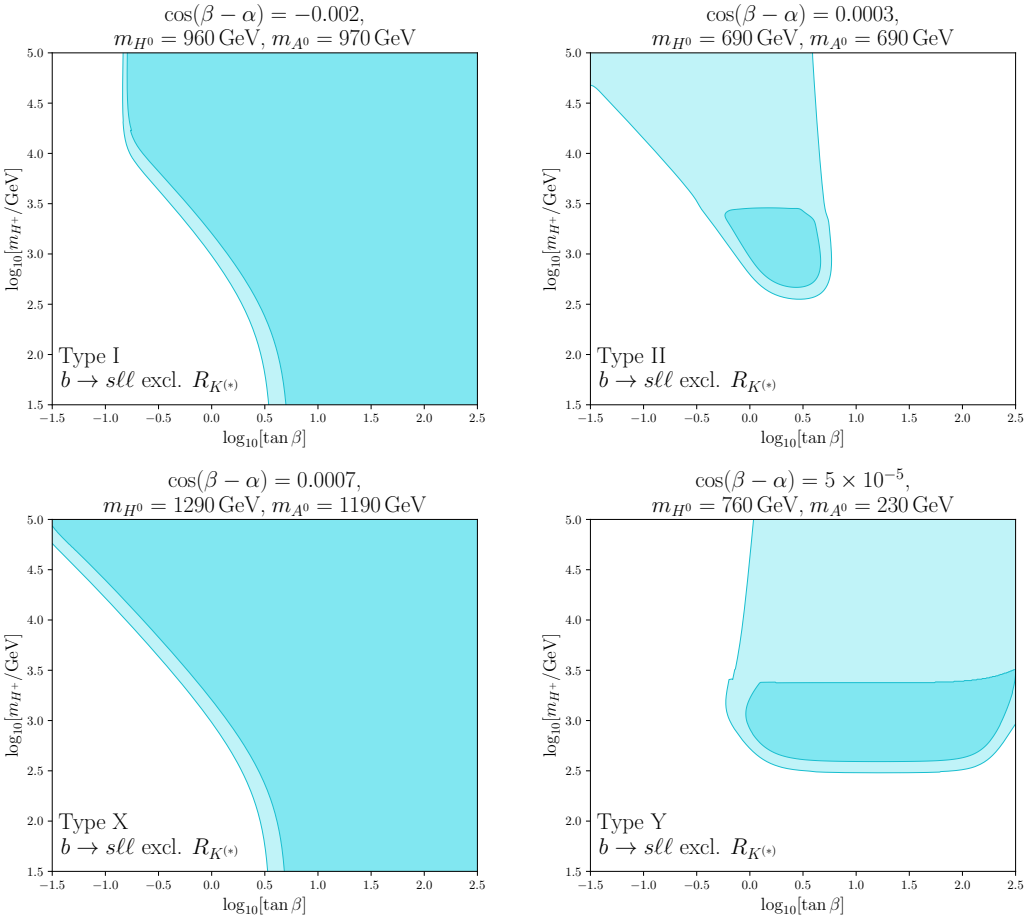

FIGURE 4.11: Contour plots of allowed 2HDM parameter space in the $(\tan\beta, m_{H^+})$ plane from all $b \to s\ell^+\ell^-$ transitions for each flavour-conserving type. The additional 2HDM parameters are fixed to their best fit point of the global fits performed in [41–43] and shown in table 4.3. The darker contour indicates allowed parameter space at 1σ confidence level and the lighter at 2σ.

possible new physics. It was found however that the 2HDM struggled to accommodate the 10 bins of $R_{K^{(*)}}$ considered at the time [282, 308–311], always finding best fit scenarios poorer than in the SM. Therefore the approach was taken to consider global fits both with and without $R_{K^{(*)}}$ since (as with the tree-level $R_{D^{(*)}}$ LFU ratios) even in a realised 2HDM, the data suggests further new physics would be required to accommodate these observables. The situation is actually much improved now since the measurements of $R_{K^{(*)}}$ were updated and now agree nicely with the SM predictions [32, 33]. For the analysis here, this essentially equates to the global fit scenarios neglecting $R_{K^{(*)}}$ since in most of the parameter region considered these ratios gained only tiny corrections from the 2HDM and remained close to their Standard Model predictions, meaning now close to the measurements as well.

Global Fits

Next we consider the global fits to all observables in each flavour-conserving type of 2HDM. As well as the Higgs signal strengths and flavour observables mentioned so far, we also include the electroweak precision observables S, T, and U in the global fits; the observables considered are summarised in tables 4, 5, 6, 7, and 8 of [41]. For each type, a global fit to all observables (excluding the LFU ratios as discussed in the text) is performed in the frequentist picture, the best fit point for the five 2HDM parameters $\tan\beta$, m_{H^+}, m_{H^0}, m_{A^0}, $\cos(\beta-\alpha)$ is found, and the quality of its fit assessed. The best fit points of the global fits for each type to all observables and also to only the $b \to s\ell\ell$ observables are shown in table 4.3.

Scenario	# Observables	Best-fit point $\{\tan\beta, m_{H^+}, m_{H^0}, m_{A^0}, \cos(\beta-\alpha)\}$	χ^2_{min}	p-value
Type I global	263	$\{80, 1720\,\text{GeV}, 1770\,\text{GeV}, 1770\,\text{GeV}, -0.003\}$	281	15.5%
Type I $b \to s\ell\ell$	192	$\{35, 1020\,\text{GeV}, 960\,\text{GeV}, 970\,\text{GeV}, -0.002\}$	234	1.1%
Type II global	265	$\{4.3, 2340\,\text{GeV}, 2380\,\text{GeV}, 2390\,\text{GeV}, 0.009\}$	295	6.6%
Type II $b \to s\ell\ell$	192	$\{4.0, 820\,\text{GeV}, 690\,\text{GeV}, 690\,\text{GeV}, 0.0003\}$	238	0.7%
Type X global	263	$\{320, 1540\,\text{GeV}, 1480\,\text{GeV}, 1490\,\text{GeV}, 8\times10^{-5}\}$	279	17.6%
Type X $b \to s\ell\ell$	192	$\{320, 1240\,\text{GeV}, 1290\,\text{GeV}, 1190\,\text{GeV}, 0.0007\}$	233	1.3%
Type Y global	263	$\{320, 1270\,\text{GeV}, 1240\,\text{GeV}, 1150\,\text{GeV}, 1\times10^{-4}\}$	284	12.8%
Type Y $b \to s\ell\ell$	192	$\{15, 460\,\text{GeV}, 760\,\text{GeV}, 230\,\text{GeV}, 5\times10^{-5}\}$	237	0.8%

TABLE 4.3: Best fit points of 2HDM parameter fits using the constraints from theory to inform the physical parameter values.

The results of the fits in the $(\tan\beta, m_{H^+})$ plane, fixing the additional parameters to their best fit points, are shown in figure 4.12. By further varying the fixed parameters within their allowed phenomenological and theoretical bounds, we find the allowed regions for the 2HDM parameters; these regions are presented in table 4.4 at 2σ confidence level.

	m_{H^+} [TeV]	$\cos(\beta-\alpha)$	$\tan\beta$
Type I	$[0.1, 10]$	$[-0.14, 0.14]$	$[0.55^*, 320)$
Type II	$[0.86, 10]$	$[-0.04, 0.04]$	$[0.32^*, 50^*)$
Type X	$[0.13, 10]$	$[-0.05, 0.10]$	$[0.38^*, 320)$
Type Y	$[0.74, 3.61]$	$[-0.01, 0.04]$	$[110, 320)$

TABLE 4.4: Regions of allowed 2HDM parameters [43]. We consider the 2σ regions from the global fit (excluding LFU observables $R(K^{(*)}), R(D^{(*)})$) for each type, and also do not exceed the region of $m_{H^+} \in [0.1, 10]\,\text{TeV}$ in order to not conflict with direct search limits [312] or approach the decoupling limit. The additional neutral Higgs masses are constrained from the charged Higgs mass as found in [41] (Table 1). * indicates quantities which are not general, but depend on m_{H^+}; we show values for $m_{H^+} = 10\,\text{TeV}$ where the allowed regions are at their maximum.

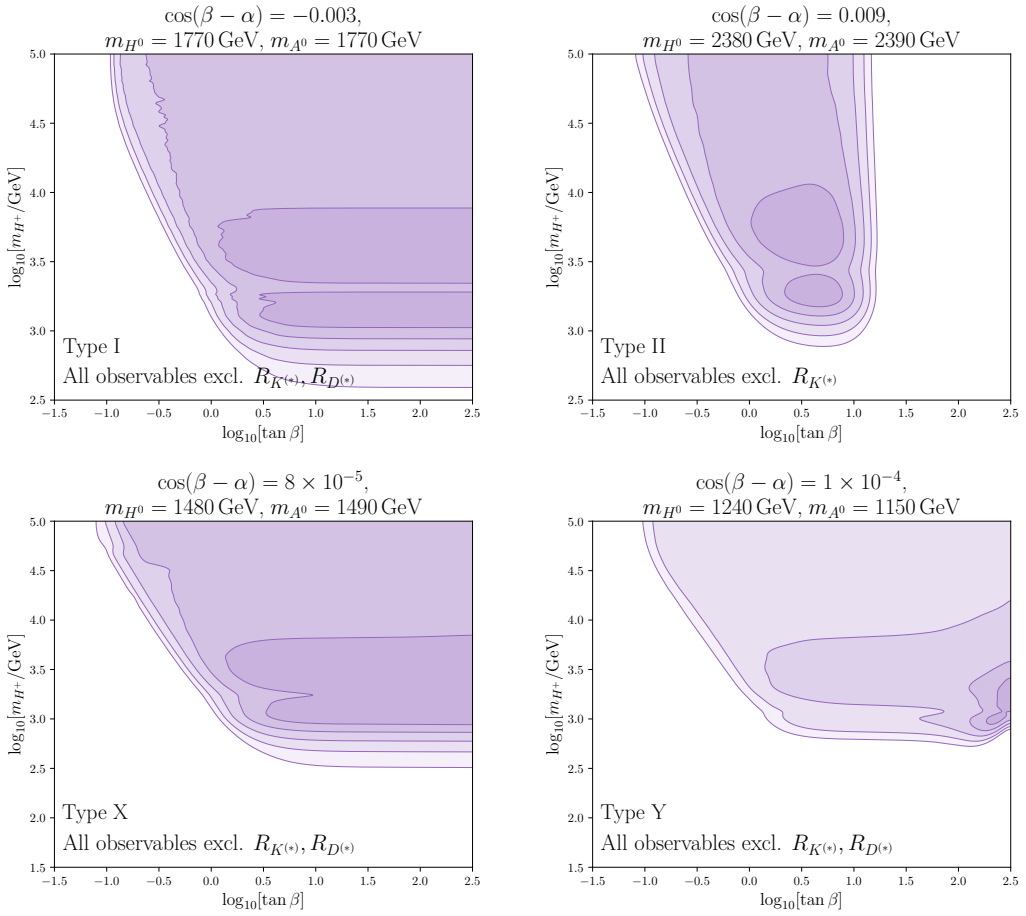

FIGURE 4.12: Contour plots of allowed parameter space in the $(\tan\beta, m_{H^+})$ plane for each flavour-conserving type of 2HDM. The additional parameters are fixed to their best fit point of the global fits performed in [41–43] and shown in table 4.3. The contours indicate allowed parameter space at $1, 2, 3, 4, 5\sigma$ confidence level going from darker to lighter.

Anomalous Magnetic Moment of the Muon

Another observable typically of interest in BSM analyses is the anomalous magnetic moment of the muon, a_μ. This has had a long-standing tension between experiment and the SM since the original BNL experiment [313] which was recently confirmed by FNAL [314]. This has been a strong motivation to consider new physics signals since the quantum loop nature of a_μ means it can be sensitive to new heavy mediators in these loops and many new physics models have been tested over the years in attempts to resolve the tension with experiment, see e.g. [315]. Examples of the contributions in the 2HDM are shown in figure 4.13.

While a great deal of machinery has been implemented over many years to calculate the perturbative contributions to a_μ at five-loop order in QED, the dominant source of uncertainty in the calculation lies in the hadronic contributions, namely the hadronic vacuum polarisation (HVP) and hadronic light-by-light scattering (HLbL). Two separate methods are typically used to calculate these hadronic contributions: the data-driven

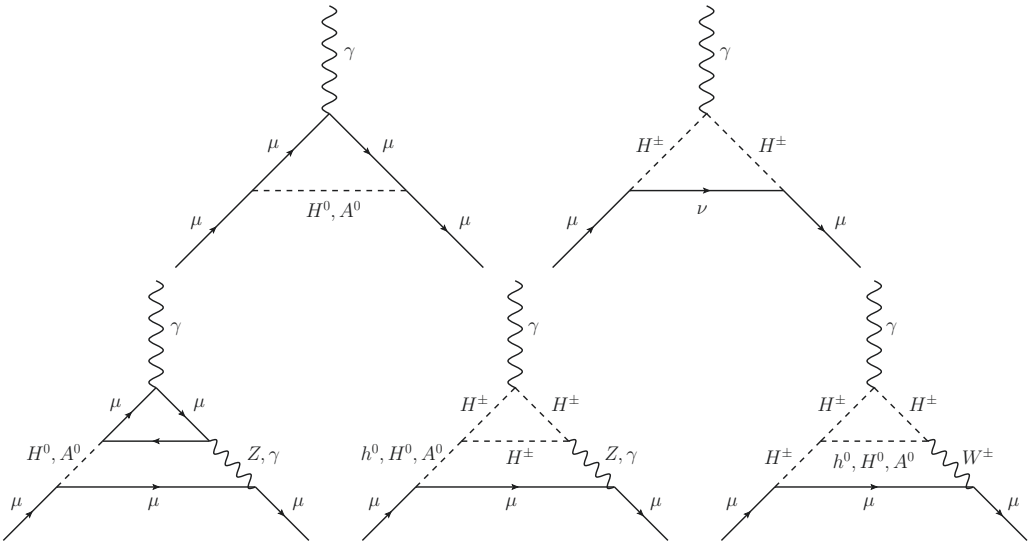

FIGURE 4.13: Examples of LO and NLO diagrams in the 2HDM contributing to a_μ [41, 316, 317].

R-ratio method taking experimental input of $\sigma(e^+e^- \to \text{hadrons})$, and lattice QCD simulations. At the time of analysis, the SM prediction from the Theory Initiative White Paper using the data-driven approach yielded a 4.2σ discrepancy with experiment [318]. Although lattice QCD simulations had estimated the hadronic contributions to a_μ previously [319–328], the spread between the results was large and the uncertainties of these calculations were also larger than the data-driven alternative such that any deviations they may have suggested from the data-driven approach were not taken to be significant. However, the BMW collaboration in 2020 released a new lattice calculation with uncertainties competitive with the data-driven approach for the first time [329]. Of note in this calculation was a significant shift from the data-driven approach, reporting only a 1.6σ tension with experiment. While this is the only complete lattice calculation to date with this increased precision, other lattice collaborations are now reporting similar results in the 'intermediate window' for HVP [327], suggesting that these could align more closely with the BMW result when they complete the full calculation as well [330–333]. Very recently, the BMW collaboration released an update to their 2020 result with even higher precision, reducing the difference from experiment to only 0.9σ [334].

In the original analysis it was chosen to comment on both the White Paper and BMW predictions as separate scenarios. Neither a_μ scenario however was considered in the global fits, anticipating further clarification in the future. It was found that within the perturbative regime of the 2HDM, the contributions to a_μ were tiny and therefore strongly disfavoured using the White Paper SM prediction which expected large BSM contributions, whereas using the BMW prediction which anticipated only small deviations from the SM allowed the relevant parameter space within 2σ. For future

BSM analyses, the community eagerly awaits further high-precision lattice calculations to hopefully settle the tension between the SM predictions.

4.2.2 Models without $\mathbb{Z}_2$ symmetry

While 2HDMs with a $\mathbb{Z}_2$ symmetry can be found appealing because they forbid FCNCs at tree-level, the features of a general 2HDM without this additional symmetry can also be interesting to study. In particular, by allowing both Higgs doublets to couple to all fermions, the Yukawa structure of the type III 2HDM no longer replicates that of the SM, and can lead to enhanced couplings between the fermions and the neutral Higgses of the model.

In section 4.2.1 above, we discussed the FCNC leptonic decays $B_{d,s} \to \mu^+\mu^-$ as some of the smallest branching ratios measured by experiment. The small size of these decays' branching ratios stems from helicity suppression by being proportional to m_μ^2. This suppression is therefore even stronger for the electron channels $B_s \to e^+e^-$; while $\mathcal{B}^{\text{SM}}(B_s \to \mu^+\mu^-) = (3.55 \pm 0.10) \times 10^{-9}$, the equivalent channel with electrons has $\mathcal{B}^{\text{SM}}(B_s \to e^+e^-) = (8.30 \pm 0.36) \times 10^{-14}$. This tiny branching ratio, if accurate, is still orders of magnitude below the experimental upper bounds set by the LHCb experiment [335] of

$$\mathcal{B}(B_s \to e^+e^-) < 9.4 \times 10^{-9}. \tag{4.31}$$

With such a large separation between the experimental limit and the SM prediction, any clear observation of this channel by experiment in the near-future would be a clear indication of new physics. In [336], it was shown model-independently how the branching ratio of $B_s \to e^+e^-$ could be enhanced from the SM value to an observable level by the presence of new pseudoscalar interactions. To achieve this effect however requires that the new pseudoscalar coupling is not proportional to the electron mass m_e. This therefore excludes models such as the flavour-conserving 2HDMs where the Yukawa coupling is directly proportional to the fermion mass. However, it was shown in [44] for the first time how a general type III 2HDM allows the possibility of enhancing $B_s \to e^+e^-$ in a specific new physics model.

In the type III 2HDM, one has some freedom to choose the structure of the Yukawa sector, and a scenario can be arranged where the Yukawa coupling to the electron is suitably enhanced in order to make $B_s \to e^+e^-$ experimentally accessible. The Yukawa matrix for charged leptons in this type III 2HDM is close to flavour diagonal and can

be expressed as

$$\tilde{Y}^{\ell} = \begin{pmatrix} y_{ee} & \epsilon & \epsilon \\ \epsilon & y_{\mu\mu} & \epsilon \\ \epsilon & \epsilon & y_{\tau\tau} \end{pmatrix}, \tag{4.32}$$

where $\epsilon \ll y_{jj}$. Suppressing the off-diagonal elements ϵ is favourable in order to avoid lepton flavour violating processes, such as $\mu \to e\gamma$ [337]. Since we are mostly interested in enhancing the electron coupling, we assume $y_{\mu\mu} \ll y_{ee}$ and $\epsilon \ll y_{\tau\tau}$. We can similarly express the Yukawa matrix for the down-type quarks as

$$\tilde{Y}^{d} = \begin{pmatrix} y_{dd} & \epsilon & \epsilon \\ \epsilon & y_{ss} & y_{bs}/2 \\ \epsilon & y_{bs}/2 & y_{bb} \end{pmatrix}, \tag{4.33}$$

where again $\epsilon \ll y_{ij}$. Here we suppress some off-diagonal elements in order to e.g. avoid the strong bounds on FCNCs from neutral kaon mixing [54], however we keep the entry y_{bs} such that the quark current of $B_s \to e^+e^-$ can be coupled to the scalar H^0 and pseudoscalar A^0, thus giving a tree-level contribution to this process, seen in figure 4.14. Similar Yukawa structures, without keeping the off-diagonal elements symmetric, have been studied in [338, 339]. The 2HDM Wilson coefficients of the operators $\mathcal{O}^{(\prime)}_{S,P}$ impact-

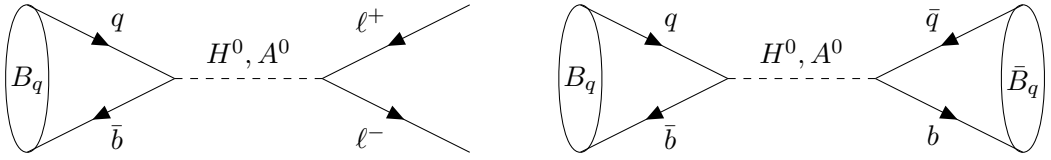

FIGURE 4.14: Tree-level FCNC diagrams for $B_q \to \ell^+\ell^-$ and neutral B_q meson mixing induced in the general type III 2HDM [44].

ing $B_s \to e^+e^-$ are

$$\begin{aligned} C_S &= \frac{y_{bs}y_{ee}}{m^2_{H^0}} \left(\frac{\sqrt{2}\pi}{m_b G_F V_{tb} V^*_{ts} \alpha} \right), \qquad C'_S = C_S, \\ C_P &= -\frac{y_{bs}y_{ee}}{m^2_{A^0}} \left(\frac{\sqrt{2}\pi}{m_b G_F V_{tb} V^*_{ts} \alpha} \right), \quad C'_P = -C_P. \end{aligned} \tag{4.34}$$

Since $\mathcal{B}(B_s \to e^+e^-)$ actually depends on differences $\Delta C_S = C_S - C'_S$ and $\Delta C_P = C_P - C'_P$, one can see that the CP-even scalar H^0 does not contribute to the branching ratio, however the CP-odd scalar A^0 does.

The type III 2HDM with such couplings can even be embedded in a UV theory of quark-lepton unification as further motivation and validation for testing such a scenario. The idea of quark-lepton unification was first proposed by Pati and Salam [340] where SM quarks and leptons belong to the same multiplet and this remains a well-motivated and

popular scenario on which to base BSM theories. However, the original theory relates the top-quark Yukawa coupling to the neutrino coupling, which then requires the associated energy scale to be very high ($\sim 10^{14}\,\text{GeV}$) via the seesaw mechanism [341–344]. Instead, here and in [44], a low energy limit of the original Pati-Salam theory, proposed in [345], is considered in which the neutrino mass arises from the inverse seesaw mechanism and the required energy scale of the theory can be much lower.

As seen in figure 4.14, allowing the off-diagonal Yukawa coupling y_{bs} introduces tree-level FCNCs between b and s quarks. This not only allows the decay $B_s \to e^+e^-$ to proceed at tree level, but also induces 2HDM contributions to the mass difference ΔM_s in neutral $B_s - \bar{B}_s$ mixing at tree level. This will impose strict bounds on the size of the coupling y_{bs} since these 2HDM contributions are not loop-suppressed and can in principle be very sizeable compared to the SM contributions while the difference between experiment and the SM prediction is not so large. These bounds will also be correlated with the Higgs masses m_{H^0}, m_{A^0}; larger Higgs masses will further suppress the Wilson coefficients such that the coupling y_{bs} can be larger.
Similarly, this allows semileptonic $b \to s e^+e^-$ decays to proceed at tree level also. These processes have the same new contributions to operators $\mathcal{O}^{(\prime)}_{S,P}$ as $B_s \to e^+e^-$ from equation (4.34), and thus depend on the combined coupling $y_{bs}y_{ee}$ and the Higgs masses m_{H^0}, m_{A^0}. The $b \to s e^+e^-$ observables considered are listed in table 1 of [44], using [286, 346–348]. Note that the LFU ratios $R_{K^{(*)}}$ would also be modified in this model and could have been included in our fits, however these do not change the conclusions of the study significantly and it was decided that a new physics treatment of $R_{K^{(*)}}$ without properly developing also the muon sector of the model would be inaccurate.
Furthermore, since $B_s \to e^+e^-$ depends on the combined coupling $y_{bs}y_{ee}$, the bounds on y_{bs} found from neutral $B_s - \bar{B}_s$ mixing can be correlated with bounds on the y_{ee} coupling from the measurement of the cross-section of $e^+e^- \to e^+e^-$ by the LEP collaboration. The constraints on the four-electron axial-vector interaction [349] can be translated into bounds on the scalar and pseudoscalar interactions, finding

$$\frac{y_{ee}^2}{m_{H^0}^2} + \frac{y_{ee}^2}{m_{A^0}^2} < \frac{1}{(4\,\text{TeV})^2} \overset{m_{A^0}=m_{H^0}}{\Longrightarrow} \frac{y_{ee}}{m_{H^0}} < \frac{1}{5.7\,\text{TeV}}. \tag{4.35}$$

The allowed parameter space in the $(y_{bs}y_{ee}, m_{A^0})$ plane from all phenomenological constraints is shown in figure 4.15, where we consider two scenarios: first the limit $m_{A^0} = m_{H^0}$ and second allowing the maximum freedom between m_{A^0} and m_{H^0} from the theoretical constraints of the model. The blue shaded regions indicated the space allowed by the semileptonic $b \to s e^+e^-$ decays at 1σ and 2σ confidence levels, while the green region is the combined LEP and ΔM_s constraints at 2σ confidence level. The black lines correspond to contours of constant enhancement factor $\mathcal{B}^{\text{2HDM}}(B_s \to$

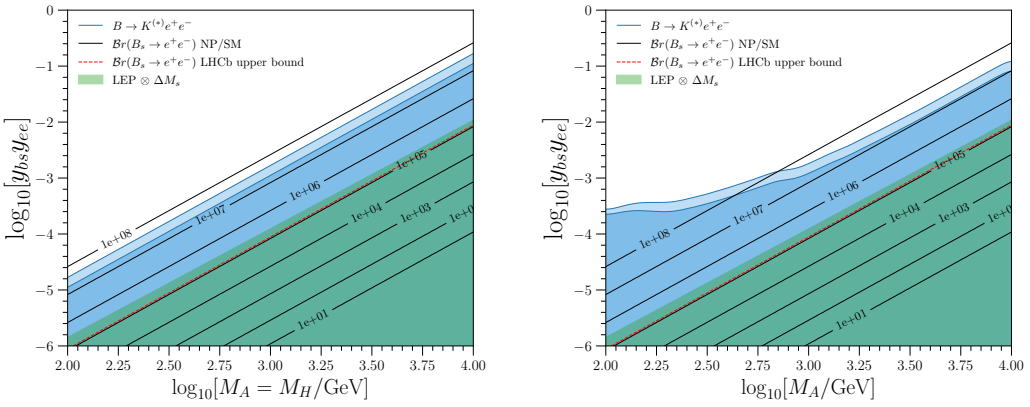

FIGURE 4.15: Allowed parameter space for the combined coupling $y_{bs}y_{ee}$ and the mass of the pseudoscalar Higgs m_{A^0}; in the limit of $m_{A^0} = m_{H^0}$ (left) and allowing m_{A^0} and m_{H^0} to differ within the theoretical constraints of the model (right). The contours in dark and light blue represent allowed space within 1σ and 2σ confidence levels respectively. The black lines represent contours of enhancement for the ratio $\mathcal{B}^{\mathrm{2HDM}}(B_s \to e^+e^-)/\mathcal{B}^{\mathrm{SM}}(B_s \to e^+e^-)$. The red dashed line indicates the enhancement (10^5) needed to saturate current experiment bounds [44].

$e^+e^-)/\mathcal{B}^{\mathrm{SM}}(B_s \to e^+e^-)$; one can see that an enhancement factor as large as $\sim 10^5$ is allowed by all constraints. In fact, the current experimental bounds corresponds to an enhancement of 10^5 above the SM (marked on the figures with a red dashed line) which can therefore even be saturated by the allowed enhancements of the type III 2HDM considered here.

4.2.3 Improvements Needed for Future Analysis

A recurring factor in this section has been that while many observables are calculated to a high precision in the SM, further control of their uncertainties is to be welcomed for making statements both about the compatibility of the SM with experiment and the suitability of new physics models. While the hadronic physics in the simplest processes such as leptonic decays is well-controlled these days, increased precision in these non-perturbative contributions to more complex decays, such as semileptonic decays and neutral meson mixing, is required in order to have full control over their uncertainties and increase their power in the search for new physics. In the following chapters, we will turn our focus to the calculation of these non-perturbative hadronic contributions with increased precision in order to improve future SM and BSM analyses using these processes.

Chapter 5

Non-Perturbative Methods for Hadronic Physics

In this chapter we will introduce some common methods used for calculating the effects of hadronic physics in QCD. As discussed in section 2.3.2, the QCD coupling α_s is large at low energies. This leads to the phenomenon of confinement where strongly-interacting particles cannot overcome the strong coupling and the degrees of freedom in QCD are better described by the hadronic bound states formed by the individual quarks and gluons. In this regime, the 'standard' method of perturbation theory (where one calculates diagrams progressively as a Taylor expansion in the coupling constant) breaks down and we require new, non-perturbative methods in order to make meaningful predictions.

In section 5.1 we will introduce *lattice QCD*, a framework of calculating hadronic observables numerically by discretising spacetime on a finite 4-dimensional grid and simulating on large computer systems. The alternative method of QCD sum rules is then discussed in section 5.2, which allows for an analytical evaluation of hadronic observables combining perturbative QCD and vacuum condensate contributions (or light-cone distribution amplitudes). Other non-perturbative methods also exist, although not covered here in any further detail. These include AdS/CFT approaches [350] and effective field theories such as HQET and chiral perturbation theory.

We will find that all methods are powerful tools for calculating hadronic observables and are oftentimes complimentary to one another where, for example, regions of phase space difficult to access for one method are simpler in another. In the case where a hadronic observable is accessible to multiple methods, this provides a useful, independent cross-check to validate that two separate methods converge and agree when expected.

5.1 Lattice Quantum Chromodynamics

We now present a basic introduction to the important features of lattice QCD, first outlined by Wilson in 1974 [40]. Starting with a basic outline, we then discuss how to discretise the QCD Lagrangian (the gauge fields in particular) in section 5.1.1. We will take a moment to describe how the path integral formulation of QFT can be solved stochastically on Euclidean lattices using Monte Carlo methods in section 5.1.2 before returning to the problems encountered when discretising fermions in section 5.1.3 and how these are circumvented. We briefly outline how a real physical scale can be associated with lattice simulations in section 5.1.4. We will then discuss how correlation functions of fermion currents are formed and what information can be extracted from these in section 5.1.5. Finally, we stress the challenges of simulating heavy charm and bottom quarks on the lattice in section 5.1.6 and conclude with a summary of the statistical and systematic errors associated with a lattice calculation in section 5.1.7. This section stands as an introduction to the topic of lattice QCD, where the knowledge presented here has been collected from [351–353] (and references within), discussions with colleagues, and further lectures and schools attended.

Typically, other methods for non-perturbative predictions such as effective field theories are based on model-dependent assumptions and/or are only valid in certain ranges of e.g. phase space. Lattice QCD is an ab initio framework providing predictions directly from the QCD Lagrangian, where all uncertainties are systematically improvable through improved computer algorithms, understanding of the discrete field theory, and increased computer power and resources. This is a first-principles method which has a well-defined trajectory to continuum QCD starting from the path integral formulation of quantum field theory, without additional assumptions and approximations which are required by other methods.

In the path integral formalism in Minkowski space, the n-point correlation function is given by

$$\langle \mathcal{O}_1 \dots \mathcal{O}_n \rangle = \frac{1}{Z} \int \mathcal{D}[A, \psi, \bar{\psi}] \mathcal{O}_1 \dots \mathcal{O}_n \exp\left(iS[A, \psi, \bar{\psi}]\right), \tag{5.1}$$

for gauge fields A and fermion fields ψ, and the action S. The partition function Z is given by

$$Z = \int \mathcal{D}[A, \psi, \bar{\psi}] \exp\left(iS[A, \psi, \bar{\psi}]\right), \tag{5.2}$$

and the path integral measure $\mathcal{D}[A, \psi, \bar{\psi}]$ by

$$\mathcal{D}[A, \psi, \bar{\psi}] = \prod_{t,\vec{x}} dA(\vec{x}, t)\, d\psi(\vec{x}, t)\, d\bar{\psi}(\vec{x}, t). \tag{5.3}$$

The integrand in equation (5.1) depends on $\exp\left(iS[A, \psi, \bar{\psi}]\right)$ where the action S is real[1]. However, integrands of the form e^{ix} are numerically unstable since this exhibits oscillatory behaviour and there are many cancellations between the 'peaks' and 'troughs' of these oscillations in the contributions to the sum. One can avoid this problem by performing a *Wick rotation* [354] from Minkowski spacetime to Euclidean spacetime [40, 94], which is done by simultaneously rotating all time arguments $t \to -i\tau$; this rotation is shown in figure 5.1. The Euclidean n-point correlation function is then given by

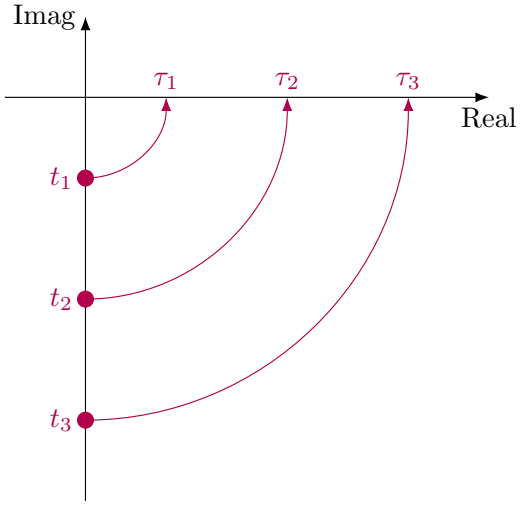

FIGURE 5.1: Wick rotation from imaginary (Minkowski) to real (Euclidean) time.

$$\langle \mathcal{O}_1 \dots \mathcal{O}_n \rangle_E = \frac{1}{Z_E} \int \mathcal{D}[A, \psi, \bar{\psi}] \mathcal{O}_1 \dots \mathcal{O}_n \exp\left(-S_E[A, \psi, \bar{\psi}]\right), \tag{5.4}$$

where the subscript E indicates quantities in Euclidean spacetime, and importantly S_E is both real and positive. Formally, equation (5.4) is infinite-dimensional and thus performing this integral in continuous and infinite spacetime is ill-defined. We will overcome this by placing the theory on a finite lattice, where the number of degrees of freedom is still large, but now finite and the path integral can be numerically estimated. Furthermore, now in Euclidean spacetime, the factor $\exp\left(-S_E[A, \psi, \bar{\psi}]\right)$ can be interpreted as a Boltzmann weight. Now for any Euclidean n-point function $\langle \mathcal{O}_1 \dots \mathcal{O}_n \rangle_E$, one can numerically estimate this in a statistical framework based on the Boltzmann weight. This will allow for Markov Chain Monte Carlo (MCMC) simulations of QCD to sample

[1] Strong CP violation is not typically included in lattice simulations.

the phase space and estimate the integral numerically, i.e.

$$\langle \mathcal{O}_1 \dots \mathcal{O}_n \rangle_E \approx \frac{1}{N} \sum_i \mathcal{O}_1[U_i] \dots \mathcal{O}_n[U_i] + O\left(\frac{1}{\sqrt{N}}\right), \tag{5.5}$$

for N 'gauge field configurations' $U_i[A, \psi, \bar{\psi}]$ which have probability proportional to the Boltzmann weight $\exp(-S_E[U_i])$. A collection of N gauge field configurations U_i prepared for the estimation of expectation values is called a *lattice ensemble*.

We define the finite lattice used to reduce the dimensionality of the integral by its lattice spacing a[2] and the 4-dimensional length L_μ/a. It is common for the spatial volume to be cubical, $L_x = L_y = L_z = L$, such that the 3D spatial volume $V_3 = L^3$ and to make the time extent T larger (commonly $T = 2L$); the 4D volume is then $V_4 = L^3 \times T$. Note that the lattice spacing a is a dimensional quantity and not a parameter of the discretised theory. Its value in physical units is derived from the dynamics of the lattice. The lattice can be described by a set of coordinates defining the *sites* of the lattice,

$$\Lambda = \{x_\mu = a n_\mu, \text{ for } n_\mu = 0, 1, \dots, L_\mu - 1 \text{ and } \mu = x, y, z, t\}. \tag{5.6}$$

A sketch of a 2-dimensional lattice is given in figure 5.2. In the discrete theory, partial

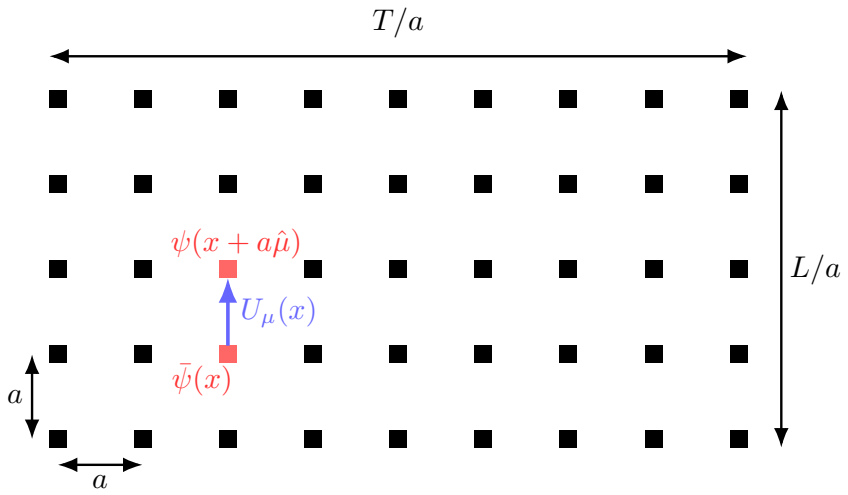

FIGURE 5.2: Sketch of a 2D lattice with $L/a \times T/a$ lattice sites and lattice spacing a. Fermion fields $\psi(x)$, $\bar{\psi}(x)$ live on the lattice sites and the gauge links $U_\mu(x)$ describe the paths between nearest-neighbour sites.

[2] In principle the lattice spacing can be defined separately in the spatial and temporal directions, i.e. $a_{x,y,z} \neq a_t$.

derivates are replaced by finite differences, i.e.

$$\begin{aligned}\partial_\mu\psi &\to \frac{1}{a}\left(\psi(x+a\hat{\mu})-\psi(x)\right),\\ \partial^*_\mu\psi &\to \frac{1}{a}\left(\psi(x)-\psi(x-a\hat{\mu})\right),\\ \frac{1}{2}(\partial_\mu+\partial^*_\mu)\psi &\to \frac{1}{2a}\left(\psi(x+a\hat{\mu})-\psi(x-a\hat{\mu})\right)\equiv\Delta_\mu\psi(x),\end{aligned} \tag{5.7}$$

where $\hat{\mu}$ is the unit vector in the μ direction on the lattice and from here on we will assume use of the symmetric derivative Δ_μ unless otherwise stated. Spacetime integrals are also replaced by sums, i.e.

$$\int d^4x\, f(x) \to a^4 \sum_{x\in\Lambda} f(x), \tag{5.8}$$

and the measure $\mathcal{D}$ is taken over the lattice sites. Now only a discrete set of variables is to be integrated over a finite volume and the path integral is finite dimensional. Note that going from infinite spacetime to a finite volume requires that we choose boundary conditions (BCs) for our box; most commonly used are *periodic* BCs.

Discretising spacetime with a non-zero lattice spacing a introduces a cut-off in momentum-space. For periodic BCs, we can perform the Fourier transform

$$\tilde{\psi}(p) = \sum_{x\in\Lambda} a^4 e^{-ipx}\psi(x) \tag{5.9}$$

such that the $\tilde{\psi}(p)$ are also periodic in momentum-space, i.e.

$$p_\mu \simeq p_\mu + \frac{2\pi}{a}, \tag{5.10}$$

and are discretised as

$$p_\mu = \frac{2\pi}{a}\frac{l_\mu}{L_\mu},\ \text{for } l_\mu = 0,1,\ldots,L_\mu-1. \tag{5.11}$$

Now one sees that the momenta are restricted to the first Brillouin zone:

$$-\frac{\pi}{a} < p_\mu \leq \frac{\pi}{a}. \tag{5.12}$$

Applying the inverse Fourier transform

$$\psi(x) = \frac{1}{a^4L^3T}\sum_{l_\mu} e^{ipx}\tilde{\psi}(p), \tag{5.13}$$

we find the UV cut-off

$$|p_\mu| \leq \frac{\pi}{a}. \tag{5.14}$$

Thus, QCD on the lattice is automatically regularised since the inverse of the lattice spacing acts as a cut-off and a UV regulator. Furthermore, the finite volume restricts momentum modes to be quantised and therefore introduces an infrared (IR) regulator. All functional integrals are now both regularised and finite. Real, continuous physics in infinite spacetime is then recovered in the limit of infinite volume ($L, T \to \infty$) and where the cut-off is taken to infinity $a^{-1} \to \infty$, i.e. $a \to 0$. Typically the *continuum limit* $a \to 0$ is non-trivial and understanding how to safely and appropriately take this limit is a critical component of extracting hadronic observables correctly.

5.1.1 Discretising the QCD Lagrangian

Starting with the QCD Lagrangian written in equation (2.30), we can write the regular QCD action ($S = \int d^4x\, \mathcal{L}$) as

$$\begin{aligned} S_{\text{QCD}} &= \int d^4x \left(-\frac{1}{4} G^a_{\mu\nu}(x) G^{a\mu\nu}(x) + \sum_f \bar{\psi}_{f,\alpha}(x)(i\not{D}_{\alpha\beta} - m_f \delta_{\alpha\beta})\psi_{f,\beta}(x) \right) \\ &= S_G[A] + S_F[A, \psi_f, \bar{\psi}_f], \end{aligned} \tag{5.15}$$

where we separate the action into the pure gauge action S_G and the fermion action S_F.

Next, we must require that the gauge transformations ensuring gauge invariance in the continuum theory also hold in the discretised theory. We start by choosing an element of the SU(3) group $\Omega(x)$ at each lattice site x. The fermion fields will then transform as

$$\begin{aligned} \psi(x) &\to \psi'(x) = \Omega(x)\psi(x) \\ \bar{\psi}(x) &\to \bar{\psi}'(x) = \bar{\psi}(x)\Omega^\dagger(x). \end{aligned} \tag{5.16}$$

This will not however remain gauge invariant due to the discretised kinetic term $\bar{\psi}\gamma^\mu D_\mu \psi$, which will introduce terms with fields at different sites, e.g.

$$\bar{\psi}(x)\psi(x + a\hat{\mu}) \to \bar{\psi}(x)\Omega^\dagger(x)\Omega(x + a\hat{\mu})\psi(x + \hat{\mu}). \tag{5.17}$$

To maintain gauge invariance, we introduce a new quantity $U_\mu(x)$ which transforms as

$$U_\mu(x) \to U'_\mu(x) = \Omega(x)U_\mu(x)\Omega^\dagger(x + a\hat{\mu}). \tag{5.18}$$

This is the *link variable* which describes the path connecting the lattice site x to $x + a\hat{\mu}$ where $\hat{\mu}$ is the unit vector in the $\mu \in \{x, y, z, t\}$ direction; see figure 5.2. Now the terms which would previously break gauge invariance such as $\bar{\psi}(x)U_\mu(x)\psi(x + a\hat{\mu})$ are gauge invariant. We can relate the link variables $U_\mu(x)$ to the discretised Lie algebra-valued

gauge fields $A^a_\mu(x)$ as

$$U_\mu(x) \equiv \exp\left\{ig_s a A^a_\mu(x) T_a\right\}, \tag{5.19}$$

for T^a the gauge group generators and g_s the bare coupling constant. In the discretised theory, we treat these Lie algebra-valued fields $A^a_\mu(x)$ as the fundamental degrees of freedom. From here, we can properly define the discretised fermion action S_F, replacing the integral in equation (5.15) with a sum over all lattice sites. Assuming only one fermion flavour to remove the additional sum for now,

$$\begin{aligned} S_F[U,\psi,\bar{\psi}] &= a^4 \sum_{x,y\in\Lambda} \bar{\psi}_\alpha(x) D_{\alpha\beta}(x,y)\psi_\beta(y) \\ &= a^4 \sum_{x\in\Lambda} \bar{\psi}_\alpha(x) \left(\sum_\mu \gamma_{\mu,\alpha\beta} \frac{U_\mu(x)\psi_\beta(x+a\hat{\mu}) - U^\dagger_\mu(x-a\hat{\mu})\psi_\beta(x-a\hat{\mu})}{2a} + m\psi_\beta(x) \right), \end{aligned} \tag{5.20}$$

where Einstein summation convention is **not** used, the Euclidean gamma matrices are used (see appendix A.2), and note that in Euclidean space upper and lower indices are equivalent. In equation (5.20), we used the Dirac operator connecting lattice sites x and y defined as

$$D(x,y)_{\alpha\beta} = \sum_\mu \gamma_{\mu,\alpha\beta} \frac{U_\mu(x)\delta_{x+a\hat{\mu},y} - U_{-\mu}(x)\delta_{x-a\hat{\mu},y}}{2a} + m\delta_{\alpha\beta}\delta_{xy}, \tag{5.21}$$

where we suppress colour indices, and define

$$U_{-\mu}(x) = U^\dagger_\mu(x - a\hat{\mu}). \tag{5.22}$$

This is defined such that each lattice site only stores the link variables in the positive μ directions; other conventions are possible, but less common. We will find that the above Dirac operator is not unique and only the naive choice – it it thus called the *naive Dirac operator*. We will see in section 5.1.3 that the naive Dirac operator actually leads to 16 *doublers* instead of a single fermion, and so we look to other formulations of the Dirac operator without these unwanted doublers. As long as our choice correctly reduces to equation (5.15) in the continuum limit $a \to 0$, we are free to choose different formulations in the discretised theory, and in fact, different formulations can approach the continuum differently with different advantages in the discrete setup.

We now turn to the pure gauge sector of the QCD action, S_G. After defining the link variables $U_\mu(x)$, it is clear that the discretised version of S_G should be constructed from these link variables; as mentioned above for the fermion action, we are also free to choose how we define QCD on the lattice so long as it reduces to the correct continuum action and is gauge invariant. Recall that the link variables $U_\mu(x)$ define the path from lattice site x to $x + a\hat{\mu}$ for the unit vector $\hat{\mu}$ in direction $\mu \in \{x, y, z, t\}$. To define a gauge

invariant gauge action, we can make use of the gauge transformation rules for $U_\mu(x)$. Extending equation (5.18) along multiple links, e.g. for two link variables

$$\begin{aligned} U_\mu(x)U_\nu(x+a\hat{\mu}) &\to \Omega(x)U_\mu(x)\Omega^\dagger(x+a\hat{\mu})\Omega(x+a\hat{\mu})U_\nu(x+a\hat{\mu})\Omega^\dagger(x+a\hat{\mu}+a\hat{\nu}) \\ &\to \Omega(x)U_\mu(x)U_\nu(x+a\hat{\mu})\Omega^\dagger(x+a\hat{\mu}+a\hat{\nu}), \end{aligned} \tag{5.23}$$

one can see that the intermediate Ω all cancel and only the first Ω on the left and last $\Omega^\dagger$ on the right remain. From this, it can be seen that if one draws out a closed path on the lattice, e.g.

$$\Omega(x)U_\mu(x)U_\nu(x+a\hat{\mu})\dots U_{-\nu}(x+a\hat{\nu})U_\mu(x-a\hat{\mu})\Omega^\dagger(x), \tag{5.24}$$

that the trace of this closed loop will be gauge invariant due to cyclicity. These are known as *Wilson loops* [40]. It is then possible to construct a gauge-invariant action for the gauge sector of lattice QCD using traces of these Wilson loops.
The smallest Wilson loop on the lattice is the *plaquette* (shown in figure 5.3(a)), defined

$$P_{\mu\nu}(x) = U_\mu(x)U_\nu(x+a\hat{\mu})U_\mu^\dagger(x+a\hat{\nu})U_\nu^\dagger(x). \tag{5.25}$$

From this, the Wilson (plaquette) gauge action [40] can be defined as

$$S_W = \frac{2}{g_s^2}\sum_{x\in\Lambda}\sum_{\mu<\nu}\mathrm{Re}[\mathrm{Tr}(1-P_{\mu\nu}(x))]. \tag{5.26}$$

By replacing the link variables with the gauge fields A_μ and performing a Taylor expansion, one can see how this replicates the continuum action, i.e.

$$S_W = \frac{a^4}{2g_s^2}\sum_x\sum_{\mu,\nu}\mathrm{Tr}(G_{\mu\nu}(x)G_{\mu\nu}(x)) + O(a^2), \tag{5.27}$$

so the continuum action is replicated by the lattice Wilson action, up to order a^2 discretisation effects. This is therefore a perfectly valid lattice description of the gauge action, although the understanding of the additional discretisation effects at non-zero lattice spacing is important to understand how to appropriately take the continuum limit and recover the QCD gauge action.

Other choices of lattice gauge action may be preferred to obtain e.g. improved discretisation effects. Other lattice gauge actions are typically derived from modifying the Wilson action and adding additional terms based on more complex Wilson loops than the plaquette. There exists a procedure to systematically improve the discretisation errors from a lattice action by cancelling the error terms for lower powers of a – the *Symanzik improvement program* [355–357]. Examples of gauge observables added to

actions in the Symanzik improvement program are shown in figure 5.3. An example of a commonly-used improved gauge action is the tree-level improved Symanzik action [358, 359]. Another improved gauge action which is used in the lattice ensembles considered in this thesis is the Iwasaki gauge action [360, 361], which is based on the idea of renormalisation group transformations, and reads

$$S_I = -\frac{\beta}{3}\left[(1-8c_1)\sum \mathrm{Tr}(\text{plaquette loop}) + c_1 \sum \mathrm{Tr}(\text{rectangle loop})\right], \tag{5.28}$$

with $c_1 = -0.331$ from perturbation theory [362]. The Iwasaki gauge action is chosen because it has an $O(a^2)$-improved discretisation error, and allows for a small m_{res} parameter in the Domain-Wall fermion action (to be discussed below) favoured by the RBC/UKQCD collaboration who generated the ensembles considered here [363–366].

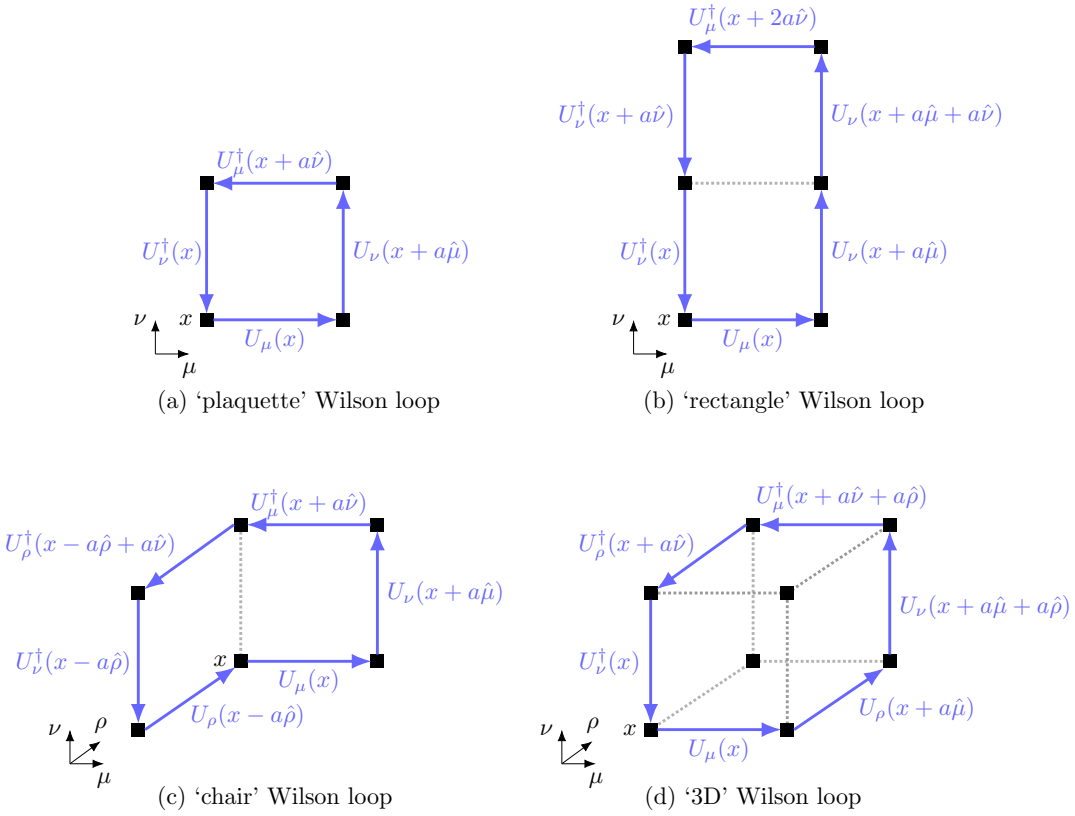

FIGURE 5.3: Examples of four different Wilson loops used in the definition of various gauge actions, defined starting from lattice site x and directions $\mu, \nu, \rho \in \{x, y, z, t\}$.

5.1.2 Monte Carlo Integration

We have already mentioned that discretising our path integral and Wick rotating to Euclidean space will allow for numerical evaluations of the integral via Monte Carlo methods. Here we give a brief introduction to Monte Carlo integration with Markov

Chains. In equation (5.5), we replaced the exact definition of the Euclidean n-point correlation function $\langle \mathcal{O}_1 \dots \mathcal{O}_n \rangle_E$ with its *sample mean*. We see that the uncertainty that the sample mean approaches the exact mean scales as $O(1/\sqrt{N})$. Naively one might think this sounds like poor scaling, however this turns out to be a very good scaling behaviour for the integrals considered in lattice QCD. For low-dimensional integrals, $O(1/\sqrt{N})$ can be argued to be a poor scaling, however the fact is that Monte Carlo integration *always* scales $O(1/\sqrt{N})$ and this is excellent for lattice QCD; for the very high-dimensional integrals needing evaluated, other common methods scale with some exponent proportional to the dimensionality of the problem, e.g. $O(N^{-2/d})$, and therefore the uncertainties involved for lattice integrals would be huge.

Recall that the Euclidean path integral has a Boltzmann factor $\exp(-S_E)$ multiplying the observable $\mathcal{O}_1 \dots \mathcal{O}_n$. This gives a *weight* to every sampled point in the Monte Carlo sum such that different gauge field configurations in the Monte Carlo chain have a different importance to the overall sample mean. While selecting from a uniform probability distribution will converge on an accurate estimation for the sample mean given this weighted importance of the different contributions, we can in fact use this Boltzmann factor to reshape the random-number generator into sampling from a non-uniform probability such that it is more biased towards the higher-weighted contributions to the sample mean and we will converge more quickly on a suitable estimate; this is known as *importance sampling*.

Importance Sampling

The expectation value of a function $f(x)$ for a probability distribution $\rho(x)$ is given by

$$\langle f \rangle_\rho = \frac{\int_a^b dx\ \rho(x)\, f(x)}{\int_a^b dx\ \rho(x)}. \tag{5.29}$$

Monte Carlo integration approximates this relation using the sample mean, i.e.

$$\langle f \rangle_\rho = \lim_{N\to\infty} \frac{1}{N} \sum_{n=1}^{N} f(x_n), \tag{5.30}$$

where we can re-parameterise the integral measure as a normalised probability density,

$$dP(x) = \frac{dx\, \rho(x)}{\int_a^b dx\, \rho(x)}, \tag{5.31}$$

and randomly sample the $x_n \in (a, b)$ from this distribution. Equating this language to the definition of the sample mean for some n-point function in equation (5.5), we can find the probability distribution from which the gauge field configurations U_i must be

sampled as

$$dP(U) = \frac{e^{-S_G[U]}\mathcal{D}[U]}{\int \mathcal{D}[U]e^{-S_G[U]}}. \tag{5.32}$$

This is known as the *Gibbs measure*. Thus in our Monte Carlo integration of the lattice QCD path integral, the gauge configurations U_n are generated such that they take the place of the random numbers drawn from the distribution defined by the Gibbs measure and we sample N configurations in order to get an uncertainty $O(1/\sqrt{N})$ in our sample mean.

Markov Chains

The idea of a Markov chain in the Monte Carlo integration is to start with some arbitrary gauge field configuration and stochastically move through a sequence of configurations which should progressively approach the target distribution,

$$U_0 \to U_1 \to U_2 \to U_3 \to \cdots \tag{5.33}$$

Here, the index n of this sequence of configurations represents the position of the U_n along the chain and can be referred to as the *Monte Carlo time* τ (entirely independent of and not to be confused with the Euclidean time). Markov chain progression is 'memory-less', i.e. the probability of choosing any particular field configuration as the next step in the chain only depends on the current configuration and the proposed next configuration[3]. We can then construct the transition probability between successive steps such that the Markov chain will be guided from any arbitrary initial configuration towards the configurations with the highest weight in the Boltzmann factor – the *equilibrium state*.

Markov chains are therefore characterised by the conditional probability to transition to configuration U' from configuration U,

$$P(U_n = U'|U_{n-1} = U) = T(U'|U). \tag{5.34}$$

One can see that indeed this depends on the specific states U and U' but not the position n along the Monte Carlo time. The transition probability obeys

$$0 \leq T(U'|U) \leq 1 \qquad\qquad \sum_{U'} T(U'|U) = 1, \tag{5.35}$$

i.e. the probability of any transition probability lies between 0 and 1, and the sum of transition amplitudes from state U to all states U' (including $U' = U$) is 1. It is also required that in the equilibrium state, there is no preference of direction for the Markov chain progression, so the probability of taking any particular transition step must be

[3]There will however be autocorrelations between configurations over multiple MC time steps.

equal to reversing that same step. This requirement gives us the *balance equation*:

$$\sum_{U} T(U'|U)P(U) = \sum_{U'} T(U|U')P(U'), \tag{5.36}$$

where the left-hand side is the total probability to transition into state U' and the right-hand side is the total probability to leave state U'. Using the normalisation condition in equation (5.35), we find

$$\sum_{U} T(U'|U)P(U) = P(U'). \tag{5.37}$$

This shows that the equilibrium state is a fixed point of the system, and the Markov chain will gradually evolve towards it as more transition steps are applied. Once it reaches this equilibrium state, it will stay near to this state even when the transition probability is applied, with small, random fluctuations around this point.

In order to correctly reach the equilibrium state, all points in the allowed configuration space need to be accessible by the Markov chain, i.e. the transition probability $T(U'|U)$ must be positive for all U, U'. This is know as *strong ergodicity* and it is always an important check for simulations to obey this. From this, we can formulate our Markov chain such that the balance equation holds term-by-term, i.e.

$$T(U'|U)P(U) = T(U|U')P(U'), \tag{5.38}$$

which is known as the *detailed balance condition*. Most lattice calculations make use of the detailed balance condition, which implies that an initial *thermalisation* period must be allowed in the Monte Carlo procedure where early configurations in the Markov Chain are not used to calculate the sample mean of observables. This ensures that the Markov Chain has had suitable time to converge on the equilibrium state and fluctuations are only small, thus increasing the reliability of our estimate.

The Metropolis Algorithm

For the above use of Markov chains, some rule is required in order to generate the transition probabilities $T(U'|U)$. One such algorithm used in almost all *exact* Monte Carlo algorithms is the 'Metropolis' or 'Metropolis-Hastings' algorithm [367, 368]. The steps of this algorithm are:

1. Choose a candidate U' for the next configuration U_n according to a selection probability $T_0(U'|U)$ where $U = U_{n-1}$ is the current gauge configuration;

2. Calculate the acceptance probability

$$T_A(U'|U) = \min\left\{1\,,\,\frac{T_0(U|U')\exp\left(-S[U]\right)}{T_0(U'|U)\exp\left(-S[U']\right)}\right\}. \tag{5.39}$$

   Generate a random number η uniformly distributed in $[0,1)$; if $\eta < T_A(U'|U)$, accept U' as U_n. If the suggested update to U' is not accepted, keep U, i.e. $U_n = U_{n-1}$ such that U is used to sample the observable again.

3. Repeat the steps.

By choosing symmetric selection probabilities $T_0(U|U') = T_0(U'|U)$, we can simplify the acceptance probability to

$$T_A(U'|U) = \min\left\{1\,,\,\exp\left(-\Delta S\right)\right\} \text{ for } \Delta S = S[U'] - S[U], \tag{5.40}$$

such that only the change in the action ΔS is needed to accept or reject the candidate configuration.

Hybrid Monte Carlo

Recall the Gibbs measure as defined in equation (5.32). This is highly local, i.e. simply a few gauge links can be independently updated in the Monte Carlo step to create the new Wilson loop. However, as we will see with the Haar measure in equation (5.50), introducing dynamical fermions into the sea introduces the Dirac operator into the measure. Due to the nature of the Dirac operator, this will become highly non-local and performing an update step will affect all gauge links. Naively, this will lead to very large differences in the gauge configuration between update steps, which will significantly decrease the acceptance probability of the candidate configurations. Having low acceptance probabilities results in very poor efficiency of the algorithm since very many update configurations will be generated before one is accepted into the Markov chain.

The *Hybrid Monte Carlo* (HMC) algorithm [369] (also mislabelled as *Hamiltonian Monte Carlo*) is one algorithm used to overcome this issue in ensemble generation, belonging to a family of algorithms using *Molecular Dynamics* (MD) methods. The gauge field configuration at a given update step is a field of coordinates. Following from Hamiltonian mechanics, we can define a conjugate field of momenta generated from a Gaussian distribution. For coordinates Q and conjugate momenta P, we can write a Hamiltonian of our gauge configuration as

$$H[Q,P] = \frac{1}{2}P^2 + S[Q]. \tag{5.41}$$

From a Hamiltonian description, we can of course write down the equations of motion for our system, where we define the time evolution through the Monte Carlo time τ:

$$\dot{P} = -\frac{\partial H}{\partial Q} = \frac{\partial S}{\partial Q}, \qquad \dot{Q} = \frac{\partial H}{\partial P} = P. \tag{5.42}$$

These equations can be solved numerically by evolving over n time steps $\epsilon = \Delta\tau$, such that we have a deterministic evolution of the system – the evolution is referred to as a 'trajectory'. Due to the finite step size, we do introduce numerical errors into this evolution, which would divert the update steps from the correct 'continuous' trajectory. We correct for this by introducing a Metropolis check for the transition probability of an evolution step, i.e.

$$T(Q', P'|Q, P) = \min\left\{1, \frac{\exp(-H[Q', P'])}{\exp(-H[Q, P])}\right\}. \tag{5.43}$$

As long as we require that Q obeys SU(3) symmetry, then the HMC equations of motion can be expressed in terms of the gauge and fermion fields, and thus the algorithm will generate gauge field configurations in a more efficient way than before.

5.1.3 Fermions on the Lattice

We will now discuss in further details adding fermion fields to our lattice theory and how these can be discretised. First, we will remind ourselves of the full lattice QCD path integral for an observable $\mathcal{O}$. In equation (5.15), we separated the action into a pure gauge part and a fermionic part. Propagating this separation into the path integral yields

$$\langle\mathcal{O}\rangle = \frac{1}{Z}\int \mathcal{D}[\psi,\bar{\psi}]\mathcal{D}[U]e^{-S_F[U,\psi,\bar{\psi}]}e^{-S_G[U]}\mathcal{O}[U,\psi,\bar{\psi}], \tag{5.44}$$

with the partition function

$$Z = \int \mathcal{D}[U,\psi,\bar{\psi}]\mathcal{D}[U]e^{-S_F[U,\psi,\bar{\psi}]}e^{-S_G[U]} \tag{5.45}$$

and the fermion action

$$S_F[U,\psi,\bar{\psi}] = a^4 \sum_{x,y\in\Lambda} \bar{\psi}_\alpha(x) D_{\alpha\beta}(x,y)\psi_\beta(y) \tag{5.46}$$

for the Dirac operator $D_{\alpha\beta}(x,y)$. Factorising this further, the fermionic path integral is given by

$$\langle\mathcal{O}\rangle_F = \frac{1}{Z_F[U,\psi,\bar{\psi}]}\int \mathcal{D}[\psi,\bar{\psi}]e^{-S_F[U,\psi,\bar{\psi}]}\mathcal{O}[U,\psi,\bar{\psi}], \tag{5.47}$$

with the fermionic partition function

$$Z_F[U,\psi,\bar{\psi}] = \int \mathcal{D}[\psi,\bar{\psi}] e^{-S_F[U,\psi,\bar{\psi}]}. \tag{5.48}$$

The defining behaviour of fermions is that they obey *Fermi statistics*, i.e. they anticommute:

$$\psi^a_{f_1,\alpha}(x)\,\psi^b_{f_2,\beta}(y) = -\psi^b_{f_2,\beta}(y)\,\psi^a_{f_1,\alpha}(x), \tag{5.49}$$

for flavour indices f_1, f_2, colour indices a, b, and Dirac indices α, β. Antifermions also anticommute with one another and fermions and antifermions also anticommute. Therefore to evaluate the fermionic path integral, we will find that the integral measure $\mathcal{D}[\psi,\bar{\psi}]$ is a function of anticommuting numbers, known as *Grassmann variables*. Through expressing the measure via these Grassmann variables, we can then make use of Wick's theorem [370] to integrate out the fermion fields, rewriting the path integral such that the fermions only enter through the determinant of the Dirac operator D_f, i.e.

$$\langle \mathcal{O} \rangle = \frac{\int \mathcal{D}[U] e^{-S_G[U]} \prod_f \det[D_f] \mathcal{O}[U, D_f^{-1}]}{\int \mathcal{D}[U] e^{-S_G[U]} \prod_f \det[D_f]}. \tag{5.50}$$

The integration measure $\mathcal{D}[U]$ left is the *Haar measure*, which defines the path integral over the gauge links and allows us integrate while maintaining gauge invariance. A summary of Grassmann variables and Wick's theorem is given in appendix A.3, or see e.g. [351].

Naive Fermions

In equation (5.21), we defined what we called the naive Dirac operator. For a free fermion ($U_\mu(x) = \mathbb{1}$), we can compute the Fourier transform of the naive Dirac operator and find

$$\begin{aligned}
\tilde{D}(p,q) &= \frac{1}{|\Lambda|} \sum_{n,m\in\Lambda} e^{-ip\cdot an} D(an, am) e^{iq\cdot am} \\
&= \frac{1}{|\Lambda|} \sum_{n,m\in\Lambda} e^{-i(p-q)\cdot an} \left(\sum_\mu \gamma_\mu \frac{e^{iq_\mu a} - e^{-iq_\mu a}}{2a} + m\mathbb{1} \right) \\
&= \delta(p-q)\tilde{D}(p),
\end{aligned} \tag{5.51}$$

where $|\Lambda| = L^3 \times T$ is the number of lattice sites and

$$\tilde{D}(p) = m\mathbb{1} + \frac{i}{a} \sum_\mu \gamma_\mu \sin a p_\mu. \tag{5.52}$$

In the momentum basis (p, q), the Dirac operator is diagonal in the momenta. Thus, in order to compute the inverse Dirac operator in position space $D^{-1}(an, am)$, it should be easier to compute $\tilde{D}^{-1}(p)$ and then perform the inverse Fourier transform. The inverse

Dirac operator in momentum space is given by

$$\tilde{D}^{-1}(p) = \frac{m\mathbb{1} - ia^{-1}\sum_\mu \gamma_\mu \sin(ap_\mu)}{m^2 + a^{-2}\sum_\mu \sin^2(ap_\mu)}, \tag{5.53}$$

and the inverse Fourier transform then reads

$$D^{-1}(an, am) = \frac{1}{|\Lambda|}\sum_{p\in\tilde{\Lambda}} \tilde{D}^{-1}(p)e^{ipa(n-m)}, \tag{5.54}$$

where one of the momentum sums from equation (5.51) is absorbed by the Dirac delta $\delta(p-q)$. The inverse of the Dirac operator $D^{-1}(an, am)$ is referred to as the *quark propagator*, which will be necessary for computing n-point correlation functions following Wick's theorem. To investigate the properties of the quark propagator, we can consider the case of a massless free fermion ($m = 0$) in momentum space:

$$\tilde{D}^{-1}(p)\Big|_{m=0} = \frac{-ia^{-1}\sum_\mu \gamma_\mu \sin(ap_\mu)}{a^{-2}\sum_\mu \sin^2(ap_\mu)} \overset{a\to 0}{\Longrightarrow} \frac{-i\sum_\mu \gamma_\mu p_\mu}{p^2}. \tag{5.55}$$

Taking the naive continuum limit $a \to 0$, we see that the propagator has a pole at $p = (0,0,0,0)$, corresponding to a single fermion, as expected from the continuum theory. However, on the lattice, this expectation is not the only case. We find poles in the lattice theory whenever $\sin^2(ap_\mu) = 0$, which due to periodicity occurs whenever $p_\mu = 0, \frac{\pi}{a}$. Therefore, we find $2^{D=4} = 16$ poles when

$$p = (0,0,0,0),\ \left(\frac{\pi}{a},0,0,0\right),\ \left(0,\frac{\pi}{a},0,0\right),\ \ldots,\ \left(\frac{\pi}{a},\frac{\pi}{a},\frac{\pi}{a},\frac{\pi}{a}\right), \tag{5.56}$$

and thus the naive Dirac operator gives rise to 15 unwanted additional fermions – these are known as *doublers*. We need some different formulation of the lattice Dirac operator in order to remove these unwanted doublers.

Wilson Fermions

Since we only require that the lattice description matches the continuum theory in the limit $a \to 0$, we are free to add additional terms to our discrete theory which vanish in the continuum limit, but can have an important impact at non-zero lattice spacing. Wilson was the first to propose a method of removing these unwanted fermion doublers by adding an additional term to the Dirac operator [40]. The Wilson Dirac operator in momentum space reads

$$\tilde{D}_W(p) = m\mathbb{1} - \frac{i}{a}\sum_\mu \gamma_\mu \sin(ap_\mu) + \frac{\mathbb{1}}{a}\sum_\mu (1 - \cos(ap_\mu)). \tag{5.57}$$

For the pole at $p_\mu = 0$, this additional term does not change the propagator, leaving the physical fermion intact. However, for the additional poles with $p_\mu = \frac{\pi}{a}$, an extra contribution $\propto \frac{2}{a}$ is added which acts like an additional mass. It is clear that in the continuum limit $a \to 0$, this term will cause these unwanted doublers to become infinitely heavy and will thus decouple from the physical spectrum. Performing a Fourier transform back to position space, the Wilson Dirac operator reads

$$\begin{aligned} D_W(x,y)_{\alpha\beta} = & \sum_\mu \gamma_{\mu,\alpha\beta} \frac{U_\mu(x)\delta_{x+a\hat{\mu},y} - U_{-\mu}(x)\delta_{x-a\hat{\mu},y}}{2a} + m\delta_{\alpha\beta}\delta_{xy} \\ & - \sum_\mu \frac{U_\mu(x)\delta_{x+a\hat{\mu},y} - 2\delta_{xy}\delta_{\alpha\beta} + U_{-\mu}(x)\delta_{x-a\hat{\mu},y}}{2a} \\ = & \left(m + \frac{4}{a}\right)\delta_{xy}\delta_{\alpha\beta} - \frac{1}{2a}\sum_{\mu=\pm1}^{\pm4} (\mathbb{1} - \gamma_\mu)_{\alpha\beta} U_\mu(x)\delta_{x+a\hat{\mu},y}. \end{aligned} \tag{5.58}$$

We now have a lattice description of the Dirac operator without unwanted additional fermion propagators arising from the finite volume. However, the Wilson fermion description comes at the expense of chiral symmetry. Spontaneous chiral symmetry breaking is an important feature in the phenomenology of QCD, generating the low masses of pseudoscalar mesons as pseudo-Nambu-Goldstone bosons, and so replicating this in the discrete theory is clearly sought after as well. This is not actually a problem in principle though, since the chiral symmetry of QCD and its spontaneous breaking can be recovered in the continuum limit. However it does result in other problems on the lattice, such as unwanted additional operator mixing in renormalisation procedures. So, Wilson fermions are a possible choice to solve the doubler problem, however they come with their own disadvantages which may be improved upon using another formulation of the Dirac operator.

Clover Actions

One of the caveats of using Wilson fermions was the $O(a)$ discretisation errors. The Symanzik improvement program was applied to the Wilson action by Sheikholeslami and Wohlert [371], from which they found the discretisaton error can be improved to $O(a^2)$ by adding a single term:

$$S_{\text{Clover}} = S_W + a^4 \sum_{x\in\Lambda} \bar{\psi}(x)\, c_{sw} \sum_{\mu<\nu} \frac{i}{4}\sigma_{\mu\nu}\hat{G}_{\mu\nu}\psi(x), \tag{5.59}$$

where c_{sw} is a coefficient which must be non-perturbatively tuned to appropriately improve the discretisation error, $\sigma_{\mu\nu}$ is the commutator of two Dirac matrices (see appendix A.2) and $\hat{G}_{\mu\nu}$ is the discretised field strength tensor. The field strength can be expressed on the lattice through the *clover operator* (shown in figure 5.4) which is the

sum of the 4 plaquettes in a 2D plane of the lattice around lattice site x, i.e.

$$\hat{G}_{\mu\nu} = \frac{i}{8a^2}(C_{\mu\nu}(x) - C_{\nu\mu}(x)), \tag{5.60}$$

$$C_{\mu\nu}(x) = P_{\mu\nu}(x) + P_{\nu,-\mu}(x) + P_{-\mu,-\nu}(x) + P_{-\nu,\mu}(x), \tag{5.61}$$

where the plaquette is defined in equation (5.25) and negative indices on gauge links are expressed through equation (5.22). Heavy quarks such as charm and in particular

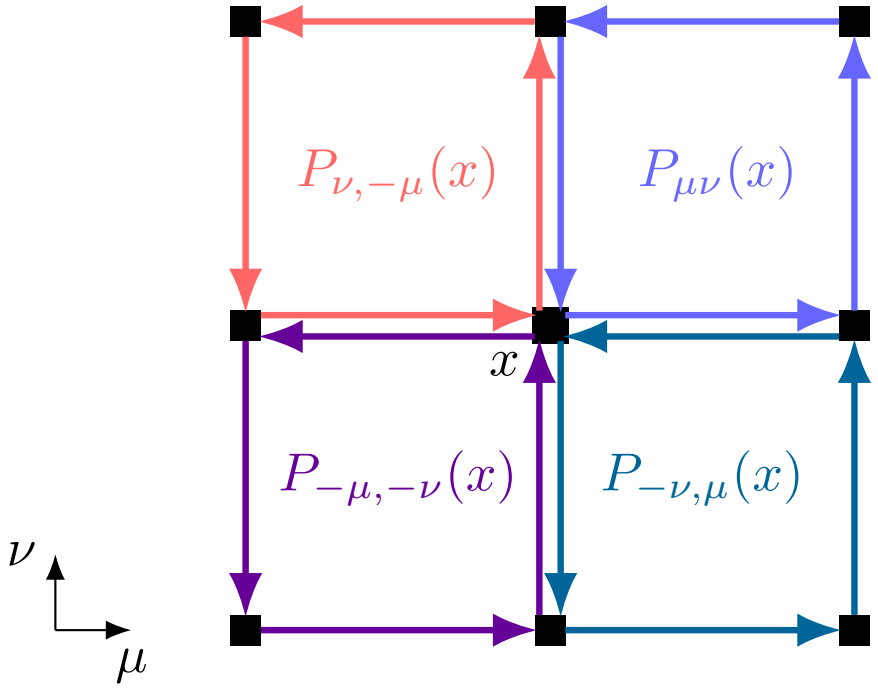

FIGURE 5.4: The clover operator used in the definition of the discretised field strength tensor $\hat{G}_{\mu\nu}$. It is the sum of the 4 plaquettes in a 2D plane (μ, ν) around lattice site x.

bottom present additional challenges to simulate on the lattice compared to light quarks. A common method for tackling the challenge of simulating heavy quarks involves an effective action based on an anisotropic version of the Sheikholeslami-Wohlert (or clover) action. The inclusion of the clover term, as well as other Symanzik-type improvements, helps reduce some of the otherwise uncontrolled errors. The Relativistic Heavy Quark (RHQ) action is based on the Fermilab action [372] using the same principles, and has been parameterised both in the Tsukuba [373] and Columbia [374] formulations. The RHQ action reads

$$S_{RHQ} = a^4 \sum_{x,y\in\Lambda} \bar{\psi}(x) \left[m_0 + \gamma_0 D_0 + \zeta \vec{\gamma}\cdot\vec{D} - \frac{a}{2}(D^0)^2 - \frac{a}{2}\zeta\vec{D}^2 + \frac{ia}{4}c_P \sum_{\mu<\nu} \sigma_{\mu\nu}\hat{G}_{\mu\nu} \right] \psi(y), \tag{5.62}$$

where ζ, c_P, and am_0 are the three parameters which must be non-perturbatively tuned. We will discuss heavy quarks on the lattice, the benefits and drawbacks of the RHQ action, and our strategy for simulating heavy quarks in more detail in section 5.1.6.

The Nielson-Ninomiya Theorem

The Nielson-Ninomiya theorem [375] is a no-go theorem which states that it is impossible to construct a local action for fermions on the lattice that is free of doublers while preserving chiral symmetry in an even number of Euclidean spacetime dimensions. Explicitly, the following conditions cannot all be satisfied simultaneously:

- Locality: $D(x-y) \lesssim \exp\{-\gamma|x-y|\}$. This implies that the momentum space Dirac operator $\tilde{D}$ is an analytic and periodic function of the momentum p_μ with period $2\pi/a$.
- Continuum limit: $\lim_{a\to 0} \tilde{D}(p) = \sum_\mu \gamma^\mu p_\mu$. The Dirac operator must be of a form such that it recovers the correct continuum behaviour in the continuum limit.
- No doublers: $\tilde{D}(p)$ is invertible if $p_\mu \neq 0$. A single propagator with pole at $p_\mu = 0$ is recovered from the Dirac operator, and no additional doublers appear.
- Chiral symmetry: $\{D, \gamma_5\} = 0$. The (continuum) condition for chirality is that the position space Dirac operator D anticommutes with γ_5.

We have already seen some lattice descriptions of fermions which clearly sacrifice one of these conditions. Naive fermions have doublers present in the theory, while Wilson (and Wilson-clover) fermions remove the doublers but give up chiral symmetry. *Staggered* (*Kogut-Susskind*) fermions [376] have one staggered fermion field describing four degenerate *tastes* of Dirac fermion. *Twisted mass* fermions [377] form an isospin doublet of Wilson fermions and therefore also give up chiral symmetry.

There exists however a modification to the continuum description of chiral symmetry $\{D, \gamma_5\} = 0$ in the discrete theory. The *Ginsparg-Wilson relation* [378] reads

$$D(x|y)\gamma_5 + \gamma_5 D(x|y) = aD(x|z)\gamma_5 D(z|y), \tag{5.63}$$

which can be written equivalently as

$$\gamma_5 D^{-1}(x|y) + D^{-1}(x|y)\gamma_5 = a\gamma_5 \delta(x-y). \tag{5.64}$$

This tells us that for $x \neq y$ we recover the continuum condition for chiral fermions, but for $x = y$ we will find a contact term.

In the continuum, chiral symmetry corresponds to the field rotations

$$\psi \to e^{i\alpha\gamma_5}\psi, \qquad \bar{\psi} \to \bar{\psi}e^{i\alpha\gamma_5}. \tag{5.65}$$

Now we can introduce modified chiral rotations for the lattice description which recover equation (5.65) in the continuum limit:

$$\psi \to e^{i\alpha\gamma_5(\mathbb{1}-\frac{a}{2}D)}\psi, \qquad \bar{\psi} \to \bar{\psi}e^{i\alpha(\mathbb{1}-\frac{a}{2}D)\gamma_5}. \tag{5.66}$$

This allows us to introduce generalised chiral projectors through the definitions

$$\hat{\gamma}_5 = \gamma_5(\mathbb{1} - aD), \qquad \hat{P}_R = \frac{1+\hat{\gamma}_5}{2}, \qquad \hat{P}_L = \frac{1-\hat{\gamma}_5}{2}. \tag{5.67}$$

Then, like in the continuum, we can separate the fermion spinor into left-handed and right-handed components, i.e.

$$\psi_{L,R} = \hat{P}_{L,R}\psi, \qquad \bar{\psi}_{L,R} = \bar{\psi}\hat{P}_{R,L}. \tag{5.68}$$

Now just like in the continuum, the massless part of the action does not mix chiralities while the mass term does:

$$\begin{gathered} \bar{\psi}D\psi = \bar{\psi}_L D\psi_L + \bar{\psi}_R D\psi_R, \\ m(\bar{\psi}_R\psi_L + \bar{\psi}_L\psi_R) = m\bar{\psi}(P_L\hat{P}_L + P_R\hat{P}_R)\psi = m\bar{\psi}\left(\mathbb{1} - \frac{a}{2}D\right)\psi. \end{gathered} \tag{5.69}$$

Note that the concept of chiral symmetry is clearly different between the continuum and the lattice. In the continuum, chiral symmetry is a strictly local concept, only concerned with the fermion spinor at a given spacetime coordinate and completely independent of the gauge field. However, on the lattice, chiral rotations involve the Dirac operator, which in the discrete formulation involves neighbouring lattice sites and is therefore dependent on the gauge field (links) to connect the sites.

There are two common fermion descriptions which make use of the Ginsparg-Wilson relation. There are the *domain wall* fermions (DWF) [379–383] which live in 5 dimensions (with a fifth dimension of coordinate s and extent L_s) and approximate the Ginsparg-Wilson relation (it is recovered exactly in the limit $L_s \to \infty$). Secondly, there are *overlap* fermions [384, 385]. Overlap fermions and DWF are shown to be equivalent in the $L_s \to \infty$ limit [386, 387].

Domain Wall Fermions

We consider a five-dimensional fermion field $\Psi(x_\mu, s)$ where x_μ is the standard 4D coordinate vector and s is the coordinate of the fifth dimension. The Dirac equation for

this fermion is

$$[\not{D} + \gamma_5 \partial_s + m(s)]\Psi(x_\mu, s) = 0, \tag{5.70}$$

where we assume that the gauge field interacting via the 4D Dirac operator exists only in the standard 4 dimensions, and we have introduced a mass term dependent on the position in the fifth dimension, i.e.

$$m(s) = \begin{cases} +m, & s > 0, \\ -m, & s < 0. \end{cases} \tag{5.71}$$

We can separate this fermion spinor into its chiral components, with additional functional dependence on the fifth dimension, and decompose this into an eigenvalue problem:

$$\Psi(x_\mu, s) = \sum_n \left[a_n(s)P_R + b_n(s)P_L\right] \psi_n(x). \tag{5.72}$$

The 5D Dirac equation then reads

$$[\partial_s + m(s)]\, a_n(s) = \alpha_n b_n(s), \tag{5.73}$$

$$[-\partial_s + m(s)]\, b_n(s) = \alpha_n a_n(s), \tag{5.74}$$

$$\left[\not{D} + \alpha_n\right] \psi_n(x) = 0, \tag{5.75}$$

for eigenvalues α_n. Note that for $\alpha_n = 0$, equation (5.75) is the Dirac equation for a massless fermion. Equations (5.73) and (5.74) decouple in this limit and can be solved exactly:

$$a_n(s) = A \exp\left\{-\int_0^s m(s')\, ds'\right\} = A \exp\left\{-m|s|\right\}, \tag{5.76}$$

$$b_n(s) = B \exp\left\{+\int_0^s m(s')\, ds'\right\} = B \exp\left\{+m|s|\right\}. \tag{5.77}$$

One can see however that equation (5.77) is not normalisable and thus cannot be a physical solution. This excludes normalisable left-handed zero mode fermions from the spectrum, while equation (5.76) gives rise to a single right-handed massless fermion bound to the defect at $|s| = 0$ and prevents further doublers appearing at other parts of the Brillouin zone. Applying this to the lattice changes the results however, since we cannot work in an infinite 5th dimension and instead are limited to some size $L_s = 2s_0$. We assume Dirichlet boundaries in the 5th dimension and also that there are two defects at $s = 0, s_0$. Now, both equations (5.76) and (5.77) are normalisable and there are two chiral modes: the original right-handed fermion bound at $s = 0$ and now also a left-handed fermion bound at $s = \pm s_0$. Assuming L_s is suitably large (but still computationally viable), the overlap of the left- and right-handed fermion fields is

expected to be small since they are defined to be exponentially localised at their defects. Thus, in the discrete theory, there will exist some residual chiral symmetry breaking from this overlap, which contributes to the mass of the fermions – this is parametrised as the *residual mass*. For an input mass m and residual mass m_{res}, the simulated DWF mass m_q will then be

$$m_q = m + m_{res}. \tag{5.78}$$

Now we have a picture of how the 5th dimension can result in (mostly) chiral fermions, we need to formally define the 5-dimensional theory. We extend the set of coordinates Λ defined in equation (5.6) to the 5th dimension (with extent L_s) as

$$\Lambda_5 = \Lambda \times L_s = \{(x_\mu, s)\,,\ \text{for } x_\mu \in \Lambda;\ s \in 0, 1, \ldots, L_s - 1\}\,. \tag{5.79}$$

We write the 5D DWF action for a single flavour of fermion Ψ with mass m as

$$S_{\text{DWF}} = \sum_{(x,s),(y,t)\in\Lambda_5} \bar{\Psi}(x,s) D_{\text{DWF}}(x,s;y,t;m;M_5)\Psi(y,t), \tag{5.80}$$

where we recall that the gauge fields entering the Dirac operator D_{DWF} live in the standard 4D spacetime, and M_5 is the *domain wall height*. In order to remove the bulk infinity appearing for $L_s \to \infty$ (recall equation (5.77)), another term including bosonic Pauli-Villars type fields is included [388], reading

$$S_{PV} = \bar{\Phi}(x,s) D_{\text{DWF}}(x,s;y,t;1)\Phi(y,t). \tag{5.81}$$

Notice that the same Dirac operator D_{DWF} is used, but with input mass $m = 1$. The DWF Dirac operator reads

$$D_{\text{DWF}}(x,s;y,t;m;M_5) = \delta_{st} D_{\text{DWF},4}(x,y,M_5) + \delta_{xy} D_{\text{DWF},5}(s,t,m), \tag{5.82}$$

where $D_{\text{DWF},4}$ is a 4-dimensional Dirac operator, defined

$$D_{\text{DWF},4}(x,y,M_5) = (4 - M_5)\delta_{xy} - \frac{1}{2}\sum_{\mu=\pm1}^{\pm4} (\mathbb{1} - \gamma_\mu)\, U_\mu(x)\delta_{x+\hat{\mu},y}. \tag{5.83}$$

We introduced the parameter M_5 above as the domain wall height, which removes doublers from the action and maintains positivity of the transfer matrix. The second term in the DWF Dirac operator is orthogonal to the usual spacetime dimensions and connects the sites of the fifth dimension, reading

$$\begin{aligned} D_{\text{DWF},5}(s,t,m) = \delta_{st} &- (1 - \delta_{s,L_s-1})P_L\delta_{s+1,t} - (1 - \delta_{s0})P_R\delta_{s-1,t} \\ &+ m(P_L\delta_{s,L_s-1}\delta_{0t} + P_R\delta_{s0}\delta_{L_s-1,t}). \end{aligned} \tag{5.84}$$

Here, surface terms of the fifth dimension have been forbidden. The only term which connects the boundaries at $s = 0$, $L_s - 1$ is proportional to the fermion mass m, and in fact, one can see this term resembles a mass term of the usual 4D theory.

We can now construct the physical fermion fields living in 4 dimensions from the 5D boundary as

$$\begin{aligned} \psi(x) &= P_L \Psi(x, 0) + P_R \Psi(x, L_s - 1), \\ \bar{\psi}(x) &= \bar{\Psi}(x, L_s - 1) P_L + \bar{\Psi}(x, 0) P_R, \end{aligned} \tag{5.85}$$

i.e. the physical 4D fields are constructed from a left-handed fermion mode at $s = 0$ and right-handed mode at $s = L_s - 1$.

The traditional DWF formulation is referred to as using the *Shamir kernel* [380–383], while a generalisation of this action known as the *Möbius kernel* [365, 389–391] was found to have the same level of residual chiral symmetry breaking, i.e. m_{res}, for a smaller extent of the fifth dimension for a particular choice of the action parameters. This reduces the cost of computation for the same m_{res} (or allows for the calculation of a smaller m_{res}). In chapter 6, lattice ensembles with Shamir DWFs in the sea are used, where the light/strange valence quarks are also simulated with the Shamir kernel while the heavy quarks used the Möbius kernel.

5.1.4 Scale Setting

Here we briefly comment on an important aspect of lattice QCD in the generation and understanding of lattice ensembles: scale setting. The full theory of QCD requires the fixing of 7 parameters to be fully defined – the masses of the 6 quarks and the coupling constant. Lattice formulations have fewer parameters to fix since we restrict simulations to include only a subset of the quarks in the sea, which is favoured computationally and the heavy quark effects on the sea may not be resolvable within the uncertainties of the simulation anyway. In particular, the huge mass of the top quark (see table 2.3) rules it out from being considered in the low energy regimes considered in lattice simulations. We label lattice ensembles e.g. $N_f = 2$, $N_f = 2+1$, $N_f = 2+1+1$ to indicate the number of quark flavours included in the sea, where the 2 indicates that the lightest quarks, up and down, are treated as degenerate. Next included is the strange quark and then even the charm quark is more commonly included these days as part of $N_f = 2+1+1$ ensembles. The inclusion of the bottom quark in the sea was demonstrated in [392], however it is not clear what practical improvement will be gained from simulating $N_f = 2+1+1+1$ ensembles over $N_f = 2+1+1$.

For whichever number of flavours in our ensemble, it is clear how many parameters must be fixed, N_f. We require $N_f - 1$ parameters to fix the quark masses since the up and

down are simulated as one degenerate *light* quark. In addition the coupling constant needs to be fixed, which is expressed through the determination of the lattice spacing a. Typically, meson or baryon state masses such as m_π, m_K, m_Ω are used, where the comparison of lattice values with experimental measurements allows for fixing e.g. m_l and m_s alongside the lattice spacing a (since lattice values for the mass are given in units of the lattice spacing, i.e. aM). Setting the scale a can also be related to pure gauge field quantities such as the Sommer scale [393] or the Wilson flow [394, 395].

For further details on scale setting and its importance to lattice simulations, we refer to, for instance, the FLAG review [249].

5.1.5 Hadronic Observables

Finally, most of the formalism behind lattice QCD has now been set, and we can move towards the practical goal of this field: performing a measurement of some observable $\mathcal{O}$ on each gauge field configuration in a lattice ensemble, and from that determine a stochastic estimate of the expectation value $\langle\mathcal{O}\rangle$. We have already seen some observables of the gauge field sector like the plaquette and clover operators (see figures 5.3 and 5.4), but now we take the steps needed to construct operators involving fermion fields such that we can connect these to expectation values to be measured.

Quark Bilinears and Interpolating Operators

From Grassmann algebra and Wick's theorem, we can see that Grassmann variables representing fermion fields in correlation functions will come in pairs – these pairs are known as *quark bilinears*. The quark bilinear then describes a meson state at lattice position x with quark content f_1, f_2. Furthermore, mesons carry quantum numbers of spin J, parity P, and charge conjugation C, typically written as J^{PC}. These quantum numbers can be derived from the Dirac structure of the interpolating quark bilinear. The creation and annihilation operators of this meson state are then

$$\mathcal{O}_M(x) = \bar{\psi}_{f_1}(x)\Gamma\,\psi_{f_2}(x), \qquad \mathcal{O}_M^\dagger(x) = \pm\bar{\psi}_{f_2}(x)\Gamma\,\psi_{f_1}(x), \tag{5.86}$$

where Γ is the Dirac structure of the bilinear and the sign of the creation operator is determined by the particular choice of Γ. Referring to the PDG [54], the types of meson state are:

- Scalar, $J^{PC} = 0^{++}$: created by $\Gamma = \mathbb{1}$; examples are a_0, f_0.
- Pseudoscalar, $J^{PC} = 0^{-+}$: created by $\Gamma = \gamma_5$; examples are π, K, D_s, B_s.
- Axial vector, $J^{PC} = 1^{++}$: created by $\Gamma = \gamma_i\gamma_5$; examples are a_1, f_1.

- Vector, $J^{PC} = 1^{--}$: created by $\Gamma = \gamma_i$; examples are ρ, K^*, D_s^*.
- Tensor, $J^{PC} = 1^{+-}$: created by $\Gamma = \gamma_i\gamma_j$; examples are b_1, h_1.

The above formula will only result in the creation of mesons with zero momentum, however inducing momentum in these states is also required for studying momentum-dependent processes such as, for instance, semileptonic meson decays. The interpolating operator is projected to a discrete momentum using a Fourier Transform, i.e.

$$\mathcal{O}(\vec{p}, t) = \frac{1}{\sqrt{L^3}} \sum_{\vec{x} \in \Lambda_3} \mathcal{O}(\vec{x}, t) e^{-i\vec{x}\cdot\vec{p}}, \tag{5.87}$$

where Λ_3 is the set of lattice sites in the 3-dimensional spatial volume of the lattice, i.e. at fixed time t.

Interpolating operators are used to induce definite meson states at the boundaries of correlation functions, i.e. at the 'start' and 'end' of their time extent. After covering the other building blocks required, we will see how these interpolating operators are 'married' in different ways to describe different correlation functions which in turn describe different hadronic processes.

Quark Propagators

By Wick's theorem, we can contract two quark fields of the same flavour at positions x and y into a propagator which describes a quark of flavour f propagating from y to x, i.e.

$$S_f(x, y) = \overbrace{\psi_f(x)\bar{\psi}}_f(y). \tag{5.88}$$

Furthermore, since the Dirac operator of many fermion actions (including any relevant here) has the property of γ_5 hermiticity, defined

$$(\gamma_5 D_\mu(x))^\dagger = \gamma_5 D_\mu(x) \implies D_\mu^\dagger(x) = \gamma_5 D_\mu(x) \gamma_5, \tag{5.89}$$

then propagators, originating from the inverse Dirac operator, also inherit this property:

$$S_f(x, y)^\dagger = \gamma_5 S_f(y, x) \gamma_5. \tag{5.90}$$

This is an important relation for minimising computing time – a propagator calculated in the direction $x \to y$ also gives the anti-propagator in direction $y \to x$. For example, for two point correlation functions of a $q\bar{q}$ state, γ_5 hermiticity means that only one propagator needs to be calculated and then the anti-propagator is taken from this relation.

So already we have hinted that reducing the number of propagators to be calculated is key to saving computing time, i.e. calculating these propagators is a large portion of

the cost involved in extracting hadronic matrix elements. To calculate a propagator, we must solve

$$D(x,y)_{ij}^{\alpha\beta} S(y,z)_{jk}^{\beta\gamma} = \delta_{ik}\delta_{\alpha\gamma}\delta_{xz}. \tag{5.91}$$

The Dirac operator is a very large (but sparse) matrix, so to invert it requires use of numerical solvers. However, the propagator $S(y,z)$ is also very large and not sparse; it is a square matrix in lattice volume $\times$ spin $\times$ colour space, i.e. a $(|\Lambda| \times 4 \times 3)^2$ matrix. Even for lattices considered small by today's standard (e.g. $L^3 \times T = 24^3 \times 64$), the propagator is of a size $O(10^{12})$; inverting this matrix even numerically quickly loses any feasibility.

The solution is to calculate one column of the inverse matrix $\psi(\vec{x},t)$ through a linear equation

$$\sum_{\vec{y},t} = D(\vec{x},t;\vec{y},t')\psi(\vec{y},t') = \eta(\vec{x},t), \tag{5.92}$$

where we suppress spin and colour indices. We call η the *source vector* describing the position on the lattice from which the propagator originates (discussed in more detail below), and ψ is a vector describing the propagator from the source position to all other points. This equation is solved for each spin-colour combination (a total of $4 \times 3 = 12$). We thus find our vector ψ as

$$\psi(\vec{x},t) = \sum_{\vec{y},t'} S(\vec{x},t;\vec{y},t')\eta(\vec{y},t'). \tag{5.93}$$

Many inversion algorithms converge polynomially, e.g. in $O(n^3)$ time; for the very large size of the matrices on these lattices, these algorithms would be prohibitively expensive, and thus alternative algorithms must be sought after. There is a large amount of machinery and human effort put in by lattice practitioners to find efficient algorithms to solve equation (5.92), which is typically very dependent on the type of fermion action used since this determines the definition of the Dirac operator. The solving algorithm used for calculating the propagators in this work was the *Conjugate Gradient* (CG) algorithm [396], which converges $\propto \sqrt{\kappa}$ (with κ the condition number of the matrix) for large size n. Note that the condition number of the Dirac matrix scales inversely with the quark mass – smaller quark masses can largely increase the condition number of the Dirac matrix, in turn increasing the convergence time of the numerical solve. When addressed with this problem, the earlier strategy was typically to simulate with unphysically massive up/down quarks and then extrapolate to the physical values in the later stages of analysis. However algorithmic improvements, such as the *Hierarchically Deflated Conjugate Gradient* (HDCG) [397], have been found in order to make simulations of the light up/down quarks at physical masses feasible. In chapter 6, no light quarks are considered in the valence sector, and the effects of light quarks from the sea are

expected to be minimal for the heavier states being considered, thus the issue of reliably inverting physical light quarks is not relevant to this work. An entire thesis can easily be written on the subject of these algorithms, however this is not the focus of this work and we will simply make use of the great efforts gone in to designing and improving these algorithms without discussing further.

Quark Sources

The full quark propagator matrix describes the quark propagating from every lattice site to every other lattice site (always as well for each spin-colour combination). This full matrix is referred to as an 'all-to-all' propagator for obvious reasons, however this is the most expensive possible way to compute a propagator. Also note that the elements of the 'all-to-all' propagator are highly correlated due to translation invariance, so not only does calculating the full matrix cost a large amount of computing time, but it also requires a lot of memory. As mentioned above, we can reduce the computational cost (and the memory footprint) of calculating propagators by choosing to instead select just a single column vector $\psi(\vec{x}, t)$ of the full propagator matrix. This corresponds to a source vector $\eta(\vec{x}, t)$, i.e. we calculate the propagator only originating from a single point on the lattice to all other points – this is called a *point source* and can be defined using a delta function:

$$S_0(x) = \delta(x - x_0), \tag{5.94}$$

where x is again the 4-coordinate and x_0 is the position of the source.

Point sources may be the simplest definition of a source for a propagator, however they are not the only choice away from the massive 'all-to-all' limit, and there are effects of a point source one may wish to improve upon. Using a completely localised source results in large sensitivity to local fluctuations in the gauge field and can e.g. lead to largely deviating results when placed by a near-zero mode of the Dirac operator; using some volume-averaged source on each gauge field configuration is expected to smoothen out the larger deviations caused from local fluctuations and yield more reliable estimates of observables [398]. Replacing a point source with N_{hit} stochastic sources drawn from some distribution $\mathcal{D}$ which is symmetric about 0 is expected to increase the precision of calculations given the property

$$\langle \eta^{(n)}_{a\alpha}(x)\eta^{\dagger(n)}_{b\beta}(y)\rangle_n \equiv \frac{1}{N}\sum_{n=1}^{N_{\text{hit}}} \eta^{(n)}_{a\alpha}(x)\eta^{\dagger(n)}_{b\beta}(y) \overset{N_{\text{hit}}\to\infty}{\to} \delta_{ab}\delta_{\alpha\beta}\delta_{xy}. \tag{5.95}$$

Placing a stochastic source on a fixed timeslice t_{src} of the lattice but over the entire spatial volume then allows for full L^3 volume averaging, clearly avoiding the issue of local gauge fluctuations to a much better degree. Furthermore, using γ_5 hermiticity, we can see that the same noise vector can be used for all propagators either originating from

or propagating to t_{src}, so these sources do not have increased multiplicity required in the calculation and with one propagator inversion (per colour-spin combination) we have an average over the entire spatial volume – this is referred to as the *one-end trick* [398, 399]. It is important to note as well that while sampling over the whole spatial volume, these sources are still by definition *localised* since they simply amount to the average over L^3 point sources with stochastic noise, so we still have clearly-defined local sources for our propagators but benefit from the spatial averaging such that significant fluctuations in the local gauge field for any single lattice site are suppressed.

The distribution these stochastic sources are drawn from (having first been suggested in [400, 401]) is here given by complex $\mathbb{Z}_2 \times \mathbb{Z}_2$ numbers:

$$\mathcal{D} = \left\{ \frac{1}{\sqrt{2}}(\pm 1 \pm i) \right\}. \tag{5.96}$$

As such, we will commonly refer to these sources as '$\mathbb{Z}_2$ wall sources' throughout this thesis. Other noise reduction techniques exist (which may be used independently of or in addition to $\mathbb{Z}_2$ wall sources), such as *all-mode-averaging* [402–404], *deflation* [405], and *distillation* [406], but these are not relevant for this thesis and are not discussed further here.

A caveat of the $\mathbb{Z}_2$ wall source however is the loss of momentum projection "for free". In the case of point sources, it is possible to define the momentum of a correlation function entirely at the *sink* (or contraction point) such that a single point-sourced propagator can be calculated and then contracted with all necessary momentum projections at no additional cost. For $\mathbb{Z}_2$ wall sources, this is not the case since these explicitly project to the zero momentum mode. It is still possible with an additional momentum projection to calculate correlation functions for non-zero momentum, but since this requires a projection at the source, i.e. before the propagator inversion, each momentum requires an additional propagator calculation.

We have so far focused on local sources. These are necessary in order to correctly extract all matrix elements from a correlation function, however one must keep in mind that they include the entire tower of states with the quantum numbers induced by the interpolating operator used. For some systems, it is possible that these excited states do not decay fast enough and contaminate the signal of the desired ground state. Instead, one can apply some smearing operator H to the local point/$\mathbb{Z}_2$ wall source such that it is now an extended source in some volume around the local position. This smeared source can be beneficial in that its extended volume can absorb some of the higher states of the system which do not travel as far from the source such that the signal of the correlation function resolves the lower-lying states (the ground state in particular)

more cleanly. By itself, these smeared sources can assist in extracting the energy/mass of the ground state of the system, or combined in an analysis with also locally-sourced correlation functions, they can help in resolving the ground state of the system such that the matrix elements can be appropriately extracted from the local signal. Jacobi (or Gaussian) smearing [407] is one such method of creating a smeared source. This is an iterative procedure which applies the smearing operator N times, where the smearing operator H takes a Gaussian shape (since this is common to many simple wavefunctions) with some smearing radius σ. It is defined

$$M_a(x)\eta_a(x) = \sum_b \sum_y \left(\delta_{xy}\delta_{ab} + \frac{\sigma^2}{4N}\Delta^N_{ab}(x,y)\right)\eta_b(y), \tag{5.97}$$

where Δ is the gauge-covariant Laplace operator (acting in the spatial directions only):

$$\Delta(x,y) = \sum_{i=1}^{3} 2\delta_{xy} - U_i(x)\delta_{x+\hat{i},y} - U_i^\dagger(x-\hat{i})\delta_{x-\hat{i},y}. \tag{5.98}$$

Note that above we discussed smearing to suppress excited state contamination from the interpolating operator at the source position. The same holds true for the sink position, i.e. we can apply the smearing kernel to the propagator after its inversion such that its effect is for the interpolating operator at the sink. More information can typically be found from a combination for smeared and local sources/sinks, for example, 3 source-sink combinations are commonly considered for extracting information about matrix elements and the ground state energy from 2-point correlation functions – local-local (LL, also referred to as point-point PP), smeared-local (SL, or SP), and smeared-smeared (SS).

2-Point Correlation Functions

Now with the foundation of interpolating operators, quark propagators, and spin-colour sources, we can begin to construct correlation functions from which we can extract physical observables such as meson masses/energies and hadronic matrix elements. We start with the 2-point correlation function as the product of two interpolating operators. One operator is placed at some source position and creates a mesonic state ($\mathcal{O}^\dagger_{\text{src}}$) and another is placed at the sink position and annihilates the state ($\mathcal{O}_{\text{snk}}$). For simplicity, we set the source position as $x_{\text{src}} = (\vec{x}, 0)$ (which is always valid due to translational invariance), and the sink at $x = (\vec{x}, t)$. A 2-point correlation function with fixed 3-momentum $\vec{p}$ is then written as

$$C_{2pt}(\vec{p}, t) = \sum_{\vec{x}} e^{-i\vec{p}\cdot\vec{x}} \langle 0|\mathcal{O}_{\text{snk}}(\vec{x}, t)\mathcal{O}^\dagger_{\text{src}}(\vec{0}, 0)|0\rangle. \tag{5.99}$$

Following the Heisenberg picture, we can insert a complete set of states

$$\sum_{n=0}^{\infty} \frac{|n\rangle\langle n|}{2E_n}, \tag{5.100}$$

with $E_0 \leq E_1 \leq E_2 \ldots$, into the correlation function. This reads

$$\begin{aligned} C_{2pt}(\vec{p},t) &= \sum_{\vec{x}} e^{-i\vec{p}\cdot\vec{x}} \sum_n \frac{1}{2E_n(\vec{p}_n)} \langle 0|\mathcal{O}_{\text{snk}}(\vec{x},t)|n\rangle\langle n|\mathcal{O}^\dagger_{\text{src}}(\vec{0},0)|0\rangle \\ &= \sum_n \sum_{\vec{x}} \frac{e^{-i\vec{p}\cdot\vec{x}}}{2E_n(\vec{p}_n)} \langle 0|e^{Ht-i\vec{k}\cdot\vec{x}}\mathcal{O}_{\text{snk}}(\vec{0},0)e^{-Ht+i\vec{k}\cdot\vec{x}}|n\rangle\langle n|\mathcal{O}^\dagger_{\text{src}}(\vec{0},0)|0\rangle \\ &= \sum_n \sum_{\vec{x}} \frac{e^{i(\vec{p}_n-\vec{p})\cdot\vec{x}}}{2E_n(\vec{p}_n)} \langle 0|\mathcal{O}_{\text{snk}}(\vec{0},0)|n\rangle\langle n|\mathcal{O}^\dagger_{\text{src}}(\vec{0},0)|0\rangle e^{-E_n(\vec{p}_n)t} \\ &= \sum_n \frac{\langle 0|\mathcal{O}_{\text{snk}}(\vec{0},0)|n\rangle\langle n|\mathcal{O}^\dagger_{\text{src}}(\vec{0},0)|0\rangle}{2E_n(\vec{p}_n)} e^{-E_n(p_n)t}|_{p_n=p} \\ &= \sum_n \frac{Z^{(n)}_{\text{snk}} Z^{(n)*}_{\text{src}}}{2E_n(\vec{p})} e^{-E_n(\vec{p})t}, \end{aligned} \tag{5.101}$$

where we define $Z_i^{(n)} = \langle 0|\mathcal{O}_i|n\rangle$ as the meson-to-vacuum matrix element of the nth energy state of the interpolating operator $\mathcal{O}_i$. So far in this derivation, we ignored the fact that the signal of a correlation function will propagate in all directions from the source position, i.e. there will be both a forwards- and backwards-propagating signal in Euclidean time. Accounting for this, the 2-point function is

$$C_{2pt}(\vec{p},t) = \sum_n \frac{Z^{(n)}_{\text{snk}} Z^{(n)*}_{\text{src}}}{2E_n(\vec{p})} \left(e^{-E_n(\vec{p})t} \pm e^{-E_n(\vec{p})(T-t)}\right), \tag{5.102}$$

where T is the time extent of the lattice. There is the possibility of a relative sign between the forwards and backwards signals depending on the choice of operators $\mathcal{O}_{\text{src}}$, $\mathcal{O}_{\text{snk}}$; for $\mathcal{O}_{\text{src}} = \mathcal{O}_{\text{snk}}$ this is positive, while for, e.g. $\mathcal{O}_{\text{src}} = \gamma_5$, $\mathcal{O}_{\text{snk}} = \gamma_t\gamma_5$ it is negative.[4] This comes from the anti-periodic boundary conditions given to fermions and how these interact with the different gamma structures as the signal crosses the boundary. In Euclidean time, we have a real exponent for increasing energies E_n such that higher-energy states have a faster exponential decay in the time signature and therefore in the limit of large Euclidean time separation from the source $0 \ll t \ll T$, only the lowest-lying state, i.e. the ground state, will remain and we can then extract its energy/mass from the exponent and its matrix element(s) from the prefactor.

[4] This particular combination of operators is commonly used as, although they have different matrix elements $Z^{(n)}$, the axial-vector current $\gamma_t\gamma_5$ replicates the same energy/mass eigenvalues as the pseudoscalar γ_5.

From equation (5.102), we can see that, when neglecting excited states, the 2-point function actually has either a cosh or sinh form depending on the relative sign between the forwards and backwards signals. Furthermore, we see that the only quantity in the exponent of this correlator is the energy of the state (or mass for $\vec{p} = 0$). Starting with this functional form of only the ground state, we can then define an *effective energy* of the 2-point function, i.e. (for the cosh form)

$$E_{\text{eff}}(\vec{p}, t) = \cosh^{-1}\left(\frac{C_{2pt}(\vec{p}, t) + C_{2pt}(\vec{p}, t+2)}{2C_{2pt}(\vec{p}, t+2)}\right), \tag{5.103}$$

where this can inform us how quickly we converge on the ground state as for large enough time, the effective energy will converge on a plateau at the ground state value. Note that by neglecting the backwards-propagating state (typically suitable for $0 < t < T/2$ and T sufficiently large), the effective energy can be defined using a log form instead. One can also average over the forwards and backwards signals (known as *folding*) and which will effectively double the statistics of your data in $0 \leq t \leq T/2$. An example of the effective mass M_{eff} of a 2-point pseudoscalar-pseudoscalar correlator is shown in figure 5.5. Note that in the initial definition of the 2-point function in equation (5.99),

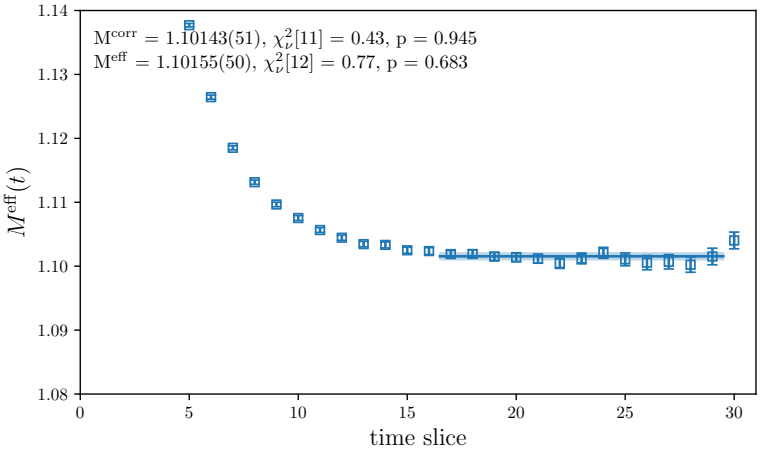

FIGURE 5.5: The effective mass of a zero-momentum 2-point correlation function for a pseudoscalar state, i.e. $\mathcal{O}_{\text{src}} = \mathcal{O}_{\text{snk}} = \gamma_5$. A fit to a plateau is performed at sufficiently large timeslices that only the ground state of the system remains.

it is assumed that all Wick contractions of the quark fields composing the interpolating operators are summed over to obtain the expectation value. For two distinct flavours $f_1 \neq f_2$, this is clear that we only have a single Wick contraction, corresponding to the

connected correlation function:

$$\begin{aligned}\langle 0|\mathcal{O}_{\text{snk}}(x)\mathcal{O}^{\dagger}_{\text{src}}(0)|0\rangle_{\text{conn.}} &= -\langle \bar{\psi}_{f_1,a}(x)(\Gamma_{\text{snk}})_{ab}\psi_{f_2,b}(x)\,\bar{\psi}_{f_2,c}(0)(\Gamma^{\dagger}_{\text{src}})_{cd}\psi_{f_1,d}(0)\rangle \\ &= \langle \psi_{f_1,d}(0)\bar{\psi}_{f_1,a}(x)(\Gamma_{\text{snk}})_{ab}\psi_{f_2,b}(x)\,\bar{\psi}_{f_2,c}(0)(\Gamma^{\dagger}_{\text{src}})_{cd}\rangle \\ &= \langle \text{Tr}\left[S_{f_1,da}(0,x)(\Gamma_{\text{snk}})_{ab}\,S_{f_2,bc}(x,0)(\Gamma^{\dagger}_{\text{src}})_{cd}\right]\rangle.\end{aligned} \tag{5.104}$$

However, if $f_1 = f_2$, it turns out that there is a second *disconnected* contribution, where the two quark propagators are not joined together in a single trace:

$$\begin{aligned}\langle 0|\mathcal{O}_{\text{snk}}(x)\mathcal{O}^{\dagger}_{\text{src}}(0)|0\rangle_{\text{disc.}} &= -\langle \bar{\psi}_{f_1,a}(x)(\Gamma_{\text{snk}})_{ab}\psi_{f_1,b}(x)\,\bar{\psi}_{f_1,c}(0)(\Gamma^{\dagger}_{\text{src}})_{cd}\psi_{f_1,d}(0)\rangle \\ &= -\langle \psi_{f_1,b}(x)\bar{\psi}_{f_1,a}(x)(\Gamma_{\text{snk}})_{ab}\,\psi_{f_1,d}(0)\bar{\psi}_{f_1,c}(0)(\Gamma^{\dagger}_{\text{src}})_{cd}\rangle \\ &= -\langle \text{Tr}\left[S_{f_1,ba}(x,x)(\Gamma_{\text{snk}})_{ab}\right]\,\text{Tr}\left[S_{f_1,dc}(0,0)(\Gamma^{\dagger}_{\text{src}})_{cd}\right]\rangle.\end{aligned} \tag{5.105}$$

By disconnected contribution, we refer to diagrams where the fermion lines form two separate traces such that they are only connected in the expectation value through the gauge field. Disconnected diagrams therefore suffer from much more statistical noise in their signal than the connected contributions, and are typically neglected when their contribution has been estimated to be within the final precision of the result. Noise-reduction techniques come in to play here to improve the signal of these disconnected pieces when aiming for higher-precision results where these small contributions become important to quantify. The quark-line diagrams for the different Wick contractions are shown in figure 5.6.

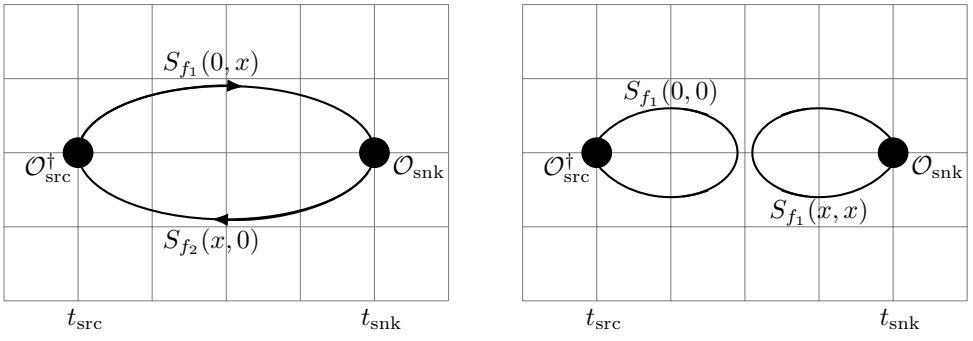

FIGURE 5.6: Quark line diagrams of the connected (left) and disconnected (right) contributions to the expectation value $\langle \mathcal{O}_{\text{snk}}(x)\mathcal{O}^{\dagger}_{\text{src}}(0)\rangle$ of a 2-point correlation function. The connected piece is present for all combinations of quark flavour f_1, f_2, while the disconnected piece is only present for $f_1 = f_2$.

3-Point Correlation Functions

Next we increase the level of complexity from 2-point correlation functions to 3-point functions. As suggested by the name, we now consider the use of 3 operator insertions

instead of 2. We place interpolating operators $\mathcal{O}_f^\dagger$ and $\mathcal{O}_i$ at two source positions t_{src} and $t_{\text{src}} + \Delta T$ which describe the final and initial state mesons of the process being considered, and some other operator $\mathcal{O}_{\text{op}}$ which acts on the propagators for each time t_{snk} between the two interpolating currents. 3-point functions can be used to study different processes depending on the exact setup of initial and final states and intermediary operator. Two common examples are: semileptonic meson decays where the interpolating currents define the initial and final state mesons and the intermediary operator describes the flavour-changing weak current transforming one quark of the initial state into one quark of the final state; four-quark operator transitions such as $\Delta Q = 2$ operators describing neutral meson mixing, i.e. a neutral meson M^0 with quark content $q_1\bar{q}_2$ oscillates with its anti-meson partner $\overline{M}^0$ with quark content $\bar{q}_1 q_2$[5]. The quark line diagrams of these processes are shown in figure 5.7.[6] The general form of a 3-point function is given by (assuming $t_{\text{src}} = 0$ w.l.o.g.)

$$\begin{aligned} C_{3pt}(\vec{p}, t, \Delta T) &= \sum_x e^{-i\vec{p}\cdot\vec{x}} \langle \mathcal{O}_i(\vec{x}, \Delta T) \mathcal{O}_{\text{op}}(\vec{y}, t_{\text{snk}}) \mathcal{O}_f^\dagger(\vec{0}, 0) \rangle \\ &= \sum_{n,m} \langle 0|\mathcal{O}_i|n\rangle \langle n|\mathcal{O}_{\text{op}}|m\rangle \langle m|\mathcal{O}_f^\dagger|0\rangle \frac{e^{-E_m^{(f)} t} e^{-E_n^{(i)}(\Delta T - t)}}{4 E_m^{(f)} E_n^{(i)}}, \end{aligned} \tag{5.106}$$

where n, m are summed over the towers of states of the initial and final interpolating operators respectively. In chapter 6, our main analysis will involve 3-point functions to extract the matrix elements of dimension-six four-quark operators of type $\Delta Q = 2$ and $\Delta Q = 0$, i.e. for neutral meson mixing and meson lifetimes respectively.

5.1.6 Heavy Quarks on the Lattice

Putting heavy charm or bottom quarks on the lattice is not as simple as for light or strange quarks. In order to properly resolve a quark field on the lattice and keep discretisation effects under control, we require that the quark mass is sufficiently smaller than the ultraviolet cut-off a^{-1} [355, 356], i.e.

$$m_q \ll a^{-1} \implies a m_q \ll 1. \tag{5.107}$$

Discretisation errors from a fermion field enter as $O((am_q)^n)$, $O((ap)^n)$, $O((ap)(am_q)^n)$, which clearly become uncontrolled if the condition of equation (5.107) is not satisfied. Lattices relevant to this thesis have inverse lattice spacings $2\,\text{GeV} \lesssim a^{-1} \lesssim 4\,\text{GeV}$, and it is clear when compared to the physical mass of the b quark (see table 2.3) that

[5] These four-quark operators can be alternatively evaluated by keeping the operator position fixed in the middle and varying the source positions at either side.

[6] Note that only the connected contribution to the semileptonic process is shown, while a disconnected contribution also exists if either the initial or final state propagators are the same flavour as the spectator.

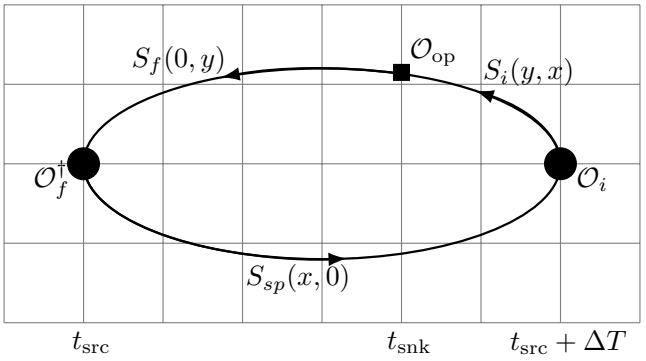

(a) Semileptonic meson decay.

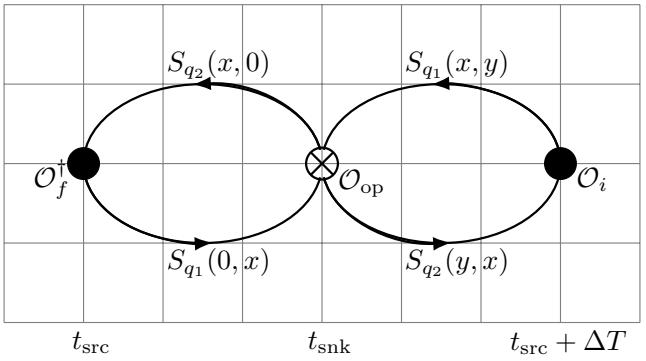

(b) Neutral meson mixing via $\Delta Q = 2$ four-quark operator.

FIGURE 5.7: Quark line diagrams of the 3-point correlation functions for (a) a semileptonic meson decay and (b) neutral meson mixing. In (a), the 'initial' quark propagator S_i interacts with a flavour-changing weak current through $\mathcal{O}_{\text{op}}$ to become the 'final' quark propagator S_f, while the spectator quark S_{sp} simply propagates between the final and initial states. In (b), the initial meson state M induced by $\mathcal{O}_i$ has its quark content $\bar{q}_1 q_2$ transformed through the four-quark operator $\mathcal{O}_{\text{op}}$ into quark content $q_1 \bar{q}_2$ which induces the final meson state $\bar{M}$ from interpolating operator $\mathcal{O}_f^\dagger$.

simulating a b quark on these lattices will introduce uncontrollable discretisation errors. Considering the mass of the charm quark (see table 2.3), the finer of the lattices available today, i.e. larger a^{-1}, should be suitable to simulate physical c quarks although without additional techniques, some of the coarser lattices still used may be questionable even for charm. With increased computational power and improved algorithms for ensemble generation, finer lattices where physical b quarks are feasible are expected to become common in the near future.

The historic solution to circumvent the issue of uncontrolled discretisation effects has been to use effective actions to describe the heavy quarks by using an OPE to detach the heavy degrees of freedom from the simulated fields. We previously discussed the RHQ action as one such effective action, which combines the Symanzik improvement procedure with HQET. Quark currents constructed with an RHQ quark carry a discretisation

error of $O(a)$; in order to reduce this and have $O(a)$-improved RHQ currents, we must introduce additional operators with a derivative insertion which along with coefficients from lattice perturbation theory are added to the leading order current to remove the leading discretisation effects. Furthermore, the parameters of the RHQ action m_0, ζ, c_P (recall equation (5.62)) can be tuned (non-)perturbatively. Another effective action commonly used is Non-Relativistic QCD (NRQCD) – see [408] for the original formulation and [409, 410] for the lattice construction.
So we can see that the effective action procedure practically has limits in how well the systematic effects of the effective action can be controlled. For calculations with lower precision, this is not necessarily the limiting factor and the effective action is still the better (and cheaper) approach for simulating the heavy quarks, however if aiming for high precision results (e.g. $O(1\%)$ or lower) these inherent systematic effects can become a limiting factor in the calculation.

An alternative approach which has begun to be explored recently is the fully relativistic approach where the heavy quarks are simulated using the same action as the light quarks. This is possible with the finer lattice spacings now accommodating charm-like quark masses with controlled discretisation effects as well as the use of improved actions where the discretisation effects in the heavy quark mass enter at higher powers, e.g. $O((am_q)^2)$. While physical b quark masses are still mostly out of reach, a range of heavy quark masses from charm to near-to-bottom are becoming feasible and then the additional extrapolation to physical b can be controlled using HQET.
It was shown in [218, 411, 412] that the region of charm and heavier-than-charm masses with controlled discretisation errors using the DWF action can be extended by using the Möbius kernel with a stout-smearing of the gauge field [413]. The approach for handling heavy quarks chosen for the research presented in chapter 6 follows that of [218, 414], where we will consider charm quarks at physical mass using the stout-smeared Möbius DWF kernel.

5.1.7 Statistics and Systematics

Statistics

We have described that we evaluate the path integral in lattice simulations by stochastically through Monte Carlo methods. The expectation value of some observable is given by the average of the value on a number of gauge field configurations. We must associate a statistical error with this estimate of the expectation value, for which we use resampling techniques. Resampling techniques estimate statistical observables by building a 'resampled data set' from averages of subsets of the original data. In particular this method allows for reliably propagating statistics into secondary observables derived from the raw simulation data.

In this thesis, we will make use of single elimination jackknife resampling to estimate statistical observables and propagate these through fitting procedures. At the later stages of analysis when it is required to combine results for an observable from multiple lattice ensembles, i.e. for the continuum extrapolation, the super jackknife method is used. The jackknife and super jackknife methods are discussed in more detail in appendix B.1.

Observables are extracted from correlation function data using a frequentist χ^2 approach to perform fits to the data. The basics of frequentist fitting are covered in appendix B.2.

Systematics

Of course, the nature of the stochastic estimate of expectation values means there is always an associated statistical error, however there also exist important systematic effects in the formulation of our lattice simulations which must be addressed and the associated uncertainties estimated. Here we list (not exhaustively) some of the important systematic effects commonly considered in lattice analyses.

- Finite volume: signals permeate across the boundary of the lattice and create 'around-the-world' effects which affect the light degrees of freedom. These effects are proportional to $e^{-m_\pi L}$, where using the constraint $m_\pi L \gtrsim 4$ for lattice ensemble generation is commonly used to keep these effects under control [415, 416].
- Heavy quarks: As discussed in section 5.1.6, heavy quarks can introduce large discretisation effects proportional to the heavy quark mass and momentum. Use of effective actions or finer lattice ensembles can help manage these effects.
- Continuum extrapolation: after extracting some physical observable on multiple lattice ensembles with different lattice spacings, this information is used to extrapolate the value to the continuum $a = 0$. This extrapolation can be dependent on details such as the renormalisation procedure or the lattice discretisations used for the gauge and fermion fields. Typically one discusses $O(a)$ improvement such that the leading lattice artefacts to be modelled in the extrapolation are $O(a^2)$, however for some quantities in some setups, it may be necessary to also consider higher powers in a such as $O(a^4)$, in particular for higher precision calculations.
- For higher precision calculations when the uncertainties reach $\sim 1\%$, it can also be necessary to estimate e.g. QED effects which can otherwise become the leading source of uncertainty at this precision. To properly estimate QED effects requires a discretisation scheme for QED which is itself a very broad topic to discuss. For further reading, see e.g. [417].

5.2 QCD Sum Rules

This section provides a brief overview to the method of QCD sum rules, where perturbative QCD calculations can be related to hadronic observables. This has been an important tool for many years in predicting hadronic observables, and is typically complementary to lattice QCD discussed above, since these methods often work better in e.g. different q^2 ranges for form factor calculations. The bag parameter calculations to be discussed in chapter 6 have been performed in both lattice QCD and HQET sum rules for the $\Delta B = 2$ case and provide comparable results, while the case of $\Delta B = 0$, HQET sum rules have provided the only predictions of these parameters to date. In relevance to the calculations of bag parameters for heavy mesons (an important topic of this thesis), we will introduce sum rules in HQET for a heavy-light meson H_Q.

The information presented here is based off [418–420].

5.2.1 A Basic Example: The Two-Point Correlation Function

Consider the 2-point correlation function between two currents $\tilde{j}_q = \bar{q}\gamma^5 h_v$,

$$\Pi(\omega) = i \int d^D x \, e^{ik\cdot x} \langle 0|T\{\tilde{j}_q^\dagger(0)\tilde{j}_q(x)\}|0\rangle, \tag{5.108}$$

where k is the residual momentum of the heavy quark (recall equation 3.32) and $\omega = k \cdot v$ is the residual energy. The integral is defined in dimensional regularisation where $D = 4 - 2\epsilon$ dimensions are used. The correlation function has a *dual* nature: at large negative ω, the quarks in the currents are highly virtual and can be described clearly in perturbation theory for QCD; at positive ω, they can form bound states which are observed as resonances of single meson states and a continuous spectrum of multiparticle states along the real axis of ω. To describe the hadronic content of the correlation function along the positive real axis, one can insert a complete set of hadronic states and derive the *unitarity relation*,

$$2\,\mathrm{Im}\,\Pi(\omega) = \sum_n \langle 0|\tilde{j}_q^\dagger|n\rangle\langle n|\tilde{j}_q|0\rangle \, d\tau_n \, (2\pi)^4 \delta^{(4)}(k - p_n), \tag{5.109}$$

where the sum over n represents the infinite tower of hadronic states (starting at the ground state, the pseudoscalar meson H_Q) and $d\tau_n$ the integration over phase space. So relating the two regimes of the correlator (analytic, perturbative quark content vs non-perturbative hadronic states), we can use the Cauchy formula to derive a *dispersion relation* between an arbitrary point with $\omega < 0$ and the hadronic sum along the positive

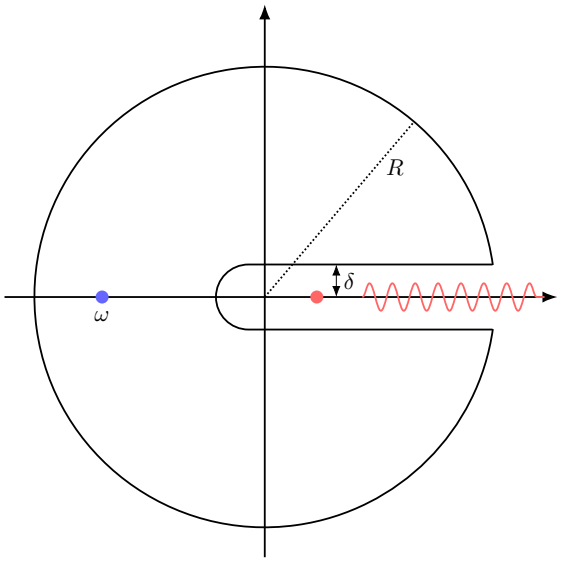

FIGURE 5.8: Contour integral for the correlation function isolating a pole at ω (blue circle) and avoiding the positive real axis where analyticity breaks down. The red circle represents the lowest single-meson hadronic resonance and the red line represents the continuous spectrum of multiparticle states.

real axis, as shown in figure 5.8:

$$\begin{aligned}\Pi(\omega) &= \frac{1}{2\pi i}\oint_C ds\,\frac{\Pi(s)}{s-\omega} \\ &= \frac{1}{2\pi i}\lim_{\delta\to 0}\int_0^\infty ds\,\frac{\Pi(s+i\delta)-\Pi(s-i\delta)}{s-\omega} + \frac{1}{2\pi i}\int_R ds\,\frac{\Pi(s)}{s-\omega} \\ &= \int_0^\infty ds\,\frac{\rho(s)}{s-\omega},\end{aligned} \tag{5.110}$$

where $\rho(s)$ is the discontinuity in $\Pi(s)$ along the positive real axis,

$$\rho(s) = \lim_{\delta\to 0}\frac{1}{2\pi i}\left[\Pi(s+i\delta)-\Pi(s-i\delta)\right], \tag{5.111}$$

and we assume that the integral over the circle vanishes as $R\to\infty$. However, this may not always be the case, and the correlation function can be further modified to account for this, e.g.

$$\Pi^n(\omega) = \omega^n\int_0^\infty ds\,\frac{\rho(s)}{s^n(s-\omega)} + \sum_{i=0}^{n-1} a_i\omega^i, \tag{5.112}$$

where n can be chosen such that the integration over the circle will vanish. Notice that now we have gained a polynomial contribution with coefficients a_i; since this is a polynomial to finite order $n-1$, these can be removed by taking sufficient derivatives of $\Pi^n(\omega)$.

For ω along the positive real axis, we can express ρ for the 2-point correlator as a combination of some hadronic parameter for the lowest-lying meson state and also the

spectral density of the continuum of multi-particle and excited states:

$$\rho^{\text{had}}(\omega) = F^2\delta(\omega - (m_{H_Q} - m_Q)) + \rho^{\text{cont}}(\omega), \tag{5.113}$$

where F^2 is the HQET decay constant of the ground state meson H_Q. Finally, our correlation function can be written as

$$\Pi(\omega) = \frac{F^2}{m_{H_Q} - m_Q - \omega} + \int_{\omega_0}^{\infty} ds\, \frac{\rho^{\text{cont}}(s)}{s - \omega}, \tag{5.114}$$

where the threshold energy ω_0 indicates the point from which the continuous spectrum begins.

5.2.2 Operator Product Expansion

We stress again that the description of the correlation function through perturbation theory is valid for large, negative ω, however if one takes some moderate (and negative) value for ω, we can still be sensitive to long-distance non-perturbative QCD effects, which also must be accounted for. These non-perturbative vacuum effects can be separated from the perturbation theory calculations in an OPE, i.e.

$$\Pi(\omega) = i \int d^D x\, e^{ik\cdot x} \langle 0|T\{\tilde{j}_q^\dagger(0)\tilde{j}_q(x)\}|0\rangle = \sum_d C_d(\omega)\langle 0|\mathcal{O}_d|0\rangle, \tag{5.115}$$

where we order the OPE as usual by the dimension of the operators d. Note that the lowest-dimension contribution is at $d = 0$ where $C_0(\omega) = \Pi^{\text{pert}}(\omega)$ and $\langle 0|\mathcal{O}_0|0\rangle = 1$. Beyond $d = 0$, we have a sum of *vacuum condensates* of quark and gluon fields, however we are able to safely truncate this sum after typically only a few terms since high-dimensional condensates are proportional to ω^{-d} and are thus suppressed so long as the magnitude of ω is not too small. The prediction of the condensates themselves is beyond perturbation theory and must be determined by other means, such as lattice QCD. Another method is treating them as phenomenological parameters which can be extracted from fitting to experimental data; an example proving the viability of this method is the prediction of the gluon condensate in one of the original sum rule works [38], which is a value still used to date.

Note that there is some *critical dimension* d_{crit} from which it is said the validity of the OPE picture breaks down since the vacuum condensates become sensitive also to short-distance fluctuations and the idea of separation of scales which is a foundation of the OPE is no longer sound. Due to this breakdown, the OPE must be truncated at some point, however finding the optimal truncation to both describe the correlator accurately and avoid the OPE breakdown is difficult and clearly separates our prediction from

the exact solution to the physics. Neglecting these terms from the correlation function predicted for large negative ω may actually have a more significant impact after the analytical continuation to the positive real axis is taken. The impact of this truncation is clearly a violation of quark-hadron duality; for further details on d_{crit} and QHD, see e.g. [37, 421, 422].

While below the critical dimension, the OPE picture remains valid, and the correlation function can be extracted from a combination of the vacuum condensates and perturbation. The 'sum rule' of QCD sum rules is then given by equating the OPE and hadronic pictures of the correlator:

$$\frac{F^2}{m_{H_Q} - m_Q - \omega} + \int_{\omega_0}^{\infty} ds\, \frac{\rho^{\text{cont}}(s)}{s-\omega} = \int_0^{\infty} ds\, \frac{\rho^{\text{OPE}}(s)}{s-\omega}. \tag{5.116}$$

5.2.3 Borel Transformations

The current form of the correlation function is not actually very useful for estimating the hadronic parameters of the lowest-lying state, since we still have to define the continuum spectral density $\rho^{\text{cont}}(s)$. To improve this situation, the Borel transformation can be applied [37]:

$$\Pi(t) = \mathcal{B}_t \Pi(\omega) = \lim_{\substack{-\omega, n \to \infty \\ -\omega/n \to t}} \frac{(-\omega)^{n+1}}{n!} \left(\frac{d}{d\omega}\right)^n \Pi(\omega). \tag{5.117}$$

There are important consequences of the Borel transformation:

- Applying infinite derivatives will remove any polynomial terms, i.e.

$$\mathcal{B}_t[\omega^i] = 0. \tag{5.118}$$

  As discussed above, this will remove the subtraction terms in equation (5.112).

- The relation

$$\begin{aligned} \mathcal{B}_t\left[\frac{1}{(s-\omega)^i}\right] &= \lim_{\substack{-\omega, n \to \infty \\ -\omega/n \to t}} \frac{(-\omega)^{n+1}}{n!} \left(\frac{d}{d\omega}\right)^n \frac{1}{(s-w)^i} \\ &= \frac{\exp\{-s/t\}}{(i-1)! t^{i-1}}, \end{aligned} \tag{5.119}$$

  where $i > 0$. This introduces an exponential weight to the hadronic side of the sum rule and reduces sensitivity to ρ_{cont}, while on the OPE side, the convergence will be improved since higher-order terms are factorially suppressed. However, it turns out that optimising t for this set-up is tricky since the two sides of our sum rule prefer opposite scenarios: small t better isolates the ground state in the hadronic

picture but this means the higher-order terms in the OPE are not as suppressed (and vice versa). One must find some *Borel window* [418] for t where both sides of the sum rule are stable, however it is not guaranteed for all sum rules that such a window exists.

Now using QHD and some cut-off energy ω_c, we can approximate

$$\int_{\omega_0}^{\infty} ds\, \frac{\rho^{\text{cont}}(s)}{s-\omega} = \int_{\omega_c}^{\infty} ds\, \frac{\rho^{\text{OPE}}(s)}{s-\omega}. \tag{5.120}$$

Using the Borel transformation, we suppress contributions from $\rho^{\text{cont}}(s)$ and as such violations to QHD are also suppressed. Finally, this allows us to write down the Borel sum rule in HQET for the decay constant (as written by [423–425])

$$F^2(\mu) = \int_0^{\omega_c} d\omega\, \exp\left\{\frac{m_{H_Q} - m_Q - \omega}{t}\right\} \rho^{\text{OPE}}(\omega). \tag{5.121}$$

In this form, we now have a clear method to calculate the non-perturbative decay constant F using standard perturbation theory techniques (and the addition of vacuum condensates). The HQET decay constant can then be related to the full QCD equivalent through standard matching procedures.

5.2.4 Sum Rules for Bag Parameters

The sum rule for a bag parameter of a four-quark operator $\mathcal{O}_i$ can be defined by a simple extension to the case for the decay constant above. The leading-order diagram and one diagram at NLO for the four-quark operators are shown in figure 5.9. We start with the 3-point correlator

$$K_{\mathcal{O}_i}(\omega_1, \omega_2) = \int d^D x_1 d^D x_2 e^{ik_1\cdot x_1 - ik_2\cdot x_2} \langle 0|T\left\{\tilde{j}_+(x_2)\mathcal{O}_i(0)\tilde{j}_-(x_1)\right\}|0\rangle, \tag{5.122}$$

where $\omega_{1,2}$ are the residual energies from $k_{1,2}$ and the pseudoscalar interpolating currents for the HQET fields $h^{(+)}$, $h^{(-)}$ are defined

$$\tilde{j}_+ = \bar{q}\gamma^5 h^{(+)}, \qquad \tilde{j}_- = \bar{q}\gamma^5 h^{(-)}. \tag{5.123}$$

We continue as before to now write the dispersion relation for this correlator as

$$K_{\mathcal{O}_i}(\omega_1, \omega_2) = \int_0^{\infty} ds_1\, ds_2\, \frac{\rho_{\mathcal{O}_i}(s_1, s_2)}{(s_1-\omega_1)(s_2-\omega_2)} + \cdots, \tag{5.124}$$

where we do not write any subtraction terms which will be removed by the Borel transform later. This is the equivalent to equation 5.110, except now since we have two variables ω_1 and ω_2, $\rho_{\mathcal{O}_i}(s_1, s_2)$ is the *double* discontinuity in both ω_1 and ω_2.

Through the standard algebra, one finds the finite-energy sum rule

$$F^2(\mu)\langle\mathcal{O}_i(\mu)\rangle \exp\left\{-\frac{m_{H_Q}-m_Q}{t_1}-\frac{m_{H_Q}-m_Q}{t_2}\right\} = \int_0^{\omega_c} d\omega_1\, d\omega_2\, \exp\left\{-\frac{\omega_1}{t_1}-\frac{\omega_2}{t_2}\right\}\rho_{\mathcal{O}_i}(\omega_1,\omega_2). \tag{5.125}$$

By making use of the sum rule for the HQET decay constant, we can obtain a sum rule for $\Delta B = B - 1$ – the deviation of the bag parameter B from the VIA – which reads

$$\Delta B^{\text{pert}}_{\mathcal{O}_i}(\mu) = \frac{C_F}{N_c A_{\mathcal{O}_i}}\frac{\alpha_s(\mu)}{4\pi}\, r_{\mathcal{O}_i}\left(1, \log\frac{\mu^2}{4\bar{\Lambda}^2}\right), \tag{5.126}$$

where $r_{\mathcal{O}_i}(x, L_\omega)$ is related to the spectral density of the *non-factorisable*[7] contributions to the 3-point correlator which appear at NLO,

$$\Delta\rho_{\mathcal{O}_i}(\omega_1,\omega_2) = \frac{N_c C_F}{4}\frac{\omega_1^2\omega_2^2}{\pi^4}\frac{\alpha_s}{4\pi}\, r_{\mathcal{O}_i}(x, L_\omega), \tag{5.127}$$

where $x = \omega_2/\omega_1$ and $L_\omega = \log\left(\frac{\mu^2}{4\omega_1\omega_2}\right)$. For further details, and advancements including strange-quark mass effects, we refer to the calculations of [168, 169, 221].

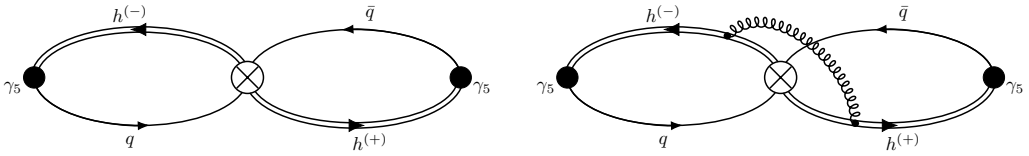

FIGURE 5.9: Leading-order diagram (left) and example of NLO non-factorisable diagram (right) contributing to the 3-point HQET correlator for the calculation of the $\Delta B = 2$ bag parameter.

[7] By *non-factorisable*, we refer to the diagrams with a gluon exchange across the point of operator insertion such that the diagram cannot be decomposed into the product of two simpler diagrams (see figure 5.9).

Chapter 6

Four-Quark Matrix Elements and Gradient Flow Renormalisation

Throughout the discussions in chapter 3, we stress that further determinations of the dimension-six four-quark $\Delta B = 0$ matrix elements contributing to the lifetimes of B mesons are wanted, in particular from lattice QCD in order to compare to the existing sum rule calculations. In addition, in chapter 4, we show that further understanding and higher precision in the dimension-six four-quark $\Delta B = 2$ matrix elements contributing to neutral B meson mixing will be very useful in constraining new physics beyond the Standard Model.

Calculating four-quark matrix elements in lattice QCD is a well-established task in processes such as neutral B meson mixing [214–217, 219, 414, 426] and rare kaon decays [427–430]. While the calculation of bare four-quark matrix elements is similar for B mixing and B lifetimes, a distinct difference comes from the renormalisation procedure, where the dimension-six $\Delta B = 0$ operators mix with operators of lower mass dimension, making physical predictions of these quantities very challenging. In sum rule calculations, this is circumvented by calculating the matrix elements in HQET and matching to QCD [168, 169]. In lattice QCD, as the name suggests, matrix elements are calculated in N_f-flavour QCD, so the simplifications of HQET do not apply. As such, the history of the dimension-six four-quark $\Delta B = 0$ matrix elements on the lattice is short: after early quenched studies [171, 172], preliminary unquenched results were presented in 2001 [173] however a subsequent publication was never released. The difficulty of dealing with operator mixing has left this challenge unpursued in the following years and to date no lattice calculations of four-quark matrix elements for lifetime operators has been completed. Just recently however, similar interest in the matrix elements for lifetime ratios and baryonic decays was revived [431]. A further challenge for lattice

calculations is the contributions from disconnected diagrams where the signal-to-noise ratio worsens.

In this chapter, we introduce a new non-perturbative renormalisation scheme for matrix elements calculated using lattice QCD utilising the gradient flow [394, 432, 433] and specifically its short-flow-time expansion [434–437] in order to match to a phenomenologically relevant renormalisation scheme, in this case $\overline{\text{MS}}$. The gradient flow is introduced in section 6.1 and its short-flow-time expansion in section 6.1.1. The goal of this renormalisation procedure is to tackle the challenge of renormalising operators which mix with operators of lower mass dimension, such that a full calculation of the dimension-six four-quark $\Delta B = 0$ matrix elements from lattice QCD can be performed for the first time. Through section 6.2, we describe the early research developing this procedure. We use a simplified setup simulating a neutral charm-strange meson at physical mass values and consider both the $\Delta Q = 2$ operators for neutral meson mixing and the $\Delta Q = 0$ operators for lifetimes, where the $\Delta B = 0, 2$ notation is replaced with $\Delta Q = 0, 2$ for generic heavy quark Q. As a test case to validate this new method, we consider the $\Delta Q = 2$ matrix elements and renormalise these in the gradient flow scheme, before matching to $\overline{\text{MS}}$ and comparing to existing results for short-distance D^0 mixing. We expect the spectator effects of using a strange quark instead of a light quark to be small. Our analysis can also be extended to the $\Delta Q = 0$ matrix elements to yield results in QCD for the first time. These can be compared to the existing HQET results, and eventually the resulting prediction of the lifetime can be compared to experiment. The short-flow-time expansion has similarly been used in the study of other quantities such as neutral kaon mixing [438, 439], the energy-momentum tensor [440, 441], and the electric dipole moment of the neutron [442]. The results presented in this chapter are based on the proceedings [45].

Finally, in section 6.4, we will outline future prospects to extend this work to the large-scale lattice simulations needed to consider physical B mesons and other improvements anticipated.

6.1 Gradient Flow

The gradient flow (GF) [394, 432–434, 443–447] is a versatile tool in lattice simulations, with applications such as scale setting [249, 394], studying the β function [448, 449], and renormalisation. Inspired by the heat equation, gauge and fermion fields are evolved along an auxiliary dimension, the flow time τ [GeV^{-2}], by means of the first-order

differential equations

$$\partial_\tau B_\mu(\tau, x) = \mathcal{D}_\nu(\tau) G_{\nu\mu}(\tau, x), \quad B_\mu(0, x) = A_\mu(x), \tag{6.1}$$

$$\partial_\tau \chi(\tau, x) = \mathcal{D}^2(\tau)\chi(\tau, x), \quad \chi(0, x) = q(x), \tag{6.2}$$

where $G_{\nu\mu}(\tau) = \partial_\nu B_\mu(\tau) - \partial(\mu)B_\nu(\tau) + [B_\nu(\tau), B_\mu(\tau)]$ is the flowed gluon field strength tensor, $\mathcal{D}_\nu = \partial_\nu + [B_\nu(\tau), \cdot]$ is the flowed covariant derivative, A_μ and q are the regular gauge and fermion fields respectively whereas $B_\mu(\tau)$ and $\chi(\tau)$ are those extended in the flow time. Practically, GF applies an infinitesimal smearing procedure of the gauge and fermion fields; formally, this suppresses and removes UV fluctuations such that operators evolved along the gradient flow are renormalised. The effect of the gradient flow can be seen by sampling the plaquette (recall figure 5.3) throughout a 2D slice of a lattice and comparing this along the flow time, as shown in figure 6.1. One can see that without GF, there exists large local ultraviolet fluctuations in the plaquette, while once the gauge field has been evolved along the flow time, these fluctuations are 'smoothened over' such that the variation of the plaquette across the lattice is now significantly smaller. The central value of the plaquette clearly shifts significantly and also is resolved to a precision from ~ 0.6 to ~ 0.99995.

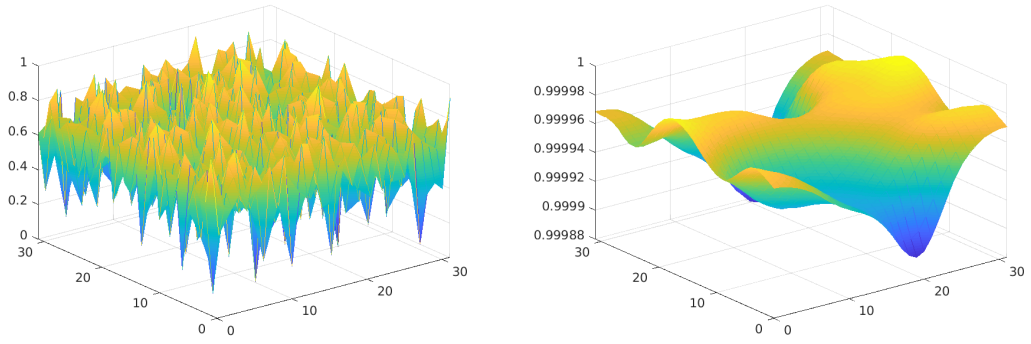

(a) $\tau/a^2 = 0.00$ (b) $\tau/a^2 = 16.00$

FIGURE 6.1: Variation of the plaquette over a 2D slice of a lattice without the gradient flow (a) and after suitable evolution in the flow time (b) [450].

In this thesis, we will focus on the use of GF for renormalisation. With respect to renormalisation, there are two concepts:

- The gradient flow as a renormalisation group transformation [451, 452].
- The short-flow-time expansion can be considered in order to relate the gradient flow renormalisation to another scheme, such as the $\overline{\text{MS}}$ [434, 436, 437]. This concept is discussed further below and used in the analysis of this chapter.

6.1.1 The Short-Flow-Time Expansion

To begin, we consider an effective Hamiltonian which is typically expressed as a sum of the products of operators $\mathcal{O}_m$ and Wilson coefficients C_m. With the gradient flow, this can be alternatively expressed in terms of 'flowed' operators $\tilde{\mathcal{O}}_n(\tau)$ and 'flowed' Wilson coefficients $\tilde{C}_n(\tau)$. As long as the sum is over a full operator basis, the described Hamiltonian is the same:

$$\mathcal{H}_{\text{eff}} = \sum_m C_m \mathcal{O}_m = \sum_n \tilde{C}_n(\tau)\tilde{O}_n(\tau), \tag{6.3}$$

where the flow-time dependence of the flowed operators and Wilson coefficients cancel each other [437, 440, 453, 454]. In the short-flow-time expansion, one relates the flowed operators to the regular ones as

$$\mathcal{O}_n(\tau) = \sum_m \zeta_{nm}(\tau)\mathcal{O}_m + O(\tau) \implies \sum_n \zeta^{-1}_{nm}(\mu,\tau)\langle\tilde{\mathcal{O}}^{\text{GF}}_n\rangle(\tau) = \langle\mathcal{O}^{\overline{\text{MS}}}_m\rangle(\mu), \tag{6.4}$$

where higher-dimensional operators accompany higher powers of τ such that they are expected to be negligible for small τ [434–437]. The perturbatively-calculated matrix $\zeta^{-1}(\mu,\tau)$ matches the GF-renormalised matrix elements to the $\overline{\text{MS}}$ scheme[1]. Note that from here on, when discussing the dimension-six four-quark $\Delta Q = 0$ operators defined in equation (3.88), we will drop the '$\sim$' written over the regular operators such that $\tilde{\mathcal{O}}$ always refers to the flowed operators.

The perturbative matching matrices $\zeta^{-1}(\mu,\tau)$ used in this study for both the $\Delta Q = 0, 2$ operator bases are calculated in [454, 455]. In the case of $\Delta Q = 2$, the matching matrix is block diagonal with only a single element for the operator $\mathcal{O}_1$. Since the quantities of interest are ultimately the bag parameters B_i of the operators $\mathcal{O}_i$, the matching matrix is calculated for the same ratio of currents. At NNLO, the perturbative matching from GF to $\overline{\text{MS}}$ schemes for the bag parameter B_1 with number of flavours N_f[2] is given by

$$\begin{aligned}\zeta^{-1}_{B_1}(\mu,\tau) = 1 &+ \frac{a_s}{4}\left(-\frac{11}{3} - 2L_{\mu\tau}\right) \\ &+ \frac{a_s^2}{43200}\Big[-2376 - 79650L_{\mu\tau} - 24300L^2_{\mu\tau} + 8250N_f + 6000\,N_f\,L_{\mu\tau} \\ &\qquad + 1800\,N_f\,L^2_{\mu\tau} - 2775\pi^2 + 300\,N_f\,\pi^2 - 241800\log 2 \\ &\qquad + 202500\log 3 - 110700\,\text{Li}_2\left(\frac{1}{4}\right)\Big],\end{aligned} \tag{6.5}$$

[1] Evanescent operators are considered in the matching calculation, however it is ensured via a finite renormalisation that the physical operators do not mix into them [454].

[2] Note that this is not the number of dynamical flavours in the lattice simulations, but the number of effective flavours in the continuum picture at the renormalisation scale μ (recall equation (3.30)).

where $L_{\mu\tau} = \log(2\mu^2\tau) + \gamma_E$ and $a_s = \alpha_s/\pi$. The expressions for the other bag parameters for both $\Delta Q = 0, 2$ are similar, but lie in 2×2 matrices such that two GF bag parameters mix to yield each $\overline{\text{MS}}$ result. In regards to the $\Delta Q = 0$ operators, while it is anticipated that the calculation is more straightforward than the original challenge without gradient flow, the lower-dimension operator mixing avoided so far in the non-perturbative gradient flow arises again in the matching procedure. The work to tackle this in full is ongoing. Meanwhile to give first estimates for these quantities, we consider the matching matrices calculated for the difference of the $\Delta Q = 0$ operators with different spectator quarks, which contain the same diagrams as the full operators but with the troublesome terms removed.

The final result for a bag parameter B_i in the $\overline{\text{MS}}$ scheme is given by the zero-flow-time limit of the product of the perturbative matching matrix and the flowed bag parameters in the GF scheme, i.e.

$$B_i^{\overline{\text{MS}}}(\mu) = \lim_{\tau \to 0} \zeta_{ji}^{-1}(\mu, \tau) B_j^{\text{GF}}(\tau). \tag{6.6}$$

Strictly speaking, taking this limit presents a *window problem*, i.e. we must balance two opposing effects:

- For GF-renormalised operators to be cleanly resolved, we must have evolved them far enough in the flow time such that the gradient flow has also taken care of regulating the UV and cut-off effects.
- The flow time region to be considered must be small enough that the short-flow-time expansion is still valid and higher-dimensional operators are suppressed.

We will see below when the short-flow-time expansion is applied to real lattice data how this "window problem" is practically seen and addressed.

6.2 Lattice Calculation of Four-Quark Matrix Elements

6.2.1 Lattice Setup

In this lattice calculation, we make use of six 2+1-flavour gauge field ensembles generated by the RBC/UKQCD collaboration with the DWF and Iwasaki gauge actions, at three lattice spacings $a \sim 0.11$, 0.08, 0.07 fm and pion masses $\in [267, 433)$ MeV [218, 365, 366]. Light and strange quarks are simulated with the Shamir DWF kernel [379, 380, 383, 456] with $M_5 = 1.8$. These ensembles are listed in table 6.1.

	L	T	a^{-1}/GeV	am_l^{sea}	am_s^{sea}	am_c^{val}	m_π/MeV	srcs$\times N_{\text{conf}}$	σ	N_σ
C1	24	64	1.7848	0.005	0.040	0.64	340	32×101	4.5	400
C2	24	64	1.7848	0.010	0.040	0.64	433	32×101	4.5	400
M1	32	64	2.3833	0.004	0.030	0.45	302	32×79	6.5	400
M2	32	64	2.3833	0.006	0.030	0.45	362	32×89	6.5	100
M3	32	64	2.3833	0.008	0.030	0.45	411	32×68	6.5	100
F1S	48	96	2.785	0.002144	0.02144	0.37	267	24×98		

TABLE 6.1: RBC/UKQCD ensembles used in the discussed simulations [363–366]. am_l^{sea} and am_s^{sea} are the light and strange sea quark masses and m_π is the unitary pion mass. am_s^{val} are the valence strange quark masses, set to the physical mass.

Heavy quarks are simulated using stout-smeared gauge fields [413] and the Möbius DWF action [391], where the mass has been tuned to the physical charm on each ensemble through the D_s pseudoscalar meson [54]. Using a similar setup as [218], all propagators are generated with $\mathbb{Z}_2$ wall sources where the number of sources (separated evenly across the time dimension) and smearing parameters are listed in table 6.1. Gaussian smearing [407] is also applied for the strange quarks. Using chiral DWFs for this pilot study has the advantage that additional mixing of different chiralities does not occur.

The parameters used in the gradient flow evolution of the quark fields in the lattice simulation are listed in table 6.2. For all ensembles, the third-order Runge-Kutta procedure is taken in steps of $\epsilon/a^2 = 0.01$, with measurements of the flowed correlation functions taken every 10 steps for earlier flow times which is extended to every 40 steps as the flow time increases. The maximum flow time for each lattice spacing is chosen such that all ensembles approximately cover the same physical range of flow time. The number of measurements along the flow time for each lattice spacing is also listed. Note that the M1 ensemble was first run at an early stage of the project alongside the C1 and C2 ensembles and as such was given the same flow time parameters as these. This results in a smaller physical reach in the flow time, however the variation between different ensembles at the same lattice spacing due to the sea quark effects is expected to be small and so the M2 and M3 ensembles will cover the range missed.

Recall the $\Delta Q = 2$ operator basis defined in equation (3.103) and their matrix elements in equations (3.104)-(3.106). We will refer to this as the "BSM" basis. We saw that the parity invariance of QCD reduces the number of required matrix elements from 8 to 5. Furthermore practically for lattice calculations, it is convenient to define a basis containing only colour-singlet operators, referred to as the "lattice" or "NPR" basis:

	$a^{-1} = 1.785\,\text{GeV}$ (C)	$a^{-1} = 2.383\,\text{GeV}$ (M)*	$a^{-1} = 2.785\,\text{GeV}$ (F)
step size, ϵ/a^2	0.01	0.01	0.01
measurement interval	$\tau/a^2 < 5$ 0.10 $\tau/a^2 > 5$ 0.40	$\tau/a^2 < 8$ 0.10 $\tau/a^2 > 8$ 0.40	$\tau/a^2 < 12$ 0.10 $\tau/a^2 > 12$ 0.40
max τ/a^2	8.00	12.00	20.00
# measurements	58	58	141

TABLE 6.2: Features of the gradient flow evolution. The evolution is performed in Runge-Kutta steps of ϵ and measurements of the flowed correlation functions are stored at even intervals which increase at larger flow times. * indicates that the parameters of the 'M' lattice spacing are only used for the M2 and M3 ensembles; the M1 ensemble uses the same parameters as the 'C' lattice spacing.

$$\begin{aligned}
Q_1 &= (\bar{q}\gamma^\mu(1-\gamma_5)Q)(\bar{q}\gamma_\mu(1-\gamma_5)Q),\\
Q_2 &= (\bar{q}\gamma^\mu(1-\gamma_5)Q)(\bar{q}\gamma^\mu(1+\gamma_5)Q),\\
Q_3 &= (\bar{q}(1-\gamma_5)Q)(\bar{q}(1+\gamma_5)Q),\\
Q_4 &= (\bar{q}(1-\gamma_5)Q)(\bar{q}(1-\gamma_5)Q),\\
Q_5 &= \frac{1}{4}(\bar{q}\sigma_{\mu\nu}(1-\gamma_5)Q)(\bar{q}\sigma_{\mu\nu}(1+\gamma_5)Q).
\end{aligned} \tag{6.7}$$

We further reduce these to their parity-even components in the lattice simulation and follow the linear transformation $\mathcal{O}^+ = TQ^+$ to relate these back to the operators of the "BSM" basis:

$$\begin{aligned}
Q_1^+ &= (\bar{q}\gamma_\mu Q)(\bar{q}\gamma_\mu Q) + (\bar{q}\gamma_\mu\gamma_5 Q)(\bar{q}\gamma_\mu\gamma_5 Q),\\
Q_2^+ &= (\bar{q}\gamma_\mu Q)(\bar{q}\gamma_\mu Q) - (\bar{q}\gamma_\mu\gamma_5 Q)(\bar{q}\gamma_\mu\gamma_5 Q),\\
Q_3^+ &= (\bar{q}Q)(\bar{q}Q) - (\bar{q}\gamma_5 Q)(\bar{q}\gamma_5 Q),\\
Q_4^+ &= (\bar{q}Q)(\bar{q}Q) + (\bar{q}\gamma_5 Q)(\bar{q}\gamma_5 Q),\\
Q_5^+ &= \sum_{\nu>\mu}(\bar{q}\gamma_\mu\gamma_\nu Q)(\bar{q}\gamma_\mu\gamma_\nu Q),
\end{aligned} \qquad T = \begin{pmatrix} 1 & 0 & 0 & 0 & 0\\ 0 & 0 & 0 & 1 & 0\\ 0 & 0 & 0 & -\frac{1}{2} & \frac{1}{2}\\ 0 & 0 & 1 & 0 & 0\\ 0 & -\frac{1}{2} & 0 & 0 & 0 \end{pmatrix}. \tag{6.8}$$

For further details on the use of the "NPR" basis and its relation to the "BSM" basis, see [218, 414, 457–459]. The quark line diagrams contributing to the simulation of these operators are shown in figure 6.2.

Next recall the $\Delta Q = 0$ operator basis defined in equation (3.88). For convenience in the lattice calculation, we look to remove the generator t^a from the direct definition of the operators used in the simulation. Using the definition $t^a_{\alpha\beta}t^a_{\gamma\delta} = -\frac{1}{2N_c}\delta_{\alpha\beta}\delta_{\gamma\delta} + \frac{1}{2}\delta_{\alpha\delta}\delta_{\gamma\beta}$

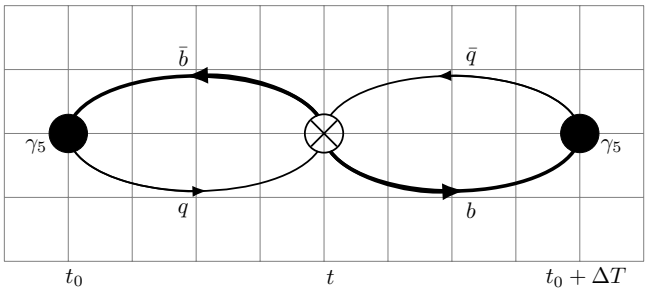

FIGURE 6.2: Quark line diagram to calculate the three-point correlation function with a $\Delta Q = 2$ four-quark operator insertion at time t between two sources at t_0 and $t_0 + \Delta T$.

and Fierz operations, we can rewrite our operator basis as

$$\begin{aligned}
\mathcal{Q}_1 &= (\bar{Q}\gamma_\mu(1-\gamma_5)q)(\bar{q}\gamma_\mu(1-\gamma_5)Q), \\
\mathcal{Q}_2 &= (\bar{Q}(1-\gamma_5)q)(\bar{q}(1+\gamma_5)Q), \\
\tau_1 &= (\bar{Q}\gamma_\mu(1-\gamma_5)Q)(\bar{q}\gamma_\mu(1-\gamma_5)q), \\
\tau_2 &= (\bar{Q}\gamma_\mu(1+\gamma_5)Q)(\bar{q}\gamma_\mu(1-\gamma_5)q).
\end{aligned} \tag{6.9}$$

Similarly to the process for $\Delta Q = 2$, we can reduce these to the parity-even components for the lattice simulation and relate back to the original basis later:

$$\begin{aligned}
\mathcal{Q}_1^+ &= (\bar{Q}\gamma_\mu q)(\bar{q}\gamma_\mu Q) + (\bar{Q}\gamma_\mu\gamma_5 q)(\bar{q}\gamma_\mu\gamma_5 Q), \\
\mathcal{Q}_2^+ &= (\bar{Q}q)(\bar{q}Q) - (\bar{Q}\gamma_5 q)(\bar{q}\gamma_5 Q), \\
\tau_1^+ &= (\bar{Q}\gamma_\mu Q)(\bar{q}\gamma_\mu q) + (\bar{Q}\gamma_\mu\gamma_5 Q)(\bar{q}\gamma_\mu\gamma_5 q), \\
\tau_2^+ &= (\bar{Q}\gamma_\mu Q)(\bar{q}\gamma_\mu q) - (\bar{Q}\gamma_\mu\gamma_5 Q)(\bar{q}\gamma_\mu\gamma_5 q),
\end{aligned} \tag{6.10}$$

$$\begin{pmatrix} \mathcal{O}_1^+ \\ \mathcal{O}_2^+ \\ T_1^+ \\ T_2^+ \end{pmatrix} = \begin{pmatrix} 1 & 0 & 0 & 0 \\ 0 & 1 & 0 & 0 \\ -\frac{1}{2N_c} & 0 & -\frac{1}{2} & 0 \\ 0 & -\frac{1}{2N_c} & 0 & \frac{1}{4} \end{pmatrix} \begin{pmatrix} \mathcal{Q}_1^+ \\ \mathcal{Q}_2^+ \\ \tau_1^+ \\ \tau_2^+ \end{pmatrix}. \tag{6.11}$$

For the operators $\mathcal{Q}_1^+$, $\mathcal{Q}_2^+$, these are calculated through the quark line diagram in figure 6.3, which is the expected $\Delta Q = 0$ operator insertion between two heavy mesons H_Q. With the rearrangement to the operators in equation (6.9), this resembles a $Q\bar{Q}$ pseudoscalar state decaying to a $q\bar{q}$ pseudoscalar state via the four-quark operators τ_1, τ_2. This rearranged operator insertion is constructed via the quark line diagram in figure (6.4).

Finally, the $\Delta Q = 0$ operators also have contributions from the so-called 'eye' diagrams. These diagrams have been calculated in HQET sum rules where their contributions were found to be small [168, 169]. On the lattice, these diagrams are more expensive

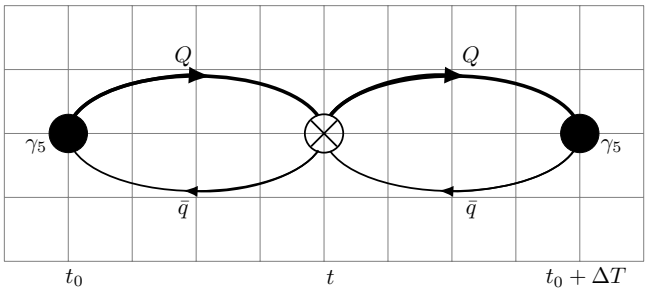

FIGURE 6.3: Quark line diagram to calculate the three-point correlation function with a $\Delta Q = 0$ four-quark operator $\mathcal{Q}_1$, $\mathcal{Q}_2$ insertion at time t between two sources at t_0 and $t_0 + \Delta T$.

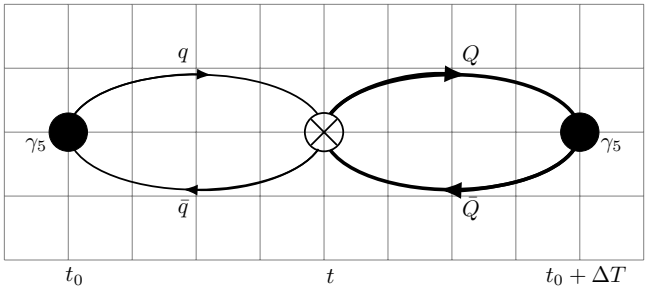

FIGURE 6.4: Quark line diagram to calculate the three-point correlation function with a $\Delta Q = 0$ four-quark operator τ_1, τ_2 insertion at time t between two sources at t_0 and $t_0 + \Delta T$.

to calculate to a statistically-viable level due to the internal quark loop. One method to generate the propagators for this uses *sparse sources* and is discussed in [430] in the context of rare kaon decays where these diagrams also appear. Due to the additional

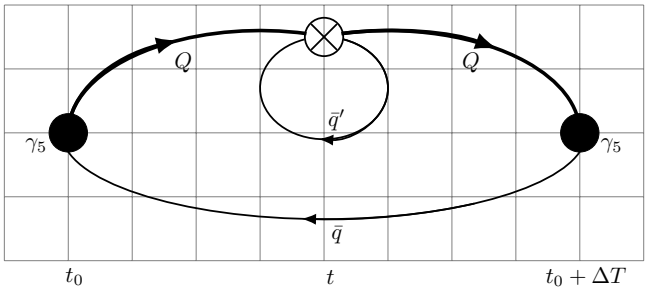

FIGURE 6.5: Quark line 'eye' diagram contributing to the matrix elements of $\Delta Q = 0$ four-quark operators inserted at time t between two sources at t_0 and $t_0 + \Delta T$.

cost of calculating these diagrams and the expectation that their contribution is small, we chose to not calculate these in this pilot study where the focus is on first results and validation of the gradient flow renormalisation. We plan to include the eye diagrams in future advances of this research (see section 6.4). The quark line eye diagram is shown in figure 6.5.

Due to their definition as ratios of the operator matrix element to some meson-to-vacuum matrix elements, the bag parameters B_i, ϵ_i of the operators discussed above can be conveniently defined on the lattice. First, recall equation (5.106) which for the case of the same meson H_Q induced at both source positions, can be written as (for $\Delta Q = 2$)

$$C^{\text{3pt}}_{\mathcal{O}_i^{\Delta Q=2}}(t, \Delta T, \tau) = \sum_{n,m} \langle 0|Q\gamma_5\bar{q}|H_Q^{(n)}\rangle\langle H_Q^{(n)}|\mathcal{O}_i|\bar{H}_Q^{(m)}\rangle\langle \bar{H}_Q^{(m)}|q\gamma_5\bar{Q}|0\rangle \frac{e^{-M_{\bar{H}_Q}^{(m)}t} e^{-M_{H_Q}^{(n)}(\Delta T - t)}}{4M_{\bar{H}_Q}^{(m)} M_{H_Q}^{(n)}}$$
$$= \frac{\langle 0|Q\gamma_5\bar{q}|H_Q\rangle^2}{4M_{H_Q}^2}\langle H_Q|\mathcal{O}_i|\bar{H}_Q\rangle^{-M_{H_Q}\Delta T} + \sum_{n\geq 0, m>0}[\dots] + \sum_{n>0,m\geq 0}[\dots]. \tag{6.12}$$

The $\Delta Q = 0$ case follows similarly by swapping the anti-H_Q mesons above with H_Q mesons. One can see from comparing to equation (5.102) that the product of two 2-point functions (with one being reversed in time from ΔT) of the meson H_Q will have the same time behaviour as the 3-point function. In the limit of large Euclidean time signature and large source separation, this ratio will approach the bag parameter. The B_i are isolated by taking the appropriate ratios of the 3-point correlation functions shown above in figures 6.2 and 6.3 to some 2-point correlation functions:

$$R_1^{\Delta Q=0,2}(t, \Delta T, \tau) = \frac{C^{\text{3pt}}_{\mathcal{O}_1^{\Delta Q=0,2}}(t, \Delta T, \tau)}{\eta_1 C_{AP}^{\text{2pt}}(t, \tau) C_{AP}^{\text{2pt}}(\Delta T - t, \tau)} \to B_1^{\text{GF}}(\tau), \tag{6.13}$$

$$R_i^{\Delta Q=0,2}(t, \Delta T, \tau) = \frac{C^{\text{3pt}}_{\mathcal{O}_i^{\Delta Q=0,2}}(t, \Delta T, \tau)}{\eta_i C_{PP}^{\text{2pt}}(t, \tau) C_{PP}^{\text{2pt}}(\Delta T - t, \tau)} \to B_i^{\text{GF}}(\tau), \tag{6.14}$$

where $i = 2 \to 5$ for $\Delta Q = 2$ and $i = 2$ for $\Delta Q = 0$. In the original operator bases (i.e. one must transform the lattice operators first), $\eta_i = \{\frac{8}{3}, -\frac{5}{3}, \frac{1}{3}, 2, \frac{2}{3}\}$ for $\Delta Q = 2$ and $\eta_i = \{1, 1, 1, 1\}$ for $\Delta Q = 0$. Note that the $\mathcal{O}_1$ operators for both $\Delta Q = 0, 2$ use the C_{AP} 2-point function, that is, the *axial-pseudoscalar* correlation function which has $Z_{\text{src}}^{(0)} = \langle 0|Q\gamma_5\bar{q}|H_Q\rangle = P$ (pseudoscalar matrix element) and $Z_{\text{snk}}^{(0)} = \langle 0|Q\gamma_t\gamma_5\bar{q}|H_Q\rangle = A$ (axial matrix element). Readers familiar with these definitions for $\Delta Q = 2$ operators will recall that the source and sink operators can be switched for the 'time-reversed' $C(\Delta T - t)$ correlator and that this is equivalent. For the gradient flow renormalisation procedure, it is important that the axial matrix element is at the sink position for both 2-point correlators since the gradient flow evolution is applied on the sink and only the local sink matrix elements are evolved along the gradient flow. The axial matrix elements must always be the ones 'flowed' to properly define the 'flowed' bag parameters for $\mathcal{O}_1$. For other operators, the C_{PP} 2-point functions are used which have the pseudoscalar matrix element at both source and sink. Still only the matrix element at the sink is evolved along the flow time and is used for defining the 'flowed' bag parameters, while

the source matrix elements cancel the same source matrix element appearing in the definition of the three-point function.

Due to the rearranged structure of the 3-point correlators for the τ_i operators on the lattice which relate to the T_i operators, these do not have the same simplification as for the other operators and must be defined slightly differently, since the induced state at either side of the 3-point function is not the same. Labelling the $Q\bar{Q}$ state η_Q and the $q\bar{q}$ state η_q since we induce pseudoscalar meson states, the correlation function reads

$$C^{\mathrm{3pt}}_{\tau_i}(t,\Delta T,\tau) = \sum_{n,m}\langle 0|Q\gamma_5\bar{Q}|\eta_Q^{(n)}\rangle\langle\eta_Q^{(n)}|\tau_i|\eta_q^{(m)}\rangle\langle\eta_q^{(m)}|q\gamma_5\bar{q}|0\rangle\frac{e^{-M_{\eta_q}^{(m)}t}e^{-M_{\eta_Q}^{(n)}(\Delta T-t)}}{4M_{\eta_q}^{(m)}M_{\eta_Q}^{(n)}}. \tag{6.15}$$

In a similar fashion to what is common in form factor analysis (see e.g. [460]), the matrix elements $\langle\tau_i\rangle$ can be extracted as

$$\langle\tau_i\rangle(\tau) = \lim_{0\ll t\ll\Delta T}\frac{C^{\mathrm{3pt}}_{\tau_i}(t,\Delta T,\tau)}{\sqrt{C^{\mathrm{2pt}}_{\eta_q}(t)C^{\mathrm{2pt}}_{\eta_Q}(\Delta T-t)}}\sqrt{\frac{4M_{\eta_q}M_{\eta_Q}}{e^{-M_{\eta_q}t-M_{\eta_Q}(\Delta T-t)}}}, \tag{6.16}$$

where the 2-point functions used are the PP correlators for the η_Q and η_q states. Note that these do not show a τ dependence since they are only used for cancelling the source matrix elements of the 3-point function and thus are always taken at zero flow time. By combining the extracted bag parameters B_i with the $\langle\tau_i\rangle$ following equation (6.11), the bag parameters ϵ_i are given by

$$\epsilon_1(\tau) = -\frac{1}{2}\frac{\langle\tau_1\rangle(\tau)}{\langle 0|Q\gamma_t\gamma_5\bar{q}|H_Q\rangle(\tau)^2} - \frac{1}{2N_c}B_1(\tau), \tag{6.17}$$

$$\epsilon_2(\tau) = \frac{1}{4}\frac{\langle\tau_2\rangle(\tau)}{\langle 0|Q\gamma_5\bar{q}|H_Q\rangle(\tau)^2} - \frac{1}{2N_c}B_2(\tau). \tag{6.18}$$

For this rearranged method of extracting the bag parameters, the pseudoscalar and axial matrix elements must be independently extracted from the 2-point functions.

6.2.2 Preliminary Work

Valence sector measurements are performed using the `Grid` [461, 462] and `Hadrons` [463] frameworks. The fermionic gradient flow evolution had not yet been implemented in `Grid` or `Hadrons`, and the first milestone of the project presented here was developing and validating new modules into `Hadrons` to perform the fermionic gradient flow required for the renormalisation procedure[3]. The validation procedure was performed against an implementation of the fermionic gradient flow [452, 464] written in `QLUA` [465]. To

[3] https://github.com/mbr-phys/Hadrons/tree/test/GradientFlowLumi/Hadrons/Modules/MGradientFlow

validate, gauge observables such as the plaquette and rectangle as well as fermionic 2-point functions were evolved along the gradient flow in both implementations and agreement was found at double precision. The modules written for this project are listed in appendix C. In addition, we greatly benefited from the recent 'file bundling' feature added to `Hadrons` such that the very large output of the gradient flow could be better controlled in fewer files.

While the physical charm masses on the C and M ensembles were known from previous studies [218], this set-up had not previously been used before on the F1S ensemble. Therefore an important step before running the full simulation for the $\Delta Q = 0, 2$ matrix elements was tuning the charm mass on the F1S ensemble to its physical value. 2-point correlation functions are analysed in a ground + first-excited state fit to precisely extract the ground state mass of the D_s meson simulated at multiple charm-like masses. Charm-

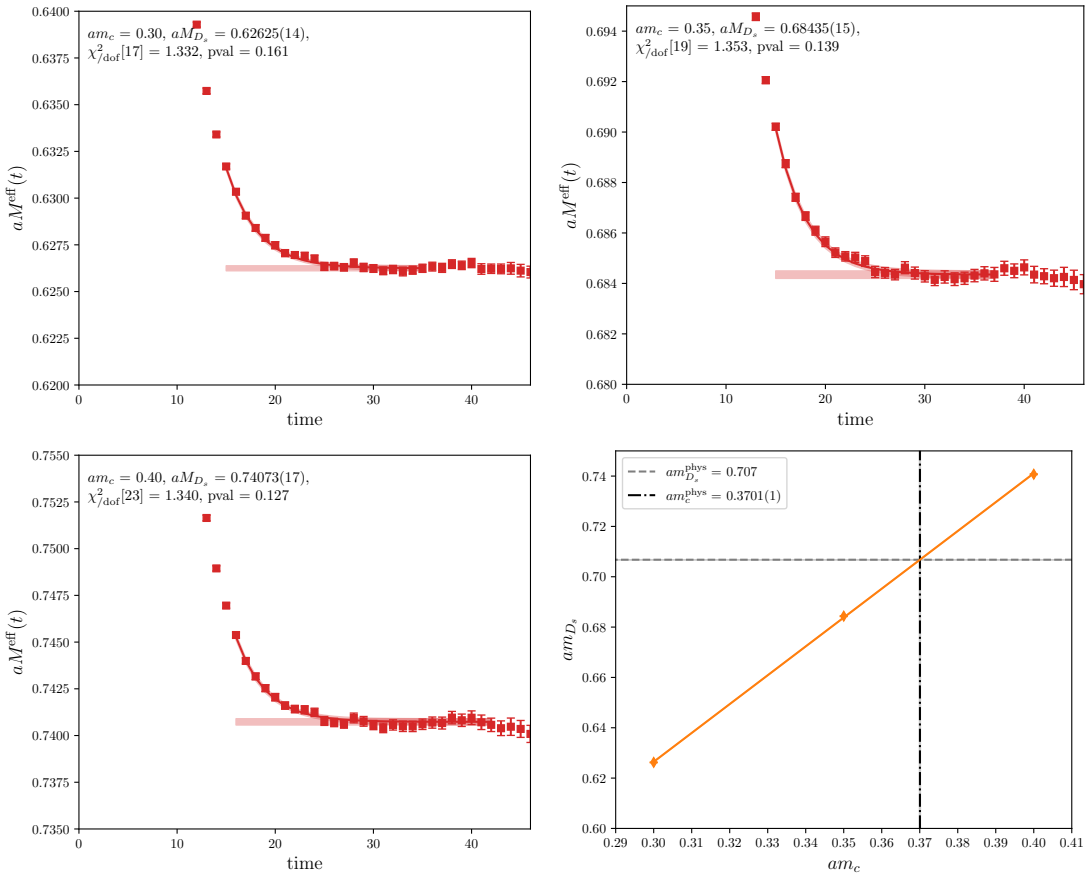

FIGURE 6.6: Physical charm mass interpolation on F1S from the D_s meson simulated at $am_c = 0.30, 0.35, 0.40$.

like masses were chosen such that these would bracket the expected value to replicate the physical mass of the D_s meson, and the resulting value could then be interpolated from the fitted results. The analysed charm masses and the interpolation to the physical value used in the full scale simulation on F1S are shown in figure 6.6.

6.2.3 Correlator Analysis

In the following we cover the analysis of the correlation functions obtained from the lattice simulations. For all analyses, we use the single-elimination jackknife resampling procedure and perform correlated frequentist fits to the data, see appendix B for details.

The first data considered for analysis are 2-point correlation functions. From these we can validate that the meson states we anticipate are being well-resolved and that the heavy quark mass indeed yields a physical D_s mass as desired for this pilot study. Furthermore, we extract the meson-to-vacuum matrix elements required for e.g. the analysis of the τ_i operators. In figure 6.7, we show examples of fits to 2-point correlation functions at different flow times on the M2 ensemble. On the left is shown the fit for

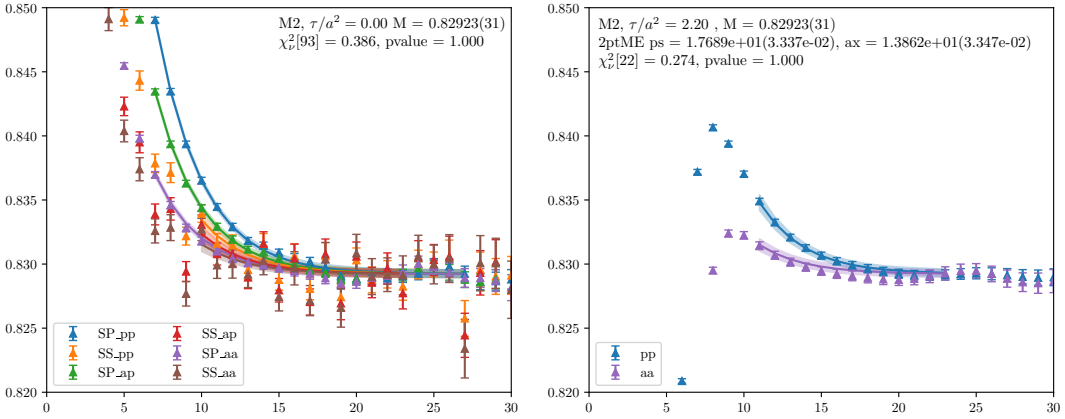

FIGURE 6.7: Examples of ground + first-excited state fits to 2-point correlation functions on the M2 ensemble at zero flow time (left) and $\tau/a^2 = 1.50$ (right). 6 correlators are fitted simultaneously on the left, and two on the right, where the right also uses information from the zero-flow-time fit for better constraint. SS, SP and aa, ap, pp are explained in the text.

zero flow time, where we have access to a larger set of correlation functions from which we extract our information. Without the gradient flow, we use 'smeared-smeared' (SS) data, i.e. with Gaussian smearing at both source and sink, or 'smeared-point' (SP) data with Gaussian smearing at the source and a point sink. Due to the nature of the 3-point correlators and therefore the bag parameter ratios, it only makes sense that the local matrix element defined at a point sink is evolved along the gradient flow. So we have fewer correlation functions to work with for extracting this directly. The axial-axial (aa) and axial-pseudoscalar (ap) correlators have the benefit of having the same meson mass states as the pseudoscalar-pseudoscalar (pp) case and as such all six (aa, ap, pp for both SS or SP) can be fitted simultaneously. We perform a ground + first-excited state fit to the data of all correlators, since it is commonly found that including an excited state in the analysis improves the statistical resolution of the ground state. The resulting fit at zero flow time outputs the meson mass (as written on the figure) and also the axial and

pseudoscalar matrix elements for both smeared and local operators. The meson mass and smeared-source matrix elements will not be changed by the gradient flow, and can be used as input to the fits on the 'flowed' correlators to better constrain the 'flowed' local matrix elements. As can be seen in the right of figure 6.7, the gradient flow also results in a smearing effect as the flow time is increased and the signal of the data for earlier timeslices is 'destroyed', such that some information can be lost at larger flow times without other constraints. Similar analysis is performed on all ensembles and also for the η_Q and η_q states needed for the τ_i matrix elements.

Next we turn our attention to the analysis of the bag parameters. With the focus on testing and validation of the gradient flow renormalisation, we consider only $\mathcal{O}_1$ for $\Delta Q = 2$ and $\mathcal{O}_1$ and T_1 for $\Delta Q = 0$. First we discuss the similar $\mathcal{O}_1$ operators for $\Delta Q = 0, 2$. The bag parameters (recall equations (6.12) and (6.13)) are symmetric in the Euclidean time between 0 and ΔT (the two source positions) such that we expect to find a plateaued region in the centre as the value of the bag parameter with excited state contributions growing as we move further from the centre. Example fits to the bag

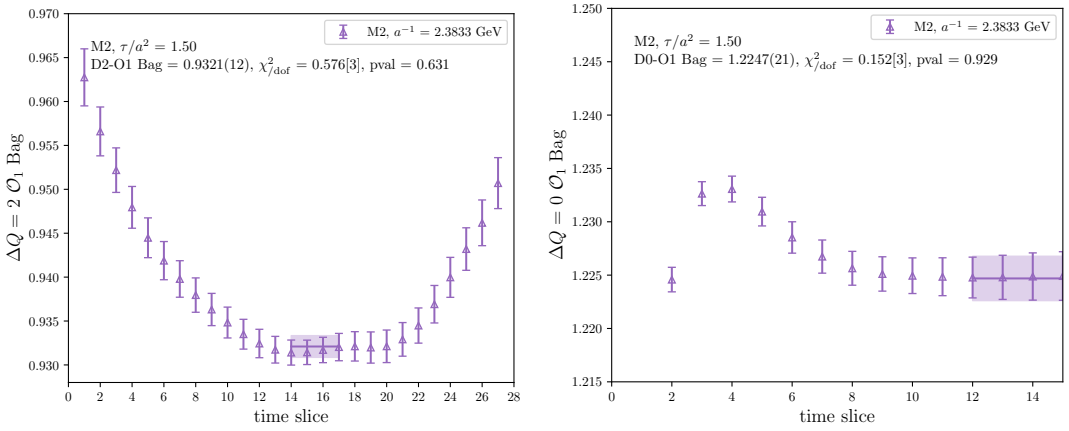

FIGURE 6.8: Examples of ground state fits to the $\mathcal{O}_1$ operators for $\Delta Q = 2$ (left) and $\Delta Q = 0$ (right) on the M2 ensemble at fixed flow time $\tau/a^2 = 1.50$.

parameters at fixed flow time $\tau/a^2 = 1.50$ on the M2 ensemble are shown in figure 6.8. Note that for the case of the $\Delta Q = 0$ operator on the right, we have exploited the symmetry of the signal and 'folded' the data in order to gain some improvement in the statistical signal of the plateau and to make the fitting procedure easier by reducing the number of data points[4]. In both cases, we find that extending the fits to include excited states does not improve the precision of the results while worsening the quality of the fits and therefore we choose to only consider ground state 'plateau' fits here.

The case of the T_1 operator is different since the operator is no longer symmetric in Euclidean time (recall equations (6.15) and (6.16)) due to the states defined at either

[4]In principle, this can be also be done for the $\Delta Q = 2$ correlator which is also symmetric.

side of the 3-point correlator being different. However, one still expects a plateau to be reached at some point where the excited states from both sides die off and the ground state matrix element $\langle \tau_i \rangle$ is found. Examples of fits to the bag parameter of T_1 at

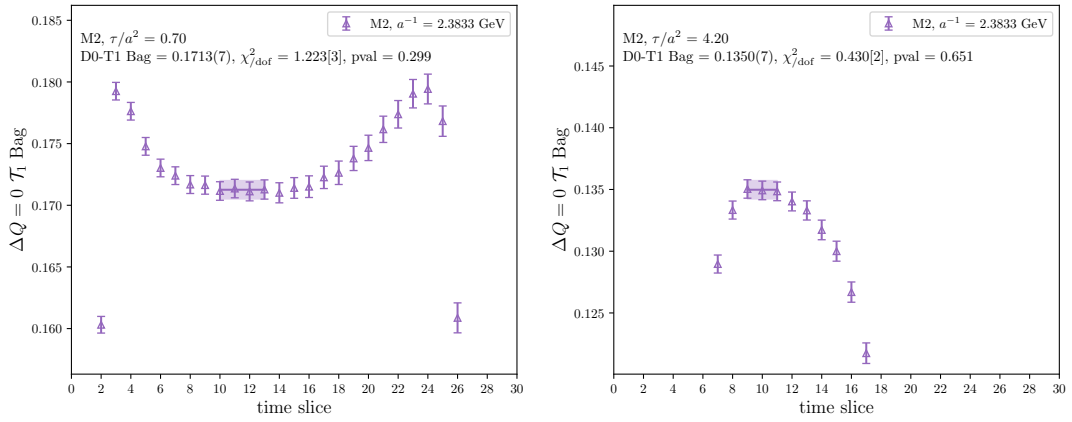

FIGURE 6.9: Examples of ground state fits to the T_1 operator for $\Delta Q = 0$ on the M2 ensemble at fixed flow times $\tau/a^2 = 0.70$ (left) and $\tau/a^2 = 4.20$ (right).

fixed flow times on the M2 ensemble are shown in figure 6.9. We find that for smaller flow times (as shown in the left of the figure), a ground state fit is sufficient to extract the signal, however for larger flow times the signal region becomes poorer (as shown in the right of the figure) and in future analysis more complex fits to e.g. multiple source separations ΔT simultaneously will also be studied. Extending the usable range of flow times in earlier steps of the analysis is always favoured for propagating onwards. It is however worth noting that the typical flow time values where the signal significantly worsens are beyond the scope of expected validity for the short-flow-time expansion and as such it can be argued to disregard these already at this stage.

Furthermore, the reliability of the extraction of T_1 depends on how reliable the meson-to-vacuum matrix elements are extracted from the 2-point correlator analysis. As the flow time increases, the 'smearing' effect of the gradient flow increases, which first enhances the overlap with the ground state but eventually the smearing grows too large and even the ground state matrix elements and masses can become difficult to resolve. Therefore for later flow times (again expected to be outside the range of the short-flow-time expansion), we cannot trust the analysis for T_1.

The fits discussed above to extract the bag parameters are performed at each discrete flow time as described in table 6.2, such that we can see the evolution of these bag parameters with the gradient flow as they are renormalised. In figures 6.10 and 6.11 the evolutions of B_1 for $\Delta Q = 2$ and $\Delta Q = 0$ are respectively shown, where the flow time evolution is shown on the left in lattice units τ/a^2 and on the right in physical units $\tau\,[\mathrm{GeV}^{-2}]$. One sees that while $\Delta Q = 2$ and $\Delta Q = 0$ are of different magnitude, they

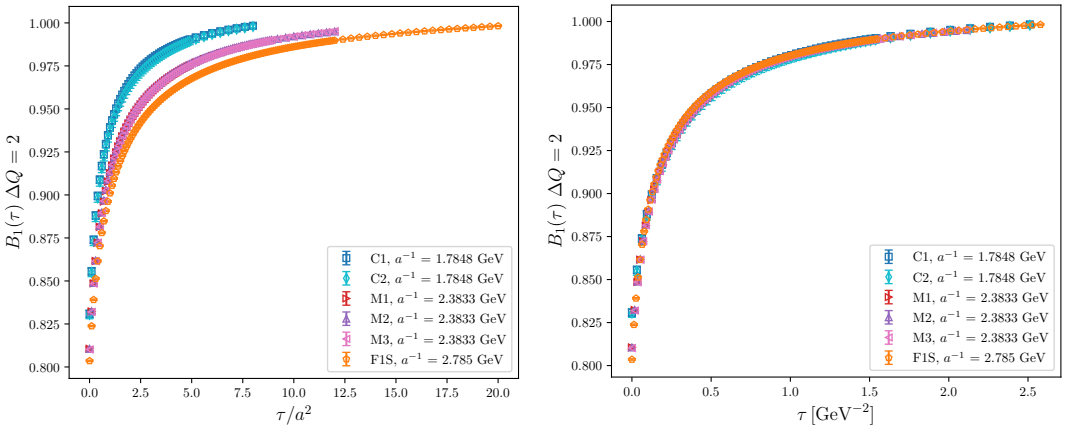

FIGURE 6.10: Flow time evolution of the $\Delta Q = 2$ bag parameter B_1 in lattice units τ/a^2 (left) and τ [GeV^{-2}] (right).

behave almost identically in the gradient flow evolution. On the left, we observe overlap between ensembles with the same lattice spacing differing only in the mass of the light sea quarks. Hence we can infer that sea quark effects are negligible. Furthermore on the right once at physical flow time, we find that all data at different lattice spacings and/or sea quark masses overlap beautifully. Thus we expect a mild continuum limit extrapolation.

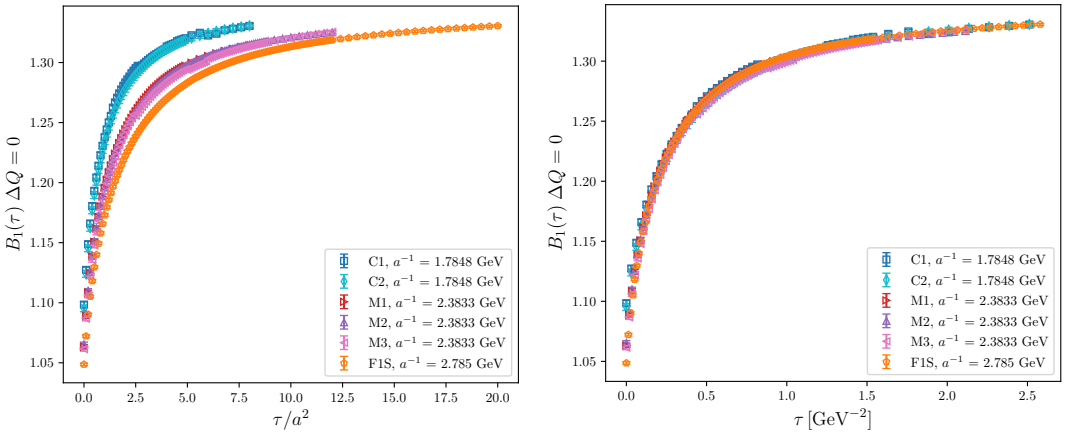

FIGURE 6.11: Flow time evolution of the $\Delta Q = 0$ bag parameter B_1 in lattice units τ/a^2 (left) and τ [GeV^{-2}] (right).

Next in figure 6.12 we show the flow time evolution of the ϵ_1 bag parameter for $\Delta Q = 0$. Notice that the extent in flow time of these plots is smaller than that for the B_1 parameters; this is due to the discussion above where for larger flow times the data of both the 2- and 3-point functions exhibit large smearing effects and the required matrix elements cannot be reliably extracted. In the left plot, one can see that while differences between ensembles at the same lattice spacing are small, they are still more noticeable than they were for B_1. This is understood to be down to fit systematics

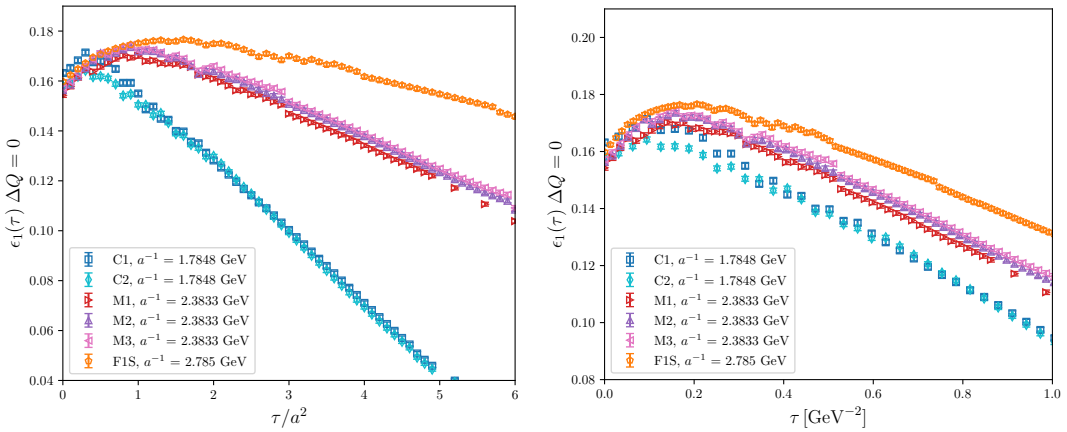

FIGURE 6.12: Flow time evolution of the $\Delta Q = 0$ bag parameter ϵ_1 across in lattice units τ/a^2 (left) and τ [GeV^{-2}] (right).

and these differences should be minimised by further improvement in the extraction of individual data points. In the centre region of the plots, where the flow time is not too small nor too large such that it is more suited to the short-flow-time expansion, the systematic effects of the fitting procedure are better controlled and there is more overlap of these ensembles. In the right plot in physical units, we notice that the continuum limit of this operator is not as mild as for B_1 since one sees a clear difference between the ensembles at different lattice spacings. While the stability and 'smoothness' of the evolutions leaves some space for improvement, the data within the typical range for short-flow-time analysis still looks to behave well such that a continuum limit seems viable and the short-flow-time expansion can be performed.

6.2.4 The Continuum Limit

After completing the correlator analyses along the flow time, the next step is taking the continuum limit. As already mentioned in the discussion around figures 6.10 and 6.11, additional systematics appear to be relatively small, such that we can advocate for a simple continuum limit fit of the form

$$B = \mathcal{B} + a^2\Gamma, \tag{6.19}$$

i.e. a linear fit in a^2 since that is the lowest order at which discretisation errors of the used actions are expected. We perform this fit at each discrete flow time step of the finest ensemble F1S. To do this, we first interpolate the values of the C and M ensembles from their discrete flow times to the F1S values, assuming a linear region between two data points bracketing the desired value. In figure 6.13, we show the continuum limit extrapolations at two values of the flow time for the B_1 bag parameter for $\Delta Q = 2$, where

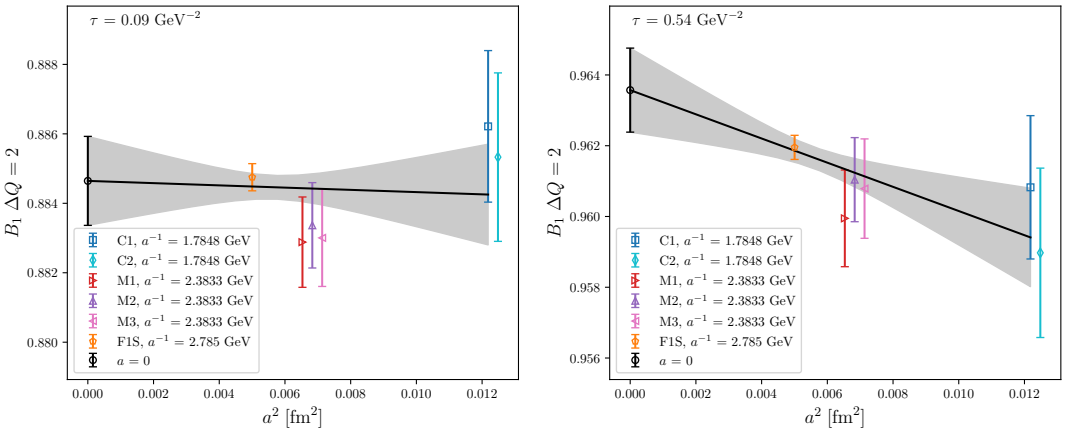

FIGURE 6.13: Examples of continuum limit extrapolations for the B_1 bag parameter for $\Delta Q = 2$ at flow time $\tau = 0.09\,\text{GeV}^{-2}$ (left) and $\tau = 0.54\,\text{GeV}^{-2}$ (right). For visibility, the M1 ensemble (red) is plotted with a slight offset to the left, and the C2 (cyan) and M3 (pink) ensembles to the right.

the left plot shows one of the 'flattest' extrapolations and the right plot one with the largest slope, which is however still relatively mild. The continuum limit extrapolations at other flow times and also for B_1 for $\Delta Q = 0$ look similar, as shown in figure 6.14.

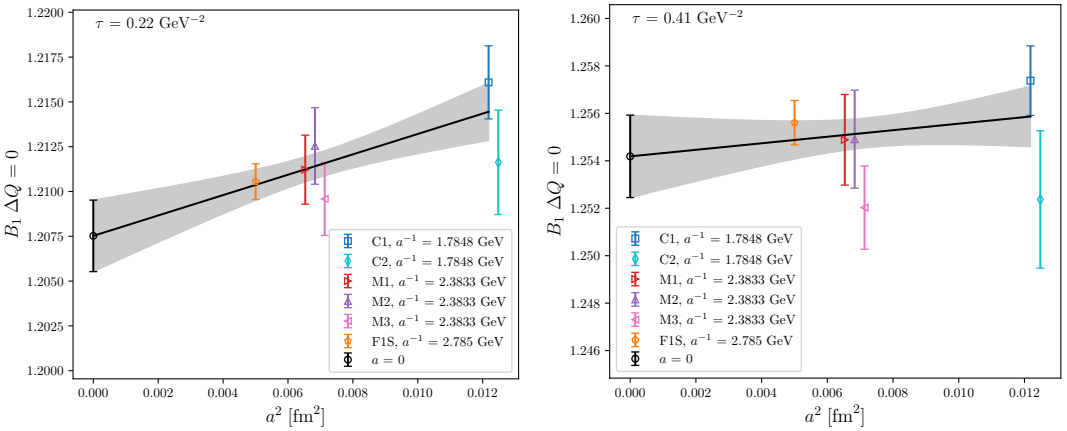

FIGURE 6.14: Examples of continuum limit extrapolations for the B_1 bag parameter for $\Delta Q = 0$ at flow time $\tau = 0.19\,\text{GeV}^{-2}$ (left) and $\tau = 0.41\,\text{GeV}^{-2}$ (right). For visibility, the M1 ensemble (red) is plotted with a slight offset to the left, and the C2 (cyan) and M3 (pink) ensembles to the right.

As expected from figure 6.12, the continuum limits for ϵ_1 are not as flat as those above. The procedure for the continuum limit is however similar to that for the B_1's: the data is first interpolated on the C and M ensembles to match the flow time values of the F1S ensemble, then a naive linear fit in a^2 is used to take the continuum limit. In figure 6.15, we show continuum limit extrapolations at two values of the flow time for ϵ_1. Although these data show a steeper line than the cases for B_1, they are still in good agreement with a linear ansatz. The spread between the values corresponding the different sea quark masses at the same lattice spacing may be indicative of unaccounted systematic

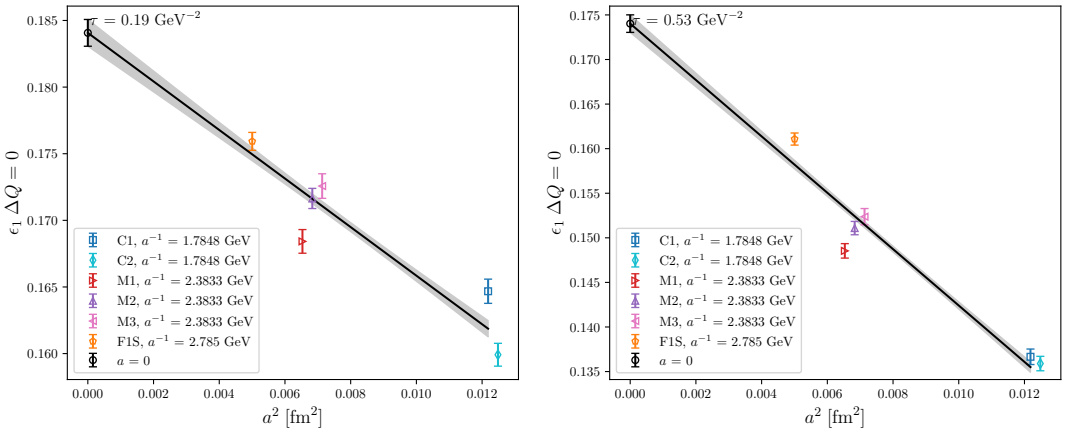

FIGURE 6.15: Examples of continuum limit extrapolations for the ϵ_1 bag parameter for $\Delta Q = 0$ at flow time $\tau = 0.19\,\text{GeV}^{-2}$ (left) and $\tau = 0.53\,\text{GeV}^{-2}$ (right). For visibility, the M1 ensemble (red) is plotted with a slight offset to the left, and the C2 (cyan) and M3 (pink) ensembles to the right.

uncertainties in fitting the plateaus and less likely to be resolving effects due to the different sea quark masses.

6.2.5 Matching to $\overline{\text{MS}}$

With continuum results as a function of the flow time, the final step of the procedure is to match these GF-renormalised results to the $\overline{\text{MS}}$ scheme.

First, we consider the B_1 bag parameter for the $\Delta Q = 2$ operator. The perturbative calculation of $\zeta_{B_1}^{-1}$ is taken at both NLO and NNLO such that we can observe the systematic effects of the use of perturbation theory. In addition, we also include the logarithmic terms at higher powers of α_s to observe these effects, although the full calculation beyond NNLO has not been performed. In figure 6.16, we show the flow-time dependence of $\zeta_{B_1}^{-1}(\tau)$ at NLO and NNLO, including the effects of the logarithms at higher powers of α_s.

The matching factor in the different perturbative scenarios is then combined with the continuum-limit lattice data; this combination is shown in figure 6.17. As discussed above, the short-flow-time expansion now relates this quantity to the $\overline{\text{MS}}$-renormalised result $B_1^{\overline{\text{MS}}}$ in the limit of $\tau \to 0$, assuming a linear extrapolation in the flow time. Recall that this extrapolation involves the consideration of a 'window' problem where we recognise that the data at very small τ suffers from e.g. interference with UV fluctuations, and higher-power effects dominate at larger τ. At NLO we choose the flow time window $0.28\,\text{GeV}^{-2} \leq \tau \leq 0.49\,\text{GeV}^{-2}$ and at NNLO (as well as with higher logarithms) we choose $0.18\,\text{GeV}^{-2} \leq \tau \leq 0.49\,\text{GeV}^{-2}$. Within the flow time windows, an uncorrelated linear fit to the data is performed and then extrapolated to $\tau = 0$. The uncertainty on

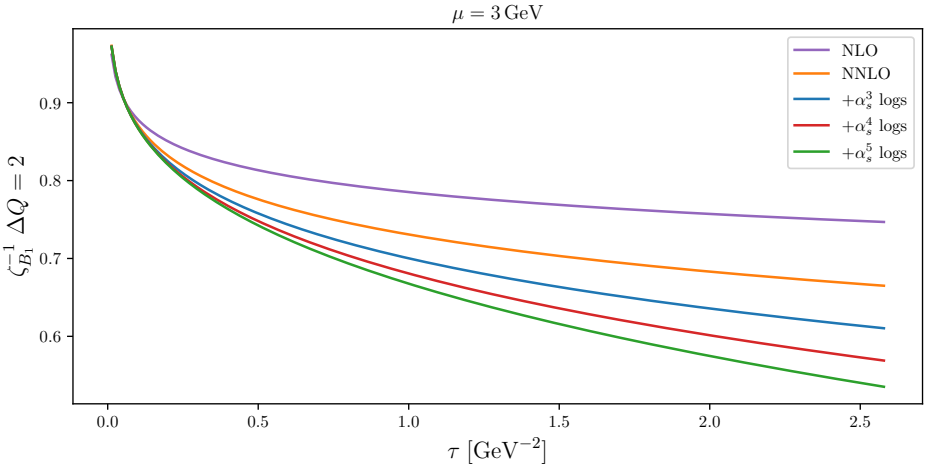

FIGURE 6.16: Flow-time dependence of $\zeta_{B_1}^{-1}(\tau)$ at NLO (purple) and NNLO (orange), where at NNLO we also consider logarithms at higher powers of α_s (blue, red, green). The renormalisation scale is set to $\mu = 3\,\mathrm{GeV}$.

the extrapolation is taken as the difference between the fit for the central values and the fit for the upper limits of the data. As can be seen both in the figure and from the chosen flow time windows, the effect of going to higher order in perturbation theory extends the region of validity for the flow time window towards smaller τ.

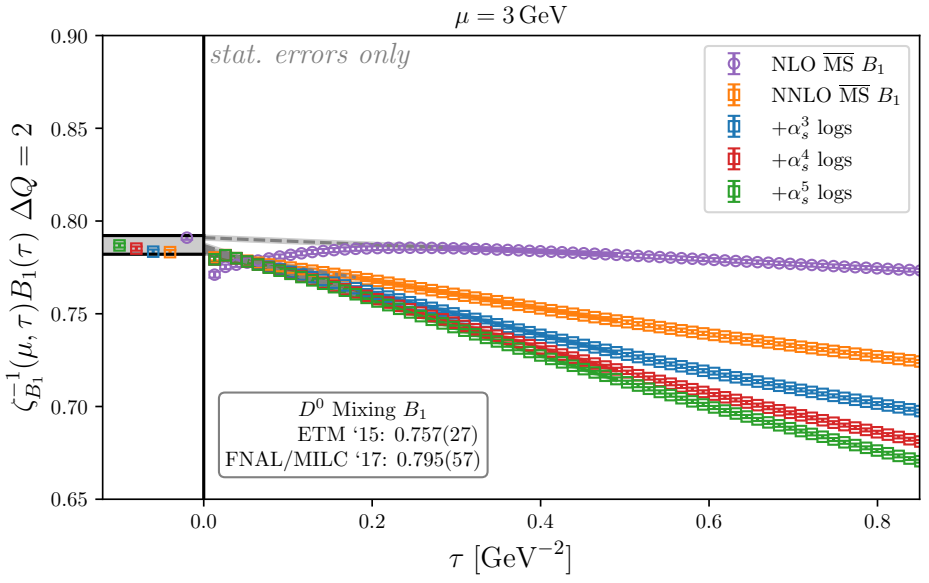

FIGURE 6.17: Flow-time dependence of the combination $\zeta_{B_1}^{-1}(\mu,\tau)B_1(\tau)$ with different perturbative orders: NLO (purple), NNLO (orange), $+\alpha_s^3$ logs (blue), $+\alpha_s^4$ logs (red), $+\alpha_s^5$ logs (green). Error bars represent statistical uncertainties only, however the continuum extrapolation particularly at small flow times ($\tau \lesssim 0.2\,\mathrm{GeV}^{-2}$) will contribute large systematic effects. The gray bands leading from each coloured data set represent the $\tau \to 0$ extrapolations taken from uncorrelated linear fits; the results at $\tau = 0$ are then shown in the left panel.

As previously mentioned, we simulate an unphysical 'neutral charm-strange' meson which does not have exact phenomenological meaning for its $\Delta Q = 2$ operators, however this can be seen as a proxy to the short-distance effects of D^0 meson mixing, up to some spectator effects which are likely to be small. In the literature, the short-distance matrix elements for D^0 mixing have been calculated on the lattice by FNAL/MILC at $N_f = 2 + 1$ and ETMC at $N_f = 2 + 1 + 1$, with $\mu = 3\,\text{GeV}$. ETMC finds a value of $B_1^{\overline{\text{MS}}} = 0.757(27)$ [466]. FNAL/MILC quotes a values for $\langle \mathcal{O}_1 \rangle^{\overline{\text{MS}}}$; using PDG [54] and equation (3.104), this leads to $B_1^{\overline{\text{MS}}} = 0.795(57)$ [467]. There also exists a prediction from HQET sum rules which, again using PDG [54], results in $B_1^{\overline{\text{MS}}} = 0.654^{+0.060}_{-0.052}$ [168]. By comparing to figure 6.17, one can see that the preliminary results found here lie between the two literature values from lattice QCD and slightly above that from HQET sum rules. We take the range from the different perturbative orders, including their uncertainties, as the range of our final value and assume symmetric errors. This yields

$$B_1^{\overline{\text{MS}}}(3\,\text{GeV}) = 0.787(5), \tag{6.20}$$

where the uncertainty incorporates the statistical uncertainty of the data and the systematic error of different truncations in perturbation theory. While treatment of further systematic effects is still required (see section 6.3), this agreement with the literature is a clear sign of success for the gradient flow and short-flow-time expansion as a renormalisation and matching procedure.

Next, we consider the B_1 and ϵ_1 bag parameters for the $\Delta Q = 0$ operators. The perturbative matching matrix ζ_{nm}^{-1} is taken at NLO, and we remind the reader again that a simplified picture of the operators for lifetime differences is used to calculate the matching where the complications of lower-dimensional perturbative mixing are removed. We assume this matching is sufficient to give first estimates of these quantities while the method is tested and validated, and the full calculation will be completed for future results with increased accuracy. The flow-time dependence of the components of $\zeta_{nm}^{-1}(\tau)$ for matching to $B_1^{\overline{\text{MS}}}$ (left) and $\epsilon_1^{\overline{\text{MS}}}$ (right) are shown in figure 6.18.

The matching matrices are then combined with the continuum-limit lattice data as shown in figure 6.19 for $B_1^{\overline{\text{MS}}}$ and figure 6.20 for $\epsilon_1^{\overline{\text{MS}}}$. We choose the flow time window $0.39\,\text{GeV}^{-2} \leq \tau \leq 0.61\,\text{GeV}^{-2}$ for both bag parameters and perform an uncorrelated linear fit to the data to then extrapolate to $\tau = 0$. Unlike the case for $\Delta Q = 2$, the $\Delta Q = 0$ QCD matrix elements for a charm-strange meson do have phenomenological meaning on their own to determine the D_s meson lifetime. However, as stressed in the goal of this project, there are no existing predictions for these from lattice QCD in the literature. There does exist a HQET sum rule calculation for D^0 lifetimes, predicting

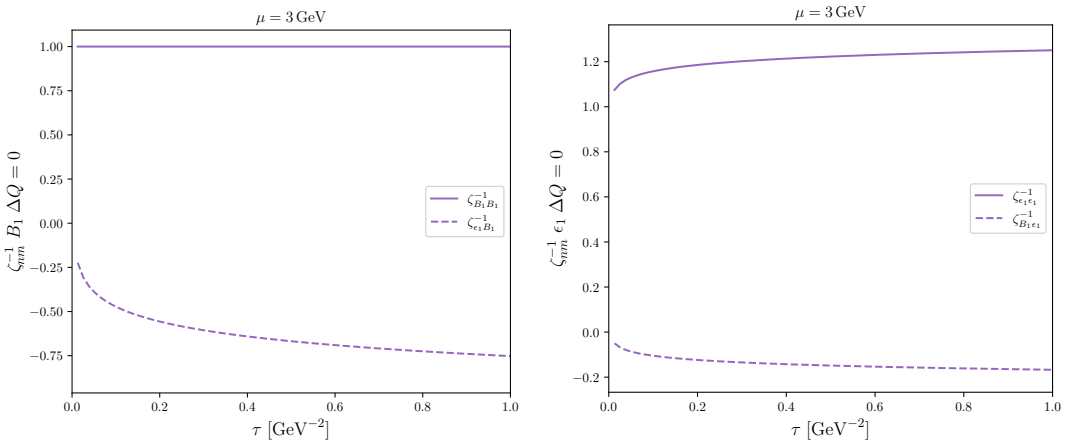

FIGURE 6.18: Flow-time dependence of $\zeta^{-1}_{nm}(\tau)$ at NLO for $B_1^{\overline{\mathrm{MS}}}$ (left) and $\epsilon_1^{\overline{\mathrm{MS}}}$ (right). The solid line indicates the component of ζ^{-1} which multiplies B_1^{GF} (left) / ϵ_1^{GF} (right) and the dashed line indicates the component of ζ^{-1} which multiplies ϵ_1^{GF} (left) / B_1^{GF} (right). The renormalisation scale is set to $\mu = 3\,\mathrm{GeV}$.

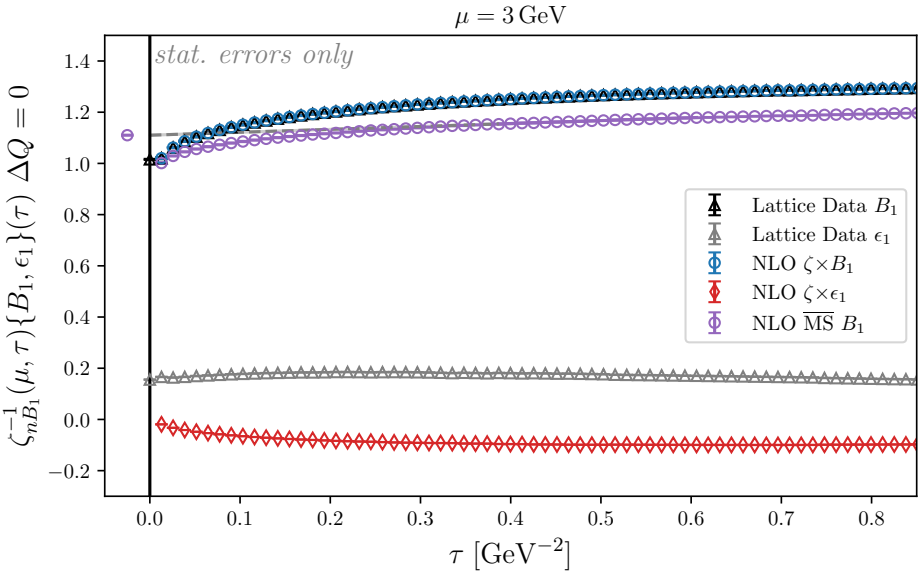

FIGURE 6.19: Flow-time dependence of the combination $\zeta^{-1}_{nB_1}(\mu,\tau)\{B_1,\epsilon_1\}(\tau)$ at NLO (purple). The continuum-limit lattice data for B_1 (ϵ_1) is shown in black (gray) and their individual combinations with ζ^{-1} in blue (red). Error bars represent statistical uncertainties only, however the continuum extrapolation particularly at small flow times ($\tau \lesssim 0.2\,\mathrm{GeV}^{-2}$) will contribute large systematic effects. The gray band represents the $\tau \to 0$ extrapolation taken from the purple data in the chosen window; the result at $\tau = 0$ is shown in the left panel.

$B_1 = 0.902^{+0.077}_{-0.051}$ and $\epsilon_1 = -0.132^{+0.041}_{-0.046}$ [168]. In our calculation we find

$$B_1^{\overline{\mathrm{MS}}}(3\,\mathrm{GeV}) = 1.110(2), \tag{6.21}$$

$$\epsilon_1^{\overline{\mathrm{MS}}}(3\,\mathrm{GeV}) = 0.119(1), \tag{6.22}$$

with statistical uncertainties only; see section 6.3 for a breakdown of further uncertainties

to be quantified. We see that both B_1 and ϵ_1 bag parameters have the correct order of magnitude with respect to the literature values, which we take as a promising sign for these early results. However, one also notices that the ϵ_1 parameter currently has a sign difference to the literature value. It it still to be understood how this sign difference arises which is to be included in future work, although it is worth noting that the existing HQET sum rules result is also currently under scrutiny.

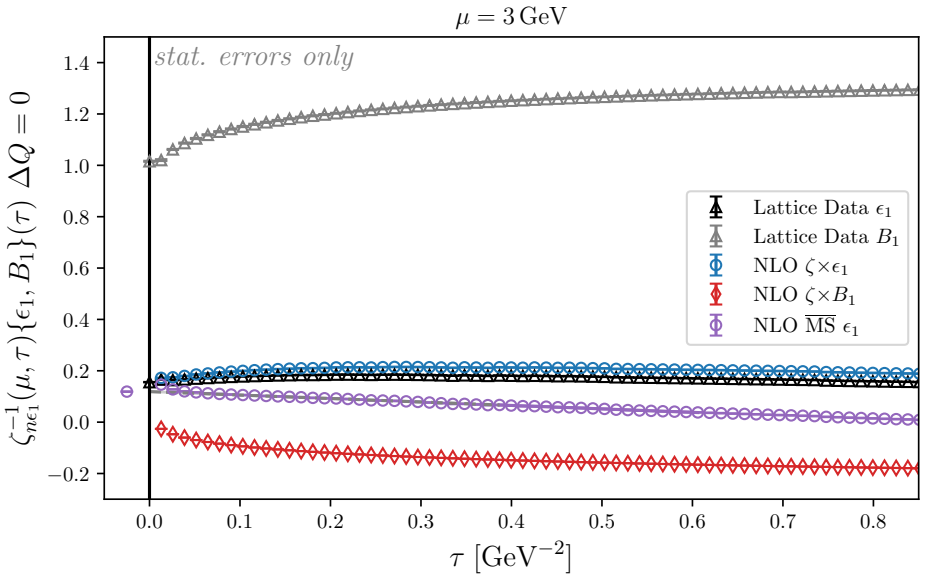

FIGURE 6.20: Flow-time dependence of the combination $\zeta^{-1}_{n\epsilon_1}(\mu,\tau)\{\epsilon_1, B_1\}(\tau)$ at NLO (purple). The continuum-limit lattice data for ϵ_1 (B_1) is shown in black (gray) and their individual combinations with ζ^{-1} in blue (red). Error bars represent statistical uncertainties only, however the continuum extrapolation particularly at small flow times ($\tau \lesssim 0.2\,\mathrm{GeV}^{-2}$) will contribute large systematic effects. The gray band represents the $\tau \to 0$ extrapolation taken from the purple data in the chosen window; the result at $\tau = 0$ is shown in the left panel.

We stress again that this does not yet represent a complete calculation of the bag parameters for $\Delta Q = 0$ from lattice QCD since we are still to include the 'eye' diagram contributions and the complete perturbative matching. However, these results show a first estimate from lattice QCD and represent a promising first step towards a complete calculation of the bag parameters for $\Delta Q = 0$ operators.

6.3 Systematics

As the research presented here is a pilot study aimed at establishing the gradient flow renormalisation and matching procedure, we have not yet been concerned about propagating all systematic effects through the analysis and into the results in figures 6.17, 6.19, and 6.20 and equations (6.20)-(6.22). However, these must be kept in mind as they will

represent an important aspect of the final results. Below we briefly collect and discuss some of the important systematic effects in our calculation.

Correlator Fitting

The fitting of the 2- and 3-point correlation functions can introduce a bias and systematic effect through the choice of specific fit ranges being favoured over others. We can minimise our bias, and estimate any systematic uncertainties, by varying the fit ranges used for fitting and observing the subsequent spread of results. Furthermore, since we do not expect significant sea quark effects for the heavy-light system considered, the ensembles at the same lattice spacing should give compatible results and the fit ranges used on the different ensembles are therefore in most cases the same. This serves as a necessary but not sufficient condition to reduce bias in choosing the fit range.

Continuum Limit

A systematic uncertainty from the continuum limit extrapolation can be estimated by varying the fit ansatz to test for e.g. $O(a^4)$ effects, finite volume corrections, etc. Furthermore, different subsets of the lattice ensembles can be considered instead, for example omitting the two coarsest ensembles.

Discretisation Errors

The dominant discretisation errors associated with the gauge and fermion actions are $O((a\Lambda_{\mathrm{QCD}})^2)$, which will be accounted for in the continuum limit extrapolations as long as a term $\propto a^2$ is present.

Sub-dominant effects from the discretisation can also be considered, however these are typically seen to be $< 1\%$ and taken as negligible here.

Lattice Scale Uncertainty

The uncertainties on the lattice scales of the various ensembles are well-determined; see table 6.1. These uncertainties can be accounted for as part of the continuum limit analysis by varying the lattice spacings input to the continuum fit by 1σ and assigning an uncertainty from the resulting spread of continuum values.

The gradient flow time in physical units is also determined using the lattice scale as a conversion factor, and as such the lattice scale uncertainty must also be propagated into the flow time. Similarly to above, the lattice scale in this conversion can be varied by 1σ and the systematic effect estimated from any difference.

Quark Mass Tuning

The simulated strange quark masses have a slight mistuning to the determined physical values on each ensemble, with the mistuning effect varying by ensemble. In general, light spectator effects are expected to be small for four-quark operators and heavy-light

systems such that the small mistuning of their value is not anticipated to present a significant effect. Simulations with varied values of the charm and/or strange quark mass allow however to properly estimate these effects.

The value of the charm quark on each ensemble is tuned to replicate the physical D_s meson mass. On all ensembles, the D_s meson mass is reproduced within 10 MeV of the physical value and mistuning effects are expected to be subleading.

In a larger-scale simulation, measurements can be performed at multiple values of the valence quark masses for both charm and strange such that systematic uncertainties from mistuning can be quantitatively evaluated.

Perturbative Matching

As mentioned in the discussion around figure 6.17, we can associate a systematic uncertainty with the perturbative matching calculation by observing the variation in the result at different perturbative orders. The results between NLO and NNLO for the $\Delta Q = 2$ B_1 parameter are in close agreement with one another where their difference implies an uncertainty associated with the perturbative truncation which is already incorporated into the quoted error.

The systematic effects for the $\Delta Q = 0$ perturbative matching remain to be evaluated and will be meaningful in the context of the complete matching calculation still to be done.

$\tau \to 0$ limit

An effect which will be correlated with the perturbative matching procedure above is how to take the $\tau \to 0$ limit. In a full analysis, this extrapolation should be performed using a fully-correlated fit instead of the simple uncorrelated fit chosen so far for this pilot study. In this way, some of the additional effects of this extrapolation will already be accounted for properly as part of the quoted statistical uncertainty of the final result.

Further systematic effects in this extrapolation could be considered by e.g. varying the fit ansatz to include further terms such as quadratic or logarithmic behaviour in the flow time; any additional ansätze should however be well-motivated from the theoretical perspective of the gradient flow.

6.4 Future Prospects

In the above discussions, we have laid out a pilot study to establish the gradient flow as a non-perturbative renormalisation procedure for lattice QCD calculations and its short-flow-time expansion as a perturbative matching method to the $\overline{\text{MS}}$ scheme. While

this pilot study shows promising first results for this method, further work is required to expand and improve upon this study. Below we list some of the future tasks we have in mind to develop this study further and extend its reach to the main phenomenological motivation – B meson lifetimes.

Eye Diagram Contributions

The simulations carried out for this pilot study do not take into account the 'eye' diagram contributions to the $\Delta Q = 0$ operators (recall figure 6.5). These diagrams are much more expensive to simulate to a statistically-viable level and are meanwhile expected to have only small contributions to the final result. It is however important to validate the expectation of their size by calculating these and including their effects in a final result. These diagrams are planned to be simulated in the future using the method discussed in [430].

Full Operator Bases

In addition to the $\mathcal{O}_1$ operator for $\Delta Q = 2$ and $\mathcal{O}_1$, T_1 operators for $\Delta Q = 0$ considered here, we extend our analysis to cover the full operator bases of $\Delta Q = 2$ and $\Delta Q = 0$ as defined in equations (6.7) and (6.9) respectively.

Perturbative Matching Calculation

We have so far stressed that the perturbative matching calculation for $\Delta Q = 0$ is taken in the simplified limit of the lifetime difference operators where the mixing with operators of lower mass-dimension completely cancels out. It is difficult to estimate how large the impact of this simplification is to the complete result. Work is ongoing to calculate the full perturbative matching to more accurately predict our final values.

In addition, the perturbative matching has not yet been calculated for the full $\Delta Q = 2$ operator basis; for predictions of this set of operators, this calculation must also be undertaken.

Large-scale Simulation

For this pilot study, we minimised simulation cost by only simulating at a single fixed charm and strange quark mass, targeting the physical D_s meson. For a full-scale run in order to better account for all systematic effects in the quark mass values and also to extend the project to D^0, B^0, B_s mesons, we want to perform the simulation for multiple 'heavy' quark masses ranging from charm to 'near-to-bottom'. The reach above the charm quark mass must be carefully controlled to keep discretisation effects under control (recall section 5.1.6) while minimising the extrapolation to the physical b quark. We will also simulate multiple spectator quark masses for both light and strange quarks to consider all spectator effects and control all systematics towards the physical systems.

Simulating at both light and strange spectator quarks will in addition allow us to consider the matrix elements for the lifetime differences and predict ratios such as τ_{B_s}/τ_{B_d}.

Further Observables

While the bag parameters studied here are a particularly well-suited choice for the gradient flow renormalisation since in the ratios used to define them, additional multiplicative renormalisation factors cancel out which would otherwise also have to be calculated. For other observables, it can nonetheless be possible to calculate this additional renormalisation if needed and the gradient flow procedure could be beneficial to many calculations in the future.

Chapter 7

Conclusions

It is obvious both phenomenologically and cosmologically that there must be more to the fundamental laws of physics at the smallest scales than what is currently described by the Standard Model. While a number of experimental measurements lie in tension with their SM predictions, none yet are taken to be significant enough to confirm a discovery of some new physics effect. Attention should be given in the search for new physics to quark flavour physics where important insights into the limitations of the Standard Model and the accessibility of new physics can be made.

We performed global fits to the current experimental state of the quark flavour sector and others in the context of indirect searches for new physics, specifically Two-Higgs-Doublet Models of various types. The collection of flavour observables considered were a powerful tool in shaping the landscape of the allowed parameter space for various types of the Two-Higgs-Doublet Model, which better informs experiment where direct searches may reveal new particles if such a scenario has been chosen by nature.

Furthermore, in the search for new physics at collider experiments, one can motivate searches for decay channels which will never be observed in the Standard Model as 'smoking gun' signatures for new physics. Specifically, we showed that the decay mode $B_s \to e^+e^-$, while orders of magnitude too small to be observed in the foreseeable future in the Standard Model, can be significantly enhanced by a Two-Higgs-Doublet Model without contradicting other measurements, such that any observation of this in a modern particle collider is not only a smoking gun signature of new physics, but a theoretically well-motivated one.

From the analysis of these indirect BSM searches, it is clear that a significant limitation to the leverage of quark flavour physics observables is the precision of their non-perturbative hadronic parameters. Many observables, such as the mass difference

of neutral B meson mixing, are in a strong place to further constrain our tests for new physics, however their hadronic uncertainties decrease their significance. Therefore an important factor towards refining the Standard Model and constraining possible new physics is the increased precision of these hadronic observables.

We therefore followed the goal to improve the precision of the predictions of hadronic observables through non-perturbative methods. We perform a lattice QCD calculation aimed at predicting the matrix elements of the dimension-six four-quark operators describing neutral meson mixing ($\Delta Q = 2$) and meson lifetimes ($\Delta Q = 0$). The main highlight of this calculation is that we demonstrate a new non-perturbative renormalisation procedure based on the gradient flow which is then perturbatively matched to the $\overline{\text{MS}}$ using the short-flow-time expansion. Since $\Delta Q = 2$ matrix elements are well-established, these provide a test case for validation of our method, while the goal is to use this new method to provide first predictions from full lattice QCD for the $\Delta Q = 0$ matrix elements.

The results of this pilot study are simulated at the physical charm and strange masses to produce a 'neutral charm-strange' meson. We determined the bag parameters of the $\Delta Q = 2$ matrix elements which can be compared to the existing literature results from both lattice QCD and HQET sum rules for short-distance D^0 mixing. These should be equivalent up to spectator effects. Indeed, we find good agreement between the literature values and our results based on the new renormalisation procedure presented here. We quote a value of

$$B_1^{\overline{\text{MS}}}(3\,\text{GeV}) = 0.787(5), \tag{7.1}$$

where the preliminary uncertainty incorporates the statistical uncertainty of the data and the systematic of different truncations in perturbation theory.

Furthermore, we pioneer first estimates for the bag parameters of the $\Delta Q = 0$ operators for meson lifetimes at the D_s mass scale, finding

$$B_1^{\overline{\text{MS}}}(3\,\text{GeV}) = 1.110(2), \tag{7.2}$$

$$\epsilon_1^{\overline{\text{MS}}}(3\,\text{GeV}) = 0.119(1), \tag{7.3}$$

with statistical uncertainties only. These early results show promise towards a final prediction, with the expected magnitudes comparable to HQET sum rules. However a sign difference in the ϵ_1 bag parameter is still to be understood. With the encouraging pilot study almost complete, we look forward to the prospects of performing the full calculation including all diagrams and perturbative contributions in the future.

With the method of gradient flow renormalisation and the short-flow-time expansion matching showing promising early signs, next steps will be towards a larger-scale simulation to improve upon the study presented here, where the goal will be to give first-time lattice QCD predictions for the $\Delta Q = 0$ bag parameters for D and B mesons with different spectator quarks. Finally, with the method established from the bag parameter calculations, the gradient flow renormalisation procedure can be further applied to other lattice QCD calculations as a new non-perturbative renormalisation scheme.

Appendix A

Algebra of the Standard Model

A.1 Gauge Groups

A.1.1 SU(2)

The generators τ_i of the SU(2) group in the fundamental representation are proportional to the Pauli matrices σ_i, i.e.

$$\tau_i = \frac{1}{2}\sigma_i, \tag{A.1}$$

where the Pauli matrices are defined

$$\sigma_1 = \begin{pmatrix} 0 & 1 \\ 1 & 0 \end{pmatrix}, \qquad \sigma_2 = \begin{pmatrix} 0 & -i \\ i & 0 \end{pmatrix}, \qquad \sigma_3 = \begin{pmatrix} 1 & 0 \\ 0 & -1 \end{pmatrix}. \tag{A.2}$$

These satisfy

$$\sigma_j \sigma_k = \delta_{jk} + i\epsilon_{jkl}\sigma_l, \tag{A.3}$$

where the 3-dimensional Levi-Civita tensor elements are the structure constants of su(2) and the convention used is that $\epsilon_{123} = 1$. In the 3-dimensional adjoint representation of SU(2), the generators T_i are defined by the structure constants themselves:

$$(T^i)_{jk} = -\frac{i}{2}\epsilon_{ijk}. \tag{A.4}$$

A.1.2 SU(3)

The generators τ_a of the su(3) group in the fundamental representation are related to the Gell-Mann matrices λ_a which are derived as an extension of the Pauli matrices to a

3-dimensional space as

$$\tau_a = \frac{1}{2}\lambda_a. \tag{A.5}$$

The Gell-Mann matrices are written as

$$\begin{aligned}
\lambda_1 &= \begin{pmatrix} 0 & 1 & 0 \\ 1 & 0 & 0 \\ 0 & 0 & 0 \end{pmatrix}, \quad \lambda_2 = \begin{pmatrix} 0 & -i & 0 \\ i & 0 & 0 \\ 0 & 0 & 0 \end{pmatrix}, \quad \lambda_3 = \begin{pmatrix} 1 & 0 & 0 \\ 0 & -1 & 0 \\ 0 & 0 & 0 \end{pmatrix}, \\
\lambda_4 &= \begin{pmatrix} 0 & 0 & 1 \\ 0 & 0 & 0 \\ 1 & 0 & 0 \end{pmatrix}, \quad \lambda_5 = \begin{pmatrix} 0 & 0 & -i \\ 0 & 0 & 0 \\ i & 0 & 0 \end{pmatrix}, \\
\lambda_6 &= \begin{pmatrix} 0 & 0 & 0 \\ 0 & 0 & 1 \\ 0 & 1 & 0 \end{pmatrix}, \quad \lambda_7 = \begin{pmatrix} 0 & 0 & 0 \\ 0 & 0 & -i \\ 0 & i & 0 \end{pmatrix}, \quad \lambda_8 = \frac{1}{\sqrt{3}} \begin{pmatrix} 1 & 0 & 0 \\ 0 & 1 & 0 \\ 0 & 0 & -2 \end{pmatrix}.
\end{aligned} \tag{A.6}$$

These satisfy the commutation relation

$$[\lambda^a, \lambda^b] = 2if^{abc}\lambda^c, \tag{A.7}$$

where f^{abc} are the structure constants of SU(3). The generators T_a in the adjoint representation are defined by

$$(T^a)_{bc} = -if^{abc}. \tag{A.8}$$

A.2 Clifford Algebra and Dirac matrices

A.2.1 Minkowski Dirac Matrices

We define the Dirac matrices γ_μ, $\mu = 0, 1, 2, 3$ in four-dimensional Minkowski space as

$$\gamma_0 = \begin{pmatrix} \mathbb{1}_2 & 0 \\ 0 & -\mathbb{1}_2 \end{pmatrix}, \quad \gamma_j = \begin{pmatrix} 0 & \sigma_j \\ -\sigma_j & 0 \end{pmatrix}, \quad \gamma_5 = i\gamma_0\gamma_1\gamma_2\gamma_3 = \begin{pmatrix} 0 & \mathbb{1}_2 \\ -\mathbb{1}_2 & 0 \end{pmatrix}. \tag{A.9}$$

These obey the Clifford algebra

$$\{\gamma_\mu, \gamma_\nu\} = 2g_{\mu\nu}\mathbb{1}_4, \tag{A.10}$$

where $g_{\mu\nu}$ is the Minkowski metric tensor

$$g_{\mu\nu} = \mathrm{diag}(1, -1, -1, -1). \tag{A.11}$$

The commutator of two Dirac matrices is written

$$\sigma^{\mu\nu} = \frac{i}{2}[\gamma^\mu, \gamma^\nu]. \tag{A.12}$$

A.2.2 Euclidean Dirac Matrices

With the Wick rotation to Euclidean space, the Euclidean Dirac matrices γ^E_μ, $\mu = 1, 2, 3, 4$ are related to the Minkowski matrices as

$$\gamma^E_4 = \gamma^M_0, \qquad \gamma^E_j = -i\gamma^M_j, \qquad \gamma^E_5 = \gamma_1\gamma_2\gamma_3\gamma_4. \tag{A.13}$$

The Euclidean Clifford algebra is

$$\{\gamma^E_\mu, \gamma^E_\nu\} = 2\delta_{\mu\nu}\mathbb{1}_4, \tag{A.14}$$

where $\delta_{\mu\nu}$ is the Kronecker delta.

A.3 Grassmann Variables

Here we summarise the basic algebra of Grassmann variables. The interested reader should turn to e.g. [351] for further details.

A.3.1 Basic Rules

We define θ_i, $i = 1, 2, \ldots, N$ to be Grassmann numbers. Then, the basic anticommuting definition of these requires

$$\theta_i\theta_j = -\theta_j\theta_i \quad \forall\ i, j. \tag{A.15}$$

This further implies the Grassmann variables are *nil-potent*, i.e.

$$\theta_i^2 = 0, \tag{A.16}$$

and also that a power series for some function $f(\theta_i)$ will terminate after a finite number of terms. The only relevant class of functions are the polynomials

$$P = a + \sum_i a_i\theta_i + \sum_{i<j} a_{ij}\theta_i\theta_j + \sum_{i<j<k} a_{ijk}\theta_i\theta_j\theta_k + \cdots + a_{12\ldots N}\theta_1\theta_2\ldots\theta_N, \tag{A.17}$$

with complex coefficients a, a_i, $a_{ij}, \ldots, a_{12\ldots N}$. These polynomials can be added and multiplied, i.e. they form the basis for the *Grassmann algebra*.

A.3.2 Differentiation

Elements of the Grassmann algebra can be differentiated with respect to the Grassmann variables θ_i – the θ_i can also be described as the *generators* of the Grassmann algebra. Consider the polynomial A and its derivative in θ_1:

$$\begin{aligned} A &= a + a_1\theta_1 + a_2\theta_2 + a_{12}\theta_1\theta_2, \\ \frac{\partial A}{\partial \theta_1} &= a_1 + a_{12}\theta_2. \end{aligned} \tag{A.18}$$

If we rewrite A using the anticommutation rule (equation (A.15)), we can see that to maintain consistency, we require to define the Grassmann anticommutation property for the derivative also:

$$\frac{\partial}{\partial\theta_1}\theta_2 = -\theta_2\frac{\partial}{\partial\theta_1}. \tag{A.19}$$

Further applying the derivative $\frac{\partial}{\partial\theta_2}$ to $\frac{\partial A}{\partial\theta_1}$ reveals that derivatives must anticommute as well. In summary, this all results with the following Grassmann rules for differentiation:

$$\begin{aligned} \frac{\partial}{\partial\theta_i}1 &= 0, & \frac{\partial}{\partial\theta_i}\frac{\partial}{\partial\theta_j} &= -\frac{\partial}{\partial\theta_j}\frac{\partial}{\partial\theta_i}, \\ \frac{\partial}{\partial\theta_i}\theta_i &= 1, & \frac{\partial}{\partial\theta_i}\theta_j &= -\theta_j\frac{\partial}{\partial\theta_i} \text{ for } i \neq j. \end{aligned} \tag{A.20}$$

A.3.3 Integration

To perform integration for Grassmann variables, we need a consistent definition of integration in $\mathbb{R}^N$. For an integral of $f(x)$ over the domain $\Omega \in \mathbb{R}^N$ that vanishes at the boundary $\partial\Omega$,

$$\int_\Omega d^N x\, f(x) = \int_\Omega dx_1 \dots dx_N\, f(x_1, x_2, \dots, x_N), \tag{A.21}$$

$$\int_\Omega d^N x\, \frac{\partial}{\partial x_i} f(x_1, \dots, x_N) = 0, \tag{A.22}$$

we consider this a linear functional of f. We want an equivalent definition for an integral $\int d^N\theta$ of a Grassmann polynomial P. The integral then must have the properties

$$\begin{aligned} &\int d^N\theta\, P = \mathbb{C}, \\ &\int d^N\theta\, (\lambda_1 P_1 + \lambda_2 P_2) = \lambda_1 \int d^N\theta\, P_1 + \lambda_1 \int d^N\theta\, P_2 \quad \text{for } \lambda_1,\, \lambda_2 \in \mathbb{C}. \end{aligned} \tag{A.23}$$

Then the Grassmann integral

$$\int d^N\theta\, \frac{\partial}{\partial\theta_i} P = 0 \tag{A.24}$$

is the equivalent of equation (A.22). This implies that $\int P$ vanishes if $P = \frac{\partial}{\partial\theta_i} P'$ for some other polynomial P'. This in turn reveals that $\int P$ must be proportional to $a_{12\ldots N}$ for the highest power of generators θ_i. Now we can write the normalisation condition

$$\int d^N\theta\, \theta_1\theta_2 \ldots \theta_N = 1 \implies \int d^N\theta\, P = a_{12\ldots N} \tag{A.25}$$

and furthermore write the integral measure $d^N\theta$ as a product of individual measures, i.e.

$$d^N\theta = d\theta_N d\theta_{N-1} \ldots d\theta_2 d\theta_1. \tag{A.26}$$

These measures then follow the rules

$$\int d\theta_i = 0, \qquad \int d\theta_i\, \theta_i = 1, \qquad d\theta_i d\theta_j = -d\theta_j d\theta_i. \tag{A.27}$$

Notice that the integral measure rules in equation (A.27) follow the same algebra as the rules for differentiation in equation (A.20).

Something which we will find useful later on is linear transformations of Grassmann variables, i.e.

$$\theta_i' = \sum_{j=1}^{N} M_{ij}\theta_j \text{ for } M_{ij} \text{ a complex } N \times N \text{ matrix.} \tag{A.28}$$

Applying this linear transformation to the normalisation condition of equation (A.25), we find

$$\begin{aligned}
\int d^N\theta\, \theta_1 \ldots \theta_N &= \int d^N\theta'\, \theta_1' \ldots \theta_N' \\
&= \int d^N\theta' \sum_{i_1,\ldots,i_N} M_{1i_1} \ldots M_{Ni_N} \theta_{i_1} \ldots \theta_{i_N} \\
&= \int d^N\theta' \sum_{i_1,\ldots,i_N} M_{1i_1} \ldots M_{Ni_N} \epsilon_{i_1 i_2 \ldots i_N} \theta_1 \ldots \theta_N \\
&= \det[M] \int d^N\theta'\, \theta_1 \ldots \theta_N.
\end{aligned} \tag{A.29}$$

From this transformation, we can read off the transformation rule for the integral measure as

$$d^N\theta = \det[M] d^N\theta'. \tag{A.30}$$

A.3.4 Gaussian Integrals with Grassmann Variables

Consider a set of $2N$ Grassmann variables $\theta_i, \bar{\theta}_i$ for $i \in \{1, 2, \ldots, N\}$, all of which anticommute with one another. For such a set, an important result is the *Matthews-Salam formula* [468, 469]:

$$Z_F = \int d\theta_N d\bar{\theta}_N \ldots d\theta_1 d\bar{\theta}_1 \exp\left\{\sum_{i,j}^{N} \bar{\theta}_i M_{ij} \theta_j\right\} = \det[M]. \tag{A.31}$$

The Matthews-Salam formula is crucial in the formulation of lattice QCD as it shows that the fermionic partition function Z_F can be expressed in terms of a determinant, i.e. the determinant of the Dirac operator. In terms of Grassmann variables, we can write the path integral formulation of an n-point correlation function as

$$\langle \bar{\theta}_{i_1} \theta_{j_1} \ldots \theta_{i_n} \bar{\theta}_{j_n} \rangle = \frac{1}{Z_F} \int \left(\prod_{k=1}^{N} d\theta_k d\bar{\theta}_k\right) \bar{\theta}_{i_1} \theta_{j_1} \ldots \theta_{i_n} \bar{\theta}_{j_n} \exp\left\{\sum_{l,m}^{N} \bar{\theta}_l M_{lm} \theta_m\right\}. \tag{A.32}$$

We can then extend the Matthews-Salam formula to the path integral formulation using *Wick's theorem* [370], resulting in

$$\langle \bar{\theta}_{i_1} \theta_{j_1} \ldots \theta_{i_n} \bar{\theta}_{j_n} \rangle = (-1)^n \sum_{P(1,2,\ldots,n)} \operatorname{sign}(P) \prod_{k}^{N} (M^{-1})_{i_k j_{P_k}}, \tag{A.33}$$

where P denotes permutations of the Grassmann variables. One can see that equation (A.33) is only non-zero for equal numbers of i and j indices; this requires that the Grassmann variables always come in pairs – these are the *quark bilinears*. Connecting the $2N$ Grassmann variables into quark bilinears then indicates that there are N propagators in the correlation function.

Appendix B

Statistical Data Analysis

B.1 Jackknife Resampling

The single elimination jackknife [470] is a method to estimate the bias of an estimator $\hat{\theta}_M$ of the parameter θ. For a dataset M of size N with entries $n \in 1, 2, \ldots, N$, it does so by removing the nth entry of the dataset and calculating $\hat{\theta}_{S_n}$ for the remaining subset S_n of the data. We say $\hat{\theta}$ is the estimator of the parameter θ extracted from all measurements $M = \{M_1, M_2, \ldots, M_N\}$, for example, the *sample mean*:

$$\hat{\theta}_M = \frac{1}{N} \sum \theta_n, \tag{B.1}$$

where θ_n is the value of θ extracted from measurement M_n. Then $\hat{\theta}_{S_n}$ is the estimator on the subset of the data without the nth entry, i.e. $S_n = \{M_1, \ldots, M_{n-1}, M_{n+1}, \ldots, M_N\}$:

$$\hat{\theta}_{S_n} = \frac{1}{N-1} \sum_{i \in S_n} \theta_i. \tag{B.2}$$

The $\hat{\theta}_{S_n}$ are alternative estimates of $\hat{\theta}$ from the subsets of the data, which may be treated as if they are independent but drawn from the same probability distribution [471] – the *jackknife samples*. The variance of the $\hat{\theta}_{S_n}$ can then be used to estimate the variance of $\hat{\theta}$. We derive the jackknife estimator of the variance of $\hat{\theta}$ as

$$\sigma^2 = \frac{N-1}{N} \sum_{n=1}^{N} \left(\hat{\theta}_{S_n} - \frac{1}{N} \sum_{m=1}^{N} \theta_m \right)^2. \tag{B.3}$$

Finally, an expectation value of a quantity calculated from a jackknife resampled dataset is presented as $\langle \theta \rangle = \hat{\theta} \pm \sigma$.

B.1.1 Super Jackknife

The super jackknife method is designed to connect uncorrelated datasets of different sizes in a jackknife resampling approach Consider M lattice ensembles, where on the kth ensemble, the estimator of some quantity is $\hat{\theta}^k$ with N_k jackknife samples θ_n^k for $n = 1, 2, \ldots, N_k$. We will combine these into $N = \sum_{k=1}^{M} N_k$ *super jackknife blocks* B_j where the jth block (for $j \in 1, 2, \ldots, N$) is composed of M estimators ϕ_k for $k \in 1, 2, \ldots, M$, which are selected as follows:

$$\phi_k = \begin{cases} \hat{\theta}_{S_n}, & \sum_{l=1}^{l<k} N_l \leq j < \sum_{l=1}^{l\leq k} N_l;\ n = j - \sum_{l=1}^{l<k} N_l \\ \hat{\theta}_{N_k}, & \text{otherwise} \end{cases} . \tag{B.4}$$

To make this clear, take the example of two ensembles X of size $N_X = 40$ and Y of size $N_Y = 60$. Then the jth super jackknife block B_j has two values, $\phi_{1,2}$. If $j \leq 40$ then $\phi_1 = \hat{\theta}_{S_j}$ is the jth jackknife sample from ensemble X's jackknife block and $\phi_2 = \hat{\theta}_{N_Y}$ is the sample mean from ensemble Y; if $j > 40$ then $\phi_1 = \hat{\theta}_{N_X}$ is the sample mean from ensemble X and $\phi_2 = \hat{\theta}_{S_n}$ is the nth jackknife sample from ensemble Y's jackknife block where $n = j - 40$.

The super jackknife method appropriately propagates the correlations within each ensembles dataset through the analysis chain, but implicitly assumes zero correlations between the different ensembles. By taking $M = 1$, one can recover the standard jackknife method.

B.2 Correlator Fitting

We perform frequentist fits of lattice data in order to extract bare parameters which are related to the mass, energy, and matrix elements of meson states defined inside various correlation functions. A fit range $[t_0, t_1]$ in the Euclidean time signal is chosen for which data points will enter the fit; the fit range must be chosen to avoid excited state contamination beyond the scope of the fit parameterisation in earlier timeslices while also taking advantage of the more precise data before the signal-to-noise ratio worsens with increasing Euclidean time. The fits make use of a least squares fit of the correlator data $C(t_i)$ to some fit parameterisation $f(\vec{\theta}, t_i)$, where $\vec{\theta}$ is the vector of fit parameters to be extracted and t_i are the discrete timeslices. The correlated χ^2 to be minimised is defined

$$\chi^2(\vec{\theta}) = (C(t_i) - f(\vec{\theta}, t_i)) \cdot \mathrm{cov}_{ij}^{-1} \cdot (C(t_j) - f(\vec{\theta}, t_j)), \tag{B.5}$$

where cov is the variance-covariance matrix, defined

$$\mathrm{cov}_{ij} = \frac{N-1}{N} \sum_{k=1}^{N} \left(C_{S_k}(t_i) - \hat{C}_M(t_i) \right) \left(C_{S_k}(t_j) - \hat{C}_M(t_j) \right), \tag{B.6}$$

where following the notation of appendix B.1, $\hat{C}_M(t)$ is the sample mean of the correlator $C(t)$ on the lattice ensemble M with N measurements and $C_{S_k}(t)$ is the kth jackknife sample of the correlator. Note that the prefactor to the sum is specific to jackknife resampling and other procedures (such as *bootstrap*) have different prefactors. One may find that the covariance matrix is ill-conditioned and numerical matrix inversion applies poorly. First, one may try to define an alternative (but equivalent) χ^2 where only the correlation matrix, which typically is easier to invert, gets inverted:

$$\chi^2(\vec{\theta}) = \frac{C(t_i) - f(\vec{\theta}, t_i)}{\sigma_i} \cdot \mathrm{corr}_{ij}^{-1} \cdot \frac{C(t_j) - f(\vec{\theta}, t_j)}{\sigma_j}, \tag{B.7}$$

where $\sigma_i = \mathrm{diag}(\mathrm{cov}_{ij})^{1/2}$ and the correlation matrix is defined

$$\mathrm{corr}_{ij} = \sigma_i^{-1} \cdot \mathrm{cov}_{ij} \cdot \sigma_j^{-1}. \tag{B.8}$$

However, in some scenarios this may still not be suitable, in which case one may consider a completely diagonal correlation matrix – this is known as an *uncorrelated* χ^2 fit, i.e.

$$\chi^2(\vec{\theta}) = \left(\frac{C(t_i) - f(\vec{\theta}, t_i)}{\sigma_i} \right)^2. \tag{B.9}$$

To indicate the quality of fit once the χ^2 function is minimised, one can consider the indicator the 'reduced χ^2':

$$\chi^2_\nu = \frac{\chi^2_{\mathrm{min}}}{\#\ \mathrm{dof}}, \tag{B.10}$$

where '# dof' is the number of degrees of freedom of the fit, i.e. the number of fitted data points minus the number of parameters of the fit. For a correlated χ^2 fit, this can be interpreted probabilistically and gives an evaluation of the quality of fit; for large # dof and a good fit, χ^2_ν should approach 1. This is further related to the *p-value*, defined

$$p = 1 - F(x; k) = 1 - \frac{1}{\Gamma(\frac{k}{2})} \gamma\left(\frac{k}{2}, \frac{x}{2} \right), \tag{B.11}$$

where $F(x; k)$ is the χ^2 cumulative distribution function and $\gamma(s, t)$ is the lower incomplete gamma function,

$$\gamma(s, x) = \int_0^x t^{s-1} e^{-t}\, dt. \tag{B.12}$$

The p-value interprets how likely it is that a certain fit is an acceptable description of that data; we choose the common prescription that a correlated fit is acceptable if $p \geq 5\%$.

There is no formal interpretation of the quality of fit for an uncorrelated fit to inherently-correlated data, such that the reduced χ^2 and p-value lose clear meaning. While not as rigid as for a correlated fit and must be taken with a grain of salt, these still provide some indication of the fit quality. Whenever possible, it is still preferred to perform a correlated fit which is statistically well-defined.

Appendix C

Gradient Flow Implementation in Hadrons

```
/*
 * GaugeFlow.hpp, part of Hadrons (https://github.com/aportelli/Hadrons)
 *
 * Copyright (C) 2015 - 2022
 *
 * Author: Antonin Portelli <antonin.portelli@me.com>
 * Author: Matthew Black    <matthewkblack@protonmail.com>
 *
 * Hadrons is free software: you can redistribute it and/or modify
 * it under the terms of the GNU General Public License as published by
 * the Free Software Foundation, either version 2 of the License, or
 * (at your option) any later version.
 *
 * Hadrons is distributed in the hope that it will be useful,
 * but WITHOUT ANY WARRANTY; without even the implied warranty of
 * MERCHANTABILITY or FITNESS FOR A PARTICULAR PURPOSE.  See the
 * GNU General Public License for more details.
 *
 * You should have received a copy of the GNU General Public License
 * along with Hadrons.  If not, see <http://www.gnu.org/licenses/>.
 *
 * See the full license in the file "LICENSE" in the top level
    distribution
 * directory.
 */

/*  END LEGAL */
#ifndef Hadrons_MGradientFlow_GaugeFlow_hpp_
#define Hadrons_MGradientFlow_GaugeFlow_hpp_
```

```
29
30 #include <Hadrons/Global.hpp>
31 #include <Hadrons/Module.hpp>
32 #include <Hadrons/ModuleFactory.hpp>
33 #include <Hadrons/Serialization.hpp>
34 #include <Hadrons/Modules/MGradientFlow/Utils.hpp>
35
36 BEGIN_HADRONS_NAMESPACE
37
38 /************************************************************
39  *                 Gauge Field Gradient Flow                *
40  ************************************************************/
41 BEGIN_MODULE_NAMESPACE(MGradientFlow)
42
43 class GaugeFlowPar: Serializable
44 {
45 public:
46     GRID_SERIALIZABLE_CLASS_MEMBERS(GaugeFlowPar,
47                                     std::string, output,
48                                     std::string, gauge,
49                                     int, steps,
50                                     double, step_size,
51                                     int, meas_interval,
52                                     std::string, maxTau);
53 };
54
55 template <typename GImpl,typename FlowAction>
56 class TGaugeFlow: public Module<GaugeFlowPar>
57 {
58 public:
59     INHERIT_GIMPL_TYPES(GImpl);
60     class Result : Serializable
61     {
62     public:
63         GRID_SERIALIZABLE_CLASS_MEMBERS(Result,
64                                         std::vector<double>, plaquette,
65                                         std::vector<double>, rectangle,
66                                         std::vector<double>, clover,
67                                         std::vector<double>, topcharge,
68                                         std::vector<double>, action);
69     };
70 public:
71     // constructor
72     TGaugeFlow(const std::string name);
73     // destructor
74     virtual ~TGaugeFlow(void) {};
75     // dependency relation
76     virtual std::vector<std::string> getInput(void);
```

```
77      virtual std::vector<std::string> getOutput(void);
78      // setup
79      virtual void setup(void);
80      // action
81      FlowAction SG = FlowAction(3.0);
82      // execution
83      virtual void execute(void);
84  };
85
86  MODULE_REGISTER_TMP(WilsonFlow, ARG(TGaugeFlow<GIMPL,WilsonGaugeAction<
        GIMPL>>), MGradientFlow);
87  MODULE_REGISTER_TMP(SymanzikFlow, ARG(TGaugeFlow<GIMPL,
        SymanzikGaugeAction<GIMPL>>), MGradientFlow);
88  MODULE_REGISTER_TMP(ZeuthenFlow, ARG(TGaugeFlow<GIMPL,ZeuthenGaugeAction<
        GIMPL>>), MGradientFlow);
89
90  /******************************************************
91   *             TGaugeFlow implementation              *
92   ******************************************************/
93  // constructor /////////////////////////////////////////
94  template <typename GImpl,typename FlowAction>
95  TGaugeFlow<GImpl,FlowAction>::TGaugeFlow(const std::string name)
96  : Module<GaugeFlowPar>(name)
97  {}
98
99  // dependencies/products ///////////////////////////////
100 template <typename GImpl,typename FlowAction>
101 std::vector<std::string> TGaugeFlow<GImpl,FlowAction>::getInput(void)
102 {
103     std::vector<std::string> in = {par().gauge};
104
105     return in;
106 }
107
108 template <typename GImpl,typename FlowAction>
109 std::vector<std::string> TGaugeFlow<GImpl,FlowAction>::getOutput(void)
110 {
111     std::vector<std::string> out = {getName(),getName()+"_U"};
112
113     return out;
114 }
115
116 // setup ///////////////////////////////////////////////
117 template <typename GImpl,typename FlowAction>
118 void TGaugeFlow<GImpl,FlowAction>::setup(void)
119 {
120     envCreateLat(GaugeField, getName()+"_U");
121     envCreate(HadronsSerializable, getName(), 1, 0);
```

```
122 }
123
124 // execution ////////////////////////////////////////////////
125 template <typename GImpl,typename FlowAction>
126 void TGaugeFlow<GImpl,FlowAction>::execute(void)
127 {
128     std::string type = SG.action_name();
129     std::string ga = "GaugeAction";
130     std::string::size_type i = type.find(ga);
131     if (i != std::string::npos) {
132         type.erase(i, ga.length());
133     }
134
135     LOG(Message) << "Setting up " << type << " Flow on '" << par().gauge
    << "' with " << par().steps
136                  << " step" << ((par().steps != 1) ? "s." : ".") << std::
    endl;
137
138     double mTau = -1.0;
139     if(!par().maxTau.empty()) {
140         LOG(Message) << "Using adaptive algorithm with maxTau = " << par
    ().maxTau << std::endl;
141         mTau = (double)std::stoi(par().maxTau);
142     }
143
144     auto &out    = envGet(HadronsSerializable, getName());
145     auto &result = out.template hold<Result>();
146
147     auto &U   = envGet(GaugeField, par().gauge);
148     auto &Uwf = envGet(GaugeField, getName()+"_U");
149
150     Uwf = U;
151     double time = 0;
152
153     Evolution<FlowAction> evolve(3.0, par().step_size, mTau, par().
    step_size);
154     if (par().steps == 0) { // if steps = 0, give the status of gauge
    field without flowing
155         result.plaquette.resize(1);
156         result.rectangle.resize(1);
157         result.clover.resize(1);
158         result.topcharge.resize(1);
159         result.action.resize(1);
160         evolve.template gauge_status<GImpl,GaugeField,ComplexField,
    GaugeLinkField,Result>(Uwf,result,0);
161     } else {
162         result.plaquette.resize(par().steps);
163         result.rectangle.resize(par().steps);
```

```
164         result.clover.resize(par().steps);
165         result.topcharge.resize(par().steps);
166         result.action.resize(par().steps);
167         if (mTau > 0) {
168             unsigned int step = 0;
169             do {
170                 step++;
171                 evolve.template evolve_gauge_adaptive<GImpl,GaugeField>(
    Uwf);
172                 if (step % par().meas_interval == 0) {
173                     evolve.template gauge_status<GImpl,GaugeField,
    ComplexField,GaugeLinkField,Result>(Uwf,result,step-1);
174                 }
175             } while (evolve.taus < mTau);
176         } else {
177             for (unsigned int step = 1; step <= par().steps; step++) {
178                 evolve.template evolve_gauge<GImpl,GaugeField>(Uwf);
179                 if (step % par().meas_interval == 0) {
180                     evolve.template gauge_status<GImpl,GaugeField,
    ComplexField,GaugeLinkField,Result>(Uwf,result,step-1);
181                 }
182             }
183         }
184     }
185     saveResult(par().output,"gauge_obs",result);
186 }
187
188 END_MODULE_NAMESPACE
189
190 END_HADRONS_NAMESPACE
191
192 #endif // Hadrons_MGradientFlow_GaugeFlow_hpp_
```

Listing C.1: MGradientFlow/GaugeFlow.hpp

```
1  /*
2   * FermionFlow.hpp, part of Hadrons (https://github.com/aportelli/Hadrons
       )
3   *
4   * Copyright (C) 2015 - 2022
5   *
6   * Author: Antonin Portelli <antonin.portelli@me.com>
7   * Author: Matthew Black    <matthewkblack@protonmail.com>
8   *
9   * Hadrons is free software: you can redistribute it and/or modify
10  * it under the terms of the GNU General Public License as published by
11  * the Free Software Foundation, either version 2 of the License, or
12  * (at your option) any later version.
```

```
13  *
14  * Hadrons is distributed in the hope that it will be useful,
15  * but WITHOUT ANY WARRANTY; without even the implied warranty of
16  * MERCHANTABILITY or FITNESS FOR A PARTICULAR PURPOSE.  See the
17  * GNU General Public License for more details.
18  *
19  * You should have received a copy of the GNU General Public License
20  * along with Hadrons.  If not, see <http://www.gnu.org/licenses/>.
21  *
22  * See the full license in the file "LICENSE" in the top level
       distribution
23  * directory.
24  */
25
26 /*  END LEGAL */
27 #ifndef Hadrons_MGradientFlow_FermionFlow_hpp_
28 #define Hadrons_MGradientFlow_FermionFlow_hpp_
29
30 #include <Hadrons/Global.hpp>
31 #include <Hadrons/Module.hpp>
32 #include <Hadrons/ModuleFactory.hpp>
33 #include <Hadrons/Serialization.hpp>
34 #include <Hadrons/TimerArray.hpp>
35 #include <Hadrons/Modules/MGradientFlow/Utils.hpp>
36
37 BEGIN_HADRONS_NAMESPACE
38
39 /************************************************************
40  *              Propagator Field Gradient Flow               *
41  ************************************************************/
42 BEGIN_MODULE_NAMESPACE(MGradientFlow)
43
44 class FermionFlowPar: Serializable
45 {
46 public:
47     GRID_SERIALIZABLE_CLASS_MEMBERS(FermionFlowPar,
48                                     std::string, output,
49                                     std::vector<std::string>, props,
50                                     std::string, gauge,
51                                     int, bc,
52                                     int, steps,
53                                     double, step_size,
54                                     int, meas_interval,
55                                     std::string, maxTau);
56 };
57
58 template <typename FImpl,typename GImpl,typename FlowAction>
59 class TFermionFlow: public Module<FermionFlowPar>
```

```
60 {
61 public:
62     BASIC_TYPE_ALIASES(FImpl,);
63     GAUGE_TYPE_ALIASES(GImpl,);
64     class GaugeResult : Serializable
65     {
66     public:
67         GRID_SERIALIZABLE_CLASS_MEMBERS(GaugeResult,
68                                         std::vector<double>, plaquette,
69                                         std::vector<double>, rectangle,
70                                         std::vector<double>, clover,
71                                         std::vector<double>, topcharge,
72                                         std::vector<double>, action);
73     };
74 public:
75     // constructor
76     TFermionFlow(const std::string name);
77     // destructor
78     virtual ~TFermionFlow(void) {};
79     // dependency relation
80     virtual std::vector<std::string> getInput(void);
81     virtual std::vector<std::string> getOutput(void);
82     // setup
83     virtual void setup(void);
84     // action
85     FlowAction SG = FlowAction(3.0);
86     // execution
87     virtual void execute(void);
88 };
89
90 MODULE_REGISTER_TMP(WilsonFermionFlow,ARG(TFermionFlow<FIMPL,GIMPL,
        WilsonGaugeAction<GIMPL>>),MGradientFlow);
91
92 /******************************************************
93  *             TFermionFlow implementation                *
94  ******************************************************/
95 // constructor /////////////////////////////////////////////
96 template <typename FImpl,typename GImpl,typename FlowAction>
97 TFermionFlow<FImpl,GImpl,FlowAction>::TFermionFlow(const std::string name
        )
98 : Module<FermionFlowPar>(name)
99 {}
100
101 // dependencies/products ///////////////////////////////////
102 template <typename FImpl,typename GImpl,typename FlowAction>
103 std::vector<std::string> TFermionFlow<FImpl,GImpl,FlowAction>::getInput(
        void)
104 {
```

```
105     std::vector<std::string> in = {par().gauge};
106     for (std::string q : par().props) {
107         in.push_back(q);
108     }
109 
110     return in;
111 }
112 
113 template <typename FImpl,typename GImpl,typename FlowAction>
114 std::vector<std::string> TFermionFlow<FImpl,GImpl,FlowAction>::getOutput(
    void)
115 {
116     std::vector<std::string> out = {getName(),getName()+"_U"};
117     for (int i = 1; i <= par().steps; i++)
118     {
119         if ((i % par().meas_interval == 0) || (i == par().steps)) {
120             std::stringstream st; st << i;
121             for (int j = 0; j < par().props.size(); j++) {
122                 std::stringstream qt; qt << j;
123                 out.push_back(getName()+"_q"+qt.str()+"_"+st.str());
124             }
125         }
126     }
127     return out;
128 }
129 
130 // setup ///////////////////////////////////////////////////
131 template <typename FImpl,typename GImpl,typename FlowAction>
132 void TFermionFlow<FImpl,GImpl,FlowAction>::setup(void)
133 {
134     envCreateLat(GaugeField, getName()+"_U");
135 
136     for (int j = 0; j < par().props.size(); j++) {
137         std::stringstream qt; qt << j;
138         envTmpLat(PropagatorField, "q"+qt.str()+"wf");
139     }
140 
141     for (int i = 1; i <= par().steps; i++)
142     {
143         if ((i % par().meas_interval == 0) || (i == par().steps)) {
144             std::stringstream st; st << i;
145             for (int j = 0; j < par().props.size(); j++) {
146                 std::stringstream qt; qt << j;
147                 envCreateLat(PropagatorField, getName()+"_q"+qt.str()+"_"
    +st.str());
148             }
149         }
150     }
```

```
151     envCreate(HadronsSerializable, getName(), 1, 0);
152 }
153
154 // execution ////////////////////////////////////////////////
155 template <typename FImpl,typename GImpl,typename FlowAction>
156 void TFermionFlow<FImpl,GImpl,FlowAction>::execute(void)
157 {
158     std::string type = SG.action_name();
159     std::string ga = "GaugeAction";
160     std::string::size_type i = type.find(ga);
161     if (i != std::string::npos) {
162         type.erase(i, ga.length());
163     }
164
165     std::string props = "";
166     for (std::string q : par().props) props += q + " ";
167     LOG(Message) << "Setting up " << type << " Fermion Flow on '" << par
    ().gauge << "' Gauge Field and "
168                  << props << ((par().props.size() > 1) ? "Fermion
    Propagators " : "Fermion Propagator ")
169                  << "with ppp" << ((par().bc < 0) ? "a" : "p") << "
    boundary conditions and "
170                  << par().steps << " step" << ((par().steps > 1) ? "s." :
     ".") << std::endl;
171
172     std::vector<int> bc = {1,1,1};
173     if (par().bc < 0) bc.push_back(-1);
174     else bc.push_back(1);
175
176     double mTau = -1.0;
177     if(!par().maxTau.empty()) {
178         LOG(Message) << "Using adaptive algorithm with maxTau = " << par
    ().maxTau << std::endl;
179         mTau = (double)std::stoi(par().maxTau);
180     }
181
182     auto &out     = envGet(HadronsSerializable, getName());
183     auto &Uresult = out.template hold<GaugeResult>();
184
185     Uresult.plaquette.resize(par().steps);
186     Uresult.rectangle.resize(par().steps);
187     Uresult.clover.resize(par().steps);
188     Uresult.topcharge.resize(par().steps);
189     Uresult.action.resize(par().steps);
190
191     auto &U   = envGet(GaugeField, par().gauge);
192     auto &Uwf = envGet(GaugeField, getName()+"_U");
193     Uwf = U;
```

```
194
195     for (int j = 0; j < par().props.size(); j++) {
196         auto &qj = envGet(PropagatorField, par().props[j]);
197         std::stringstream jt; jt << j;
198         PropagatorField &qjwf = *env().template getObject<PropagatorField
    >(getName()+"_tmp_q"+jt.str()+"wf");
199         qjwf = qj;
200     }
201
202     double time = 0;
203     Evolution<FlowAction> evolve(3.0, par().step_size, mTau, par().
    step_size);
204     if (mTau > 0) {
205         unsigned int step = 0;
206         do {
207             step++;
208             startTimer("gauge field step");
209             std::vector<GaugeField> Wi = evolve.template
    evolve_gaugeFF_adaptive<GImpl,GaugeField,GaugeLinkField>(Uwf,bc);
210             stopTimer("gauge field step");
211             evolve.template gauge_status<GImpl,GaugeField,ComplexField,
    GaugeLinkField,GaugeResult>(Uwf,Uresult,step-1);
212             if (step % par().meas_interval == 0) {
213                 std::stringstream st; st << step;
214                 for (int j = 0; j < par().props.size(); j++) {
215                     std::stringstream jt; jt << j;
216                     PropagatorField &qjwf = *env().template getObject<
    PropagatorField>(getName()+"_tmp_q"+jt.str()+"wf");
217                     startTimer("fermion field "+jt.str()+" step");
218                     evolve.template laplace_flow<PropagatorField,GImpl,
    GaugeField,GaugeLinkField>(Wi[0],Wi[1],Wi[2],qjwf);
219                     stopTimer("fermion field "+jt.str()+" step");
220                     auto &qji = envGet(PropagatorField, getName()+"_q"+jt
    .str()+"_"+st.str());
221                     qji = qjwf;
222                 }
223             }
224         } while (evolve.taus < mTau);
225     } else {
226         for (unsigned int step = 1; step <= par().steps; step++) {
227             startTimer("gauge field step");
228             std::vector<GaugeField> Wi = evolve.template evolve_gaugeFF<
    GImpl,GaugeField,GaugeLinkField>(Uwf,bc);
229             stopTimer("gauge field step");
230             evolve.template gauge_status<GImpl,GaugeField,ComplexField,
    GaugeLinkField,GaugeResult>(Uwf,Uresult,step-1);
231             if ((step % par().meas_interval == 0) || (step == par().steps
    )) {
```

```
232                 std::stringstream st; st << step;
233                 for (int j = 0; j < par().props.size(); j++) {
234                     std::stringstream jt; jt << j;
235                     PropagatorField &qjwf = *env().template getObject<
    PropagatorField>(getName()+"_tmp_q"+jt.str()+"wf");
236                     startTimer("fermion field "+jt.str()+" step");
237                     evolve.template laplace_flow<PropagatorField,GImpl,
    GaugeField,GaugeLinkField>(Wi[0],Wi[1],Wi[2],qjwf);
238                     stopTimer("fermion field "+jt.str()+" step");
239                     auto &qji = envGet(PropagatorField, getName()+"_q"+jt
    .str()+"_"+st.str());
240                     qji = qjwf;
241                 }
242             }
243         }
244     }
245     saveResult(par().output,"gauge_obs",Uresult);
246 }
247
248 END_MODULE_NAMESPACE
249
250 END_HADRONS_NAMESPACE
251
252 #endif // Hadrons_MGradientFlow_FermionFlow_hpp_
```

Listing C.2: MGradientFlow/FermionFlow.hpp

```
1  /*
2   * Utils.hpp, part of Hadrons (https://github.com/aportelli/Hadrons)
3   *
4   * Copyright (C) 2015 - 2022
5   *
6   * Author: Antonin Portelli <antonin.portelli@me.com>
7   * Author: Matthew Black    <matthewkblack@protonmail.com>
8   *
9   * Hadrons is free software: you can redistribute it and/or modify
10  * it under the terms of the GNU General Public License as published by
11  * the Free Software Foundation, either version 2 of the License, or
12  * (at your option) any later version.
13  *
14  * Hadrons is distributed in the hope that it will be useful,
15  * but WITHOUT ANY WARRANTY; without even the implied warranty of
16  * MERCHANTABILITY or FITNESS FOR A PARTICULAR PURPOSE.  See the
17  * GNU General Public License for more details.
18  *
19  * You should have received a copy of the GNU General Public License
20  * along with Hadrons.  If not, see <http://www.gnu.org/licenses/>.
21  *
```

```
22  * See the full license in the file "LICENSE" in the top level
       distribution
23  * directory.
24  */
25
26 /*  END LEGAL */
27 #ifndef Hadrons_MGradientFlow_Utils_hpp_
28 #define Hadrons_MGradientFlow_Utils_hpp_
29
30 #include <Hadrons/Global.hpp>
31 #include <Hadrons/Module.hpp>
32
33 BEGIN_HADRONS_NAMESPACE
34
35 BEGIN_MODULE_NAMESPACE(MGradientFlow)
36
37 // additional action(s) ////////////////////////
38 template <class GImpl>
39 class ZeuthenGaugeAction {
40 public:
41     INHERIT_GIMPL_TYPES(GImpl);
42
43     double beta;
44     SymanzikGaugeAction<GImpl> SG;
45
46     ZeuthenGaugeAction(double b): beta(b),SG(SymanzikGaugeAction<GImpl>(b
       )) {};
47
48     virtual std::string action_name(){return "ZeuthenGaugeAction";}
49
50     virtual double S(const GaugeField &U) {
51         return SG.S(U);
52     };
53
54     virtual void deriv(const GaugeField &Umu, GaugeField &dSdU) {
55                                                 //  beta = 3.0, cl =
       -1.0/12.0 -> Symanzik
56         double factor_p = 5.0/double(Nc)*0.5;   //   5.0 = beta*(1.0-8.0*
       cl)
57         double factor_r = -0.25/double(Nc)*0.5; // -0.25 = beta*cl
58
59         GridBase *grid = Umu.Grid();
60
61         std::vector<GaugeLinkField> U (Nd,grid);
62         std::vector<GaugeLinkField> U2(Nd,grid);
63
64         for(int mu=0;mu<Nd;mu++){
65             U[mu] = PeekIndex<LorentzIndex>(Umu,mu);
```

```
66              WilsonLoops<GImpl>::RectStapleDouble(U2[mu],U[mu],mu);
67          }
68
69          GaugeLinkField dSdU_mu(grid);
70          GaugeLinkField staple(grid);
71          GaugeLinkField tmp(grid),tmq(grid),tmr(grid);
72
73          for (int mu=0; mu < Nd; mu++){
74              // Staple in direction mu
75              WilsonLoops<GImpl>::Staple(staple,Umu,mu);
76              tmp = Ta(U[mu]*staple)*factor_p;
77
78              WilsonLoops<GImpl>::RectStaple(Umu,staple,U2,U,mu);
79              tmp = tmp + Ta(U[mu]*staple)*factor_r;
80
81              tmq = (adj(Cshift(U[mu],mu,-1)) * Cshift(tmp,mu,-1) * Cshift(
    U[mu],mu,-1));
82              tmr = (U[mu] * Cshift(tmp,mu,1) * adj(U[mu]));
83
84              dSdU_mu = 5.0/6.0*tmp + 1.0/12.0*tmq + 1.0/12.0*tmr;
85              PokeIndex<LorentzIndex>(dSdU, dSdU_mu, mu);
86          }
87      };
88  };
89
90  // clover ////////////////////////////////////////
91  template <typename GImpl, typename ComplexField, typename GaugeLorentz,
        typename GaugeMat>
92  void siteClover(ComplexField &Clov, const GaugeLorentz &U)
93  {
94      GaugeMat Fmn(U.Grid()), Cmn(U.Grid()), scaledUnit(U.Grid()), Umu(U.
    Grid());
95      Clov = Zero();
96      for (int mu = 1; mu < Nd; mu++) {
97          for (int nu = 0; nu < mu; nu++) {
98              Umu = PeekIndex<LorentzIndex>(U, mu);
99              scaledUnit = (1.0/Nc) * (adj(Umu) * Umu);
100             WilsonLoops<GImpl>::FieldStrength(Fmn, U, mu, nu);
101             Cmn = Fmn - trace(Fmn) * scaledUnit;
102             Clov = Clov - trace(Cmn * Cmn);
103         }
104     }
105 }
106
107 template <typename GImpl, typename ComplexField, typename GaugeLorentz,
        typename GaugeMat>
108 double avgClover(const GaugeLorentz &Umu)
109 {
```

```
110     ComplexField Clov(Umu.Grid());
111
112     siteClover<GImpl,ComplexField,GaugeLorentz,GaugeMat>(Clov, Umu);
113     auto Tc = sum(Clov);
114     auto c = TensorRemove(Tc);
115
116     double vol = Umu.Grid()->gSites();
117
118     return c.real() / vol;
119 }
120
121 // field evolution ////////////////////////////////
122 template <typename FlowAction>
123 class Evolution {
124     public:
125         double epsilon, maxTau, taus;
126         FlowAction SG;
127         Evolution(double beta, double step, double mTau, double ts) :
128             SG(FlowAction(beta)), epsilon(step), maxTau(mTau), taus(ts)
    {};
129
130         template <typename GImpl,typename GaugeField>
131         std::vector<GaugeField> gauge_RK(GaugeField U) {
132
133             std::vector<GaugeField> Wi;
134
135             GaugeField Z(U.Grid());
136             GaugeField tmp(U.Grid());
137             Wi.push_back(U);                                // W0
138             SG.deriv(U, Z);
139             Z *= 0.25;                                      // Z0 = 1/4 * F(U
    )
140             GImpl::update_field(Z, U, -2.0*epsilon);    // U = W1 = exp(
    ep*Z0)*W0
141             Wi.push_back(U);                                // W1
142
143             Z *= -17.0/8.0;
144             SG.deriv(U, tmp); Z += tmp;                     // -17/32*Z0 + Z1
145             Z *= 8.0/9.0;                                   // Z = -17/36*Z0
    +8/9*Z1
146             GImpl::update_field(Z, U, -2.0*epsilon);    // U_= W2 = exp(
    ep*Z)*W1
147             Wi.push_back(U);                                // W2
148
149             Z *= -4.0/3.0;
150             SG.deriv(U, tmp); Z += tmp;                     // 4/3*(17/36*Z0
    -8/9*Z1) + Z2
```

```
151             Z *= 3.0/4.0;                                   // Z = 17/36*Z0
    -8/9*Z1 +3/4*Z2
152             GImpl::update_field(Z, U, -2.0*epsilon);    // V(t+e) = exp(
    ep*Z)*W2
153             Wi.push_back(U);                                // W3
154
155             return Wi;
156         };
157
158         template <typename GImpl,typename GaugeField>
159         std::vector<GaugeField> gauge_RK_adaptive(GaugeField U) {
160
161             std::vector<GaugeField> Wi;
162
163             if (maxTau - taus < epsilon){
164                 epsilon = maxTau-taus;
165             }
166             GaugeField Z(U.Grid());
167             GaugeField Zprime(U.Grid());
168             GaugeField tmp(U.Grid()), Uprime(U.Grid());
169             Uprime = U;
170             Wi.push_back(U);                                // W0
171             SG.deriv(U, Z);
172             Zprime = -Z;
173             Z *= 0.25;                                      // Z0 = 1/4 * F(U
    )
174             GImpl::update_field(Z, U, -2.0*epsilon);    // U = W1 = exp(
    ep*Z0)*W0
175             Wi.push_back(U);                                // W1
176
177             Z *= -17.0/8.0;
178             SG.deriv(U, tmp); Z += tmp;                     // -17/32*Z0 +Z1
179             Zprime += 2.0*tmp;
180             Z *= 8.0/9.0;                                   // Z = -17/36*Z0
    +8/9*Z1
181             GImpl::update_field(Z, U, -2.0*epsilon);    // U_= W2 = exp(
    ep*Z)*W1
182             Wi.push_back(U);                                // W2
183
184             Z *= -4.0/3.0;
185             SG.deriv(U, tmp); Z += tmp;                     // 4/3*(17/36*Z0
    -8/9*Z1) +Z2
186             Z *= 3.0/4.0;                                   // Z = 17/36*Z0
    -8/9*Z1 +3/4*Z2
187             GImpl::update_field(Z, U, -2.0*epsilon);    // V(t+e) = exp(
    ep*Z)*W2
188             Wi.push_back(U);                                // W3
189
```

```
190             GImpl::update_field(Zprime, Uprime, -2.0*epsilon); // V'(t+e)
    = exp(ep*Z')*W0
191             Wi.push_back(Uprime);                          // Uprime
192 
193             return Wi;
194         };
195 
196         template <typename GaugeField>
197         void adaptive_eps(const GaugeField& U, const GaugeField& Uprime)
    {
198             // Compute distance as norm^2 of the difference
199             GaugeField diffU = U - Uprime;
200             double diff = norm2(diffU);
201             // adjust integration step
202 
203             taus += epsilon;
204             epsilon = epsilon*0.95*std::pow(1e-4/diff,1./3.);
205         };
206 
207         template <typename GImpl,typename GaugeField>
208         void evolve_gauge(GaugeField &U) {
209             std::vector<GaugeField> Wi = gauge_RK<GImpl,GaugeField>(U);
210             U = Wi[3];
211         };
212 
213         template <typename GImpl,typename GaugeField>
214         void evolve_gauge_adaptive(GaugeField &U) {
215             std::vector<GaugeField> Wi = gauge_RK_adaptive<GImpl,
    GaugeField>(U);
216             adaptive_eps(Wi[3],Wi[4]);
217             U = Wi[3];
218         };
219 
220         template <typename GaugeField,typename GaugeLinkField>
221         void gauge_apply_boundary(GaugeField &Umu, std::vector<int> bc) {
222             GaugeLinkField tmp1(Umu.Grid());
223             GaugeLinkField tmp2(Umu.Grid());
224             GaugeLinkField tmp3(Umu.Grid());
225             Lattice<iScalar<vInteger>> coord(Umu.Grid());
226 
227             for (int mu = 0; mu < Nd; mu++) {
228                 LatticeCoordinate(coord,mu);
229 
230                 tmp1 = PeekIndex<LorentzIndex>(Umu,mu);
231                 tmp2 = (double)bc[mu]*tmp1;
232                 int dimSize = Umu.Grid()->GlobalDimensions()[mu] - 1;
233                 tmp3 = where((coord == dimSize), tmp2, tmp1);
234                 PokeIndex<LorentzIndex>(Umu, tmp3, mu);
```

```
235             }
236         };
237 
238         template <typename FImpl,typename GImpl,typename GaugeField,
    typename GaugeLinkField>
239         FImpl generic_laplace(double a, double b, GaugeField &Umu, const
    FImpl& x_in, int skip_axis) {
240             double Nx = Nd;
241             if (skip_axis != -1) Nx--;
242 
243             FImpl x_out = (a + -2.0*Nx*b) * x_in;
244             for (int mu = 0; mu < Nd; mu++) {
245                 if (mu != skip_axis) {
246                     GaugeLinkField U = PeekIndex<LorentzIndex>(Umu, mu);
247                     x_out += b*(GImpl::CovShiftForward(U,mu,x_in) + GImpl
    ::CovShiftBackward(U,mu,x_in));
248                 }
249             }
250             return x_out;
251         };
252 
253         template <typename FImpl,typename GImpl,typename GaugeField,
    typename GaugeLinkField>
254         void laplace_flow(GaugeField &W0, GaugeField &W1, GaugeField &W2,
     FImpl &prop) {
255             FImpl psi1 = prop + (epsilon/4.0)*generic_laplace<FImpl,GImpl
    ,GaugeField,GaugeLinkField>(0.0, 1.0, W0, prop, -1);
256             FImpl psi2 = prop + (8.0*epsilon/9.0)*generic_laplace<FImpl,
    GImpl,GaugeField,GaugeLinkField>(0.0, 1.0, W1, psi1, -1) - (2.0*
    epsilon/9.0)*generic_laplace<FImpl,GImpl,GaugeField,GaugeLinkField
    >(0.0, 1.0, W0, prop, -1);
257             FImpl psi3 = psi1 + (3.0*epsilon/4.0)*generic_laplace<FImpl,
    GImpl,GaugeField,GaugeLinkField>(0.0, 1.0, W2, psi2, -1);
258 
259             prop = psi3;
260         };
261 
262         template <typename GImpl,typename GaugeField,typename
    GaugeLinkField>
263         std::vector<GaugeField> evolve_gaugeFF(GaugeField &U, std::vector
    <int> &bc) {
264             std::vector<GaugeField> Wi = gauge_RK<GImpl,GaugeField>(U);
265             U = 1.0*Wi[3];
266 
267             gauge_apply_boundary<GaugeField,GaugeLinkField>(Wi[0],bc);
268             gauge_apply_boundary<GaugeField,GaugeLinkField>(Wi[1],bc);
269             gauge_apply_boundary<GaugeField,GaugeLinkField>(Wi[2],bc);
270 
```

```
271             return Wi;
272         };
273 
274         template <typename GImpl,typename GaugeField,typename
    GaugeLinkField>
275         std::vector<GaugeField> evolve_gaugeFF_adaptive(GaugeField &U,
    std::vector<int> &bc) {
276             std::vector<GaugeField> Wi = gauge_RK_adaptive<GImpl,
    GaugeField>(U);
277             U = 1.0*Wi[3];
278 
279             gauge_apply_boundary<GaugeField,GaugeLinkField>(Wi[0],bc);
280             gauge_apply_boundary<GaugeField,GaugeLinkField>(Wi[1],bc);
281             gauge_apply_boundary<GaugeField,GaugeLinkField>(Wi[2],bc);
282 
283             adaptive_eps(Wi[3],Wi[4]);
284 
285             return Wi;
286         };
287 
288         // gauge field status ////////////////////////////////
289         template <typename GImpl,typename GaugeField,typename
    ComplexField,typename GaugeLinkField,typename Result>
290         void gauge_status(GaugeField &Umu, Result &result, int index)
291         {
292             double Q = WilsonLoops<GImpl>::TopologicalCharge(Umu);
293             double plaq = WilsonLoops<GImpl>::avgPlaquette(Umu);
294             double rect = WilsonLoops<GImpl>::avgRectangle(Umu);
295             double clov = avgClover<GImpl,ComplexField,GaugeField,
    GaugeLinkField>(Umu);
296             double act = SG.S(Umu);
297 
298             result.plaquette[index] = plaq;
299             result.rectangle[index] = rect;
300             result.clover[index]    = clov;
301             result.topcharge[index] =    Q;
302             result.action[index]    =  act;
303         };
304 };
305 
306 END_MODULE_NAMESPACE
307 
308 END_HADRONS_NAMESPACE
309 
310 #endif // Hadrons_MGradientFlow_Utils_hpp_
```

Listing C.3: MGradientFlow/Utils.hpp

Bibliography

[1] S. L. Glashow, *Partial Symmetries of Weak Interactions*, Nucl. Phys. **22** (1961) 579.

[2] S. Weinberg, *A Model of Leptons*, Phys. Rev. Lett. **19** (1967) 1264.

[3] A. Salam, *Weak and Electromagnetic Interactions*, Conf. Proc. C **680519** (1968) 367.

[4] ATLAS collaboration, G. Aad et al., *Observation of a new particle in the search for the Standard Model Higgs boson with the ATLAS detector at the LHC*, Phys. Lett. B **716** (2012) 1 [arXiv:1207.7214].

[5] CMS collaboration, S. Chatrchyan et al., *Observation of a New Boson at a Mass of 125 GeV with the CMS Experiment at the LHC*, Phys. Lett. B **716** (2012) 30 [arXiv:1207.7235].

[6] Super-Kamiokande collaboration, Y. Fukuda et al., *Evidence for oscillation of atmospheric neutrinos*, Phys. Rev. Lett. **81** (1998) 1562 [arXiv:hep-ex/9807003].

[7] SNO collaboration, Q. R. Ahmad et al., *Direct evidence for neutrino flavor transformation from neutral current interactions in the Sudbury Neutrino Observatory*, Phys. Rev. Lett. **89** (2002) 011301 [arXiv:nucl-ex/0204008].

[8] Planck collaboration, P. A. R. Ade et al., *Planck 2013 results. VI. High Frequency Instrument data processing*, Astron. Astrophys. **571** (2014) A6 [arXiv:1303.5067].

[9] V. Trimble, *Existence and Nature of Dark Matter in the Universe*, Ann. Rev. Astron. Astrophys. **25** (1987) 425.

[10] M. E. Peskin and D. V. Schroeder, *An Introduction to quantum field theory*. Addison-Wesley, Reading, USA, 1995.

[11] J. W. Moffat, *Ultraviolet Complete Quantum Field Theory and Particle Model*, Eur. Phys. J. Plus **134** (2019) 443 [arXiv:1812.01986].

[12] D. Demir, C. Karahan and O. Sargın, *Dimensional regularization in quantum field theory with ultraviolet cutoff*, Phys. Rev. D **107** (2023) 045003 [arXiv:2301.03323].

[13] C.-Y. Seng et al., *Reduced Hadronic Uncertainty in the Determination of V_{ud}*, Phys. Rev. Lett. **121** (2018) 241804 [arXiv:1807.10197].

[14] A. Czarnecki, W. J. Marciano and A. Sirlin, *Radiative Corrections to Neutron and Nuclear Beta Decays Revisited*, Phys. Rev. D **100** (2019) 073008 [arXiv:1907.06737].

[15] C.-Y. Seng et al., *Joint lattice QCD–dispersion theory analysis confirms the quark-mixing top-row unitarity deficit*, Phys. Rev. D **101** (2020) 111301 [arXiv:2003.11264].

[16] A. Crivellin et al., *Global fit of modified quark couplings to EW gauge bosons and vector-like quarks in light of the Cabibbo angle anomaly*, JHEP **03** (2023) 234 [arXiv:2212.06862].

[17] M. Kirk, *Cabibbo angle anomalies and a global fit to vector-like quarks*, PoS **FPCP2023** (2023) 059 [arXiv:2308.09669].

[18] A. Crivellin and M. Hoferichter, *β Decays as Sensitive Probes of Lepton Flavor Universality*, Phys. Rev. Lett. **125** (2020) 111801 [arXiv:2002.07184].

[19] T. Huber, S. Kränkl and X.-Q. Li, *Two-body non-leptonic heavy-to-heavy decays at NNLO in QCD factorization*, JHEP **09** (2016) 112 [arXiv:1606.02888].

[20] S. Iguro and T. Kitahara, *Implications for new physics from a novel puzzle in $\bar{B}^0_{(s)} \to D^{(*)+}_{(s)}\{\pi^-, K^-\}$ decays*, Phys. Rev. D **102** (2020) 071701 [arXiv:2008.01086].

[21] M. Bordone et al., *A puzzle in $\bar{B}^0_{(s)} \to D^{(*)+}_{(s)}\{\pi^-, K^-\}$ decays and extraction of f_s/f_d fragmentation fraction*, Eur. Phys. J. C **80** (2020) 951 [arXiv:2007.10338].

[22] F.-M. Cai et al., *Probing new physics in class-I B-meson decays into heavy-light final states*, JHEP **10** (2021) 235 [arXiv:2103.04138].

[23] T. Huber, *Some recent developments in nonleptonic B decays*, PoS **CKM2021** (2023) 075 [arXiv:2204.06224].

[24] S. Iguro, *Flavor anomalies meet the LHC*, EPJ Web Conf. **289** (2023) 01007.

[25] M. L. Piscopo and A. V. Rusov, *Non-factorisable effects in decays $\overline{B}^0_s \to D^+_s\pi^-$ and $\overline{B}^0 \to D^+K^-$ from LCSR*, JHEP **10** (2023) 180 [arXiv:2307.07594].

[26] Y. Amhis et al., *Averages of b-hadron, c-hadron, and τ-lepton properties as of 2021, and web updates*, Phys. Rev. D **107** (2023) 052008 [arXiv:2206.07501].

[27] LHCb collaboration, R. Aaij et al., *Branching Fraction Measurements of the Rare $B_s^0 \to \phi\mu^+\mu^-$ and $B_s^0 \to f_2'(1525)\mu^+\mu^-$ Decays*, Phys. Rev. Lett. **127** (2021) 151801 [arXiv:2105.14007].

[28] HPQCD collaboration, W. G. Parrott, C. Bouchard and C. T. H. Davies, *Standard Model predictions for $B \to K\ell^+\ell^-$, $B \to K\ell_1^-\ell_2^+$ and $B \to K\nu\bar{\nu}$ using form factors from $N_f = 2+1+1$ lattice QCD*, Phys. Rev. D **107** (2023) 014511 [arXiv:2207.13371], [Erratum: Phys.Rev.D 107, 119903 (2023)].

[29] N. Gubernari et al., *Improved theory predictions and global analysis of exclusive $b \to s\mu^+\mu^-$ processes*, JHEP **09** (2022) 133 [arXiv:2206.03797].

[30] Q. Wen and F. Xu, *Global fits of new physics in $b \to s$ after the $R_{K^{(*)}}$ 2022 release*, Phys. Rev. D **108** (2023) 095038 [arXiv:2305.19038].

[31] L. Di Luzio, M. Kirk and A. Lenz, *Updated B_s-mixing constraints on new physics models for $b \to s\ell^+\ell^-$ anomalies*, Phys. Rev. D **97** (2018) 095035 [arXiv:1712.06572].

[32] LHCb collaboration, R. Aaij et al., *Test of lepton universality in $b \to s\ell^+\ell^-$ decays*, Phys. Rev. Lett. **131** (2023) 051803 [arXiv:2212.09152].

[33] LHCb collaboration, R. Aaij et al., *Measurement of lepton universality parameters in $B^+ \to K^+\ell^+\ell^-$ and $B^0 \to K^{*0}\ell^+\ell^-$ decays*, Phys. Rev. D **108** (2023) 032002 [arXiv:2212.09153].

[34] M. Fael, K. Schönwald and M. Steinhauser, *Third order corrections to the semileptonic $b \to c$ and the muon decays*, Phys. Rev. D **104** (2021) 016003 [arXiv:2011.13654].

[35] M. Czakon, A. Czarnecki and M. Dowling, *Three-loop corrections to the muon and heavy quark decay rates*, Phys. Rev. D **103** (2021) L111301 [arXiv:2104.05804].

[36] M. Fael and J. Usovitsch, *Third order correction to semileptonic $b \to u$ decay: Fermionic contributions*, Phys. Rev. D **108** (2023) 114026 [arXiv:2310.03685].

[37] M. A. Shifman, A. I. Vainshtein and V. I. Zakharov, *QCD and Resonance Physics. Theoretical Foundations*, Nucl. Phys. B **147** (1979) 385.

[38] M. A. Shifman, A. I. Vainshtein and V. I. Zakharov, *QCD and Resonance Physics: Applications*, Nucl. Phys. B **147** (1979) 448.

[39] I. I. Balitsky, V. M. Braun and A. V. Kolesnichenko, *Radiative Decay $\Sigma^+ \to p\gamma$ in Quantum Chromodynamics*, Nucl. Phys. B **312** (1989) 509.

[40] K. G. Wilson, *Confinement of Quarks*, Phys. Rev. D **10** (1974) 2445.

[41] O. Atkinson, M. Black et al., *Cornering the Two Higgs Doublet Model Type II*, JHEP **04** (2022) 172 [arXiv:2107.05650].

[42] O. Atkinson, M. Black et al., *The flavourful present and future of 2HDMs at the collider energy frontier*, JHEP **11** (2022) 139 [arXiv:2202.08807].

[43] O. Atkinson, M. Black et al., *MUonE, muon g-2 and electroweak precision constraints within 2HDMs*, Phys. Rev. D **106** (2022) 115031 [arXiv:2207.02789].

[44] M. Black, A. D. Plascencia and G. Tetlalmatzi-Xolocotzi, *Enhancing $B_s \to e^+e^-$ to an observable level in the two-Higgs-doublet model*, Phys. Rev. D **107** (2023) 035013 [arXiv:2208.08995].

[45] M. Black et al., *Using Gradient Flow to Renormalise Matrix Elements for Meson Mixing and Lifetimes*, PoS **LATTICE2023** (2024) 263 [arXiv:2310.18059].

[46] M. D. Schwartz, *Quantum Field Theory and the Standard Model*. Cambridge University Press, 3, 2014.

[47] T. D. Lee and C.-N. Yang, *Question of Parity Conservation in Weak Interactions*, Phys. Rev. **104** (1956) 254.

[48] C. S. Wu et al., *Experimental Test of Parity Conservation in β Decay*, Phys. Rev. **105** (1957) 1413.

[49] J. H. Christenson et al., *Evidence for the 2π Decay of the K_2^0 Meson*, Phys. Rev. Lett. **13** (1964) 138.

[50] J. Goldstone, A. Salam and S. Weinberg, *Broken Symmetries*, Phys. Rev. **127** (1962) 965.

[51] P. W. Higgs, *Broken Symmetries and the Masses of Gauge Bosons*, Phys. Rev. Lett. **13** (1964) 508.

[52] F. Englert and R. Brout, *Broken Symmetry and the Mass of Gauge Vector Mesons*, Phys. Rev. Lett. **13** (1964) 321.

[53] G. S. Guralnik, C. R. Hagen and T. W. B. Kibble, *Global Conservation Laws and Massless Particles*, Phys. Rev. Lett. **13** (1964) 585.

[54] Particle Data Group collaboration, R. L. Workman et al., *Review of Particle Physics*, PTEP **2022** (2022) 083C01.

[55] Y. Nambu, *Quasiparticles and Gauge Invariance in the Theory of Superconductivity*, Phys. Rev. **117** (1960) 648.

[56] J. Goldstone, *Field Theories with Superconductor Solutions*, Nuovo Cim. **19** (1961) 154.

[57] C.-N. Yang and R. L. Mills, *Conservation of Isotopic Spin and Isotopic Gauge Invariance*, Phys. Rev. **96** (1954) 191.

[58] H. Fritzsch, M. Gell-Mann and H. Leutwyler, *Advantages of the Color Octet Gluon Picture*, Phys. Lett. B **47** (1973) 365.

[59] E. Swanson, *New Particle Hints at Four-Quark Matter*, APS Physics **6** (2013) 69.

[60] LHCb collaboration, R. Aaij et al., *Observation of $J/\psi p$ Resonances Consistent with Pentaquark States in $\Lambda_b^0 \to J/\psi K^- p$ Decays*, Phys. Rev. Lett. **115** (2015) 072001 [arXiv:1507.03414].

[61] E. Martynov and B. Nicolescu, *Did TOTEM experiment discover the Odderon?*, Phys. Lett. B **778** (2018) 414 [arXiv:1711.03288].

[62] T. Csörgő et al., *Evidence of Odderon-exchange from scaling properties of elastic scattering at TeV energies*, Eur. Phys. J. C **81** (2021) 180 [arXiv:1912.11968].

[63] D0, TOTEM collaboration, V. M. Abazov et al., *Odderon Exchange from Elastic Scattering Differences between pp and $p\bar{p}$ Data at 1.96 TeV and from pp Forward Scattering Measurements*, Phys. Rev. Lett. **127** (2021) 062003 [arXiv:2012.03981].

[64] H. D. Politzer, *Reliable Perturbative Results for Strong Interactions?*, Phys. Rev. Lett. **30** (1973) 1346.

[65] D. J. Gross and F. Wilczek, *Ultraviolet Behavior of Nonabelian Gauge Theories*, Phys. Rev. Lett. **30** (1973) 1343.

[66] J. S. Bell and R. Jackiw, *A PCAC puzzle: $\pi^0 \to \gamma\gamma$ in the σ model*, Nuovo Cim. A **60** (1969) 47.

[67] S. L. Adler, *Axial vector vertex in spinor electrodynamics*, Phys. Rev. **177** (1969) 2426.

[68] G. 't Hooft, *Symmetry Breaking Through Bell-Jackiw Anomalies*, Phys. Rev. Lett. **37** (1976) 8.

[69] R. D. Peccei and H. R. Quinn, *CP Conservation in the Presence of Instantons*, Phys. Rev. Lett. **38** (1977) 1440.

[70] F. Wilczek, *Problem of Strong P and T Invariance in the Presence of Instantons*, Phys. Rev. Lett. **40** (1978) 279.

[71] S. Weinberg, *A New Light Boson?*, Phys. Rev. Lett. **40** (1978) 223.

[72] N. Cabibbo, *Unitary Symmetry and Leptonic Decays*, Phys. Rev. Lett. **10** (1963) 531.

[73] M. Kobayashi and T. Maskawa, *CP Violation in the Renormalizable Theory of Weak Interaction*, Prog. Theor. Phys. **49** (1973) 652.

[74] L.-L. Chau and W.-Y. Keung, *Comments on the Parametrization of the Kobayashi-Maskawa Matrix*, Phys. Rev. Lett. **53** (1984) 1802.

[75] L. Wolfenstein, *Parametrization of the Kobayashi-Maskawa Matrix*, Phys. Rev. Lett. **51** (1983) 1945.

[76] CKMfitter Group collaboration, J. Charles et al., *updated results and plots available at: http://ckmfitter.in2p3.fr*, Eur. Phys. J. C **41** (2005) 1 [arXiv:hep-ph/0406184].

[77] UTfit collaboration, M. Bona et al., *The Unitarity Triangle Fit in the Standard Model and Hadronic Parameters from Lattice QCD: A Reappraisal after the Measurements of Δm_s and $BR(B \to \tau\nu_\tau)$*, JHEP **10** (2006) 081 [arXiv:hep-ph/0606167].

[78] UTfit collaboration, M. Bona et al., *New UTfit Analysis of the Unitarity Triangle in the Cabibbo-Kobayashi-Maskawa scheme*, Rend. Lincei Sci. Fis. Nat. **34** (2023) 37 [arXiv:2212.03894].

[79] UTfit collaboration, M. Bona et al. http://www.utfit.org/.

[80] A. J. Buras, *Weak Hamiltonian, CP violation and rare decays*, in *Les Houches Summer School in Theoretical Physics, Session 68: Probing the Standard Model of Particle Interactions*, pp. 281–539, 6, 1998, arXiv:hep-ph/9806471.

[81] G. Buchalla, A. J. Buras and M. E. Lautenbacher, *Weak decays beyond leading logarithms*, Rev. Mod. Phys. **68** (1996) 1125 [arXiv:hep-ph/9512380].

[82] G. Buchalla, *Heavy quark theory*, in *55th Scottish Universities Summer School in Physics: Heavy Flavor Physics (SUSSP 2001)*, pp. 57–104, 2, 2002, arXiv:hep-ph/0202092.

[83] A. Grozin, *Effective weak Lagrangians in the Standard Model and B decays*, in *Helmholtz International Summer School on Physics of Heavy Quarks and Hadrons*, pp. 78–98, 2014, arXiv:1311.0550, DOI.

[84] M. Neubert, *Heavy quark symmetry*, Phys. Rept. **245** (1994) 259 [arXiv:hep-ph/9306320].

[85] T. Mannel, *Recent progress in the theory of heavy flavor decays*, J. Phys. **21** (1995) 1007.

[86] T. Mannel, *Heavy quark effective field theory*, Rept. Prog. Phys. **60** (1997) 1113.

[87] I. I. Y. Bigi, M. A. Shifman and N. Uraltsev, *Aspects of heavy quark theory*, Ann. Rev. Nucl. Part. Sci. **47** (1997) 591 [arXiv:hep-ph/9703290].

[88] A. V. Manohar and M. B. Wise, *Heavy quark physics*, vol. 10. 2000.

[89] A. Lenz, *Lifetimes and heavy quark expansion*, Int. J. Mod. Phys. A **30** (2015) 1543005 [arXiv:1405.3601].

[90] T. Mannel, *Operator product expansion for inclusive semileptonic decays in heavy quark effective field theory*, Nucl. Phys. B **413** (1994) 396 [arXiv:hep-ph/9308262].

[91] E. Fermi, *An attempt of a theory of beta radiation. 1.*, Z. Phys. **88** (1934) 161.

[92] F. L. Wilson, *Fermi's Theory of Beta Decay*, Am. J. Phys. **36** (1968) 1150.

[93] K. G. Wilson, *Nonlagrangian models of current algebra*, Phys. Rev. **179** (1969) 1499.

[94] K. G. Wilson and J. B. Kogut, *The Renormalization group and the epsilon expansion*, Phys. Rept. **12** (1974) 75.

[95] G. 't Hooft, *Dimensional regularization and the renormalization group*, Nucl. Phys. B **61** (1973) 455.

[96] G. Passarino and M. Trott, *The Standard Model Effective Field Theory and Next to Leading Order*, arXiv:1610.08356.

[97] H. Georgi, *An Effective Field Theory for Heavy Quarks at Low-energies*, Phys. Lett. B **240** (1990) 447.

[98] B. Grinstein, *The Static Quark Effective Theory*, Nucl. Phys. B **339** (1990) 253.

[99] T. Mannel, W. Roberts and Z. Ryzak, *A Derivation of the heavy quark effective Lagrangian from QCD*, Nucl. Phys. B **368** (1992) 204.

[100] N. Isgur and M. B. Wise, *Weak Decays of Heavy Mesons in the Static Quark Approximation*, Phys. Lett. B **232** (1989) 113.

[101] A. F. Falk and M. Neubert, *Second order power corrections in the heavy quark effective theory. 1. Formalism and meson form-factors*, Phys. Rev. D **47** (1993) 2965 [arXiv:hep-ph/9209268].

[102] M. A. Shifman, *Theory of weak inclusive decays and lifetimes of heavy hadrons*, in *27th International Conference on High-energy Physics*, 7, 1994, arXiv:hep-ph/9409359.

[103] D. King et al., *Revisiting inclusive decay widths of charmed mesons*, JHEP **08** (2022) 241 [arXiv:2109.13219].

[104] M. Artuso, G. Borissov and A. Lenz, *CP violation in the B_s^0 system*, Rev. Mod. Phys. **88** (2016) 045002 [arXiv:1511.09466], [Addendum: Rev.Mod.Phys. 91, 049901 (2019)].

[105] M. A. Shifman and M. B. Voloshin, *Preasymptotic Effects in Inclusive Weak Decays of Charmed Particles*, Sov. J. Nucl. Phys. **41** (1985) 120.

[106] Q. Ho-kim and X.-Y. Pham, *Exact One Gluon Corrections for Inclusive Weak Processes*, Annals Phys. **155** (1984) 202.

[107] G. Altarelli and S. Petrarca, *Inclusive beauty decays and the spectator model*, Phys. Lett. B **261** (1991) 303.

[108] M. B. Voloshin, *QCD radiative enhancement of the decay $b \to c\bar{c}s$*, Phys. Rev. D **51** (1995) 3948 [arXiv:hep-ph/9409391].

[109] E. Bagan et al., *Charm quark mass dependence of QCD corrections to nonleptonic inclusive B decays*, Nucl. Phys. B **432** (1994) 3 [arXiv:hep-ph/9408306].

[110] E. Bagan et al., *Next-to-leading order radiative corrections to the decay $b \to ccs$*, Phys. Lett. B **351** (1995) 546 [arXiv:hep-ph/9502338].

[111] A. Lenz, U. Nierste and G. Ostermaier, *Penguin diagrams, charmless B decays and the missing charm puzzle*, Phys. Rev. D **56** (1997) 7228 [arXiv:hep-ph/9706501].

[112] A. Lenz, U. Nierste and G. Ostermaier, *Determination of the CKM angle gamma and $|V_{ub}/V_{cb}|$ from inclusive direct CP asymmetries and branching ratios in charmless B decays*, Phys. Rev. D **59** (1999) 034008 [arXiv:hep-ph/9802202].

[113] C. Greub and P. Liniger, *The Rare decay $b \to s$ gluon beyond leading logarithms*, Phys. Lett. B **494** (2000) 237 [arXiv:hep-ph/0008071].

[114] C. Greub and P. Liniger, *Calculation of next-to-leading QCD corrections to $b \to sg$*, Phys. Rev. D **63** (2001) 054025 [arXiv:hep-ph/0009144].

[115] F. Krinner, A. Lenz and T. Rauh, *The inclusive decay $b \to c\bar{c}s$ revisited*, Nucl. Phys. B **876** (2013) 31 [arXiv:1305.5390].

[116] A. Czarnecki and K. Melnikov, *Two loop QCD corrections to semileptonic b decays at maximal recoil*, Phys. Rev. Lett. **78** (1997) 3630 [arXiv:hep-ph/9703291].

[117] A. Czarnecki and K. Melnikov, *Two - loop QCD corrections to semileptonic b decays at an intermediate recoil*, Phys. Rev. D **59** (1999) 014036 [arXiv:hep-ph/9804215].

[118] T. van Ritbergen, *The Second order QCD contribution to the semileptonic $b \to u$ decay rate*, Phys. Lett. B **454** (1999) 353 [arXiv:hep-ph/9903226].

[119] K. Melnikov, *$O(\alpha_s^2)$ corrections to semileptonic decay $b \to c\ell\bar{\nu}_\ell$*, Phys. Lett. B **666** (2008) 336 [arXiv:0803.0951].

[120] A. Pak and A. Czarnecki, *Mass effects in muon and semileptonic $b \to c$ decays*, Phys. Rev. Lett. **100** (2008) 241807 [arXiv:0803.0960].

[121] A. Pak and A. Czarnecki, *Heavy-to-heavy quark decays at NNLO*, Phys. Rev. D **78** (2008) 114015 [arXiv:0808.3509].

[122] M. Dowling, A. Pak and A. Czarnecki, *Semi-Leptonic b-decay at Intermediate Recoil*, Phys. Rev. D **78** (2008) 074029 [arXiv:0809.0491].

[123] R. Bonciani and A. Ferroglia, *Two-Loop QCD Corrections to the Heavy-to-Light Quark Decay*, JHEP **11** (2008) 065 [arXiv:0809.4687].

[124] S. Biswas and K. Melnikov, *Second order QCD corrections to inclusive semileptonic $b \to X_c\ell\bar{\nu}_\ell$ decays with massless and massive lepton*, JHEP **02** (2010) 089 [arXiv:0911.4142].

[125] M. Brucherseifer, F. Caola and K. Melnikov, *On the $O(\alpha_s^2)$ corrections to $b \to X_u e\bar{\nu}$ inclusive decays*, Phys. Lett. B **721** (2013) 107 [arXiv:1302.0444].

[126] M. Egner et al., *Revisiting semileptonic B meson decays at next-to-next-to-leading order*, JHEP **09** (2023) 112 [arXiv:2308.01346].

[127] A. Czarnecki, M. Slusarczyk and F. V. Tkachov, *Enhancement of the hadronic b quark decays*, Phys. Rev. Lett. **96** (2006) 171803 [arXiv:hep-ph/0511004].

[128] M. Egner, M. Fael, K. Schönwald and M. Steinhauser, *Nonleptonic B-meson decays to next-to-next-to-leading order*, arXiv:2406.19456.

[129] I. I. Y. Bigi, N. G. Uraltsev and A. I. Vainshtein, *Nonperturbative corrections to inclusive beauty and charm decays: QCD versus phenomenological models*, Phys. Lett. B **293** (1992) 430 [arXiv:hep-ph/9207214], [Erratum: Phys.Lett.B 297, 477–477 (1992)].

[130] B. M. Dassinger, T. Mannel and S. Turczyk, *Inclusive semi-leptonic B decays to order $1/m_b^4$*, JHEP **03** (2007) 087 [arXiv:hep-ph/0611168].

[131] M. A. Shifman, *Lectures on heavy quarks in quantum chromodynamics*, in *Theoretical Advanced Study Institute in Elementary Particle Physics (TASI 95): QCD and Beyond*, pp. 409–514, 10, 1995, arXiv:hep-ph/9510377.

[132] I. I. Y. Bigi et al., *A QCD 'manifesto' on inclusive decays of beauty and charm*, in *7th Meeting of the APS Division of Particles Fields*, pp. 610–613, 11, 1992, arXiv:hep-ph/9212227.

[133] B. Blok and M. A. Shifman, *The Rule of discarding $1/N_c$ in inclusive weak decays. 1.*, Nucl. Phys. B **399** (1993) 441 [arXiv:hep-ph/9207236].

[134] B. Blok and M. A. Shifman, *The Rule of discarding $1/N_c$ in inclusive weak decays. 2.*, Nucl. Phys. B **399** (1993) 459 [arXiv:hep-ph/9209289].

[135] A. Alberti, P. Gambino and S. Nandi, *Perturbative corrections to power suppressed effects in semileptonic B decays*, JHEP **01** (2014) 147 [arXiv:1311.7381].

[136] T. Mannel, A. A. Pivovarov and D. Rosenthal, *Inclusive semileptonic B decays from QCD with NLO accuracy for power suppressed terms*, Phys. Lett. B **741** (2015) 290 [arXiv:1405.5072].

[137] T. Mannel, A. A. Pivovarov and D. Rosenthal, *Inclusive weak decays of heavy hadrons with power suppressed terms at NLO*, Phys. Rev. D **92** (2015) 054025 [arXiv:1506.08167].

[138] T. Mannel, D. Moreno and A. A. Pivovarov, *Heavy-quark expansion for lifetimes: Toward the QCD corrections to power suppressed terms*, Phys. Rev. D **107** (2023) 114026 [arXiv:2304.08964].

[139] P. Ball and V. M. Braun, *Next-to-leading order corrections to meson masses in the heavy quark effective theory*, Phys. Rev. D **49** (1994) 2472 [arXiv:hep-ph/9307291].

[140] M. Neubert, *QCD sum rule calculation of the kinetic energy and chromo interaction of heavy quarks inside mesons*, Phys. Lett. B **389** (1996) 727 [arXiv:hep-ph/9608211].

[141] P. Gambino, A. Melis and S. Simula, *Extraction of heavy-quark-expansion parameters from unquenched lattice data on pseudoscalar and vector heavy-light meson masses*, Phys. Rev. D **96** (2017) 014511 [arXiv:1704.06105].

[142] Fermilab Lattice, MILC, TUMQCD collaboration, A. Bazavov et al., *Up-, down-, strange-, charm-, and bottom-quark masses from four-flavor lattice QCD*, Phys. Rev. D **98** (2018) 054517 [arXiv:1802.04248].

[143] P. Gambino and C. Schwanda, *Inclusive semileptonic fits, heavy quark masses, and V_{cb}*, Phys. Rev. D **89** (2014) 014022 [arXiv:1307.4551].

[144] A. Alberti et al., *Precision Determination of the Cabibbo-Kobayashi-Maskawa Element V_{cb}*, Phys. Rev. Lett. **114** (2015) 061802 [arXiv:1411.6560].

[145] P. Gambino, K. J. Healey and S. Turczyk, *Taming the higher power corrections in semileptonic B decays*, Phys. Lett. B **763** (2016) 60 [arXiv:1606.06174].

[146] M. Bordone, B. Capdevila and P. Gambino, *Three loop calculations and inclusive Vcb*, Phys. Lett. B **822** (2021) 136679 [arXiv:2107.00604].

[147] F. Bernlochner et al., *First extraction of inclusive V_{cb} from q^2 moments*, JHEP **10** (2022) 068 [arXiv:2205.10274].

[148] G. Finauri and P. Gambino, *The q^2 moments in inclusive semileptonic B decays*, JHEP **02** (2024) 206 [arXiv:2310.20324].

[149] I. I. Bigi, T. Mannel and N. Uraltsev, *Semileptonic width ratios among beauty hadrons*, JHEP **09** (2011) 012 [arXiv:1105.4574].

[150] M. Gremm and A. Kapustin, *Order $1/m_b^3$ corrections to $B \to X_c \ell \bar{\nu}$ decay and their implication for the measurement of $\bar{\Lambda}$ and λ_1*, Phys. Rev. D **55** (1997) 6924 [arXiv:hep-ph/9603448].

[151] T. Mannel, A. V. Rusov and F. Shahriaran, *Inclusive semitauonic B decays to order $\mathcal{O}(\Lambda_{QCD}^3/m_b^3)$*, Nucl. Phys. B **921** (2017) 211 [arXiv:1702.01089].

[152] M. Rahimi and K. K. Vos, *Standard Model predictions for lepton flavour universality ratios of inclusive semileptonic B decays*, JHEP **11** (2022) 007 [arXiv:2207.03432].

[153] T. Mannel and A. A. Pivovarov, *QCD corrections to inclusive heavy hadron weak decays at $\Lambda_{\rm QCD}^3/m_Q^3$*, Phys. Rev. D **100** (2019) 093001 [arXiv:1907.09187].

[154] T. Mannel, D. Moreno and A. A. Pivovarov, *NLO QCD corrections to inclusive $b \to c\ell\bar{\nu}$ decay spectra up to $1/m_Q^3$*, Phys. Rev. D **105** (2022) 054033 [arXiv:2112.03875].

[155] D. Moreno, *NLO QCD corrections to inclusive semitauonic weak decays of heavy hadrons up to $1/m_b^3$*, Phys. Rev. D **106** (2022) 114008 [arXiv:2207.14245].

[156] A. Lenz, M. L. Piscopo and A. V. Rusov, *Contribution of the Darwin operator to non-leptonic decays of heavy quarks*, JHEP **12** (2020) 199 [arXiv:2004.09527].

[157] T. Mannel, D. Moreno and A. Pivovarov, *Heavy quark expansion for heavy hadron lifetimes: completing the $1/m_b^3$ corrections*, JHEP **08** (2020) 089 [arXiv:2004.09485].

[158] D. Moreno, *Completing $1/m_b^3$ corrections to non-leptonic bottom-to-up-quark decays*, JHEP **01** (2021) 051 [arXiv:2009.08756].

[159] A. Lenz, M. L. Piscopo and A. V. Rusov, *Disintegration of beauty: a precision study*, JHEP **01** (2023) 004 [arXiv:2208.02643].

[160] T. Mannel, *Higher order $1/m$ corrections at zero recoil*, Phys. Rev. D **50** (1994) 428 [arXiv:hep-ph/9403249].

[161] B. Guberina et al., *D Meson Lifetimes and Decays*, Phys. Lett. B **89** (1979) 111.

[162] M. A. Shifman and M. B. Voloshin, *Hierarchy of Lifetimes of Charmed and Beautiful Hadrons*, Sov. Phys. JETP **64** (1986) 698.

[163] N. G. Uraltsev, *On the problem of boosting nonleptonic b baryon decays*, Phys. Lett. B **376** (1996) 303 [arXiv:hep-ph/9602324].

[164] M. Neubert and C. T. Sachrajda, *Spectator effects in inclusive decays of beauty hadrons*, Nucl. Phys. B **483** (1997) 339 [arXiv:hep-ph/9603202].

[165] M. Beneke et al., *The $B^+ - B_d^0$ Lifetime Difference Beyond Leading Logarithms*, Nucl. Phys. B **639** (2002) 389 [arXiv:hep-ph/0202106].

[166] E. Franco et al., *Lifetime ratios of beauty hadrons at the next-to-leading order in QCD*, Nucl. Phys. B **633** (2002) 212 [arXiv:hep-ph/0203089].

[167] A. Lenz and T. Rauh, *D-meson lifetimes within the heavy quark expansion*, Phys. Rev. D **88** (2013) 034004 [arXiv:1305.3588].

[168] M. Kirk, A. Lenz and T. Rauh, *Dimension-six matrix elements for meson mixing and lifetimes from sum rules*, JHEP **12** (2017) 068 [arXiv:1711.02100], [Erratum: JHEP 06, 162 (2020)].

[169] D. King, A. Lenz and T. Rauh, *SU(3) breaking effects in B and D meson lifetimes*, JHEP **06** (2022) 134 [arXiv:2112.03691].

[170] P. Colangelo and F. De Fazio, *Role of four quark operators in the inclusive Λ_b decays*, Phys. Lett. B **387** (1996) 371 [arXiv:hep-ph/9604425].

[171] UKQCD collaboration, M. Di Pierro and C. T. Sachrajda, *A Lattice study of spectator effects in inclusive decays of B mesons*, Nucl. Phys. B **534** (1998) 373 [arXiv:hep-lat/9805028].

[172] UKQCD collaboration, M. Di Pierro, C. T. Sachrajda and C. Michael, *An Exploratory lattice study of spectator effects in inclusive decays of the Λ_b baryon*, Phys. Lett. B **468** (1999) 143 [arXiv:hep-lat/9906031], [Erratum: Phys.Lett.B 525, 360–360 (2002)].

[173] D. Becirevic, *Theoretical progress in describing the B meson lifetimes*, PoS **HEP2001** (2001) 098 [arXiv:hep-ph/0110124].

[174] B. Chibisov et al., *Operator product expansion, heavy quarks, QCD duality and its violations*, Int. J. Mod. Phys. A **12** (1997) 2075 [arXiv:hep-ph/9605465].

[175] I. I. Y. Bigi and N. Uraltsev, *A Vademecum on quark hadron duality*, Int. J. Mod. Phys. A **16** (2001) 5201 [arXiv:hep-ph/0106346].

[176] I. I. Y. Bigi et al., *Heavy flavor decays, OPE and duality in two-dimensional 't Hooft model*, Phys. Rev. D **59** (1999) 054011 [arXiv:hep-ph/9805241].

[177] B. Grinstein, *Global duality in heavy flavor hadronic decays*, Phys. Lett. B **529** (2002) 99 [arXiv:hep-ph/0112323].

[178] E288 collaboration, S. W. Herb et al., *Observation of a Dimuon Resonance at 9.5-GeV in 400-GeV Proton-Nucleus Collisions*, Phys. Rev. Lett. **39** (1977) 252.

[179] E288 collaboration, W. R. Innes et al., *Observation of Structure in the Υ Region*, Phys. Rev. Lett. **39** (1977) 1240 [Erratum: Phys.Rev.Lett. 39, 1640 (1977)].

[180] CLEO collaboration, D. Andrews et al., *Observation of a Fourth Upsilon State in e+ e- Annihilations*, Phys. Rev. Lett. **45** (1980) 219.

[181] G. Finocchiaro et al., *Observation of the Upsilon"' at CESR*, Phys. Rev. Lett. **45** (1980) 222.

[182] CLEO collaboration, C. Bebek et al., *Evidence for New Flavor Production at the Upsilon (4S)*, Phys. Rev. Lett. **46** (1981) 84.

[183] S. Stone, *The discovery of the B mesons*, AIP Conf. Proc. **424** (1998) 75.

[184] BaBar collaboration, D. Boutigny et al., *The BABAR physics book: Physics at an asymmetric B factory*. 10, 1998, 10.2172/979931.

[185] BaBar, Belle collaboration, A. J. Bevan et al., *The Physics of the B Factories*, Eur. Phys. J. C **74** (2014) 3026 [arXiv:1406.6311].

[186] Belle-II collaboration, W. Altmannshofer et al., *The Belle II Physics Book*, PTEP **2019** (2019) 123C01 [arXiv:1808.10567], [Erratum: PTEP 2020, 029201 (2020)].

[187] G. Borissov, *B-Physics Results from Tevatron*, Int. J. Mod. Phys. A **28** (2013) 1330007 [arXiv:1304.2173].

[188] S. Chen et al., *Heavy Flavour Physics and CP Violation at LHCb: a Ten-Year Review*, Front. Phys. **18** (2023) 44601 [arXiv:2111.14360].

[189] LHCb collaboration, R. Aaij et al., *Measurement of the $B_s^0 \to \mu^+\mu^-$ branching fraction and effective lifetime and search for $B^0 \to \mu^+\mu^-$ decays*, Phys. Rev. Lett. **118** (2017) 191801 [arXiv:1703.05747].

[190] ATLAS collaboration, M. Aaboud et al., *Study of the rare decays of B_s^0 and B^0 mesons into muon pairs using data collected during 2015 and 2016 with the ATLAS detector*, JHEP **04** (2019) 098 [arXiv:1812.03017].

[191] CMS collaboration, A. M. Sirunyan et al., *Measurement of properties of $B_s^0 \to \mu^+\mu^-$ decays and search for $B^0 \to \mu^+\mu^-$ with the CMS experiment*, JHEP **04** (2020) 188 [arXiv:1910.12127].

[192] LHCb Collaboration collaboration, *Combination of the ATLAS, CMS and LHCb results on the $B_{(s)}^0 \to \mu^+\mu^-$ decays*, Tech. Rep. LHCb-CONF-2020-002. CERN-LHCb-CONF-2020-002, CERN, Geneva, Aug, 2020.

[193] LHCb collaboration, R. Aaij et al., *Measurement of the $B_s^0 \to \mu^+\mu^-$ decay properties and search for the $B^0 \to \mu^+\mu^-$ and $B_s^0 \to \mu^+\mu^-\gamma$ decays*, arXiv:2108.09283.

[194] LHCb collaboration, R. Aaij et al., *Analysis of neutral B-meson decays into two muons*, arXiv:2108.09284.

[195] J. Albrecht et al., *Lifetimes of b-hadrons and mixing of neutral B-mesons: theoretical and experimental status*, Eur. Phys. J. ST **233** (2024) 359 [arXiv:2402.04224].

[196] ATLAS collaboration, G. Aad et al., *Measurement of the CP-violating phase ϕ_s in $B_s^0 \to J/\psi\phi$ decays in ATLAS at 13 TeV*, Eur. Phys. J. C **81** (2021) 342 [arXiv:2001.07115].

[197] LHCb collaboration, R. Aaij et al., *Updated measurement of time-dependent CP-violating observables in $B_s^0 \to J/\psi K^+K^-$ decays*, Eur. Phys. J. C **79** (2019) 706 [arXiv:1906.08356], [Erratum: Eur.Phys.J.C 80, 601 (2020)].

[198] LHCb collaboration, I. Bezshyiko et al., *Improved Measurement of CP Violation Parameters in Bs0→J/ψK+K- Decays in the Vicinity of the ϕ(1020) Resonance*, Phys. Rev. Lett. **132** (2024) 051802 [arXiv:2308.01468].

[199] CMS collaboration, A. M. Sirunyan et al., *Measurement of the CP-violating phase ϕ_s in the $B_s^0 \to J/\psi\,\phi(1020) \to \mu^+\mu^-K^+K^-$ channel in proton-proton collisions at $\sqrt{s} = 13$ TeV*, Phys. Lett. B **816** (2021) 136188 [arXiv:2007.02434].

[200] E. Fernandez et al., *Lifetime of Particles Containing B Quarks*, Phys. Rev. Lett. **51** (1983) 1022.

[201] N. Lockyer et al., *Measurement of the Lifetime of Bottom Hadrons*, Phys. Rev. Lett. **51** (1983) 1316.

[202] DELCO collaboration, D. E. Klem et al., *Measurement of the Average B Hadron Lifetime Using Prompt Electrons*, Phys. Rev. Lett. **53** (1984) 1873.

[203] TASSO collaboration, M. Althoff et al., *Determination of the Average Lifetime of Bottom Hadrons*, Phys. Lett. B **149** (1984) 524.

[204] M. Gell-Mann and A. Pais, *Behavior of neutral particles under charge conjugation*, Phys. Rev. **97** (1955) 1387.

[205] K. Lande et al., *Observation of Long-Lived Neutral V Particles*, Phys. Rev. **103** (1956) 1901.

[206] UA1 collaboration, C. Albajar et al., *Search for $B^0 - \bar{B}^0$ oscillations at the CERN proton-antiproton collider*, Phys. Lett. B **186** (1987) 247 [Erratum: Phys.Lett.B 197, 565 (1987)].

[207] ARGUS collaboration, H. Albrecht et al., *Observation of B0 - anti-B0 Mixing*, Phys. Lett. B **192** (1987) 245.

[208] J. R. Ellis et al., *Implications of recent measurements of B meson mixing and ϵ'/ϵ_K*, Nucl. Phys. B **304** (1988) 205.

[209] CDF collaboration, A. Abulencia et al., *Observation of $B_s^0 - \bar{B}_s^0$ Oscillations*, Phys. Rev. Lett. **97** (2006) 242003 [arXiv:hep-ex/0609040].

[210] LHCb collaboration, R. Aaij et al., *Observation of $D^0 - \overline{D}^0$ oscillations*, Phys. Rev. Lett. **110** (2013) 101802 [arXiv:1211.1230].

[211] S. L. Glashow, J. Iliopoulos and L. Maiani, *Weak Interactions with Lepton-Hadron Symmetry*, Phys. Rev. D **2** (1970) 1285.

[212] T. Inami and C. S. Lim, *Effects of Superheavy Quarks and Leptons in Low-Energy Weak Processes $K_L \to \mu\bar{\mu}$, $K^+ \to \pi^+\nu\bar{\nu}$ and $K^0 \leftrightarrow \bar{K}^0$*, Prog. Theor. Phys. **65** (1981) 297 [Erratum: Prog.Theor.Phys. 65, 1772 (1981)].

[213] A. J. Buras, M. Jamin and P. H. Weisz, *Leading and Next-to-leading QCD Corrections to ϵ Parameter and $B^0 - \bar{B}^0$ Mixing in the Presence of a Heavy Top Quark*, Nucl. Phys. B **347** (1990) 491.

[214] ETM collaboration, N. Carrasco et al., *B-physics from $N_f = 2$ tmQCD: the Standard Model and beyond*, JHEP **03** (2014) 016 [arXiv:1308.1851].

[215] RBC collaboration, Y. Aoki et al., *Neutral b meson mixings and b meson decay constants with static heavy and domain-wall light quarks*, Phys.Rev.D **91** (2015) 114505 [arXiv:1406.6192].

[216] HPQCD collaboration, E. Gamiz et al., *Neutral B Meson Mixing in Unquenched Lattice QCD*, Phys. Rev. **D80** (2009) 014503 [arXiv:0902.1815].

[217] R. J. Dowdall et al., *Neutral B-meson mixing from full lattice QCD at the physical point*, Phys. Rev. D **100** (2019) 094508 [arXiv:1907.01025].

[218] RBC/UKQCD collaboration, P. A. Boyle et al., *SU(3)-breaking ratios for $D_{(s)}$ and $B_{(s)}$ mesons*, arXiv:1812.08791.

[219] Fermilab Lattice, MILC collaboration, A. Bazavov et al., *$B^0_{(s)}$-mixing matrix elements from lattice QCD for the Standard Model and beyond*, Phys. Rev. D **93** (2016) 113016 [arXiv:1602.03560].

[220] D. King, A. Lenz and T. Rauh, *B_s mixing observables and $|V_{td}/V_{ts}|$ from sum rules*, JHEP **05** (2019) 034 [arXiv:1904.00940].

[221] A. G. Grozin et al., *$B^0 - \bar{B}^0$ mixing at next-to-leading order*, Phys. Rev. D **94** (2016) 034024 [arXiv:1606.06054].

[222] LHCb collaboration, R. Aaij et al., *Precise determination of the B^0_s–$\overline{B}^0_s$ oscillation frequency*, Nature Phys. **18** (2022) 1 [arXiv:2104.04421].

[223] A. D. Sakharov, *Violation of CP Invariance, C asymmetry, and baryon asymmetry of the universe*, Pisma Zh. Eksp. Teor. Fiz. **5** (1967) 32.

[224] F. R. Klinkhamer and N. S. Manton, *A Saddle Point Solution in the Weinberg-Salam Theory*, Phys. Rev. D **30** (1984) 2212.

[225] K. Kajantie et al., *Is there a hot electroweak phase transition at $m_H \gtrsim m_W$?*, Phys. Rev. Lett. **77** (1996) 2887 [arXiv:hep-ph/9605288].

[226] T. Lee, *A Theory of Spontaneous T Violation*, Phys. Rev. D **8** (1973) 1226.

[227] J. F. Gunion et al., *The Higgs Hunter's Guide*, vol. 80. 2000.

[228] G. Branco et al., *Theory and phenomenology of two-Higgs-doublet models*, Phys. Rept. **516** (2012) 1 [arXiv:1106.0034].

[229] M. Trodden, *Electroweak baryogenesis: A Brief review*, in *33rd Rencontres de Moriond: Electroweak Interactions and Unified Theories*, pp. 471–480, 1998, arXiv:hep-ph/9805252.

[230] J. F. Gunion and H. E. Haber, *The CP conserving two Higgs doublet model: The Approach to the decoupling limit*, Phys. Rev. D **67** (2003) 075019 [arXiv:hep-ph/0207010].

[231] A. Crivellin, D. Müller and C. Wiegand, *$b \to s\ell^+\ell^-$ transitions in two-Higgs-doublet models*, JHEP **06** (2019) 119 [arXiv:1903.10440].

[232] D. Das, A. Kundu and I. Saha, *Higgs data does not rule out a sequential fourth generation with an extended scalar sector*, Phys. Rev. D **97** (2018) 011701 [arXiv:1707.03000].

[233] N. Chen et al., *Type-II 2HDM under the Precision Measurements at the Z-pole and a Higgs Factory*, JHEP **03** (2019) 023 [arXiv:1808.02037].

[234] I. Ginzburg and I. Ivanov, *Tree-level unitarity constraints in the most general 2HDM*, Phys. Rev. D **72** (2005) 115010 [arXiv:hep-ph/0508020].

[235] N. G. Deshpande and E. Ma, *Pattern of Symmetry Breaking with Two Higgs Doublets*, Phys. Rev. D **18** (1978) 2574.

[236] A. Barroso et al., *Metastability bounds on the two Higgs doublet model*, JHEP **06** (2013) 045 [arXiv:1303.5098].

[237] A. Arhrib, *Unitarity constraints on scalar parameters of the standard and two Higgs doublets model*, in *Workshop on Noncommutative Geometry, Superstrings and Particle Physics*, 12, 2000, arXiv:hep-ph/0012353.

[238] J. Horejsi and M. Kladiva, *Tree-unitarity bounds for THDM Higgs masses revisited*, Eur. Phys. J. C **46** (2006) 81 [arXiv:hep-ph/0510154].

[239] B. Grinstein, C. W. Murphy and P. Uttayarat, *One-loop corrections to the perturbative unitarity bounds in the CP-conserving two-Higgs doublet model with a softly broken $\mathbb{Z}_2$ symmetry*, JHEP **06** (2016) 070 [arXiv:1512.04567].

[240] V. Cacchio et al., *Next-to-leading order unitarity fits in Two-Higgs-Doublet models with soft $\mathbb{Z}_2$ breaking*, JHEP **11** (2016) 026 [arXiv:1609.01290].

[241] CMS collaboration, A. M. Sirunyan et al., *Combined measurements of Higgs boson couplings in proton–proton collisions at $\sqrt{s} = 13$ TeV*, Eur. Phys. J. C **79** (2019) 421 [arXiv:1809.10733].

[242] CMS collaboration, A. M. Sirunyan et al., *A search for the standard model Higgs boson decaying to charm quarks*, JHEP **03** (2020) 131 [arXiv:1912.01662].

[243] ATLAS collaboration, G. Aad et al., *Combined measurements of Higgs boson production and decay using up to 80 fb^{-1} of proton-proton collision data at $\sqrt{s} =$ 13 TeV collected with the ATLAS experiment*, Phys. Rev. D **101** (2020) 012002 [arXiv:1909.02845].

[244] ATLAS collaboration, G. Aad et al., *A search for the $Z\gamma$ decay mode of the Higgs boson in pp collisions at $\sqrt{s} = 13$ TeV with the ATLAS detector*, Phys. Lett. B **809** (2020) 135754 [arXiv:2005.05382].

[245] CMS collaboration, *A search for the dimuon decay of the Standard Model Higgs boson with the ATLAS detector*, Tech. Rep. CERN-EP-2020-117, CERN, Geneva, Jul, 2020.

[246] CMS collaboration, *Combined Higgs boson production and decay measurements with up to 137 fb^{-1} of proton–proton collisions at $\sqrt{s} = 13$ TeV*, Tech. Rep. CMS-PAS-HIG-19-005, CERN, Geneva, Jan, 2020.

[247] ATLAS collaboration, *A combination of measurements of Higgs boson production and decay using up to 139 fb^{-1} of proton–proton collision data at $\sqrt{s} = 13$ TeV collected with the ATLAS experiment*, Tech. Rep. ATLAS-CONF-2020-027, CERN, Geneva, Aug, 2020.

[248] CMS collaboration, A. M. Sirunyan et al., *Evidence for Higgs boson decay to a pair of muons*, JHEP **01** (2021) 148 [arXiv:2009.04363].

[249] Flavour Lattice Averaging Group (FLAG) collaboration, Y. Aoki et al., *FLAG Review 2021*, Eur. Phys. J. C **82** (2022) 869 [arXiv:2111.09849].

[250] F. U. Bernlochner et al., *Combined analysis of semileptonic B decays to D and D^*: $R(D^{(*)})$, $|V_{cb}|$, and new physics*, Phys. Rev. D **95** (2017) 115008 [arXiv:1703.05330], [Erratum: Phys.Rev.D 97, 059902 (2018)].

[251] I. Caprini, L. Lellouch and M. Neubert, *Dispersive bounds on the shape of $\bar{B} \to D^{(*)}\ell\bar{\nu}$ form-factors*, Nucl. Phys. B **530** (1998) 153 [arXiv:hep-ph/9712417].

[252] Y. Sakaki, M. Tanaka, A. Tayduganov and R. Watanabe, *Testing leptoquark models in $\bar{B} \to D^{(*)}\tau\bar{\nu}$*, Phys. Rev. D **88** (2013) 094012 [arXiv:1309.0301].

[253] A. Bharucha, D. M. Straub and R. Zwicky, *$B \to V\ell^+\ell^-$ in the Standard Model from light-cone sum rules*, JHEP **08** (2016) 098 [arXiv:1503.05534].

[254] N. Gubernari, A. Kokulu and D. van Dyk, *$B \to P$ and $B \to V$ Form Factors from B-Meson Light-Cone Sum Rules beyond Leading Twist*, JHEP **01** (2019) 150 [arXiv:1811.00983].

[255] W. Detmold and S. Meinel, *$\Lambda_b \to \Lambda\ell^+\ell^-$ form factors, differential branching fraction, and angular observables from lattice QCD with relativistic b quarks*, Phys. Rev. D **93** (2016) 074501 [arXiv:1602.01399].

[256] V. Bernard et al., *$K^L_{\mu 3}$ decay: A Stringent test of right-handed quark currents*, Phys. Lett. B **638** (2006) 480 [arXiv:hep-ph/0603202].

[257] V. Bernard et al., *Dispersive representation and shape of the $K_{\ell 3}$ form factors: Robustness*, Phys. Rev. D **80** (2009) 034034 [arXiv:0903.1654].

[258] FlaviaNet Working Group on Kaon Decays collaboration, M. Antonelli et al., *An Evaluation of $|V_{us}|$ and precise tests of the Standard Model from world data on leptonic and semileptonic kaon decays*, Eur. Phys. J. C **69** (2010) 399 [arXiv:1005.2323].

[259] E. McLean et al., *$B_s \to D_s\ell\nu$ Form Factors for the full q^2 range from Lattice QCD with non-perturbatively normalized currents*, Phys. Rev. D **101** (2020) 074513 [arXiv:1906.00701].

[260] LHCb collaboration, R. Aaij et al., *Measurement of $|V_{cb}|$ with $B^0_s \to D_s^{(*)-}\mu^+\nu_\mu$ decays*, Phys. Rev. D **101** (2020) 072004 [arXiv:2001.03225].

[261] LHCb collaboration, R. Aaij et al., *Precise measurement of the f_s/f_d ratio of fragmentation fractions and of B^0_s decay branching fractions*, Phys. Rev. D **104** (2021) 032005 [arXiv:2103.06810].

[262] L. Di Luzio et al., *ΔM_s theory precision confronts flavour anomalies*, JHEP **12** (2019) 009 [arXiv:1909.11087].

[263] M. Misiak, A. Rehman and M. Steinhauser, *Towards $\overline{B} \to X_s\gamma$ at the NNLO in QCD without interpolation in m_c*, JHEP **06** (2020) 175 [arXiv:2002.01548].

[264] M. Misiak and M. Steinhauser, *NNLO QCD corrections to the anti-B —> X(s) gamma matrix elements using interpolation in m(c)*, Nucl. Phys. B **764** (2007) 62 [arXiv:hep-ph/0609241].

[265] M. Misiak et al., *Updated NNLO QCD predictions for the weak radiative B-meson decays*, Phys. Rev. Lett. **114** (2015) 221801 [arXiv:1503.01789].

[266] CLEO collaboration, S. Chen et al., *Branching fraction and photon energy spectrum for $b \to s\gamma$*, Phys. Rev. Lett. **87** (2001) 251807 [arXiv:hep-ex/0108032].

[267] BaBar collaboration, J. P. Lees et al., *Precision Measurement of the $B \to X_s\gamma$ Photon Energy Spectrum, Branching Fraction, and Direct CP Asymmetry $A_{CP}(B \to X_{s+d}\gamma)$*, Phys. Rev. Lett. **109** (2012) 191801 [arXiv:1207.2690].

[268] Belle collaboration, A. Abdesselam et al., *Measurement of the inclusive $B \to X_{s+d}\gamma$ branching fraction, photon energy spectrum and HQE parameters*, in *38th International Conference on High Energy Physics*, 8, 2016, arXiv:1608.02344.

[269] W. Altmannshofer and P. Stangl, *New Physics in Rare B Decays after Moriond 2021*, arXiv:2103.13370.

[270] G. Buchalla and A. J. Buras, *QCD corrections to rare K and B decays for arbitrary top quark mass*, Nucl. Phys. B **400** (1993) 225.

[271] C. Bobeth et al., *$B_{s,d} \to l^+l^-$ in the Standard Model with Reduced Theoretical Uncertainty*, Phys. Rev. Lett. **112** (2014) 101801 [arXiv:1311.0903].

[272] M. Beneke, C. Bobeth and R. Szafron, *Power-enhanced leading-logarithmic QED corrections to $B_q \to \mu^+\mu^-$*, JHEP **10** (2019) 232 [arXiv:1908.07011].

[273] ETM collaboration, A. Bussone et al., *Mass of the b quark and B -meson decay constants from N_f=2+1+1 twisted-mass lattice QCD*, Phys. Rev. D **93** (2016) 114505 [arXiv:1603.04306].

[274] A. Bazavov et al., *B- and D-meson leptonic decay constants from four-flavor lattice QCD*, Phys. Rev. D **98** (2018) 074512 [arXiv:1712.09262].

[275] C. Hughes, C. T. H. Davies and C. J. Monahan, *New methods for B meson decay constants and form factors from lattice NRQCD*, Phys. Rev. D **97** (2018) 054509 [arXiv:1711.09981].

[276] LHCb collaboration, R. Aaij et al., *Differential branching fractions and isospin asymmetries of $B \to K^{(*)}\mu^+\mu^-$ decays*, JHEP **06** (2014) 133 [arXiv:1403.8044].

[277] LHCb collaboration, R. Aaij et al., *Angular analysis of the $B^+ \to K^{*+}\mu^+\mu^-$ decay*, arXiv:2012.13241.

[278] LHCb collaboration, R. Aaij et al., *Measurement of CP-Averaged Observables in the $B^0 \to K^{*0}\mu^+\mu^-$ Decay*, Phys. Rev. Lett. **125** (2020) 011802 [arXiv:2003.04831].

[279] ATLAS collaboration, M. Aaboud et al., *Angular analysis of $B^0_d \to K^*\mu^+\mu^-$ decays in pp collisions at $\sqrt{s} = 8$ TeV with the ATLAS detector*, JHEP **10** (2018) 047 [arXiv:1805.04000].

[280] CMS collaboration, V. Khachatryan et al., *Angular analysis of the decay $B^0 \to K^{*0}\mu^+\mu^-$ from pp collisions at $\sqrt{s} = 8$ TeV*, Phys. Lett. B **753** (2016) 424 [arXiv:1507.08126].

[281] CMS collaboration, A. M. Sirunyan et al., *Measurement of angular parameters from the decay $\mathrm{B}^0 \to \mathrm{K}^{*0}\mu^+\mu^-$ in proton-proton collisions at $\sqrt{s} = 8$ TeV*, Phys. Lett. B **781** (2018) 517 [arXiv:1710.02846].

[282] Belle collaboration, A. Abdesselam et al., *Test of lepton flavor universality in $B \to K\ell^+\ell^-$ decays*, arXiv:1908.01848.

[283] LHCb collaboration, R. Aaij et al., *Precise measurement of the f_s/f_d ratio of fragmentation fractions and of B^0_s decay branching fractions*, arXiv:2103.06810.

[284] LHCb collaboration, R. Aaij et al., *Angular analysis and differential branching fraction of the decay $B^0_s \to \phi\mu^+\mu^-$*, JHEP **09** (2015) 179 [arXiv:1506.08777].

[285] BaBar collaboration, J. Lees et al., *Measurement of the $B \to X_s l^+ l^-$ branching fraction and search for direct CP violation from a sum of exclusive final states*, Phys. Rev. Lett. **112** (2014) 211802 [arXiv:1312.5364].

[286] Belle collaboration, S. Wehle et al., *Lepton-Flavor-Dependent Angular Analysis of $B \to K^*\ell^+\ell^-$*, Phys. Rev. Lett. **118** (2017) 111801 [arXiv:1612.05014].

[287] LHCb collaboration, R. Aaij et al., *Angular analysis of the $B^0 \to K^{*0}e^+e^-$ decay in the low-q^2 region*, JHEP **04** (2015) 064 [arXiv:1501.03038].

[288] CMS collaboration, A. M. Sirunyan et al., *Angular analysis of the decay $B^+ \to K^+\mu^+\mu^-$ in proton-proton collisions at $\sqrt{s} = 8$ TeV*, Phys. Rev. D **98** (2018) 112011 [arXiv:1806.00636].

[289] LHCb collaboration, R. Aaij et al., *Differential branching fraction and angular analysis of $\Lambda^0_b \to \Lambda\mu^+\mu^-$ decays*, JHEP **06** (2015) 115 [arXiv:1503.07138], [Erratum: JHEP 09, 145 (2018)].

[290] LHCb collaboration, R. Aaij et al., *Angular moments of the decay $\Lambda^0_b \to \Lambda\mu^+\mu^-$ at low hadronic recoil*, JHEP **09** (2018) 146 [arXiv:1808.00264].

[291] A. Khodjamirian et al., *Charm-loop effect in $B \to K^{(*)}\ell^+\ell^-$ and $B \to K^*\gamma$*, JHEP **09** (2010) 089 [arXiv:1006.4945].

[292] A. Khodjamirian, T. Mannel and Y. M. Wang, *$B \to K\ell^+\ell^-$ decay at large hadronic recoil*, JHEP **02** (2013) 010 [arXiv:1211.0234].

[293] A. Khodjamirian and A. V. Rusov, *$B_s \to K\ell\nu_\ell$ and $B_{(s)} \to \pi(K)\ell^+\ell^-$ decays at large recoil and CKM matrix elements*, JHEP **08** (2017) 112 [arXiv:1703.04765].

[294] M. Algueró et al., *Emerging patterns of New Physics with and without Lepton Flavour Universal contributions*, Eur. Phys. J. C **79** (2019) 714 [arXiv:1903.09578], [Addendum: Eur.Phys.J.C 80, 511 (2020)].

[295] T. Hurth, F. Mahmoudi and S. Neshatpour, *Model independent analysis of the angular observables in $B^0 \to K^{*0}\mu^+\mu^-$ and $B^+ \to K^{*+}\mu^+\mu^-$*, Phys. Rev. D **103** (2021) 095020 [arXiv:2012.12207].

[296] A. K. Alok et al., *Continuing search for new physics in $b \to s\mu\mu$ decays: two operators at a time*, JHEP **06** (2019) 089 [arXiv:1903.09617].

[297] M. Ciuchini et al., *New Physics in $b \to s\ell^+\ell^-$ confronts new data on Lepton Universality*, Eur. Phys. J. C **79** (2019) 719 [arXiv:1903.09632].

[298] T. Hurth, F. Mahmoudi and S. Neshatpour, *Implications of the new LHCb angular analysis of $B \to K^*\mu^+\mu^-$: Hadronic effects or new physics?*, Phys. Rev. D **102** (2020) 055001 [arXiv:2006.04213].

[299] T. Hurth et al., *More Indications for Lepton Nonuniversality in $b \to s\ell^+\ell^-$*, arXiv:2104.10058.

[300] M. Algueró et al., ***$b \to s\ell\ell$** global fits after Moriond 2021 results*, in *55th Rencontres de Moriond on QCD and High Energy Interactions*, 4, 2021, arXiv:2104.08921.

[301] C. Cornella et al., *Reading the footprints of the B-meson flavor anomalies*, arXiv:2103.16558.

[302] L.-S. Geng et al., *Implications of new evidence for lepton-universality violation in $b \to s\ell^+\ell^-$ decays*, arXiv:2103.12738.

[303] M. Ciuchini et al., *Lessons from the $B^{0,+} \to K^{*0,+}\mu^+\mu^-$ angular analyses*, Phys. Rev. D **103** (2021) 015030 [arXiv:2011.01212].

[304] F. Munir Bhutta et al., *New Physics in $b \to s\ell\ell$ anomalies and its implications for the complementary neutral current decays*, arXiv:2009.03588.

[305] A. Biswas et al., *New physics in $b \to s\ell\ell$ decays with complex Wilson coefficients*, arXiv:2004.14687.

[306] C. Bobeth, G. Hiller and G. Piranishvili, *Angular distributions of $\bar{B} \to \bar{K}\ell^+\ell^-$ decays*, JHEP **12** (2007) 040 [arXiv:0709.4174].

[307] M. Bordone, G. Isidori and A. Pattori, *On the Standard Model predictions for R_K and R_{K^*}*, Eur. Phys. J. C **76** (2016) 440 [arXiv:1605.07633].

[308] LHCb collaboration, R. Aaij et al., *Test of lepton universality in beauty-quark decays*, arXiv:2103.11769.

[309] LHCb collaboration, R. Aaij et al., *Test of lepton universality with $B^0 \to K^{*0}\ell^+\ell^-$ decays*, JHEP **08** (2017) 055 [arXiv:1705.05802].

[310] BaBar collaboration, J. P. Lees et al., *Measurement of Branching Fractions and Rate Asymmetries in the Rare Decays $B \to K^{(*)}l^+l^-$*, Phys. Rev. D **86** (2012) 032012 [arXiv:1204.3933].

[311] Belle collaboration, A. Abdesselam et al., *Test of lepton flavor universality in $B \to K^*\ell^+\ell^-$ decays at Belle*, arXiv:1904.02440.

[312] ALEPH, DELPHI, L3, OPAL, LEP Working Group for Higgs Boson Searches collaboration, S. Schael et al., *Search for neutral MSSM Higgs bosons at LEP*, Eur. Phys. J. C **47** (2006) 547 [arXiv:hep-ex/0602042].

[313] Muon g-2 collaboration, G. W. Bennett et al., *Final Report of the Muon E821 Anomalous Magnetic Moment Measurement at BNL*, Phys. Rev. D **73** (2006) 072003 [arXiv:hep-ex/0602035].

[314] Muon g-2 collaboration, B. Abi et al., *Measurement of the Positive Muon Anomalous Magnetic Moment to 0.46 ppm*, Phys. Rev. Lett. **126** (2021) 141801 [arXiv:2104.03281].

[315] P. Athron et al., *New physics explanations of a_μ in light of the FNAL muon $g-2$ measurement*, JHEP **09** (2021) 080 [arXiv:2104.03691].

[316] V. Ilisie, *New Barr-Zee contributions to $(\mathbf{g-2})_\mu$ in two-Higgs-doublet models*, JHEP **04** (2015) 077 [arXiv:1502.04199].

[317] S. M. Barr and A. Zee, *Electric Dipole Moment of the Electron and of the Neutron*, Phys. Rev. Lett. **65** (1990) 21 [Erratum: Phys.Rev.Lett. 65, 2920 (1990)].

[318] T. Aoyama et al., *The anomalous magnetic moment of the muon in the Standard Model*, Phys. Rept. **887** (2020) 1 [arXiv:2006.04822].

[319] D. Giusti and S. Simula, *Lepton anomalous magnetic moments in Lattice QCD+QED*, PoS **LATTICE2019** (2019) 104 [arXiv:1910.03874].

[320] D. Giusti, F. Sanfilippo and S. Simula, *Light-quark contribution to the leading hadronic vacuum polarization term of the muon $g-2$ from twisted-mass fermions*, Phys. Rev. D **98** (2018) 114504 [arXiv:1808.00887].

[321] Fermilab Lattice, LATTICE-HPQCD, MILC collaboration, C. T. H. Davies et al., *Hadronic-vacuum-polarization contribution to the muon's anomalous magnetic moment from four-flavor lattice QCD*, Phys. Rev. D **101** (2020) 034512 [arXiv:1902.04223].

[322] Budapest-Marseille-Wuppertal collaboration, S. Borsanyi et al., *Hadronic vacuum polarization contribution to the anomalous magnetic moments of leptons from first principles*, Phys. Rev. Lett. **121** (2018) 022002 [arXiv:1711.04980].

[323] B. Chakraborty et al., *The hadronic vacuum polarization contribution to a_μ from full lattice QCD*, Phys. Rev. D **96** (2017) 034516 [arXiv:1601.03071].

[324] ETM collaboration, F. Burger et al., *Four-Flavour Leading-Order Hadronic Contribution To The Muon Anomalous Magnetic Moment*, JHEP **02** (2014) 099 [arXiv:1308.4327].

[325] A. Gérardin et al., *The leading hadronic contribution to $(g-2)_\mu$ from lattice QCD with $N_\mathrm{f}=2+1$ flavours of O(a) improved Wilson quarks*, Phys. Rev. D **100** (2019) 014510 [arXiv:1904.03120].

[326] PACS collaboration, E. Shintani and Y. Kuramashi, *Hadronic vacuum polarization contribution to the muon $g-2$ with 2+1 flavor lattice QCD on a larger than (10 fm)^4 lattice at the physical point*, Phys. Rev. D **100** (2019) 034517 [arXiv:1902.00885].

[327] RBC, UKQCD collaboration, T. Blum et al., *Calculation of the hadronic vacuum polarization contribution to the muon anomalous magnetic moment*, Phys. Rev. Lett. **121** (2018) 022003 [arXiv:1801.07224].

[328] M. Della Morte et al., *The hadronic vacuum polarization contribution to the muon $g-2$ from lattice QCD*, JHEP **10** (2017) 020 [arXiv:1705.01775].

[329] S. Borsanyi et al., *Leading hadronic contribution to the muon magnetic moment from lattice QCD*, Nature **593** (2021) 51 [arXiv:2002.12347].

[330] D. Giusti and S. Simula, *Window contributions to the muon hadronic vacuum polarization with twisted-mass fermions*, PoS **LATTICE2021** (2022) 189 [arXiv:2111.15329].

[331] M. Cè et al., *Window observable for the hadronic vacuum polarization contribution to the muon g-2 from lattice QCD*, Phys. Rev. D **106** (2022) 114502 [arXiv:2206.06582].

[332] Extended Twisted Mass collaboration, C. Alexandrou et al., *Lattice calculation of the short and intermediate time-distance hadronic vacuum polarization contributions to the muon magnetic moment using twisted-mass fermions*, Phys. Rev. D **107** (2023) 074506 [arXiv:2206.15084].

[333] RBC, UKQCD collaboration, T. Blum et al., *Update of Euclidean windows of the hadronic vacuum polarization*, Phys. Rev. D **108** (2023) 054507 [arXiv:2301.08696].

[334] A. Boccaletti et al., *High precision calculation of the hadronic vacuum polarisation contribution to the muon anomaly*, arXiv:2407.10913.

[335] LHCb collaboration, R. Aaij et al., *Search for the Rare Decays $B_s^0 \to e^+e^-$ and $B^0 \to e^+e^-$*, Phys. Rev. Lett. **124** (2020) 211802 [arXiv:2003.03999].

[336] R. Fleischer, R. Jaarsma and G. Tetlalmatzi-Xolocotzi, *In Pursuit of New Physics with $B_{s,d}^0 \to \ell^+\ell^-$*, JHEP **05** (2017) 156 [arXiv:1703.10160].

[337] MEG collaboration, A. M. Baldini et al., *Search for the lepton flavour violating decay $\mu^+ \to e^+\gamma$ with the full dataset of the MEG experiment*, Eur. Phys. J. C **76** (2016) 434 [arXiv:1605.05081].

[338] M. S. Lang and U. Nierste, *$b_s \to \mu^+\mu^-$ in a two-higgs-doublet model with flavour-changing up-type yukawa couplings*, JHEP **04** (2024) 047 [arXiv:2212.11086].

[339] M. Lang, *Leptonic Decays of Neutral B Mesons in the Three-Spurion Two-Higgs-Doublet Model*, Ph.D. thesis, KIT, Karlsruhe, KIT, Karlsruhe, 2023. 10.5445/IR/1000167276.

[340] J. C. Pati and A. Salam, *Lepton Number as the Fourth Color*, Phys. Rev. D **10** (1974) 275 [Erratum: Phys.Rev.D 11, 703–703 (1975)].

[341] P. Minkowski, *$\mu \to e\gamma$ at a Rate of One Out of 10^9 Muon Decays?*, Phys. Lett. B **67** (1977) 421.

[342] T. Yanagida, *Horizontal gauge symmetry and masses of neutrinos*, Conf. Proc. C **7902131** (1979) 95.

[343] M. Gell-Mann, P. Ramond and R. Slansky, *Complex Spinors and Unified Theories*, Conf. Proc. C **790927** (1979) 315 [arXiv:1306.4669].

[344] R. N. Mohapatra and G. Senjanovic, *Neutrino Mass and Spontaneous Parity Nonconservation*, Phys. Rev. Lett. **44** (1980) 912.

[345] P. Fileviez Perez and M. B. Wise, *Low Scale Quark-Lepton Unification*, Phys. Rev. D **88** (2013) 057703 [arXiv:1307.6213].

[346] LHCb collaboration, R. Aaij et al., *Test of lepton universality using $B^+ \to K^+\ell^+\ell^-$ decays*, Phys. Rev. Lett. **113** (2014) 151601 [arXiv:1406.6482].

[347] BELLE collaboration, S. Choudhury et al., *Test of lepton flavor universality and search for lepton flavor violation in $B \to K\ell\ell$ decays*, JHEP **03** (2021) 105 [arXiv:1908.01848].

[348] LHCb collaboration, R. Aaij et al., *Measurement of the $B^0 \to K^{*0}e^+e^-$ branching fraction at low dilepton mass*, JHEP **05** (2013) 159 [arXiv:1304.3035].

[349] ALEPH, DELPHI, L3, OPAL, LEP Electroweak Working Group collaboration, J. Alcaraz et al., *A Combination of preliminary electroweak measurements and constraints on the standard model*, arXiv:hep-ex/0612034.

[350] J. M. Maldacena, *The Large N limit of superconformal field theories and supergravity*, Adv. Theor. Math. Phys. **2** (1998) 231 [arXiv:hep-th/9711200].

[351] C. Gattringer and C. B. Lang, *Quantum chromodynamics on the lattice*, vol. 788. Springer, Berlin, 2010, 10.1007/978-3-642-01850-3.

[352] M. Creutz, *Quarks, Gluons and Lattices*. Oxford University Press, 1983, 10.1017/9781009290395.

[353] I. Montvay and G. Munster, *Quantum fields on a lattice*, Cambridge Monographs on Mathematical Physics. Cambridge University Press, 3, 1997, 10.1017/CBO9780511470783.

[354] G. C. Wick, *Properties of Bethe-Salpeter Wave Functions*, Phys. Rev. **96** (1954) 1124.

[355] K. Symanzik, *Continuum Limit and Improved Action in Lattice Theories. 1. Principles and φ^4 Theory*, Nucl. Phys. B **226** (1983) 187.

[356] K. Symanzik, *Continuum Limit and Improved Action in Lattice Theories. 2. O(N) Nonlinear Sigma Model in Perturbation Theory*, Nucl. Phys. B **226** (1983) 205.

[357] M. Luscher and P. Weisz, *Computation of the Action for On-Shell Improved Lattice Gauge Theories at Weak Coupling*, Phys. Lett. B **158** (1985) 250.

[358] G. Curci, P. Menotti and G. Paffuti, *Symanzik's Improved Lagrangian for Lattice Gauge Theory*, Phys. Lett. B **130** (1983) 205 [Erratum: Phys.Lett.B 135, 516 (1984)].

[359] M. Luscher and P. Weisz, *On-shell improved lattice gauge theories*, Commun. Math. Phys. **98** (1985) 433 [Erratum: Commun.Math.Phys. 98, 433 (1985)].

[360] Y. Iwasaki and T. Yoshie, *Renormalization Group Improved Action for SU(3) Lattice Gauge Theory and the String Tension*, Phys. Lett. B **143** (1984) 449.

[361] Y. Iwasaki, *Renormalization Group Analysis of Lattice Theories and Improved Lattice Action. II. Four-dimensional non-Abelian SU(N) gauge model*, arXiv:1111.7054.

[362] Y. Aoki et al., *Domain wall fermions with improved gauge actions*, Phys. Rev. D **69** (2004) 074504 [arXiv:hep-lat/0211023].

[363] RBC/UKQCD collaboration, C. Allton et al., *Physical Results from 2+1 Flavor Domain Wall QCD and SU(2) Chiral Perturbation Theory*, Phys. Rev. **D78** (2008) 114509 [arXiv:0804.0473].

[364] RBC/UKQCD collaboration, Y. Aoki et al., *Continuum Limit Physics from 2+1 Flavor Domain Wall QCD*, Phys.Rev. **D83** (2011) 074508 [arXiv:1011.0892].

[365] RBC/UKQCD collaboration, T. Blum et al., *Domain wall QCD with physical quark masses*, Phys. Rev. **D93** (2016) 074505 [arXiv:1411.7017].

[366] RBC/UKQCD collaboration, P. A. Boyle et al., *The decay constants f_D and f_{D_s} in the continuum limit of $N_f = 2 + 1$ domain wall lattice QCD*, JHEP **12** (2017) 008 [arXiv:1701.02644].

[367] N. Metropolis et al., *Equation of state calculations by fast computing machines*, J. Chem. Phys. **21** (1953) 1087.

[368] W. K. Hastings, *Monte Carlo Sampling Methods Using Markov Chains and Their Applications*, Biometrika **57** (1970) 97.

[369] S. Duane et al., *Hybrid Monte Carlo*, Phys. Lett. B **195** (1987) 216.

[370] G. C. Wick, *The Evaluation of the Collision Matrix*, Phys. Rev. **80** (1950) 268.

[371] B. Sheikholeslami and R. Wohlert, *Improved Continuum Limit Lattice Action for QCD with Wilson Fermions*, Nucl. Phys. B **259** (1985) 572.

[372] A. X. El-Khadra, A. S. Kronfeld and P. B. Mackenzie, *Massive fermions in lattice gauge theory*, Phys. Rev. D **55** (1997) 3933 [arXiv:hep-lat/9604004].

[373] S. Aoki, Y. Kuramashi and S.-i. Tominaga, *Relativistic heavy quarks on the lattice*, Prog. Theor. Phys. **109** (2003) 383 [arXiv:hep-lat/0107009].

[374] N. H. Christ, M. Li and H.-W. Lin, *Relativistic Heavy Quark Effective Action*, Phys. Rev. D **76** (2007) 074505 [arXiv:hep-lat/0608006].

[375] H. B. Nielsen and M. Ninomiya, *No Go Theorem for Regularizing Chiral Fermions*, Phys. Lett. B **105** (1981) 219.

[376] J. B. Kogut and L. Susskind, *Hamiltonian Formulation of Wilson's Lattice Gauge Theories*, Phys. Rev. D **11** (1975) 395.

[377] R. Frezzotti et al., *A Local formulation of lattice QCD without unphysical fermion zero modes*, Nucl. Phys. B Proc. Suppl. **83** (2000) 941 [arXiv:hep-lat/9909003].

[378] P. H. Ginsparg and K. G. Wilson, *A Remnant of Chiral Symmetry on the Lattice*, Phys. Rev. D **25** (1982) 2649.

[379] D. B. Kaplan, *A Method for simulating chiral fermions on the lattice*, Phys. Lett. B **288** (1992) 342 [arXiv:hep-lat/9206013].

[380] Y. Shamir, *Chiral fermions from lattice boundaries*, Nucl. Phys. B **406** (1993) 90 [arXiv:hep-lat/9303005].

[381] Y. Shamir, *Constraints on the existence of chiral fermions in interacting lattice theories*, Phys. Rev. Lett. **71** (1993) 2691 [arXiv:hep-lat/9306023].

[382] Y. Shamir, *Anomalies and chiral defects fermions*, Nucl. Phys. B **417** (1994) 167 [arXiv:hep-lat/9310006].

[383] V. Furman and Y. Shamir, *Axial symmetries in lattice QCD with Kaplan fermions*, Nucl. Phys. B **439** (1995) 54 [arXiv:hep-lat/9405004].

[384] H. Neuberger, *Exactly massless quarks on the lattice*, Phys. Lett. B **417** (1998) 141 [arXiv:hep-lat/9707022].

[385] H. Neuberger, *More about exactly massless quarks on the lattice*, Phys. Lett. B **427** (1998) 353 [arXiv:hep-lat/9801031].

[386] A. Borici, *Truncated overlap fermions: The Link between overlap and domain wall fermions*, NATO Sci. Ser. C **553** (2000) 41 [arXiv:hep-lat/9912040].

[387] A. D. Kennedy, *Algorithms for dynamical fermions*, arXiv:hep-lat/0607038.

[388] P. M. Vranas, *Chiral symmetry restoration in the Schwinger model with domain wall fermions*, Phys. Rev. D **57** (1998) 1415 [arXiv:hep-lat/9705023].

[389] R. C. Brower, H. Neff and K. Orginos, *Mobius fermions: Improved domain wall chiral fermions*, Nucl. Phys. B Proc. Suppl. **140** (2005) 686 [arXiv:hep-lat/0409118].

[390] R. C. Brower, H. Neff and K. Orginos, *Mobius fermions*, Nucl. Phys. B Proc. Suppl. **153** (2006) 191 [arXiv:hep-lat/0511031].

[391] R. C. Brower, H. Neff and K. Orginos, *The Möbius domain wall fermion algorithm*, Comput. Phys. Commun. **220** (2017) 1 [arXiv:1206.5214].

[392] T.-W. Chiu, *Beauty mesons in N_f=2+1+1+1 lattice QCD with exact chiral symmetry*, Phys. Rev. D **102** (2020) 034510 [arXiv:2004.02142].

[393] R. Sommer, *A New way to set the energy scale in lattice gauge theories and its applications to the static force and α_s in SU(2) Yang-Mills theory*, Nucl. Phys. B **411** (1994) 839 [arXiv:hep-lat/9310022].

[394] M. Lüscher, *Properties and uses of the Wilson flow in lattice QCD*, JHEP **08** (2010) 071 [arXiv:1006.4518], [Erratum: JHEP 03, 092 (2014)].

[395] BMW collaboration, S. Borsányi et al., *High-precision scale setting in lattice QCD*, JHEP **09** (2012) 010 [arXiv:1203.4469].

[396] M. R. Hestenes et al., *Methods of conjugate gradients for solving linear systems*, vol. 49. NBS Washington, DC, 1952.

[397] P. A. Boyle, *Hierarchically deflated conjugate gradient*, arXiv:1402.2585.

[398] P. A. Boyle et al., *Use of stochastic sources for the lattice determination of light quark physics*, JHEP **08** (2008) 086 [arXiv:0804.1501].

[399] UKQCD collaboration, C. McNeile and C. Michael, *Decay width of light quark hybrid meson from the lattice*, Phys. Rev. D **73** (2006) 074506 [arXiv:hep-lat/0603007].

[400] S.-J. Dong and K.-F. Liu, *Stochastic estimation with Z(2) noise*, Phys. Lett. B **328** (1994) 130 [arXiv:hep-lat/9308015].

[401] UKQCD collaboration, M. Foster and C. Michael, *Quark mass dependence of hadron masses from lattice QCD*, Phys. Rev. D **59** (1999) 074503 [arXiv:hep-lat/9810021].

[402] T. Blum, T. Izubuchi and E. Shintani, *New class of variance-reduction techniques using lattice symmetries*, Phys. Rev. D **88** (2013) 094503 [arXiv:1208.4349].

[403] T. Blum, T. Izubuchi and E. Shintani, *Error reduction technique using covariant approximation and application to nucleon form factor*, PoS **LATTICE2012** (2012) 262 [arXiv:1212.5542].

[404] E. Shintani et al., *Covariant approximation averaging*, Phys. Rev. D **91** (2015) 114511 [arXiv:1402.0244].

[405] A. S. Gambhir, A. Stathopoulos and K. Orginos, *Deflation as a Method of Variance Reduction for Estimating the Trace of a Matrix Inverse*, SIAM J. Sci. Comput. **39** (2017) A532 [arXiv:1603.05988].

[406] Hadron Spectrum collaboration, M. Peardon et al., *A Novel quark-field creation operator construction for hadronic physics in lattice QCD*, Phys. Rev. D **80** (2009) 054506 [arXiv:0905.2160].

[407] S. Gusken et al., *Nonsinglet Axial Vector Couplings of the Baryon Octet in Lattice QCD*, Phys. Lett. B **227** (1989) 266.

[408] W. E. Caswell and G. P. Lepage, *Effective Lagrangians for Bound State Problems in QED, QCD, and Other Field Theories*, Phys. Lett. B **167** (1986) 437.

[409] B. A. Thacker and G. P. Lepage, *Heavy quark bound states in lattice QCD*, Phys. Rev. D **43** (1991) 196.

[410] G. P. Lepage et al., *Improved nonrelativistic QCD for heavy quark physics*, Phys. Rev. D **46** (1992) 4052 [arXiv:hep-lat/9205007].

[411] P. Boyle et al., *Domain Wall Charm Physics with Physical Pion Masses: Decay Constants, Bag and ξ Parameters*, PoS **LATTICE2015** (2016) 336 [arXiv:1511.09328].

[412] Y.-G. Cho et al., *Improved lattice fermion action for heavy quarks*, JHEP **05** (2015) 072 [arXiv:1504.01630].

[413] C. Morningstar and M. J. Peardon, *Analytic smearing of SU(3) link variables in lattice QCD*, Phys. Rev. D **69** (2004) 054501 [arXiv:hep-lat/0311018].

[414] P. Boyle et al., *BSM $B - \bar{B}$ mixing on JLQCD and RBC/UKQCD $N_f = 2 + 1$ DWF ensembles*, PoS **LATTICE2021** (2022) 224 [arXiv:2111.11287].

[415] M. Luscher, *Volume Dependence of the Energy Spectrum in Massive Quantum Field Theories. 1. Stable Particle States*, Commun. Math. Phys. **104** (1986) 177.

[416] G. Colangelo, S. Durr and C. Haefeli, *Finite volume effects for meson masses and decay constants*, Nucl. Phys. B **721** (2005) 136 [arXiv:hep-lat/0503014].

[417] N. Carrasco et al., *QED Corrections to Hadronic Processes in Lattice QCD*, Phys. Rev. D **91** (2015) 074506 [arXiv:1502.00257].

[418] P. Colangelo and A. Khodjamirian, *QCD sum rules, a modern perspective*, arXiv:hep-ph/0010175.

[419] E. de Rafael, *An Introduction to sum rules in QCD: Course*, in *Les Houches Summer School in Theoretical Physics, Session 68: Probing the Standard Model of Particle Interactions*, pp. 1171–1218, 7, 1997, arXiv:hep-ph/9802448.

[420] S. Narison, *QCD spectral sum rules for heavy flavors*, Acta Phys. Polon. B **26** (1995) 687 [arXiv:hep-ph/9503234].

[421] L. J. Reinders, H. Rubinstein and S. Yazaki, *Hadron Properties from QCD Sum Rules*, Phys. Rept. **127** (1985) 1.

[422] M. A. Shifman, *Quark hadron duality*, in *8th International Symposium on Heavy Flavor Physics*, vol. 3, (Singapore), pp. 1447–1494, World Scientific, 7, 2000, arXiv:hep-ph/0009131, DOI.

[423] D. J. Broadhurst and A. G. Grozin, *Operator product expansion in static quark effective field theory: Large perturbative correction*, Phys. Lett. B **274** (1992) 421 [arXiv:hep-ph/9908363].

[424] E. Bagan et al., *QCD sum rules in the effective heavy quark theory*, Phys. Lett. B **278** (1992) 457.

[425] M. Neubert, *Heavy meson form-factors from QCD sum rules*, Phys. Rev. D **45** (1992) 2451.

[426] Tsang, Justus Tobias, $B_{(s)}$-mixing parameters from all-domain-wall-fermion simulations. Parallel Talk Lattice 2023, Fermilab, Illinois, USA, 2023.

[427] G. Isidori, G. Martinelli and P. Turchetti, *Rare kaon decays on the lattice*, Phys. Lett. B **633** (2006) 75 [arXiv:hep-lat/0506026].

[428] RBC, UKQCD collaboration, N. H. Christ et al., *Prospects for a lattice computation of rare kaon decay amplitudes: $K \to \pi\ell^+\ell^-$ decays*, Phys. Rev. D **92** (2015) 094512 [arXiv:1507.03094].

[429] N. H. Christ et al., *First exploratory calculation of the long-distance contributions to the rare kaon decays $K \to \pi\ell^+\ell^-$*, Phys. Rev. D **94** (2016) 114516 [arXiv:1608.07585].

[430] RBC, UKQCD collaboration, P. A. Boyle et al., *Simulating rare kaon decays $K+\to\pi+\ell+\ell-$ using domain wall lattice QCD with physical light quark masses*, Phys. Rev. D **107** (2023) L011503 [arXiv:2202.08795].

[431] J. Lin, W. Detmold and S. Meinel, *Lattice Study of Spectator Effects in b-hadron Decays*, PoS **LATTICE2022** (2023) 417 [arXiv:2212.09275].

[432] R. Narayanan and H. Neuberger, *Infinite N phase transitions in continuum Wilson loop operators*, JHEP **03** (2006) 064 [arXiv:hep-th/0601210].

[433] M. Lüscher, *Trivializing maps, the Wilson flow and the HMC algorithm*, Commun. Math. Phys. **293** (2010) 899 [arXiv:0907.5491].

[434] M. Lüscher and P. Weisz, *Perturbative analysis of the gradient flow in non-abelian gauge theories*, JHEP **02** (2011) 051 [arXiv:1101.0963].

[435] H. Suzuki, *Energy–momentum tensor from the Yang–Mills gradient flow*, PTEP **2013** (2013) 083B03 [arXiv:1304.0533], [Erratum: PTEP 2015, 079201 (2015)].

[436] H. Makino and H. Suzuki, *Lattice energy–momentum tensor from the Yang–Mills gradient flow—inclusion of fermion fields*, PTEP **2014** (2014) 063B02 [arXiv:1403.4772], [Erratum: PTEP 2015, 079202 (2015)].

[437] C. Monahan and K. Orginos, *Locally smeared operator product expansions in scalar field theory*, Phys. Rev. D **91** (2015) 074513 [arXiv:1501.05348].

[438] WHOT-QCD collaboration, Y. Taniguchi et al., *N_f = 2+1 QCD thermodynamics with gradient flow using two-loop matching coefficients*, Phys. Rev. D **102** (2020) 014510 [arXiv:2005.00251], [Erratum: Phys.Rev.D 102, 059903 (2020)].

[439] H. Suzuki and H. Takaura, *$t \to 0$ extrapolation function in the small flow time expansion method for the energy–momentum tensor*, PTEP **2021** (2021) 073B02 [arXiv:2102.02174].

[440] A. Suzuki et al., *Four quark operators for kaon bag parameter with gradient flow*, Phys. Rev. D **102** (2020) 034508 [arXiv:2006.06999].

[441] R. V. Harlander, Y. Kluth and F. Lange, *The two-loop energy–momentum tensor within the gradient-flow formalism*, Eur. Phys. J. C **78** (2018) 944 [arXiv:1808.09837], [Erratum: Eur.Phys.J.C 79, 858 (2019)].

[442] SymLat collaboration, M. D. Rizik, C. J. Monahan and A. Shindler, *Short flow-time coefficients of CP-violating operators*, Phys. Rev. D **102** (2020) 034509 [arXiv:2005.04199].

[443] M. Lüscher, *Chiral symmetry and the Yang–Mills gradient flow*, JHEP **04** (2013) 123 [arXiv:1302.5246].

[444] M. Lüscher, *Future applications of the Yang-Mills gradient flow in lattice QCD*, PoS **LATTICE2013** (2014) 016 [arXiv:1308.5598].

[445] M. Lüscher, *Step scaling and the Yang-Mills gradient flow*, JHEP **06** (2014) 105 [arXiv:1404.5930].

[446] L. Del Debbio, A. Patella and A. Rago, *Space-time symmetries and the Yang-Mills gradient flow*, JHEP **11** (2013) 212 [arXiv:1306.1173].

[447] A. Shindler, *Gradient Flow: Perturbative and Non-Perturbative Renormalization*, EPJ Web Conf. **274** (2022) 01005 [arXiv:2301.07438].

[448] Z. Fodor, K. Holland, J. Kuti, D. Nogradi and C. H. Wong, *The Yang-Mills gradient flow in finite volume*, JHEP **11** (2012) 007 [arXiv:1208.1051].

[449] A. Hasenfratz and O. Witzel, *Continuous renormalization group β function from lattice simulations*, Phys. Rev. D **101** (2020) 034514 [arXiv:1910.06408].

[450] O. Witzel. private communication.

[451] A. Carosso, A. Hasenfratz and E. T. Neil, *Nonperturbative Renormalization of Operators in Near-Conformal Systems Using Gradient Flows*, Phys. Rev. Lett. **121** (2018) 201601 [arXiv:1806.01385].

[452] A. Hasenfratz et al., *A novel nonperturbative renormalization scheme for local operators*, PoS **LATTICE2021** (2022) 155 [arXiv:2201.09740].

[453] R. V. Harlander, F. Lange and T. Neumann, *Hadronic vacuum polarization using gradient flow*, JHEP **08** (2020) 109 [arXiv:2007.01057].

[454] R. V. Harlander and F. Lange, *Effective electroweak Hamiltonian in the gradient-flow formalism*, Phys. Rev. D **105** (2022) L071504 [arXiv:2201.08618].

[455] J. Borgulat et al., *Short-flow-time expansion of quark bilinears through next-to-next-to-leading order QCD*, JHEP **05** (2024) 179 [arXiv:2311.16799].

[456] T. Blum and A. Soni, *QCD with domain wall quarks*, Phys. Rev. **D56** (1997) 174 [arXiv:hep-lat/9611030].

[457] RBC, UKQCD collaboration, P. A. Boyle et al., *Neutral kaon mixing beyond the Standard Model with $n_f = 2 + 1$ chiral fermions. Part 2: non perturbative renormalisation of the $\Delta F = 2$ four-quark operators*, JHEP **10** (2017) 054 [arXiv:1708.03552].

[458] N. Garron, *Fierz transformations and renormalization schemes for fourquark operators*, EPJ Web Conf. **175** (2018) 10005.

[459] P. A. Boyle et al., *Kaon mixing beyond the standard model with physical masses*, arXiv:2404.02297.

[460] RBC/UKQCD collaboration, J. M. Flynn et al., *Exclusive semileptonic $Bs \to K\ell\nu$ decays on the lattice*, Phys. Rev. D **107** (2023) 114512 [arXiv:2303.11280].

[461] P. Boyle et al., github.com/paboyle/Grid: Grid.

[462] P. A. Boyle et al., *Grid: A next generation data parallel C++ QCD library*, PoS **LATTICE2015** (2016) 023.

[463] A. Portelli et al., *github.com/aportelli/hadrons: Hadrons v1.3*, Mar., 2022. 10.5281/zenodo.6382460.

[464] A. Hasenfratz, C. J. Monahan, M. D. Rizik, A. Shindler and O. Witzel. in preparation.

[465] A. Pochinsky, *Writing efficient QCD code made simpler: QA(0)*, PoS **LATTICE2008** (2008) 040.

[466] ETM collaboration, N. Carrasco, P. Dimopoulos, R. Frezzotti, V. Lubicz, G. C. Rossi, S. Simula et al., *$\Delta S=2$ and $\Delta C=2$ bag parameters in the standard model and beyond from $N_f=2+1+1$ twisted-mass lattice QCD*, Phys. Rev. D **92** (2015) 034516 [arXiv:1505.06639].

[467] A. Bazavov et al., *Short-distance matrix elements for D^0-meson mixing for $N_f = 2 + 1$ lattice QCD*, Phys. Rev. D **97** (2018) 034513 [arXiv:1706.04622].

[468] P. T. Matthews and A. Salam, *The Green's functions of quantized fields*, Nuovo Cim. **12** (1954) 563.

[469] P. T. Matthews and A. Salam, *Propagators of quantized field*, Nuovo Cim. **2** (1955) 120.

[470] M. H. Quenouille, *Notes on bias in estimation*, Biometrika **43** (1956) 353.

[471] J. Tukey, *Bias and confidence in not quite large samples*, Ann. Math. Statist. **29** (1958) 614.